ON THE THERMOMECHANICAL BEHAVIOR OF EPOXY POLYMERS: EXPERIMENTS AND MODELING

A Dissertation

by

XAVIER MARC NICOLAS POULAIN

Submitted to the Office of Graduate Studies of
Texas A&M University
in partial fulfillment of the requirements for the degree of

DOCTOR OF PHILOSOPHY

December 2010

Major Subject: Aerospace Engineering

ON THE THERMOMECHANICAL BEHAVIOR OF EPOXY POLYMERS: EXPERIMENTS AND MODELING

A Dissertation

by

XAVIER MARC NICOLAS POULAIN

Submitted to the Office of Graduate Studies of
Texas A&M University
in partial fulfillment of the requirements for the degree of

DOCTOR OF PHILOSOPHY

Approved by:

Chair of Committee,	Amine Benzerga
Committee Members,	Ramesh Talreja
	Vikram Kinra
	Theofanis Strouboulis
	Anastasia Muliana
Head of Department,	Dimitris Lagoudas

December 2010

Major Subject: Aerospace Engineering

ABSTRACT

On the Thermomechanical Behavior of Epoxy Polymers:
Experiments and Modeling. (December 2010)
Xavier Marc Nicolas Poulain, B.S., CESTI/Supmeca;
M.S., Universite Paris VI
Chair of Advisory Committee: Dr. Amine Benzerga

Amorphous polymers under their glass transition temperature (T_g) exhibit large inelastic deformations. Their mechanical behavior is highly dependent upon temperature, strain rate, pressure and loading mode (tension, compression, shear). They also exhibit small strain isotropic hardening, softening and large strain anisotropic rehardening. In addition, while in their glassy state, polymers are far from thermodynamic equilibrium so that their properties may change over time (physical aging). This complex behavior is reflected in the response of composites and affects the onset and propagation of damage therein. Therefore, in order to design polymer composite structures, it is fundamental to develop relevant tools and methodologies which aim at understanding, capturing and predicting the full thermomechanical response of glassy polymers.

In this study, the thermomechanical behavior of a thermosetting polymer epoxy is characterized experimentally for temperatures below T_g. The intrinsic behavior of the polymer is obtained using a new methodology based on digital image correlation (DIC) in combination with video-monitored extensometry. In particular, inelastic flow localization patterns are discussed based on the full-field strain measurements and their connection to the stress-strain curves are highlighted. The Boyce-Parks-Argon

polymer constitutive model, hereafter called the macromolecular model, has been enhanced to describe the thermomechanical behavior of epoxies. The identification of the material parameters involved in the model is described in a detailed procedure that builds on a limited set of experiments. The model is shown to represent adequately the thermomechanical behavior of the studied epoxy over a wide range of temperatures and strain-rates. Using additional high strain-rate data obtained from collaborators on Kolsky bars, the model capabilities are further discussed. Using finite-element implementations of the constitutive model in both quasi-static and dynamic codes, the processes of plastic flow localization are analyzed in tensile and compression specimens. Such analysis can form the basis of an alternative method for identifying the model parameters through inverse identification.

Finally, a preliminary set of experiments were also conducted to investigate the effect of physical aging on the yield behavior and enhance the macromolecular model with the capability of modeling aging effects. Our interpretation of the aging experiments suggests that they are not conclusive and do not permit full determination of model parameters. Specific recommendations are tentatively formulated for conducting aging experiments in the future.

To my family, my friends and those who believed in me and offered their support

ACKNOWLEDGMENTS

First and foremost, I would like to pay deep gratitude to my entire family for all endeavors in my life. I would like to express my sincere thanks to my advisor, Dr. Amine Benzerga, for his financial support, rigor and guidance throughout my Ph.D. studies. I would also like to express my sincere gratitude to my other committee members: Dr. Ramesh Talreja, Dr. Vikram Kinra, Dr. Theofanis Strouboulis and Dr. Anastasia Muliana for their contributions to my education and research. In particular, special thanks to Dr. Benzerga and Dr. Talreja who gave me the opportunity to be a research and teaching assistant. I would like to extend my thanks to Dr. Robert Goldbert and Dr. Gary Roberts from NASA GRC for their scientific contributions and fruitful feedback. I did not want to forget to mention Dr. Jean-Baptiste Leblond, without whom nothing could have been made possible. Special thanks to my fellow students for their friendship and contribution to this dissertation; in particular Anthony De Castro, Soondo Kweon, Guruprasad Padubidri Janardhanachar and Shyam Keralavarma. Finally, I shall aknowledge all my friends here and there for all scientific discussions and support, as well as Mrs. Miriam Alderete and Mrs. Karen Knabe for their administrative help.

TABLE OF CONTENTS

CHAPTER Page

CHAPTER Page

LIST OF TABLES

LIST OF FIGURES

FIGURE Page

FIGURE Page

FIGURE Page

FIGURE Page

FIGURE Page

FIGURE Page

CHAPTER I

INTRODUCTION

A. Motivation

1. Polymer Matrix Composites (PMCs) in the Transportation Industry

Polymer composites offer several advantages over conventional materials. Besides their resistance to corrosion, they usually exhibit superior mechanical properties such as specific stiffness and strength in their reinforced direction(s). Consequently, polymer composites have been introduced as alternative solutions to traditional materials where performance, maintenance and operational cost are of paramount priority. Moreover, they are generally flexible for design although their manufacturing process usually remains more expensive than their metal (steel, aluminium, titanium) counterparts. Therefore, besides entering our daily life through consumer products (i.e. golf shafts, fishing rods, snow skis, motorcycle helmets, etc.) polymer composites have been progressively used for a large range of applications in major, high technology and cutting-edge activity sectors. For instance, as discussed in the review of Ramakrishna et al. (2001), they have been introduced in medicine as prosthesis or bone cement; applications in civil engineering are illustrated in Bakis et al. (2002); bipolar plates for future fuel cells may be made of polymers composites (Hermann et al., 2005); renewable energy such as wind energy has emerged as a booming targeted market (Brondsted et al., 2005); PMCs are present in ballistic applications such as combat helmet, vehicle armour or secure door structures.

This dissertation follows the style of Journal of the Mechanics and Physics of Solids.

Encouraged by the specific properties of polymer composites, the transportation sector rapidly invested in the development of efficient manufacturing process. Benefiting from a decrease in the cost of carbon fiber from $150.00/lb in 1970 to about $8.00/lb thirty years later (the global carbon market is estimated to reach $2.3 billion in 2015) the transportation industry consumed 1.3 billion pounds of composite materials in 2000; the recreational transport market (bicycles, motorcycles, pleasure boats, etc.) represented over $17 billion (Mazumder, 2002). The automobile industry initially took the lead with the incorporation of polymer composite parts in the 1953 Corvette. However, due to difficulties linked to competitive production rate, material costs, recyclability issues, and uncertainties related to crash impact resistance, the use of polymer composites had not been fully explored (Das, 2001). Das (2001) further estimates the increase in cost due to glass-fiber reinforced thermosets or carbon-fiber reinforced thermoplastics between 60% and 200% in comparison with steel unibody. Nevertheless, a new momentum may follow recent progress in nanocomposite technology (Garces et al., 2000). The promotion of natural fibre such as kenaf, flax or jute as "green" composite reinforcement for car body parts (door panels, dashboards, seat backs, etc.) conforms to an overall recycling effort[1] (Holbery and Houston, 2006). As illustration, in 2000, the automobile industry used about 320 million pounds of composites.

In the railway sector, the replacement of heavier materials by polymer composites has started more recently. Besides limiting the consumption of energy, these composite structures present additional benefits. For instance, with a lowered inertia, trains reach their cruising speeds more quickly. Dynamic loads acting on railway tracks are also decreased, which prevents excessive wearing. These new composite so-

[1]In Japan, 95% of vehicle components are to be recycled by 2015.

lutions have been introduced for (non-)structural, internal and external applications. Light thermoplastic sandwich materials are specifically designed with the objectives to decrease railway operational costs and to exhibit enhanced mechanical properties, acoustic and thermal insulation as well as chemical resistance. In the world record speed-breaking TGV, the exterior nose consists of glass/polyester incorporating woven glass fabrics along with chopped strand mat for added strength. Luggage racks, bulkheads, energy absorbers or fishplates are also composite based.

2. PMCs for Aerospace and Aeronautics Applications

In the geopolitical context of the 1950s and 1960s, the Aerospace industry pioneered the insertion of composites as a response to technical challenges. For instance, in low earth orbit, spacecraft structures experience large variations of temperature (>200°C cycles) which could jeopardize spacecraft dimensional stability. A remedy was the development of special carbon epoxy composite laminates with very low coefficient of thermal expansion (Mazumder, 2002).

However, this new composite materials age only really started with the growth of the Aeronautics and Aerospace industry after WWII. High performance and minimum weight have been critically sought in the design of commercial and military aircraft. With the objectives of more important payload and enhanced operating distance capability, the insertion of composites for non-structural parts (followed by structural components) quickly accelerated. It was facilitated by constant progress realized in the synthesis of improved and more affordable materials and by the generalization of efficient processing methods. In the 1940s, fibre reinforcement plastics radome was the first commercial aeronautical application of PMCs. The insertion of glass fibres combined with thermosetting polyester and epoxy resin continued into the early 1960s. The introduction of ultra-high-strength fibres (boron in 1966, carbon in 1968,

aramid (Kevlar) in 1972 and high-performance polyethylene (Spectra) revolutionized the performance, design, and manufacturing process of civilian and military airframes. In the 1970s, composites were utilized in combat aircrafts such as the supersonic fighter F-14, the tactical fighter F-15, the multirole jet fighter F-16 or the strategic bomber B-1. They included doors, horizontal and vertical tails, stabilizer skins, fins, rudders, speed brakes, flaps, inlets (Mazumder, 2002). This constant thrive for polymer based composites is illustrated in the latest generations of military airplanes. The F-22 has composite sine wave wing spar; the primary wing spar of the A400MM is fully made of composite; the JUCAS possesses composite fuselage structures and wings.

Simultaneously, composites were introduced in commercial airliners such as the Boeing 737 or Boeing 767 series with rudders, elevators, ailerons, spoilers, wings and fairings. Airbus A300 in 1969 was the first commercial airliners to incorporate load-bearing carbon composite (e.g. stabilizers). The latest flagship Boeing 787 Dreamliner is composed (in weight) of 50% composites, 20% aluminum, 15% titanium, 10% steel and 5% other materials whereas only 12% composites were present in the 777 series (Boeing, 2010). Solid carbon-fiber laminate trailing edge and ailerons with no honeycomb core were adopted. As a result, a 40,000 pound lighter airplane and 20% in fuel efficiency were obtained, with fewer emissions (about 20%) and an impressive reduction of holes drilled into the fuselage for assembly ($<$ 10,000 holes needed). In the "Airliner Wars", European competitor Airbus adopted a similar strategy to design high performance airplanes. In the A350-XWB, besides improvements of wings design, carbon composite materials were inserted to reduce dead weight, decrease fatigue inspection and reduce corrosion maintenance by 60% (Airbus, 2010). About 25% of the airframe weight of the A380 superjumbo is made of composites. The largest single component of this airplane, the 9,800 pound 23'x20'x7' centre section

wing box is made of carbon composite. More generally, a large range of polymers and reinforcements organized in sophisticated structures emerged: fiberglass, epoxy, carbon fiber, kevlar, nomex or polyimide honeycomb, APC-2, Radel 8320 thermoplastic, PMR-15, polyester, etc. Thermoplastics, carbon-, glass- and quartz-fibre reinforced plastic are used in wings, fuselage sections and doors.

This ferocious rivalry between the two major American and European airliner manufacturers illustrates the 36.4% vs. 51.1% repartition of the $375 billion in 2007 global sales between the European aerospace and the U.S. industry, respectively (Morales et al., 2009). The growth of the aerospace market is bolstered by the emergence of Asian countries. For example, China is expected to spend about $340 billon over the next two decades regarding commercial airplanes. Subsequently, $57 billion worth of composite materials will be consumed by the aerospace industry (Lucintel, 2010). The impetus for improved airplane performance drove airliner manufacturers and their suppliers to develop novel technological solutions involving composite materials. This continuous insertion of PMCs may rise fundamental issues regarding the detection of (fatigue) cracks, toxicity of fumes following a crash, risks of delamination due to the accumulation and expansion of moisture, lightning protection, crashworthiness, etc.

3. Needs for Insertion of PMCs in Turbofan Engines

Conventional materials present in jet engines have been progressively replaced by polymers and polymer based composites. To cite a few, carbon fiber reinforcing epoxy inlet guide vane, PMR-15 nose cone, inlet housing and exhaust flap, or BMI engine fuel pump (Mazumder, 2002). To improve safety, reliability, and lower maintenance, noise and fuel costs, the major jet engine manufacturers have recently invested in polymer composites for structural and other critical components. An average annual

growth of 7% over the next decade is expected with forecast demands of kevlar, glass and carbon fiber and epoxy reaching about 3 million lb in 2016 (Red, 2008). The adoption of composites for lighter engine components is critical. For instance, through a cascading effect, a 1 lb heavier fan blade requires a compensatory weight increase in other parts of the airplane: 1 lb for the fan case, 1/2-lb for rotor and engine structures and 1/4-lb for wing/fuselage (Red, 2008). The lattest GE's turbofan GEnx engine, which equips the Dreamliner, features 1,500 pounds of composites.

In the development of this engine, the traditional utilization of titanium alloys for blades was abandonned in the favor of 10-15% lighter and 100% stronger "GE90-115B" carbon fiber composite. These 46 lb blades were manufactured by CFAN (joint Venture created by Snecma and General Electric) from preforms that comprise up to 1000 plies of unidirectional carbon pre-impregnated tape and fabric near the blade root, with thickness decreasing from 4 in. to about 1/4 in. at the blade tip. After ultrasonic cutting, the preform is put in a mould before resin injection, cure by autoclave or precise press, and milling to give the blade its final chord shape (with titanium leading, tip and trailing edge which provides impact resistance and polyurethane erosion coating). The number of blades also tend to decrease as illustrated by the reduction from 22 blades (GE90 engine) down to 18 (GEnx engine).

The fan case is one of the biggest structures of an aircraft. Lighter turbofans have been recently developed, which resulted in lighter fan cases. However, the relative weight of these fan cases has increased. Indeed, the demand for quieter, more efficient jet engines resulted in higher engine bypass ratios and subsequently bigger fan casings. For instance, the former General Electric 5:3 bypass ratio fan cases CF6-80C2 accounted for about 20% of the total engine weight whereas the more recent 9:5 bypass ratio GEnx-1B represents a weight ratio of 33%. Therefore, it was natural for polymer matrix composites to be selected as materials for the new generation of jet

engine fan cases. GEnx, the first jet engine with both a front fan case and fan blades made of composites, features a 350 pound weight reduction.

Rolls Royce, Honeywell, Snecma and Williams International among others are developing composite jet engine fan casings independently or through joint venture. For instance, CFM International (GE/Snecma) is producing LEAP56 composite turbofan engine with composite fan containment case which propulses the Airbus A320 and Boeing 737 families. The LEAP-X technologies are adopted for the narrow-body airliner Comac C919. Pratt & Whitney are developing composite fan case for their PW1500G engine dedicated to Bombardier C series aircrafts. GKN Aerospace will provide the Honeywell HTF7500E propulsion system. Williams International are developing turbofan engines based on recent research carried out at NASA Glenn Research Center (Red, 2008). Altough the Trent 1000 Rolls Royce was the turbofan ready to equip the Boeing 787, its fan case (subcontracted to Carlton Forge Works) remained traditional. Concerned about falling behind its main competitor, Rolls Royce signed on January 28 2009 a $200 million contract with Alliant Techsystem (ATK) to produce composite aft fan cases for the Trent XWB engine which will power the Airbus A350.

4. Implications Regarding "Blade-out" Events

Based on the experience with helicopter blades, turbofan blades are expected to have a life time of about 30 years. Titanium fan blades are known for their tendency to fail at their root. The maintenance and checking of blades is costly and time consuming. An engine failure may be caused by damaged fan blades as a result of material defects or from the ingestion of external objects. Consequently, 4 ft. to 6 ft. long failed metallic blade can penetrate the nacelle and fuselage or damage fuel lines and control systems and thus jeopardize the structural integrity of the airplane.

However, since composite blades are lighter, tougher and exhibit excellent fatigue strength, they are less likely to fail. Shall this happen, they tend to disintegrate into small pieces because the brittle graphite are just held together by the polymer resin. Statistical data on the strength of composite blades[2] and the design of turbofans aiming at expelling any foreign object damage (FOD) out of the fan duct illustrate the superiority of composite blade over metal-based blades.

As a critical design requirement, a jet engine fan case must contain a failed fan blade flying at speeds in the range of 600 to 1000 ft/s and thus protect the structural integrity of the airplane. Moreover, during the period necessary to shut down the engine, the fan case has to keep its structural integrity despite the rise of dynamic loads and the propagation of damage induced by the impact of the failed blade. Specifically, it is specified (FAA, 1984) that engine tests must be conducted to demonstrate that the engine is capable of containing the damage induced by the total or minimum 80% partial failure of a turbine, compressor or fan blade without catching fire and without failure of its mounting attachments when operated for at least 15 seconds, unless the resulting engine damage induces a self shutdown.

On March 31, 2008, the GEnx-1B engine (2500 rpm, 2.8 m diameter) which co-equips the Boeing 787 Dreamliner received airworthiness engine certification from the U.S. Federal Aviation Administration. The FAR (Federal Aviation Regulation) 33 certification follows an extensive two-year ground - and flight-test program that involved nine engines and two flight-test programs on GE's 747 flying test bed. The bird ingestion certification requires the ingestion of four 2.5 lb birds and one 5.5 lb bird while maintaining required levels of thrust. During its development and certification

[2]It is reported (Mecham, 2006) that in 10 years and 7.5 million engine flight hours with jet engine GE90, only three composite blades had to be replaced due to birds and foreign object damage (FOD)

program, the GEnx ran 4,800 cycles and more than 3,600 hours. It also completed its emissions certification testing (low emissions of nitrogen oxides). In June 2010, this Genx engine equiped the fifth plane of the flight test fleet, such that the delivery of the dreamliner is scheduled for 2011.

The four previous flight test planes are equiped with the Rolls Royce Trent 1000 which was certified on August 7 2007 by the European and US regulators, the European Aviation Safety Agency (EASA) and the Federal Aviation Administration (FAA). This certification included the fan blade-out test, in which a blade was deliberately fractured at the root using an explosive charge with the engine at full power (53,000 to 75,000 pounds of thrusts), before being safely contained. Other tests involved bird ingestion and simulation of altitude testing.

The jet engines previously introduced are on their final stage of development, testing or certification. For instance, the LEAP-X engine certification is planned on 2014. The trent XWB testing campaign was to start in 2010, with certification planned in 2011, and Airbus A350 maiden flight in 2012. The PW1500G service entry is expected in 2013. The production deliveries of the HTF7000 series are supposed to start in 2012.

In March 1960, at Boston, European starlings were ingested by the 4 engines of a Lockheed Electra, which crashed. This accident initiated the FAA to take action regarding bird ingestion standards for turbine-powered engines. A large number of incidents and accidents involving bird ingestion and blade failures have been reported since. To cite a few: in August 1984, at Douala, Cameroon, an uncontained failure ruptured a fuel tank and started fire. On January 8th 1989, a Boeing 737 crashed near Kegworth, England because a CFM56 engine blade failed due to high cycle fatigue stress. More recently, on July 7th 2007, a B-767 hit a large flock of gulls which resulted in the damage of many blades leading edge. In November 2007, Nice,

France, a B-767 stoke a flock of large birds. A part of a fan blade broke off and result in a $9 million repair. On January 29th 2008, high vibrations were reported on a B-747 due to three damaged fan blades. A piece of a fan blade penetrated the cowl. On July 15th 2009, a TU-154 crashed near Janat-Abad, Iran probably due to the ingestion of a foreign object.

A few weeks ago, on August 2nd 2010, a test bed incident occured on the recently FAA certified Trent 1000 turbofan. It was described as an uncontained failure by a FAA spokeswoman and was reported to be due to a fire in the engine oil system which lead to a fire developing inside the engine and damaged the engine and the "bed 58" indoor test site in Derby, U.K. This estimated $17 million blew up officially concerned the intermediate pressure turbine (IPT). It is rumoured that an oil fire broke out in the high pressure compressor drum which lead to the failure of the intermediate pressure shaft and caused the blades of the separated IPT to impact the low pressure turbine inlet guide vanes. As a result, the freed IP turbine disk spun out of the casing and into the test stand. However, as the containment of disks spinning at a high speeds is technically too challenging and thus is not addressed by FAA and EASA certification, fan blade-out event must be contained within the casing. According to the safety director at U.K. aviation consultants Ascend Worldwide, a maximum of one or two uncontained failures occur per year and casings are often removed during testing. The impressive list of deadly crashes and life threatening accidents illustrates the need for stronger and safer Blade Containment Cases. In light of the latter incident (which occured on a turbofan equiped with a metal fan case), the already strict requirements for FAA certification may even need to be re-evaluated for stronger safety constraints.

Two different approaches are followed to design fan cases. Initially, the *hardwall* design was adopted. As its name suggests, the strength and resilience of the fan case

was provided by a minimum thickness of metal. In the case of hardwall design, the fan casing should contain the failed blade without penetration of the case (Roberts et al., 2009). In an alternative *softwall* design developed in the 1970s and 1980s, the reduction of the fan case metal thickness was compensated by the addition of a woven or braided fabric wrapping (aramid fibers) to give extra strength while being lighter. The fan case of GE CF34 engine is one of them. The choice for either of these designs is usually based on cost, weight, and design issues. The new GE Aviation engine contains a hardwall composite fan case combined with composite blades. Other type of designs for lighter fan cases have been proposed but did not mature due to costly blade-out tests and poor impact resistance. In the softwall configuration, the fan casing may be penetrated by the released blade but must retain its structural integrity through a controlled post-impact crack propagation during the engine shut down. The containment of the blade overwrapping layers of braid or fabric must stop the failed blade (Roberts et al., 2009).

The GEnx turbofan engine encompasses composite blades and a composite fan case, which direcly results from the results of NASA spearheading research for the improvement of damage tolerant fan cases. This leads to the satisfaction of both customers (enhanced safety through structural integrity) and airplane and turbofan manufacturers (rapid and low cost manufacturing, cost saving benefits). A&P Technology of Cincinnati, a leading manufacturer of braided fabrics for composite reinforcement, partnered with Honeywell International and Williams International and sponsored by GE Aviation, obtained a Small Business Innovation Research grant by NASA Glenn Research Center for the development of a fan case prototype in collaboration with the Ohio State University, the University of Akron and the FAA (Jones, 2006).

Specifically, a single-wind composite fiber braid in a herringbone shoelace pattern

was initially designed but was not strong enough. This issue was solved by the incorporation of a third braid at the center of the overlapping laces. Over-braiding process requires tooling and remains costly. Instead, a "capstan winding approach" was used (Roberts et al., 2009). As a result of an automated process on the largest braiding machine in the world, a 3/10 inch-thick triaxial carbon braid composite was obtained, with 0, +60, -60 deg. weave orientation although a biaxial configuration was prefered at the corners and bends for conveniency. This architecture enables a better load distribution between braids. The performance and cost of the braided composite highly depends on the lamina thickness, size and type of the yarn and the inter-yarn gap size. Using wide tow yarn enables to use fewer yarns and quicker braiding coverage. Small inter-yarn gaps results in enhanced composite stiffness and better load transfer away from impacted sites.

A triple layer of this triaxial braid was woven flat on the fan housing tool before resin was added by resin infusion process to the outside of the case. Contrary to the aluminum fan cases which are usually shrouded by a kevlar (aramid) or Zylon blade-containment blanket, no additional reinforcement was incorporated to the strong composite case. This eliminates moisture and subsequent corrosion that tends to develop at the aluminum/kevlar interface. To reduce noise, GKN Aerospace Services sub-contractor manufactures an acoustic liner made of glassfibre/epoxy skins that sandwich a Nomex aramid honeycomb core. The structural requirements do not allow for wet layup repairs. However, rebonding process may be performed on the acoustic layers[3].

[3]Aviation magazine, (McConnell, 2005)

B. Problem Statement and Research Objectives

The development of damage tolerant composite fan cases illustrates the current impetus towards polymer composites and the numerous challenges they represent to designers of composite structures. Indeed, the design of composite structures to satisfy specific thermomechanical properties is far more complicated than for traditional monolithic materials (typically metal alloys). The latter are essentially homogenous at relatively coarse scales. The complex thermomechanical behavior of metal alloys has been studied for decades and advanced implementations in finite element codes are available. On the contrary, the presence of a two-phase material introduces complexity regarding various aspects. Some potential difficulties are given below. For instance, the composite response is highly influenced by the thermomechanical properties of each phase, their morphology, compatibility and relative volume ratio. Consequently, the effective response of composites is usually observed to be anisotropic as well as rate– and temperature– dependent. The anisotropy may result from the anisotropic behavior of the constituents, from the accumulation of damage in priviledged directions, or from the composite structure, which may be very complex. Also, the intrinsic response of the polymer matrix, which exhibits various levels of dependence on temperature, rate and pressure plays a significant role in the composite effective response. Another difficulty is the development of gradients of thermomechanical quantities which are known to promote strain localization and stress concentration as well as initiation sites for damage accumulation. Damage mechanisms for each phase and interface should be well understood.

These issues should be addressed at the early stages of the design process of a composite structure. However, due to the lack of sophisticated methodologies, composite structures are still usually designed based on large series of testing campaigns.

These experiments are costly, lenghty and only provide design solutions for given specific conditions. They do not offer reliable input when the boundary conditions, the materials, the composition or the structure of the composite are modified. Also, the composite structures exclusively developed based on these testing methods do not give insight regarding the evolution of the thermal, mechanical or chemical properties. For instance, polymers and polymer composites are prone to aging. Therefore, their mechanical reliability over time may be questioned. In this context, one of NASA's Aeronautics Research Mission Directorate (ARMD) objectives is to improve the life-cycle durability of modern aircraft through the development of advanced diagnostic and prognostic capabilities. In particular, the Aviation Safety Program (AvSP) and the Aircraft and Durability (AAD) project focus on the prevention, detection and the mitigation of aging-related hazards. At NASA Glenn Research Center (GRC), continuum-based models and computational methods are under development in order to provide valuable input for the design of aging blade containment cases with optimum ballistic impact resistance.

NASA adopted an ambitious and sofisticated multiscale modeling strategy for the design of such composite structures. This approach, which has recently received increased attention, builds on a micromechanics based multiscale modeling strategy. Typically, a representative volume element is discretized using the composite basic constituents –fiber reinforcement and matrix– at their characteristic length scales. The lowest scale at which basic constituents are described is usually defined as "microscale". Appropriate boundary conditions and loading are prescribed, with constitutive equations for the different phases. Using homogenization techniques that fit the Hill-Mandel framework (Hill, 1962; Mandel, 1966), the effective behavior of the cell is obtained and can be entered into a structural analysis scheme (Aboudi, 2003). This intermediate length scale at which cells are represented is referred as

"mesoscale". The same method may be employed at a higher level scale to assess the effective properties of complex composite architecture, as in the case of multiple layers of braided composite or stack of distinct plies reinforced in various directions. This homogenization process may be performed from the lower scale involved up to the macroscopic level describing the actual part or component to design (e.g, blade cases). Besides the effective behavior, failure analysis may be also performed at these various length scales. For instance, damage mechanisms could be incorporated to the micromechanics framework in order to account for progressive failure of constituents and their interfaces. Thus, matrix cracking for polymers, tensile fiber failure, or fiber/matrix debonding can be analyzed at the finer scale. Braided failure bundle or delamination are representative failure modes to be accounted for at mesoscale.

Such a methodology present numerous advantages. Through homogenization, the effective properties of a composite are determined from the properties of its constituents. The reverse process, localization, enables the precise knowlegde of the distribution of thermomechanical fields within each phase. Consequently, damage mechanisms may be triggered at any scale and accounted for at higher scales through the deterioration of mechanical properties. Ideally, this strategy should greatly limit needs for testing of composite structures and configurations once the constituents behavior and the various fracture mechanisms involved are identified. Once this method is validated, the feasibility of composites and their optimization could be performed. Among other properties, the composite strength, stiffness or fracture toughness could be predicted under complex thermomechanical loadings, such as impact scenarios. The transferability of mechanical behavior and fracture properties from coupons to full composite structure could be validated as a more affordable and convenient testing tool. Moreover, this methodology should allow for an accelerated insertion of new materials, which is very useful in the case of polymers which are known to exhibit a

complex behavior.

However, the efficiency of such a powerful tool scales with the accuracy and precision of basic ingredients. In particular, adequate representative volume element should be used; material properties, boundary conditions, damage mechanisms should be well modeled; storage, manufacturing, processing or operating conditions are likely to affect the chemistry, material properties or configuration of the composite and should be accounted for in the design.

Here, focus is laid on the constituent levels: polymer matrix, fibers (and interface). Fibers are not of great interest since their behavior remains essentially elastic. However, the intrinsic response of polymers is very complex: temperature–, rate– and pressure– dependent, and prone to aging induced degradation, polymers also usually exhibit large inelastic deformations before fracture. These features common to polymer materials are transferred to the composite behavior, especially when the volume fraction of the polymer is important, or when the composite is loaded transversally to its reinforcement direction (such as impacted blade containment case). The goal of this research is to provide input into the design process of composites through a methodology aiming at the characterization and modeling of the mechanical response of polymers. The research objectives of this work are to:

- Characterize experimentally the intrinsic thermomechanical behavior of a polymer epoxy under quasi-static loading conditions.

- Develop an experimentally validated macromolecular model that represents the mechanical behavior of amorphous polymers.

- Analyze the effects of high rate loadings and physical aging on the behavior of polymers as is relevant to the impact and ballistic performance of composite structures.

- Develop a robust procedure for model parameter identification with due respect

to both quasi-static and dynamic conditions.

- Analyze plastic flow localization in epoxies using full boundary-value problem solutions and compare with experiments.

C. Background and Literature Survey

1. Mechanical Response of Polymers

Polymers are high molecular weight compounds formed of millions of repeated organic linked units, also called mers. They are characterized by their molecular weight distribution, which describes the scattering of the molecular weight around its average value. Polymer composites are constituted of a reinforcement phase, which is made of a hard and stiff material (carbon, glass, aramid) of various structures and shapes (long, woven fibers, particulates, etc.) embedded in a more ductile, softer and lighter polymeric matrix.

Besides elastomers, two major polymer classes are used: thermoplastics polymers and thermosetting polymers. Thermoplastics polymers can be melted and re-solidified without altering their properties. Thus they are utilized in molding, injecting, extruding and film blowing processes and they are recyclable. Among them are Polymethyl-methacrylate (PMMA), Polystyrene (PS), Polycarbonate (PC), Polyester, Polyamide (PA), Polybutylene terephtalate (PBT), Polyethersulfone and Nylon 6. At a microscale, the packing of the chains may show different levels of organization. In amorphous thermoplastics (PMMA, PS, PC, PVAc, etc.), the molecular chains do not exhibit any regular pattern, as opposed to semi-crystalline polymers (PE, PP, PET, PTFE, etc.) in which two and three dimensional patterns are observed. The full crystalline structure for a polymer is not reachable mainly because of the various molecular weight distribution, chain tacticities and kinetics considera-

tions. Thermoset polymers consist of a dense network of monomers as a result of a curing reaction which provides covalent bonds between the chains. In thermosetting polymers, the highly crosslinked chains hold together with strong covalent bondings whereas weak Van der Waals forces link the linear molecules in thermoplastics polymers. Thermosetting polymers such as epoxy resins are amorphous. High temperatures irreversibly destroy the bonds such their recyclability is not possible. Also, the strong bonds form important barriers for chains to move and slide. In polymers, the glass transition temperature T_g denotes the transition from the glassy behavior (rigid vibrating) to the rubbery behavior (long range molecular motion).

Stress–strain curves of glassy polymers share general features. The true stress-strain curve of an amorphous glassy polymer exhibits several stages (Boyce et al. (1988)): the initial elastic regime is followed by low strain hardening, which prolonges until a rate, pressure and temperature-dependent peak stress is reached; then strain softening (or a plateau), and eventually rate, temperature-dependent hardening occur (Spitzig and Richmond (1979)). This typical "up-down-up" shape is observed in many epoxies (Roman, 2005).

In thermoplastics, the polymeric chains are bounded by weak van der Waals forces. When sufficient thermal energy is provided to the system, the motion of chain segments through chains sliding becomes possible, which results into large macroscopic deformations. Even though this ductility is usually important, the full behavior may not be observed due to early failure, which depends on many factors such as the polymer type, the strain-rate, and the methods used to measure the strains (e.g. strain gages vs. optical methods). It has been experimentally observed an increase of stiffness with increasing strain rates (Gilat et al. (2002)). When strain rates increase, the peak stress (Roman (2005)), the low strain hardening (Gilat et al. (2002)) and the initial stress-strain slope increase as well (Rabinowitz et al. (1970), Sauer et al.

(1973), Spitzig and Richmond (1979)). Higher strain rates induces an increase in flow stresses with similar post yield response (Hope et al. (1980b)). A linear relationship between rate and strength is usually observed in the quasi-static regime, but the rate sensitivity is enhanced in dynamic conditions. In tension, the post-yield softening is sometimes not apparent (Roman (2005)), as opposed to the common observations (Gilat et al. (2002)). In compression, softening is observed after reaching the peak stress (Roman (2005)). Also, the flow stress is higher in compression than in tension (Spitzig and Richmond (1979)), which denotes the pressure sensitivity. Duckett et al. (1970), Rabinowitz et al. (1970), Sauer et al. (1973) demonstrated a linear dependence of the flow strength with (superposed) pressure. This pressure dependence was confirmed by experiments in compression and tension (G'Sell, 1986). The proximity to T_g, grades and the composition greatly affects the response (Hope et al. (1980b)). A continuous loss of shear modulus occurs with an increase of temperature, and eventually its value drops when approaching the glass transition temperature (Boyce et al. (1988)). An increase of temperature softens the response and lowers the yield stress in a seemingly linear relationship (Ferry, 1962).

The effects of loading conditions were investigated in Arruda et al. (1993) by comparing the experimental response under uniaxial compression and plane strain compression. A higher yield stress in plane strain compression was observed because of a strain constraint effect, which confirms the pressure-dependence of the flow strength. In uniaxial compression, the molecules have more space to align themselves than in plane strain compression, for which the constrained strains limit molecular rearrangements. This results in a more pronounced large-strain hardening regime in plane strain compression compared to the uniaxial case, for which the hardening and further locking are delayed.

For plastic flow to take place in glassy polymers, two molecular resistance mech-

anisms need to be overcome: an intermolecular resistance to segment rotation at low strains, and a progressive entropic resistance to molecular alignment. For temperatures below T_g, plastic flow and stress induced chain alignment initiate in a thermoactivated process when the free energy barrier to segment rotation is overcome (Argon, 1973). The second resistance mechanisms sets against the change in the configuration entropy induced by a preferred orientation of the chains and amplify with progressive chain stretching which takes place between the chain entanglements.

The evolution of the free volume at a fine scale due to its metastable glassy state is a possible explanation to the nonlinear isotropic viscoplastic behavior before peak stress (Arruda et al., 1995; Anand and Gurtin, 2003; Sarva et al., 2006). A softening stage usually follows the peak stress (Bowden, 1973; Boyce et al., 1988). This softening regime corresponds to a specific rearrangement of molecular chains after plastic flow takes place which makes the polymer more compliant. As for other materials exhibiting a drop of the true stress, localized shear bands may set and propagate (Boyce et al., 1988). The interpretation of softening is controversal. It is usually believed that softening is a feature of the true behavior of polymers. However, the drop of stress and following softening may be considered as a result of the onset of plastic instabilities such as necking (Lu and Ravi-chandar, 1999), which would denote a geometrical origin for softening. This explaination is further reinforced with results of confined compression which showed the suppression of softening in comparison with the uniaxial experiments (Ravi-Chandar and Ma, 2000). However, the absence of softening may directly result from the amount of pressure (Spitzig and Richmond, 1979). Moreover, plane strain and uniaxial compression experiments on polycarbonate showed no sign of onset of heterogeneity even at large strains, which would confirm the softening regime as part of the intrinsic response of polymers (Arruda and Boyce, 1993a; Arruda et al., 1993).

The molecular mechanisms of macroscopic yielding closely relate yielding and subsequent strain softening (Bowden and Raha, 1970). At a smaller scale, yielding is accompanied by dense network of narrow shear bands.

Aging also affects the inelastic behavior of glassy polymers. Much relevant information about the description of aging can be found in Hutchinson (1995). Aging is the phenomenon responsible of change of both bulk and molecular-scale properties over time, at given conditions (constant temperature, zero stress, etc.). It lies into two categories : the reversible physical aging, and the irreversible chemical aging. The later manifests with oxidation reactions, chain rupture, post-crosslinking (decrease of crosslinking density) which is believed to cause a drop of ultimate elongation, (Leveque et al., 2005). Because physical aging polymers are isolated from external environmental interactions, their change of properties is explained by some thermodynamically driving force. Amorphous polymers under Tg are in a non-equilibrium state (as opposed to temperatures above Tg) which can be timely monitored by the evolution of thermodynamic quantities such as volume and enthalpy under isothermal conditions. However, no consensus within the scientific community exists as to relate them to the evolution of macroscopic properties such as creep or stress relaxation, and molecular arrangements, which are measured by scattering and spectroscopic techniques. In thermoplastics, the melting-cooling down manufacturing process initiates aging. A glass has a frozen in structure. At a temperature below Tg, a driving force will tend to decrease the excess thermodynamic quantities (volume, enthalpy) until reaching an equilibrium state, which becomes virtually impossible (due to infinite time) for temperatures of 20 C under Tg.

Volume relaxation methods measure the time to reach the equilibrium state. This relaxation time, which is composed of a distribution of relaxation times and reflects thermal memory effects, was showed to evolve with the fictive temperature,

which is used to characterize the evolution of the microstructure towards the equilibrium state (Kovacs, 1963)). Neutron, light, and small angle X ray scattering (SAXS) techniques measure the change of this fictive temperatures on aging. The polymer chemical structure is not relevant to aging. However, the changes of free volume and configurational entropy have a physical meaning. Several techniques have been developed to capture the evolution of the amount and distribution of the free volume. Positron Annihilation Lifetime Spectroscopy (PALS) and Electron Spin Resonance (ESR) spectroscopy do not always give satisfactory results (Hill et al., 1990). The Fluorescence Spectroscopy technique shows a linear increase of the free volume density, with a logarithmic function of aging time (Royal and Torkelson, 1993). More precisely, Photochronic Probes and Labels methods suggest a reducing number of large free volume sites of about 100-400 Angstroms (Lamarre and Sung, 1983). These results were completed by Curro and Roe (1984) that showed that despite a decrease of the total free volume, the average size of free sites increases due to some diffusion process.

Since aging hinders the molecular rearrangement, it specifically modifies viscoelastic properties such as creep compliance, stress-relaxation modulus, loss tangent and dynamic mechanical modulus, and non-linear response. Experiments showed a linear increase of storage modulus G (Kovacs et al., 1963) and a decrease of the loss tangent and loss modulus (Cavaille et al., 1986) with log time. The stress relaxation, which is linked to the volume relaxation (McLoughlin and Tobolsky, 1952), is delayed with longer annealing time and with lower sub-Tg temperatures (Matsuoka et al., 1978). Tensile creep compliance vs. creep time curves for various aging time exhibit some pattern for time-aging time superposition, which corresponds to a shift of time-scale (Struik, 1977). Stress, rejuvenation and annealing temperature affect the creep compliance (Brinson and Gates, 1995). Also, the polymer evolves towards a preferred

disordered configuration with inelastic strains (Hasan and Boyce, 1993) and aging modifies the long range molecular movements (Muzeau et al., 1994).

More importanty, Tant and Wilkes (1981) stated that aging was accompanied by "an increase in density, tensile and flexural yield stress, and elastic modulus; a decrease in impact strength, fracture energy, ultimate elongation, and creep rate; and a transition from ductile behavior to brittle fracture." Aging PC exhibits such a trend (Bigg, 1996), as well as PET (Mininni et al., 1973). An explanation for the increase in modulus of linear epoxies is the retardation mechanisms due to reduced mobility and free volume which therefore induces longer molecular rearrangements and higher stresses (Moynihan et al., 1976). Physical aging typically results in increased brittleness of polymeric materials (Kozlov et al., 2004). In amorphous PET, longer annealing produces a higher peak for yield stress while the post-yield behavior is not much dramatically modified (Tant and Wilkes, 1981). The fracture energy for Izod impact test PC was showed to suddenly decrease with aging and this occurs sooner with lower annealing temperature (Legrand, 1969). A lower annealing temperature delays the increase of density. The work, stress and strain to failure dramatically and suddenly decrease with annealing time. Extended aging period (25 years) results in an increase of tensile strength and Young modulus, a reduction of the strength dependence on applied strain rate, whereas results differ after a shorter aging period (4 years) (Pavlov and Ogorodov, 1992). However, in compression experiments on PC and PMMA showed that annealing increases the yield stress and affects the post yield softening but do not affect the orientation hardening neither the Young's modulus (Hasan et al., 1993). Moreover, thinner layers age faster due to a higher rate of free volume diffusion (Huang and Paul, 2006). Aging occurs in the entire polymer for undeformed polymer glasses but aging is confined to microscopic zones (typically shear bands) in the case of stress-induced aging (Volynskii et al., 2007).

Exposure of PVC to radiation and chemical reactions induced by air pollutants (HCl evolution, polyenes formation, chains scissions, and crosslinks) causes the decrease of properties at break (Gallouze and Belhaneche-Bensemra, 2008). Low and high temperatures, chemical and biological agents and particularly aqueous environments drastically modify the long term performance of thermosetting resins (Frigione and Lettieri, 2008). Water enters the polymer by capillarity or diffusion through cracks, which is favored by high polar groups and low packing. As opposed to free water, bound water lowers the Tg and has a plasticizer effect which reduces the Young's modulus and strength. Also, hydrolysis reaction may degrade the resin (Frigione and Lettieri, 2008). Aged PMR-15 neat resin showed an increased crosslinking density which induces a loss of ductility (in creep), an increase of Young Modulus, and a decrease of tensile strength. A thin oxidized layer growths with time, but do not affect the overall mechanical response, but sets damage as crack initiation sites (Ruggles-Wrenn and Broeckert, 2009).

2. Constitutive Modeling of Polymers

A large variety of models aims at a proper description of the mechanical behavior of polymers. Phenomenological models may be sufficient to represent the mechanical response of polymers for simple boundary value problems. Simplification procedures are commonly used in the description of polymer behavior when used in a finite element code. For instance, the non-linearity in the elastic regime has been modeled using piecewise elastic approximations (Stahlecker et al., 2009). When the models do not account for specific features, such as rate effects, user-defined load curves are commonly employed (Lim et al., 2003). Also, various ad-hoc models and constitutive laws are often incorporated in the formulation, based on the needs (Stahlecker et al., 2009).

These models must encompass all the ingredients necessary to capture the complex inelastic response of glassy polymers which is characterized by strain-rate–, temperature– sensitive yielding, post-yield intrinsic softening followed by rehardening at large strains due to polymer chain reorientation. Viscoelastic and viscoplastic models are the most successful. One approach consists of developing a generic model based on various constitutive equations collected from validated existing models. For viscoplastic models, the representation of yielding may take several forms. In a three dimensional space, yielding may occur for complex triaxial states of stress. As for classical materials, yield criteria for polymers could be therefore defined from yield loci, hyperplane surfaces derived from the stress tensor invariants. For instance, the Tresca criterion states that plastic flow initiates when the shear stress on any plane reaches a critical value. In the case of the von Mises criterion, plastic flow starts when the second invariant of the stress tensor J_2 reached a critical value. the Mohr-Coulomb criterion has been initially used to investigate yielding for soil applications. However, this criterion and some variants have been used to model the onset of plasticity in polymers. It is based on the assumption that yielding occurs when the shear stress on any plane reaches a critical value itself dependent on the normal stress on that plane. As explained above, the polymer response is pressure sensitive. Therefore, this Mohr-Coulomb criterion should be modified to incorporate pressure effects. A simple method consists in incorporating to the usual von Mises flow potential an additional term which is a linear function of the hydrostatic stress. The resulting pressure sensitive flow potential or the modified von mises yield criterion is also know as the Drucker-Prager yield criterion (Drucker and Prager, 1952). Recent investigations used this yield criterion to describe the onset of plasticity (Goldberg et al., 2005; Chowdhury, 2007; Chowdhury et al., 2008a,b). Molecular dynamic simulations were performed to model the behavior of glassy polymers and investigate the quality

of common yielding criteria (Rottler and Robbins, 2001). It was demonstrated that the Drucker-Prager yield criterion gives satisfactory results.

Significant progress have been accomplished since the late 1960s in the modeling of the post-yield response of glassy polymers below their glass transition temperature. Various constitutive descriptions were developed which accounted for satisfactory levels of refinement at a macroscopic scale. Recently, this class of models were used by Goldberg et al. (2005), Chowdhury (2007) and Chowdhury et al. (2008a,b). Potential functions of the Drucker-Prager Drucker and Prager (1952) type (based on the Von Mises equivalent stress) were used in conjunction with the Bodner flow rule (Bodner, 2002; Bodner and Partom, 1975) for a rate-dependent plasticity model with isotropic hardening. This strain rate hardening law was originally developed to capture incubation, growth and saturation phenomena that occur in metal plasticity (Bodner and Partom, 1975) and later adapted for polymers(Zhu et al., 2006). A volume-preserving plastic flow was adopted although experiments do not infer this assumption (Powers and Caddell, 1972; Spitzig and Richmond, 1979). This work expanded on previous investigations of Li and Pan (1990), Chang and Pan (1997) and Hsu et al. (1999). These models are mostly relevant for applications where yield drop and large deformations are irrelevant.

These phenomenological criteria are surely useful to investigate the onset of plastic deformations in polymers. Physics- grounded models were developed based on the description of actual mechanisms which drive yielding. Focus is laid on the fine-scale representation of the evolution of the polymer structure which occurs during yielding. These models are part of a broader family designated under the generic term "Molecular theory of yielding". Yielding is considered as a transition between two equilibrium states characterized by the successive jumps of molecular segments. These theories have been refined from the early contribution of Eyring (1936). For instance,

pressure effects were later incorporated (Duckett et al., 1970). Bowden and Raha (1970) considered the yield stress as a representative stress at which conditions are met for dislocations to form. Other models considered the onset of plastic deformations as a consequence of the expansion of the molecular structure which flows when it reaches a critical free volume value (Rush and Beck, 1969; Bauwens, 1980). Yielding has been described as a thermally activated process which drives a series of modification of configurations of chains or successive jumps of chain segments (Robertson, 1966; Brereton et al., 1977). These thermo-activated theories of yielding are generally accepted. They consider yielding as the representation of the resistance of the environment that prevents the rotational motion of chain segments (Stachurski, 1986). Argon (1973) derived an expression from a double-kink model which describes the amount of the free energy exchange needed for the rotation of segments in a stressed surrounding elastic medium. As a result, a simple expression describing the temperature and rate dependence of yielding was derived. Boyce et al. (1988) improved this expression in incorporating pressure sensitivity based on the linear dependence of yield stress with pressure observed in experiments of Rabinowitz et al. (1970); Sauer et al. (1973); Spitzig and Richmond (1979).

Models aiming at representing the evolution of the polymer structure beyond peak have been continuously refined. A one dimensional model describing the large strain resistance to flow was initially developed based on a Langevin spring (Haward and Thackray, 1968) and the non-Gaussian statistical mechanics theory of rubber elasticity developed and enriched by **?**. Haward and Thackray (1968) also modeled the resistance of intermolecular resistance using an Eyring dashpot. The one dimensional entropic resistance model was later generalized to a full three-dimensional description and extended to incorporate the effects of pressure, intrinsic softening and temperature on the plastic resistance (Boyce et al., 1988). This sophisticated model

accounts for finite strain kinematics and orientational hardening up to large strains through a three-chain elasticity model. This large strain hardening is described in the formulation by a back stress tensor. Wu and Van der Giessen (1996) further refined the model of Boyce et al. They developed a more realistic statistical representation of the entropic resistance based on the combination of the three-chain and eight-chain rubber elasticity model (Arruda and Boyce, 1993b). The Boyce's model with the modifications brought by Wu and Van der Giessen (1996) is designated here as the *macromolecular model*. Anand and Gurtin (2003) modeled the response of glassy polymers, including the effects of temperature, rate and pressure on yielding based on a thermodynamics framework, and derived elasto-viscoplastic constitutive equations from a set of internal state variables which aimed at representing the local free-volume associated with metasble states.

In metals, material strain-rate sensitivity and temperature dependence of yield stress mainly determine the behavior of metals in the Charpy test, as for the transition between brittle and ductile failure modes (Tvergaard and Needleman (1988)).

The collection of surface temperature (infrared technique) on PC using dynamic experiments (Kolsky bar) at 2200/s concluded to a moderate temperature rise of 6K due to plastic work conversion (i.e. plastic dissipation factor of around 0.5) whereas an increase of 105K during (ductile) fracture is suggested to origin mainly (90%) from thermofracture coupling (Bjerke et al. (2002)). At higher strain rates (5000-8500/s), the temperature increases up to 40K and the plastic dissipation factor,which is dependent on strain and strain rates, may reach unity (Rittel (1999)). Similarly, an elevation of temperature up to 50K is observed by the epoxy resin LY-564 at a strain rate of 2500/s (Trojanowski et al. (1997)). Temperature during fracture is even higher. The elevation only reaches 30K for BPA resin with a plastic conversion of around 1 at a strain of 0.45 (Buckley et al. (2001)). Tests on Epon E862/W

resin in compression at 0.5/s and 2500/s exhibits a temperature rise of 15K and 45K respectively at a strain of 0.6. At high strain rates, more energy is dissipated than stored due to the increased yield stress (Garg et al. (2008)).

Thermo-mechanical coupling was investigated in PMMA in compression (Arruda et al. (1995)): isothermal conditions assumptions are coherent at low strain rates but beyond 0.01/s, thermal softening occurs and increases with strain rates. For adiabatic conditions, the softening is clearly decomposed into material strain softening as well as thermal softening. This thermal softening affects the post yield regime as a competition between post yield softening and large strain hardening is observed to result in a plateau in the stress-strain curve. Simulations that account for this thermal softening through transformation of plastic work into heat are in agreement with experiments. Simulations of Izod testing on polycarbonate showed the influence of the thickness of the tested specimen on the deformation patterns and the distribution of the stress triaxiality (Tvergaard and Needleman (2008)). Around the notch tips are found the highest plastic strains, the very stiff material, and the highest softening. However, no thermal softening through plastic work into heat conversion was included in the model. More recently, tensile dynamics (500/s-1500/s) experiments on PC exhibit deformation of necking, necking drawing or double necking depending on the cross section area and aspect ratio of the samples (Sarva and Boyce (2007)). A popular model was enhanced to better capture the viscoelastic regime, which exhibits an increase of strain rate sensitivity at low temperature and high strain rates due to the activation of the β-process (which is associated with the restriction of main chain or side groups rotations), besides the α-process (which describes the rotation of chain segments) (Mulliken and Boyce (2006)). This modified model accurately predicts the features of (Sarva and Boyce (2007)), as well as the deformation modes exhibited in Taylor impact experiments (Sarva et al. (2006)) but does not explicitly account for

thermal softening.

A few models including aging effects have been proposed even if it is recognized that existing models of time-dependent behavior including chemical and physical aging are still too limited to have real confidence in making predictions (Schapery, 1997).

The time evolution of viscosity, free volume, volume, enthalpy relaxation, etc. were studied with early theories and models based on the Vogel-Tammann-Fulcher (VTF) equation, the Kovacs-Aklonis-Hutchinson-Ramos (KAHR) model (Kovacs et al., 1979), the Tool-Narayanaswamy-Moynihan (TNM) formalism (Moynihan et al., 1976) or the Williams-Landel-Ferry (WLF) equation (Adam and Gibbs, 1965). They recognize the depart from equilibrium in the glassy state as a driving force for the relaxation kinetics and use a fictive temperature or properties as state parameters to measure the distance to thermodynamical equilibrium. However, according to Leveque et al. (2005): "It remains difficult to integrate the aging effect in a constitutive equation, since aging involves complex phenomena on different scales (molecular restructuring, microcracking, etc.)". The viscoelastic behavior of polymers during relaxation experiments beyond T_g is often described by time-temperature superposition (Kohlraush-Williams-Watts function (Williams and Watts, 1970)), which is based on the time-dependent modulus $G(t)$ expressed as:

$$G(t) = G_0 e^{-(t/\tau)^\beta} \tag{1.1}$$

with the definition of the WLF shift factor $a_T = \tau_T/\tau_{T_0}$ and vertical shifts defined as $b_T = G_{0,T}/G_{0,T_0}$ at various temperatures. Time-strain superposition has also been examined (Matsuoka et al., 1978; O'Connell and McKenna, 2002) with $a_\gamma = \tau_\gamma/\tau_{\gamma_0}$ and $b_\gamma = G_{0,\gamma}/G_{0,\gamma_0}$ as well as stress clock models (Shapery, 1969). Other models involve entropy (Shay Jr and Caruthers, 1990) and free volume considerations (Knauss

and Emri, 1981). However, these "clock" models can only predict specific behavior. Viscoelastic theories regard yielding as a loading induced consequence of nonlinear relaxation with a transition from rubbery to glassy states whereas plastic theories build on yielding and do not contain the ingredients to predict glass transition. In Caruthers et al. (2004), a thermodynamically consistent nonlinear constitutive theory was developed to bridge stress, volume and enthalpy relaxation with yield, stress-strain behavior and physical aging. This theory was based on Rational Mechanics (all thermodynamic quantities can be derived from a single time-dependent Helmholtz free energy and ensures the respect of the second law of thermodynamics) and incorporates a material clock parameter, such as the configuration entropy (Lustig et al., 1995), which depends on the thermal and deformation histories. The shift factor resulting from this theory incorporates a relaxing term which, besides "leveling off" when transitioning from the rubbery to the glassy state, also induces a slow return to equilibrium if temperature is held constant, and consequently possesses the intrinsic ingredients for physical aging modeling. The aging of the viscoelastic shift factor predicted was failry verified experimentally and the increase of peak stress with aging was qualitatively captured (Adolf et al., 2004).

Boyce et al. (1988) suggests to modify the evolution law for the athermal shear resitance by adding a positive structure-temperature-pressure dependent function which should increase with temperature as a result of annealing. Recently, UV ageing with exposure time of 12 hours was performed on Polylactic acid (PLA) films (Belbachir et al., 2010). The model of Bergstrom and Boyce (1998), which includes a non-linear temperature-dependent rate of relaxation for the modeling of elastomers response was phenomenologically modified to include the change of number average molecular weight due to aging.

Generally, the thermomechanical history and aging only influence the yield stress in stress-strain curves. Indeed, as opposed to annealing, predeformation and quenching induce a lower yield stress, less softening and less localized deformation in tension whereas slowly cooled samples develop necks. This aging kinetics was recently incorporated into an elastoviscoplastic constitutive model which incorporates i)secondary interactions between polymeric chains described by a non-Newtonian flow rule based on a deviatoric driving stress and an Eyring viscosity which includes stress, temperature, pressure and intrinsic softening, and ii)neo-Hookean strain hardening (Klompen et al., 2005). The driving stress was composed of a history independent rejuvenated stress and a yield drop, which is the increase in yield stress with time due to aging. This yield drop is modeled as a state parameter which depends on time, temperature, stress and plastic strain. It is decoupled into two opposite contributions: aging and rejuvenation. It was showed that the evolution of yield stress for mechanically rejuvenated and quenched polycarbonate could be described by a single expression involving different initial ages. This also incorporates shift functions which capture the temperature and stress accelerating aging kinetics. This theory was applied fairly successfully to predict the evolution of the yield stress for a polymeric product molded by injection (Engels et al., 2006), was extended to include the effects of rubber filling in impact strengthening on aging PC (Engels et al., 2009), was used to predict fatigue induced failure (which is influenced by aging) (Janssen et al., 2008) or to assess the time-dependent quantities directly from micro-indentation experiments (van Breemen et al., 2009). In these models, the foundation was the phenomenological description for kinetics aging with a logarithmic increase of peak stress with aging, as well as the use of master curves for time-temperature and time-stress superpositions.

The latter model van Breemen et al. (2009) included include β contribution besides the α relaxation. In Lyulin and Michels (2006), molecular dynamics simulations

and the analysis of the distribution functions of the orientational relaxation times for the second-order ACFs (Legendre polynomials) also exhibited three relaxational (above T_g)/activation (below T_g) processes: a high-frequency transient ballistic process, a β process corresponding to the motions within the cage, and final cage relaxation α. The β motion makes the difference between quenching and annealing (aging kinetics), which leads to deeper minima for energy ('rugged energy landscape") when annealed (Lyulin and Michels, 2007). Local reconfigurations of chain segments lead to a slow loss of energy and deepen the energy landscape with vibrations within local energy minima and relaxation between local minima. Also, since rejuvenation does not necessary enhance mobility and decrease the density, the free volume is not likely the parameter which governs aging (van Melicka et al., 2003). This is opposed to the use to the free volume density as an internal variable to characterize the effects of thermomechanical history on the inelastic deformation (Hasan et al., 1993). Molecular simulations suggest that thermal activation is responsible of the evolution of the system, from which a law describing the evolution of yield stress with strain rate and aging was presented and verified experimentally (Rottler and Robbins, 2005). Physical aging of polymer glasses was recently investigated through a theory segmental scale theory in which aging of thermodynamic, relaxational and mechanical properties result from the translational dynamics of nanometer-sized statistical segments (Chen and Schweizer, 2008). The yield stress is the minimum stress necessary to destroy a collective segment-segment interchain force barrier and its increase due to aging is predicted as the natural outcome of a mechanical devitrification transition. Also, the degradation of modulus and strength was recently mathematically modeled based on the temperature dependent (Arrhenius law) weight loss (Kim et al., 2002). More recently, aging entered through the phenomenological modification of the elastic modulus, the tangent modulus, the isotropic stress in the viscoplasticity based on

overstress (VBO) theory, which is a unified state variable theory with evolution laws for the equilibrium stress, the kinematic stress and the isotropic stress taken as state variables (McClung and Ruggles-Wrenn, 2009).

3. Implications for Composites

Several models have been developed to predict the effective elastic properties of composites. The shear modulus of a composite formed of a non-rigid matrix and reinforced by rigid spherical inclusions can be estimated from the volume fraction of these inclusions. Improved models followed, which accounted for: high volume fractions , non-spherical particles (Brodnyan, 1959), particles interaction (Guth, 1945), Poisson's ratio (Nielsen, 1970). Also, early models have been developed for rigid inclusions imbedded in a rigid matrix. Parallel and series models set upper and lower bounds respectively for the composite elastic modulus. They are based on unrealistic assumptions of uniform strain and stress respectively. Improved models accounted for the Poissons ratio but give too widely spaced bounds (Hashin and Shtrikman, 1963). The law of mixture is based on linear contribution from the parallel and series models (Hirsch, 1962). Some contributions focused on: perfect bonding (Counto, 1964), uniform stress or uniform displacement (Ishai and Cohen, 1967) at the bondary, ellipsoidal inclusion (Chow, 1978), aligned short fibers (Cox, 1952), disc-shaped particles, needle or spherical particles (Wu, 1966), interaction between fillers (Dickie, 1973), thermal expansion mismatch (Ahmed and Jones, 1990), inclusion adhesion (Sato and Furukawa, 1963). In general, these theories do not include clustering effects. However, packing of different sizes particles was experimentally showed to give higher modulus (Ahmed and Jones, 1990). The size of the particles gives controversial experimental results on the modulus (Spanoudakis and Young, 1984a).

More recently, the effective properties of composite materials with periodic mi-

crostructure composed of linear elastic, rigid-plastic or power-law individual phases have been investigated using the FEM with the incorporation of "macroscopic degrees of freedom" under a stress or strain controled framework, and using the Fast Fourier Transforms for a homogenous linear reference material undergoing a heterogenous periodic eigenstrain (Michel et al., 1999). The periodic conditions are accounted for using symmetry conditions, a method of elimination of nodal displacements or a Lagrange multipliers technique (Michel et al., 1999). The Fast Fourier Transform (FFT) numerical method is based on the periodic Lippmann-Schiwinger equation and the periodic Green's operator associated with the elastic stiffness of a homogenous reference material. This FFT method is faster than the FEM but do not converge for composites with infinite contrast (void or rigid inclusion) or for nonlinearities which give very contrasted stiffness matrices.

Some studies have been dedicated to assess the composite strength. It may be defined from the first failed element (Sahu and Broutman, 1972). Some models expressed the strength of the composite under the form of a power law. They may account for the stress concentration at the inclusion-matrix interface, for uniform dispersion of particles (Nicolais and Narkis, 1971) or heterogenous concentrations (Piggott and Leidner, 1974) and the particle size (Hojo et al., 1977). The strength may be calculated from the contribution of the matrix (through shear mechanism) and of the particle (through inclusion-matrix friction and interfacial compressive stress) (Leidner and Woodhams, 1974). It clearly depends on the quality of interfacial adhesion. Smaller particles give higher effective interfacial bond. A bad inclusion-matrix bond is similar to a cavity which weakens the structure and favors crack initiation but toughness is enhanced since crack propagation is hindered because of branching and bifurcations (Spanoudakis and Young, 1984b). Also, rigid particles tend to reduce the strength but crack propagation becomes more difficult because the plastic defor-

mation is enhanced and the crack front bows out. Moreover, particles modify the crack path and increase the fracture surface, which enhances the toughness. Rubber particles absorb more energy than brittle particles.

Numerical methodologies have been developed in the past decades to study the macroscopic behavior, the microscopic evolution of mechanical fields and the fracture mechanisms in Metal-Matrix Composites. One pioneer numerical contribution (Christman et al., 1989) clearly indicated the influence of the size, shape and distribution of the reinforcement phase on the MMCs macroscopic properties (yield, strain hardening, overall constitutive response, ductility and fracture) and concluded that the strengthening originated from the development of stress triaxiality in the matrix. The extension of this study (Llorca et al., 1991) incorporated fracture mechanisms through an elastic-viscoplastic ductile porous solid matrix model. The numerical simulations agreed with experiments regarding the dependence of yield strength, strain hardening and ductility on the reinforcement phase shape, volume fraction and matrix and failure by void nucleating properties.

However, only a limited studies have been applied to PMCs. A mesomechanical approach was developed for braided carbon/epoxy composites for which elastic constants were obtained from an analytical formulation but plasticity was ignored ((Miravetea et al., 2006). A study using the Hill anisotropic plasticity model for the case of braid composites emphasized on the role of the matrix material nonlineariy on the compressive strength of the composite (Song et al., 2007).

Recently, the influence of the matrix yield strength and interface properties such as interface fracture energy as well as the matrix friction angle and thermoelastic residual stresses on the strength, ductility and failure modes (shear banding vs. interface cracking) in a PMC were numerically investigated using a RVE composed of dozens of glass fibers randomly distributed in a epoxy (Gonzalez and LLorca, 2007).

The Mohr-Coulomb criterion was used for plastic yielding and a fracture of interfacial elements was governed by a traction-separation law.

A very similar approach has been used for a C/PEEK composite (in which the matrix was modeled as isotropic elastoplastic) with a focus on the role of interface properties and fracture criterion under compression and shear (Totry et al., 2008). The failure of this composite was characterized (Vogler and Kyriakides, 1999) under shear and transverse compression as well as its inelastic behavior (influence of rate as for the neat matrix, yield behavior and load history on the macroscopic response). Attempts to properly modeling the behavior of such composites did not give satisfactory results despites promising results. For example, a J2-type viscoplasticity model does not capture the stiffness in transverse compression; a rate dependent version of the non-associative Drucker-Prager model fails in shearing (Hsu et al., 1999).

The Method of Cell (MOC) has been successfully utilized to assess the effective elastic properties for plain-woven composite lamina for various fiber tow shapes (Jiang et al., 2000). The stress and strain can be distributed within each constituent (fill, warp, resin) such that criteria for micro-failure criteria for each constituent can be entered with progressive degradation of mechanical properties such as stiffness (Tabei and Jiang, 1999). This modeling technique belongs to a broader family of methods for constitutive modeling based on Classical Laminate Theory (CLT). These models, widely used by finite element commercial codes, use micromechanics equations to obtain effective properties of plies. This method is efficient for stack-up laminates but remains difficult to implement for woven or braided structures inherent to the overlapping variations of the composite constituents. These micromechanics modeling strategies present the advantages of being simple and straigthforward. Their predictions usually exhibit satisfactory accuracy in terms of stress and strain at a macroscale level, especially if the composite structure remains simple (typically, unidirectional

fiber laminates). Average thermomechanical fields such as stress and strain within each phase (i.e. polymer matrix, fibers) are also obtained.

Finite Element Analysis has been widely employed in the context of polymer composites such as fabric or woven carbon composites (Tan et al., 1997; Whitcomb and Srirengan, 1996). For instance, the effective mechanical properties and the fracture of woven composites have been numerically investigated (Woo and Whitcomb, 1996). Lately, the free edge effects have been characterized and was found to be related to the composite thickness and the waviness of the plain weave mat (Owens et al., 2010). FEA has applied for impacting scenarios involving fabric based composites. For instance, simulations of a projectile impacting at high speed a dry woven Kevlar sheet were performed based on the discretization of a representative volume cell (Stahlecker et al., 2009). Ballistic impact on Twaron has been modeled using membrane elements (Lim et al., 2003). Damage growth on impacted woven composites has been investigated using energy based damage mechanics implemented into a commercial finite element code (Iannucci and Willows, 2006).

Recently, the evolution of elastic properties of composite laminates were studied within the framework of Continuum Damage Mechanics (Talreja, 2006; Singh and Talreja, 2008). The visco-elastic response of damaged composites was also investigated (Varna et al., 2004). The visco-elastic behavior of composites was assessed from the visco-elastic behavior of polymer reinforced by elastic particles (Muliana and Kim, 2007). A concurrent micromechanical model was lately developed to predict the effective response of fiber reinforced polymers with constituents exhibiting thermo-viscoelastic response (Muliana and Kim, 2007). These examples illustrate that most of the modeling efforts has been focused on the assessment of the effective response in composite with the determination of elastic modulus, strength, etc. for a variety of composite configurations. However, less emphasis has been brought to the descrip-

tion of inelasticity taking place within composites as a consequence of the inelastic behavior of the constituents. Advanced modeling refinement has been provided by recent thermo-viscoelastic or viscoplastic models which enable a detailed description of the evolution of thermomechanical fields within composites from a systematic approach in which large variations of strain rates and temperatures for various loading modes could be considered. Such studies combined with realistic damage models give valuable insight regarding the onset and propagation of damage within composites, e.g. Chowdhury (2007).

4. Previous Work

Recently, Chowdhury (2007) modified the macromolecular model of Boyce et al. (1988) based on the observation that the original model does not have the basic ingredients to capture the nonlinear hardening regime which takes place before peak. Specifically, he modified the law that describes the evolution of the intermolecular resistance with deformation by incorporating an additional term which allows a smoother yield transition. A consequence is that yielding occurs before the peak stress is reached. He implemented this model into a finite element code and performed computational analysis of boundary value problems. In particular, he investigated the capabilities of the model on illustrative examples such as impact and shear band formation scenarios. He used this model in a micromechanics framework, e.g. the "unit cell" concept, to study competitive mechanisms leading to fracture in polymer composites.

However, this extensive numerical study has not been performed on any experimental basis at constituent level or composite level. Instead, the generic capabilities of the macromolecular model have been assessed and illustrated in the general context of ductile response and fracture of glassy polymers with applications to composite.

The effects of temperature, strain rate and loading mode (tension and compression) were studied, but the range of variation remained rather limited. Moreover, these factors were investigated independently of each other. Also, the material parameters which enter the macromolecular model were directly identified from data collected in the literature or were arbitrary chosen to best represent the behavior of the studied polymers at specific conditions.

D. Approach and Outline of the Dissertation

In this work, the capabilities of the macromolecular model are evaluated based on a large quantity of experiments performed on the same material. These experiments encompass uniaxial tests in tension, compression (and shear) performed on Epon 862, an epoxy resin potentially used as matrix of composite blade containment cases, for a large range of temperatures (from room temperature to 80°C), strain rates relevant to quasi-static and impact conditions (from 10^{-5}/s to about 10^{3}/s) and aging conditions. Cylindrical specimens were employed for both tension and compression. The experiments in quasi-static conditions were conducted at NASA GRC by Justin Littell during his Ph.D study in the Department of Civil Engineering at the University of Akron. Additional postprocessing results were performed and supplied by Tim Woodbury, undergraduate Aerospace Engineering student at Texas A& M University, who used video-based extensometry. The combination of full-field strain measurements and video-monitored mechanical measurements was used to obtain the intrinsic behavior of a ductile epoxy polymer up to large strains. Using video-monitored changes in cross-sectional area, a measure of true stress was determined. The latter is work-conjugate with an effective strain measure, also based on real-time diameter measurement. The so-obtained stress–strain response is compared with that

inferred from full-field strain measurements, and this allows a critical assessment of the former method. Using this methodology, the effects of temperature and strain rate are studied and discussed. A modified version of the macromolecular model is used to characterize the mechanical behavior of the studied epoxy. The original model is amended to better represent the prepeak hardening and to allow for yielding to occur before peak stress, as observed in experiments. Also, the parameter m is here taken as a free parameter instead of a fixed value of 5/6. A procedure to assess each material parameter is fully described. This calibration is carried out from a limited set of experimental data. The model predictive capabilities are illustrated from comparisons of stress-strain curves between experiments and numerical simulations at other conditions. Data for tension and compression Kolsky bar experiments were collected from Dr. A. Gilat, Professor in the Department of Mechanical and Aerospace Engineering of the Ohio State University. Raw aging data was gathered from Dr. R. Goldberg from NASA GRC. Finally, flow localization is investigated through finite element calculations.

This dissertation consists of six chapters. Chapter I presents motivation, goal, background, approach and objectives related to the undertaken research work in this study. Chapter II presents an experimental method aiming at determining the intrinsic mechanical response of a polymer in quasi-static conditions. Chapter III describes the capabilities of a macromolecular model in the context of an epoxy resin, and modifications brought to it for a better representation of the quasi-static mechanical response of glassy polymers below their glass temperature transition. This chapter also details a procedure for identify the material parameters involved. Chapter IV illustrates and details the effects of aging and high strain rates on the mechanical response of an epoxy used as matrix for damage tolerant composite blade containment case. Chapter V details the use of the macromolecular model for the modeling of

polymers under dynamic loadings. Chapter VI presents a numerical investigation on flow localization observed on deformed specimens tested in quasi-static and dynamic conditions. Since the chapters of this dissertation have been written as papers to be submitted, the author warns the reader that part of the experimental data is repeated in some chapters.

CHAPTER II

DETERMINATION OF THE INTRINSIC BEHAVIOR OF POLYMERS USING DIGITAL IMAGE CORRELATION COMBINED WITH VIDEO-MONITORED TESTING

A. Overview

A new experimental methodology has been developed to determine the intrinsic behavior of glassy polymers up to large strains in both tension and compression. The novelty of this work is that the true stress versus strain response was determined using both a combination of non-contact full-field strain measurements and video-monitored data collection of area variation during testing. It is shown that the technique is applicable across a wide range of test temperatures and strain rates. Its capabilities are illustrated for a polymer epoxy for which it was found that the intrinsic behavior exhibits post-yield small-strain softening, but only in compression. In particular, the sensitivity of the post-yield drop to the type of approximate true strain measure is critically discussed at room and elevated temperatures.

B. Introduction

Experimental characterization of the large-strain constitutive behavior of materials is a challenging task. The principal difficulty resides in accounting for specimen-level geometry changes that accompany large deformations. The task is further complicated by the fact that the deformation quickly becomes nonuniform within the specimen. This nonuniformity manifests itself through necking in tension and barreling in compression. Both necking and barreling are plastic instabilities. As such, they are not dependent on the intrinsic material behavior only, but also on the specimen geometry.

Therefore, a key step in data interpretation and analysis is to decouple the structural effects from the intrinsic behavior.

While the difficulty in determining large-strain behavior is common to metals and polymers, the implications for the latter are far more significant. Glassy polymers, for instance, exhibit some viscoelastic deformation, large inelastic strains with small-strain softening and large-strain rehardening. The post-yield softening is associated with free-volume rearrangement whereas the rehardening at large strains results from an induced anisotropy due to molecular chain reorientation. Because of their peculiar behavior, initially smooth bars of glassy polymers are subject to the propagation of necks along their axis, when strained in tension. Shear bands may trigger or accompany neck propagation and other similar complex patterns of localized deformation may form under compression. What is of particular significance is that conventional methods cannot be used directly to infer the intrinsic material behavior from the mechanical response of a specimen in the presence of localization. For example, the amount of post-peak strain softening inferred from nominal stress–strain data may not be representative of the true material behavior. Such uncertainties have led some investigators to conclude that the small-strain softening may not be intrinsic in some polymers, e.g. see Ravi-Chandar and Ma (2000).

To address these challenges, several approaches have been followed in the literature. One approach is to design the experiment so as to delay the onset of localization and extract the material behavior from specimens showing macroscopically homogeneous deformation. Thus, platten lubrication in uniaxial compression experiments has been shown to delay significantly barrel formation (Boyce and Arruda, 1990; Arruda et al., 1995; Liang and Liechti, 1996) but is unlikely to suppress it completely (Ravi-Chandar and Ma, 2000; Benzerga et al., 2004). Other examples include custom-designed shear specimens (G'Sell and Gopez, 1981; Santore et al., 1991; Liang

and Liechti, 1996) and confined compression (Ma and Ravi-Chandar, 2000). While promising, this approach has had limited success. In shear specimens, exploitable ranges of shear strain remain small, because of premature fracture in sheet specimens (Ravi-Chandar and Ma, 2000) or strain localization near the specimen corners in rail-shear specimens (G'Sell and Gopez, 1981; Santore et al., 1991). While larger strain levels can be reached in confined compression, they remain smaller than about 0.15. In addition, the stress state is multiaxial which complicates the analysis of tests. Another approach that has been used in tension tests is to use strain gages (Liang and Liechti, 1996; Goldberg et al., 2005). This method is obviously limited by the maximum range of the gage and by the assumption of homogeneous deformation to back-estimate the true stress. In addition, it has been shown that strain gages induce local stress concentrations, which promote premature fracture (Goldberg et al., 2005); for example, tensile strains were limited to less than 0.1 in ductile polymers capable of much greater straining (Liang and Liechti, 1996).

Yet another approach is to record full-field measurements of mechanical fields in deformed specimens. Particularly useful for heterogeneous materials, this approach potentially allows the determination of the intrinsic behavior *locally*, thus circumventing the complications due to specimen-level geometric instabilities. Real-time full-field strain determination is typically made using deposited grid patterns (Buisson and Ravi-Chandar, 1990), geometric Moiré techniques (Liang and Liechti, 1996; Shield and Kim, 1991) and in recent years using digital image correlation (DIC) (Hild and Roux, 2006; Laraba-Abbes et al., 2003; Parsons et al., 2004; Grytten et al., 2009; Fang et al., 2009; Littell et al., 2008). More difficult is the determination of stress fields. While extensions of photoelastic methods have been proposed and used (Buisson and Ravi-Chandar, 1990; Liang and Liechti, 1996), they remain difficult to generalize. Thus, when full-field strain data is available there often remains the ques-

tion of stress determination. In the above works using DIC, the stress was calculated assuming homogeneous deformation of the specimen at some level.

An alternative approach that has been used in tension experiments consists of measuring the instantaneous minimum diameter using either a diametral transducer (G'Sell and Jonas, 1979) or a video-based extensometer (G'Sell et al., 1992; Mohanraj et al., 2006). Effective measures of strain and stress can thus be obtained. This method has extensively been used by G'Sell and co-workers and bears conceptual affinity with methods used for ductile metals, e.g., (Beremin, 1981; Benzerga et al., 2004). In the case of ductile polymers, the superiority of non-contact video-based extensometry is without doubt. For example, besides the risk of slippage along the neck, diametral extensometers may cause premature failure, an effect which is somewhat similar to that of strain gages. In more recent years, variations of video-based extensometery have been developed (G'Sell et al., 2002; Gloaguen and Lefebvre, 2001; Mohanraj et al., 2006). Axial and transverse displacements of markers printed prior to the test are tracked to determine local strains. In all of these, the diameter is not directly measured so that the stress calculation is based on the assumption of strain homogeneity in the marked area. To our knowledge, methods based on video extensometry have not yet been validated against full-field strain measurements.

In this chapter, the intrinsic behavior of a ductile epoxy polymer (EPON 862) is obtained from a combination of full-field strain measurements and video-monitored mechanical testing. The characterization of the mechanical behavior of this epoxy resin is based on tension and compression experiments on cylindrical specimens performed at NASA GRC by Littell et al. (2008). Littell et al. (2008) reported *engineering* stress-strain curves plotted from DIC data. These DIC raw data were obtained from NASA. Also, a Texas A&M undergraduate student was sent to NASA to post-process video-monitored data to measure the evolution of the cross sectional area

for each experiment. These data were brought back to Texas A&M University from which the author of this dissertation determined a measure of true stress. The latter is work-conjugate with an effective strain measure, also based on real-time diameter measurement. The so-obtained stress–strain response is compared with that inferred from full-field strain measurements (DIC), and this allows a critical assessment of the former method. Using this methodology, the effects of temperature and strain rate are studied and discussed.

C. Methods

1. Material

The material used in this study is a polymeric epoxy used in advanced designs of composite jet engine fan containment cases. This epoxy is a commercial untoughened thermosetting polymer E-862. It is formed from the reaction of epoxide resin EPON Resin 862 (Diglycidyl ether of bisphenol F -DGEBF-) with the aromatic amine curing agent Epicure W which is mainly composed of diethyltoluenediamine (DETDA). Specifically, the degree of polymerization of EPON Resin, which results from the reaction of an epoxide and bisphenol F, is controlled by temperature. This curing reaction is carried out at 176°C (350°F). The addition of the curing agent DETDA creates a highly crosslinked network (Tack, 2006). When the appropriate curing agents are used to crosslink Epon 862, higher electrical, adhesive, chemical and mechanical properties are reached. Also, because of its wide availability, low viscosity and high glass transition temperature (T_g=133°C (Gilat et al., 2007)), this resin has been recently selected as potential candidate for use in new designs of composite jet engine fan cases.

2. Initial Characterization of the Mechanical Response

Littell et al. (Littell et al., 2008) investigated the quasi-static response of EPON 862 using round smooth bars. These were smaller than ASTM standard tensile specimens (D638, 2004) because the bars had to be machined out of a plate having a thickness of 0.25 in. Specimen geometry and dimensions are given in Fig. 1.

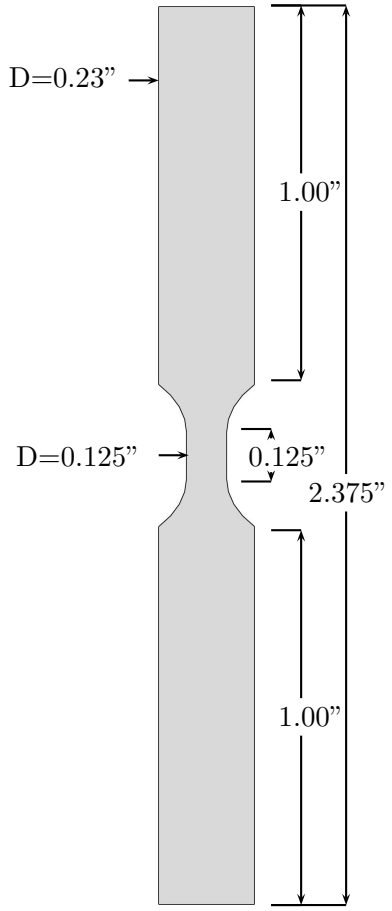

Fig. 1. Geometry and dimensions of the cylindrical specimen used by Littell et al. Littell et al. (2008) in tension and compression testing.

The specimens were tested in tension and compression at various temperatures below T_g ($T = 25°C$, 50°C and 80°C) and at various nominal strain-rates ($\dot{\epsilon} = 10^{-5}$/s, 10^{-3}/s and 10^{-1}/s). The nominal strain rate is defined as the crosshead speed divided by the initial gauge length. At least three, and up to seven realizations of the same test condition were carried out (with one exception). This includes some unloading–reloading tests. Details of the experimental procedure may be found in Ref. (Littell et al., 2008). Full-field surface strain measurements were carried out using a precise non-contact DIC technique. Image data processing was carried out using the DIC software ARAMIS[1], which provided the pointwise dilatational and shear strains. A detailed mapping of local surface strains could therefore be obtained, as illustrated in Fig. 2.

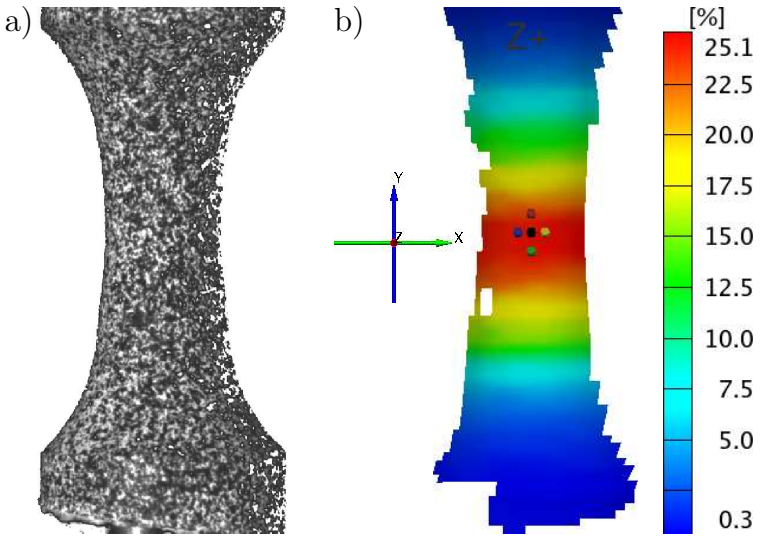

Fig. 2. (a) Specimen with speckles; (b) Contours of extensional axial strain. The five markings correspond to stage points at which strains are collected to calculate an average strain used for post processing stress–strain curves.

With the above measurements as basis, Littell et al. (Littell et al., 2008) re-

[1]ARAMIS^{TM}, GOM, Braunschweig, Germany

ported stress versus strain curves for multiple test temperatures and strain rates, including some unloading–reloading sequences. More specifically, they provided the experimental data in terms of the engineering stress defined as:

$$\sigma^{\text{eng}} = \frac{F}{S_0} \tag{2.1}$$

versus a local strain inferred by averaging from the full field measurements. A precise definition of the latter will be provided below. In (2.1), F is the force given by the load cell and S_0 is the initial cross sectional area. Unfortunately, the experimental data as presented in Ref. (Littell et al., 2008) cannot be used directly to infer the intrinsic behavior of the polymer. As a consequence, the data generated in Ref. (Littell et al., 2008) had to be re-analyzed to obtain the true stress–strain behavior of EPON 862.

In order to characterize the overall uniaxial behavior of the material, specimen-level stresses and strains had to be calculated. The principal difficulty resides in accounting for geometry changes that accompany large deformations. In particular, the issue of whether the post-peak strain softening is intrinsic in polymers has been debated at length in the literature; see e.g. Ravi-Chandar and Ma (2000). In this regard, obtaining full-field strain measurements, if only on part of the surface, allows one to make an assessment as to whether the local behavior exhibits the post-peak softening. This technique was applied in a previous study to characterize the mechanical behavior of the same epoxy resin EPON-862 Littell et al. (2008). However, results were there given in terms of *engineering* stresses, and become quickly intractable as soon as deformations become heterogenous.

3. Measures of (True) Strains and Stresses

In what follows, we will work with two strain measures. The first measure is that used in Littell et al. (2008). It is defined as some axial strain averaged spatially

over five locations in the current configuration. These five points are marked by large dots in Fig. 2b and are located in the region where the highest strains are expected, i.e., in the central region of the gauge section. Averaging over a limited set of points allows to smear out pointwise fluctuations while keeping the "local" character of the measurement. What is to be averaged depends on the choice of the local deformation tensor. For instance, let $\delta\mathbf{S}^{(2)} = \delta S_2 \mathbf{e}_2$ be a line element along x_2 in the reference (e.g., undeformed) configuration, with x_2 being the loading axis (vertical in Fig. 2) and $\mathbf{e}_2$ a unit vector. Also, let $\delta\mathbf{s}^{(2)} = \delta s_2 \mathbf{n}$ be the deformed material element[2]. For the DIC software, the values of δS_2 constitute initial data and the set of values δs_2 are continuously tracked during the experiment. With that basis, one can work with the stretches $\delta s_2/\delta S_2$ or the elongations $(\delta s_2 - \delta S_2)/\delta S_2$. Either measure can be used in the averaging procedure above. While the former is preferable in a finite strain setting, we have used the elongations following Littell et al. (2008). This choice is of no consequence on the main issue at stake, i.e., the decoupling of structural effects from intrinsic material behavior in regards to the potential material softening. In summary, this first average strain measure is formally written as

$$\bar{\epsilon}_{22} = \langle \frac{\partial u_2}{\partial x_2} \rangle_{\text{five points}} \tag{2.2}$$

where $\langle \cdot \rangle$ stands for averaging over the five locations (material points) and u_2 denotes the axial displacement. It is important to notice that the initial reference configuration could be updated at each stage. Under such circumstances, the measure $\bar{\epsilon}_{22}$ would not be very different from a Lagrangian strain measure in the absence of large rotations.

[2]In uniaxial loading, $\mathbf{n}$ is not very different from $\mathbf{e}_2$ so long as deformation is not localized.

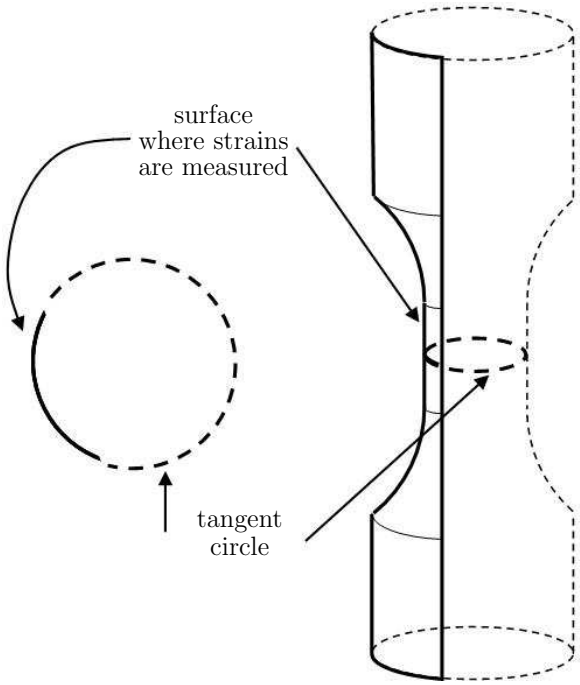

Fig. 3. Determination of the current cross-sectional diameter Φ in (2.3) and (2.4) using the tangent circle method (DIC post-processing).

One disadvantage of the above strain measure is that it is a surface measure. Also, the recorded strains may substantially vary among the five points once necking or barreling occurs. In addition, some points are located above the neck (or section of maximum diameter under compression) and tend to become farther apart or closer to each other as deformation proceeds. One characteristic of plastic instabilities such as necking of bars or barreling of cylinders is that strain gradients are mostly in the axial direction. For each experiment on EPON 862, the values of $\bar{\epsilon}_{22}$ as measured by Littell et al. (2008) was communicated to us by NASA GRC.

The second measure of strain is thus defined based on the reduction of cross-sectional area within the neck:

$$\varepsilon = \ln \frac{S_0}{S} = 2 \ln \frac{\Phi_0}{\Phi} \tag{2.3}$$

where S is the current cross-sectional area at the neck (or section of maximum diameter under compression), Φ is the diameter and the subscript 0 refers to initial values. The rationale for choosing this measure is as follows. If the material were incompressible, ε would be an approximation of the Hencky strain integrated over the deformation history. It is only an approximation, notably because of strain gradients in the radial direction. In addition, the strain measure ε is based on confining the measurement to the section of extremal diameter where strains are maximum.

Definition (2.3) requires that the diameter Φ be measured at the desired location. Since experiments were already performed by Littell et al. (2008), the only possibility of have access to Φ post-mortem was to use the post-processing capabilities of the DIC software, only available at NASA GRC. A domestic Texas A&M undergraduate[3] was sent to NASA to measure the evolution of Φ using the tangent circle method as sketched in Fig. 3.

An important consequence of the measurement of Φ is that the true stress can be evaluated as

$$\sigma = \frac{F}{S} = \frac{4F}{\pi\Phi^2} \tag{2.4}$$

In what follows, curves of the above measure of true stress, σ, versus an approximate measure of true strain (either $\bar{\epsilon}_{22}$ or ε) will be referred to as the (true) stress–strain curves of the material.

D. Results

The experimental results presented in this section are the outcome of a detailed statistical analysis of data and interpretation of trends involving a total of 52 experimental realizations. They include true stress-strain curves (based on the two measures of

[3]The author of this dissertation was not granted access to NASA

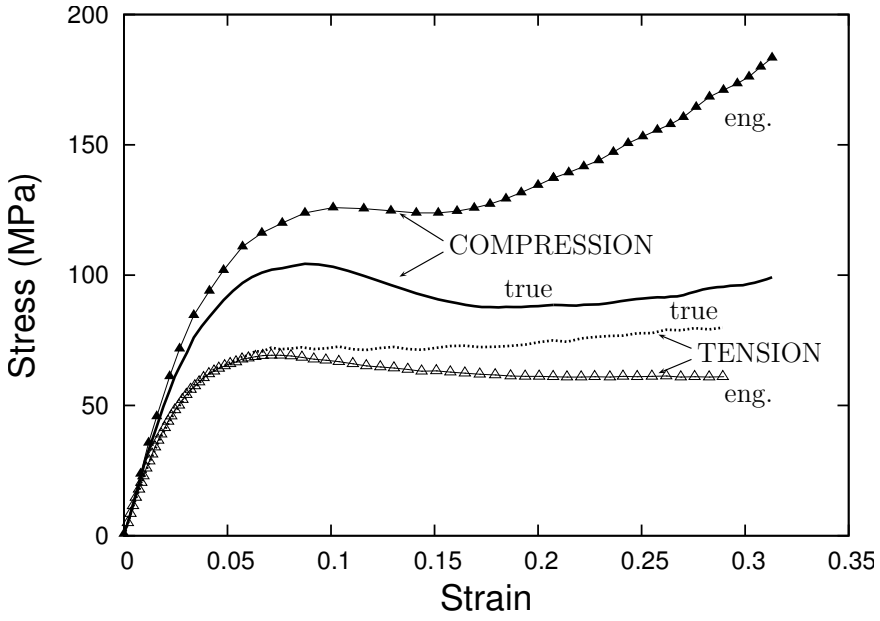

Fig. 4. Comparison between the true stress–strain response of EPON 862 (σ in (2.4) versus $\bar{\epsilon}_{22}$ in (2.2)) with the engineering response ($\sigma^{\rm eng}$ in (2.1) versus $\bar{\epsilon}_{22}$). Example 1: compression at $T = 25°$C and nominal strain-rate $\dot{\epsilon} = 10^{-1}$/s; Example 2: tension at $T = 25°$C and $\dot{\epsilon} = 10^{-5}$/s.

strains $\bar{\epsilon}_{22}$ and ε) as well as detailed analysis of videos of full-field strain contours.

1. The Intrinsic Material Behavior

Examples of the true stress σ given by (2.4) versus true strain $\bar{\epsilon}_{22}$ given by (2.2) are shown in Fig. 4. The first example is for compression at room temperature and $\dot{\epsilon} = 10^{-1}$/s; the second is for tension at the same temperature and $\dot{\epsilon} = 10^{-5}$/s. In each case, the true response is compared with the engineering stress $\sigma^{\rm eng}$ in (2.1) versus $\bar{\epsilon}_{22}$. Figure 4 clearly shows that the engineering stress is significantly greater (respectively smaller) than the true stress under compression (respectively tension). For example, at the peak stress in compression the difference between the two measures is a little over 20 MPa and increases to about 80 MPa at larger strains. In

tension, the difference is smaller; as will be illustrated below, this is due to the fact that barreling in compression is more pronounced than is necking in tension. Even though the difference is smaller in tension, the amount of post-peak softening inferred from the engineering response is misleading.

We now proceed to compare the two measures of "true strain": $\bar{\epsilon}_{22}$ in (2.2) versus ε in (2.3). This is illustrated in Fig. 5 for two values of strain rate. Again two cases are selected, one in tension, the other in compression. For the examples in tension, the two measures are very close to each other. For our purposes, they will be considered as indistinguishable. On the other hand, the examples chosen in compression illustrate other observed instances where the strain measure $\bar{\epsilon}_{22}$ is found to be considerably smaller than the measure ε. This difference occurs subsequent to strain localization. As indicated above, the strain measure ε is more reliable post-localization. Despite the fact that $\bar{\epsilon}_{22}$ has more of a local character, it was systematically found to be smaller than the logarithmic measure ε at room temperature, irrespective of strain rate or whether the testing was in tension or compression[4].

[4]There is only one exception among all experiments at 25C: one case of tension at $\dot{\epsilon} = 10^{-3}$/s shows end-of-test values of $\varepsilon = 0.32$ and $\bar{\epsilon}_{22} = 0.38$. The corresponding realization is shown in Fig. 6.

(a)

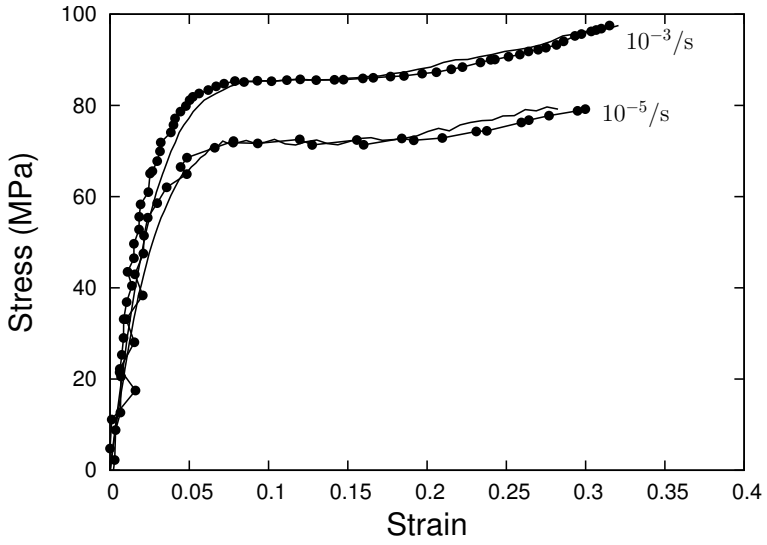

(b)

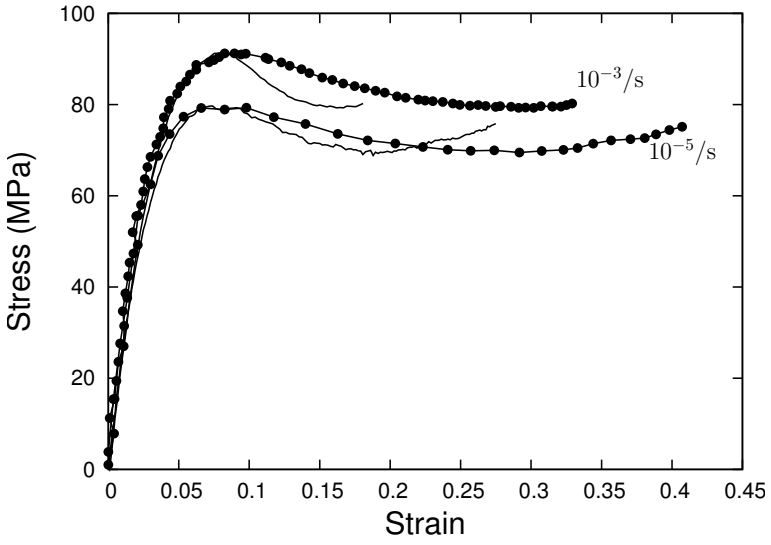

Fig. 5. True stress versus strain curves for $T = 25°\text{C}$ and two definitions of the "true" strain: $\bar{\epsilon}_{22}$ in (2.2) (solid lines) or ε in (2.3) (filled circles). (a) Tension at $\dot{\epsilon} = 10^{-3}/\text{s}$ and $\dot{\epsilon} = 10^{-5}/\text{s}$; (b) Compression under the same conditions.

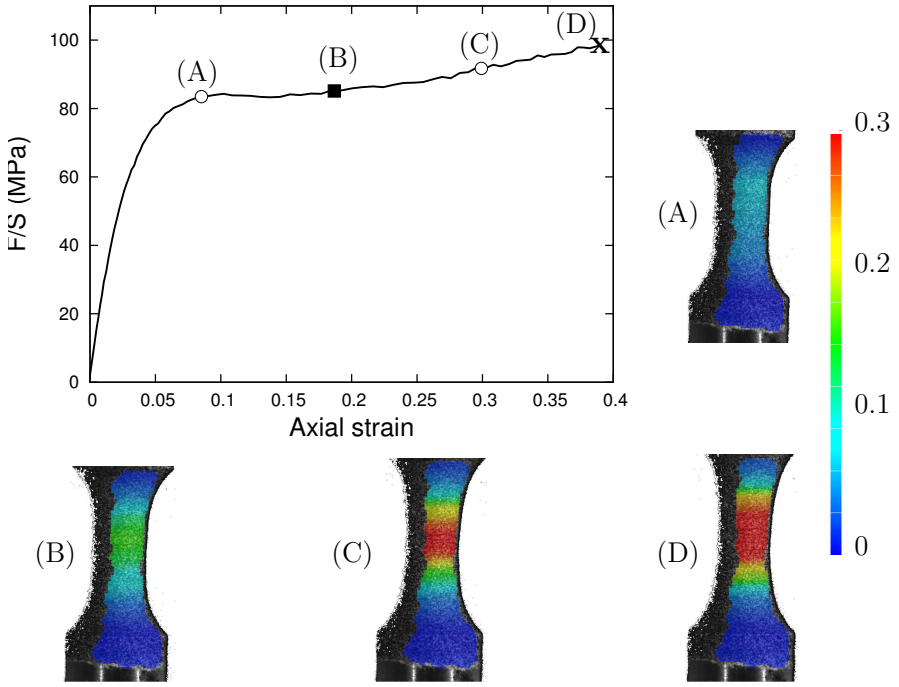

Fig. 6. True stress versus true strain $\bar{\epsilon}_{22}$ and corresponding select snapshots of DIC strain contours in tension at $T = 25°\text{C}$ and $\dot{\epsilon} = 10^{-3}/\text{s}$. The circles on the curve correspond to stages before and after the onset of necking (resp. (A) and (C)), which is clearly observable at (B). The cross indicates fracture which occurs slightly after stage (D).

In order to appreciate these differences further, it is worth examining the phenomenology of deformation in EPON 862 by correlating the full-field strain mapping with the overall stress–strain response. Figure 6 illustrates such a correlation in the case of tension at $T = 25°\text{C}$ and $\dot{\epsilon} = 10^{-3}/\text{s}$ (the test realization being different from that in Fig. 5.). The contours of axial strain are shown using the same scale.

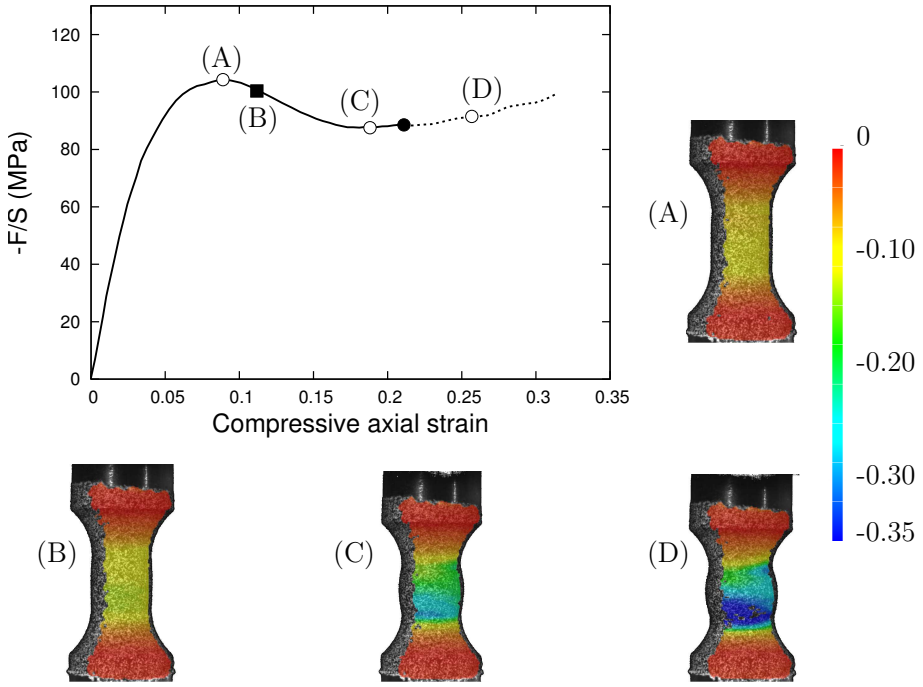

Fig. 7. True stress versus true strain $\bar{\epsilon}_{22}$ and corresponding select snapshots of DIC strain contours in compression at $T = 25°\text{C}$ and $\dot{\epsilon} = 10^{-1}/\text{s}$. The circles on the curve correspond to stages before and after the onset of barreling (resp. (A) and (C)), which is clearly observable at (B). The full circle indicates the loss of consistency of DIC data. At (D) the dark spot in the highly deformed region is an example of the absence of calculated strains.

After the initially linear elastic response the material behavior becomes nonlinear. At a strain of $\bar{\epsilon}_{22} = 0.083$, i.e., slightly before peak, the strain distribution is essentially homogeneous within the gauge area, Snapshot (A). Shortly thereafter, deformation localizes because of the development of a shallow neck. Difficult to visualize with the naked eye, the onset of necking is ascertained based on two observations: (i) the drop in the force, as seen for example in the engineering curve of Fig. 4; and (ii) the deformation becomes nonunifom along the x_2-axis (Snapshot (B) in Fig. 6). The filled square at (B) means that at this stage it has become visually evident that localization took place. In actuality, localization is likely to have set in earlier than stage (B).

Strains reach values around 0.18 and decrease down to about 0.08 near the ends of the specimen gauge section. Subsequent deformation is characterized by a rehardening stage starting at a strain of about $\bar{\epsilon}_{22} = 0.14$. This rehardening stage is peculiar in polymeric materials. As a consequence, material in the vicinity of the incipient neck hardens again and deformation becomes more uniform going from snapshot (B) to (D) through (C). Finally, fracture takes place at a strain of about 0.39. The corresponding snapshot (D), taken right before fracture, exhibits some strain concentration at the center with most of the gauge section experiencing strains higher than 0.3.

Figure 7 depicts a typical response in uniaxial compression as well as snapshots of strain contours at various stages of deformation. As observed in tension, the strains at peak stress (σ=102 MPa) are rather homogeneous (about 0.10), snapshot (A). During the softening regime, which is more pronounced than in tension, barreling becomes clear within the specimen gauge, snapshot (B). A subtle discoloration in the strain contours is observed in the neighborhood of the center, which marks the onset of strain gradient therein. Additional compression is accompanied by a growing barreling instability as well as strain concentrations. The minimal stress, also called lower yield stress or dip stress (σ=87 MPa), is obtained at $\bar{\epsilon}_{22}$= 0.18. A mapping of strains at the beginning of the rehardening stage is detailed in snapshot (C). Contrary to the symmetric distribution of strains in tension, an asymmetric strain distribution pattern develops within the specimen which induces a macroscopically visible asymmetry between the top and bottom parts of the specimen. In this particular case, the maximum compressive strains are obtained in the lower half of the gauge section. It is likely that the asymmetry in strain distribution be caused by the non-standard specimen geometry.

In addition, the DIC software may not be capable of capturing and calculating strains in highly deformed regions (dark spots in Fig. 7 at stage (D)). When such

problems occur in the center of the specimen, where strain values are used for post-processing the measure $\bar{\epsilon}_{22}$, the software calculates the strain at a nearby location, which is problematic for consistency. In the example shown, this data capturing problem occurred at a strain of about $\bar{\epsilon}_{22} = 0.215$. It is indicated by a filled circle in the figure. The data acquired beyond this point is plotted as dotted line, simply to indicate that it may not be as reliable as data before that stage. Snapshot (D) depicts the strain contours at $\bar{\epsilon}_{22}= 0.255$. The strain distribution is heterogeneous with maxima exceeding a value of 0.35, concentrated at the bottom of the gauge section.

Going back to the difference between the two strain measures $\bar{\epsilon}_{22}$ in (2.2) and ε in (2.3) (see Fig. 5), the picture is now much clearer in light of the results shown in Figs. 6 and 7. In particular, barreling in compression often leads to a strain distribution that is asymmetric with respect to the horizontal x_1-axis. Because the strain measure $\bar{\epsilon}_{22}$ includes some material points above and below the section of maximum diameter, $\bar{\epsilon}_{22}$ ends up being smaller than the maximum value. In tension, the local strains may vary among the five points once necking occurs. In some cases, the two measures lead to nearly identical stress–strain curves (e.g. Fig. 5a, 10^{-3}/s), but in other cases (e.g. Fig. 5a, 10^{-5}/s), some differences are noted, although less dramatic than under compression loading.

In summary, the engineering stress–strain response of EPON 862 is significantly different from the true response (Fig. 4). Differences are greater under compression loading. In all cases, the amount of post-peak softening changes depending on the stress measure. Also, two approximate measures of true strain were used: $\bar{\epsilon}_{22}$ used in Ref. Littell et al. (2008) and a new measure ε. In tension, the two measures are very close to each other. In compression, however, $\bar{\epsilon}_{22}$ is found to be considerably smaller than ε at room temperature (Fig. 5). This difference occurs because of the onset of

a plastic instability (necking or barreling) and subsequent strain localization.

2. Effects of Temperature

The reader may have noticed that all of the illustrative results discussed above are for room temperature testing. The essential conclusions remain the same for testing at higher temperatures. In particular, large differences are seen between the engineering curves and true stress–strain curves (regardless of what measure of true strain is adopted), just like in Fig. 4[5]. Nonetheless, when comparing the strain measures ε and $\bar{\epsilon}_{22}$, in most cases the latter is found to be greater than ε, unlike for room temperature testing. In tension, differences are small. In compression, in the extreme case shown the strain difference is over 0.1.

One possible explanation of this trend is that, for the high temperature testing, surfaces are hotter than the interior of the specimen. Consequently, the strains at the surface would be greater than at the core of the specimen, which is consistent with greater values of $\bar{\epsilon}_{22}$ in comparison with ε. If that is the case, then the measure ε would be once again more appropriate to work with since it averages out the radial gradient of strains associated with a nonuniform temperature distribution. In any case, the two curves fall on top of each other, up to the largest recorded strain ε. Therefore, this kind of difference in inconsequential on the identification of model parameters, unlike the differences seen in Fig. 5 for room temperature testing.

Fig. 8 summarizes the temperature-sensitivity of Epon 862 in tension at a strain-rate of 10^{-3}/s (top) and in compression at a strain-rate of 10^{-1}/s (bottom). The same effects of temperature on the mechanical response are observed in tension at 10^{-1}/s

[5]No other engineering curve is provided in this chapter. This data may be found in Ref. Littell et al. (2008). On that basis, comparison with the results included throughout this chapter can readily be made.

and in compression at 10^{-3}/s. Note that $\bar{\epsilon}_{22}$ is used as the true strain measure. It is important to notice that, except for room temperature testing in compression, the use of σ–$\bar{\epsilon}_{22}$ in lieu of σ–ε curves is acceptable and will not impact much the identification of material parameters entering the constitutive model. The bars indicate the extent of scatter in experimental data collected for multiple realizations[6] of the same test condition. As explained above, a filled square on each stress–strain curve refers to that stage at which necking or barreling has become evident to the naked eye. In tension, the failure of specimens is marked by a cross at the end of the curve. In compression, the full circles and dotted line correspond to questionable data due to data collection problems.

The amount of thermal softening of E862 epoxy, as inferred from Fig. 8, is significant over the temperature range investigated. In tension, for example, the peak stress reaches about 80 MPa at room temperature, and decreases down to 47 MPa at 80°C. In compression, the peak stress decreases from 105 MPa at 25°C down to 65 MPa at 80°C. It is worth noting that thermal softening does not affect the shape of the stress–strain curve. The only exception in the σ–$\bar{\epsilon}_{22}$ plots of Fig. 8b is for room-temperature compression. This particular data is not reliable, as analyzed above. When σ–ε plots are made the shape of the curve is essentially the same as at higher temperatures[7]. In tension, the true stress–strain curve is characterized by a hardening stage at small strains, followed by a plateau then a rehardening stage at larger strains. In compression, the amount of post-peak softening is noticeable. The care taken in analyzing the data leads us to conclude that this softening is intrinsic

[6]Number of realizations "()" in tension at 10^{-3}/s: 25°C (7), 50°C (5), 80°C (4); in compression at 10^{-1}/s: 25°C (5), 50°C (3), 80°C (3)

[7]We have chosen to present σ–$\bar{\epsilon}_{22}$ plots instead of the more reliable σ–ε ones because, as indicated above, some of the σ–ε curves suffer from serrations at small strains.

to the material behavior.

3. Effects of Strain Rate

The influence of (nominal) strain-rate on the epoxy behavior was investigated at room temperature, 50°C and 80°C. Experiments in tension and compression were conducted at 10^{-1}/s and 10^{-3}/s at these three temperatures. Additional experiments were performed at 10^{-5}/s at room temperature. All these experiments were analyzed following the same methodology as described earlier to obtain the true material behavior.

Figure 9 depicts the influence of strain rate on the room temperature tensile and compressive behavior of the epoxy. The data correspond to constant nominal, not true, strain rate. As expected, the higher the strain rate the greater the flow stress. In both tension and compression, the peak stress increases by about 25 MPa when the strain rate increases from 10^{-5}/s to 10^{-1}/s. Hence, a variation of the strain rate by four orders of magnitude leads to a variation of the flow stress smaller than that effected by a 55K variation in the temperature (see Fig. 8 above where the peak-stress difference was about 35 MPa).

E. Discussion

As shown in Fig. 4 epoxy E-862 is able to sustain very large strains, even in tension. In the literature, tension data is often reported up to a few percent of total strain because of premature fracture. In fact, previous investigations (Goldberg et al., 2005) have clearly shown that this behavior is the artifact of using strain gauges. The latter concentrate strains and thus lead to specimen failure.

The main advantage of this analysis consists in obtaining the intrinsic response

of EPON-862 regardless of the plastic instabilities such as necking in tension and barreling in compression, or of any geometry induced deformation pattern. Therefore, this methodology could give new insight regarding the debate of whether the softening which is exhibited by many polymers is intrinsic to the material behavior or whether it is merely a consequence of the specimen geometry, the testing conditions or any plastic instabilities.

For instance, experiments on PC and PMMA under plane strain conditions exhibited softening with macroscopic homogeneous deformations (Arruda and Boyce, 1993b) (Arruda and Boyce, 1993a). However, tensile behavior does not show any softening (Buisson and Ravi-Chandar, 1990).

With proper experimental apparatus which avoids localization, the suppression of strain softening for PC and PMMA under confined compression was also obtained Ravi-Chandar and Ma (2000).

Moreover, even without softening in true stress-strain curves, axisymmetric and plane strain neck propagation may still occur Buisson and Ravi-Chandar (1990) Hutchinson and Neale (1983); Kyriakides (1994).

Also, the effect of mechanical dilatation on the free volume (e.g. annealing) may induce true material softening Hasan et al. (1993). With this in mind, the precise characterization of the epoxy mechanical response can then be used as experimental basis in view of the calibration of parameters entering constitutive models and of future comparisons between experimental stress-strain curves and numerical simulations.

F. Conclusion

The main conclusions of this study are:

- The engineering stress–strain response of EPON 862 is significantly different from the true response (Fig. 4). Differences are greater under compression loading. In all cases, the amount of post-peak softening changes depending on the stress measure.

- Two approximate measures of true strain were used: $\bar{\epsilon}_{22}$ used in Ref. Littell et al. (2008) and a new measure ε. In tension, the two measures are very close to each other. In compression, however, $\bar{\epsilon}_{22}$ is found to be considerably smaller than ε at room temperature (Fig. 5). This difference occurs because of the onset of a plastic instability (necking or barreling) and subsequent strain localization.

- The essential conclusions remain the same for testing at higher temperatures. Nonetheless, in most cases $\bar{\epsilon}_{22}$ is found to be greater than ε (Fig. 5). One possible explanation of this trend is that, for the high temperature testing, surfaces are hotter than the interior of the specimen.

- The strain measure ε is more reliable than $\bar{\epsilon}_{22}$ both at room temperature and at elevated temperatures, albeit for different reasons.

- The amount of thermal softening of EPON 862 is significant over the temperature range investigated. The thermal softening does not affect the shape of the true stress–strain curve provided that the measure ε is used.

- In tension, the true stress–strain curve is characterized by a hardening stage at small strains, followed by a plateau then a rehardening stage at larger strains. The amount of softening, if any, is very small. In compression, the amount of post-peak softening is noticeable.

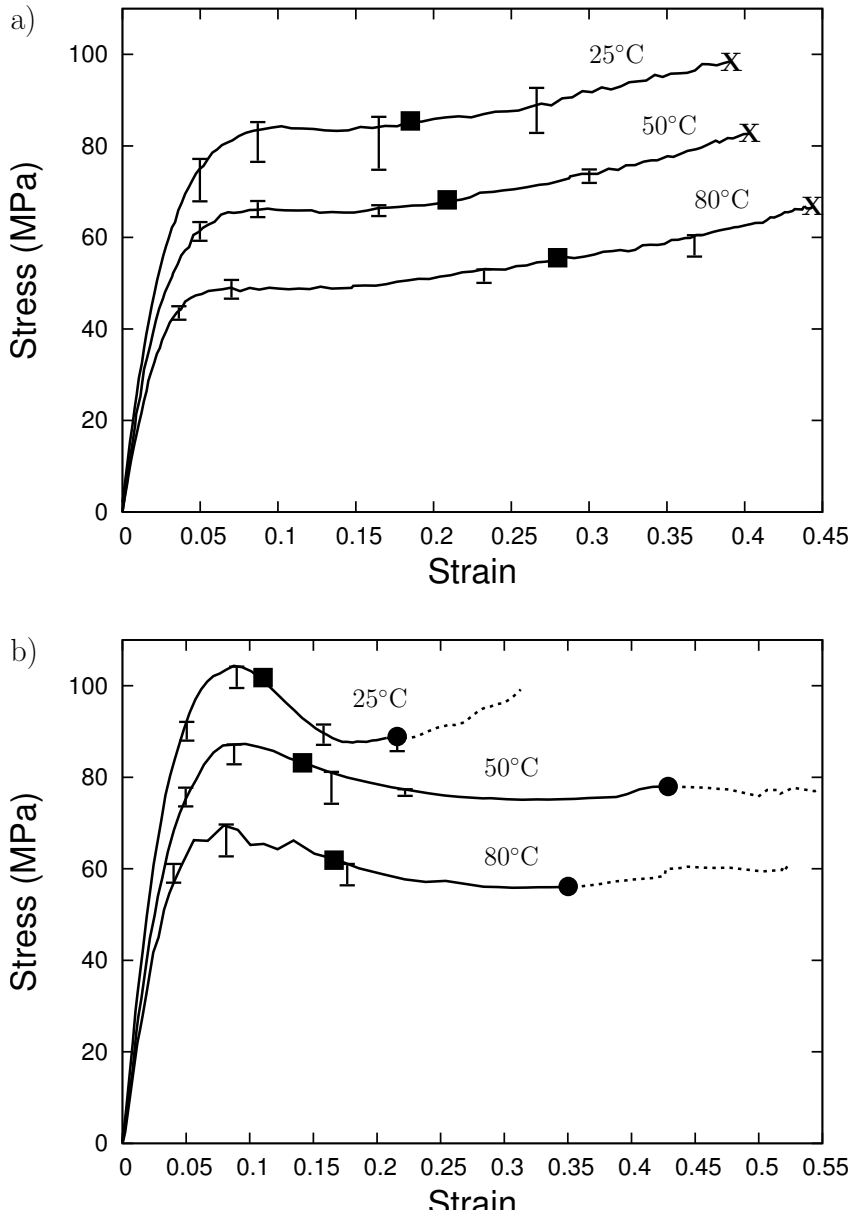

Fig. 8. Effect of temperature on the true stress–strain behavior of EPON 862 (σ versus $\bar{\epsilon}_{22}$). (a) Under tension at a nominal strain-rate of 10^{-3}/s and (b) under compression at a nominal strain-rate of 10^{-1}/s.

(a)

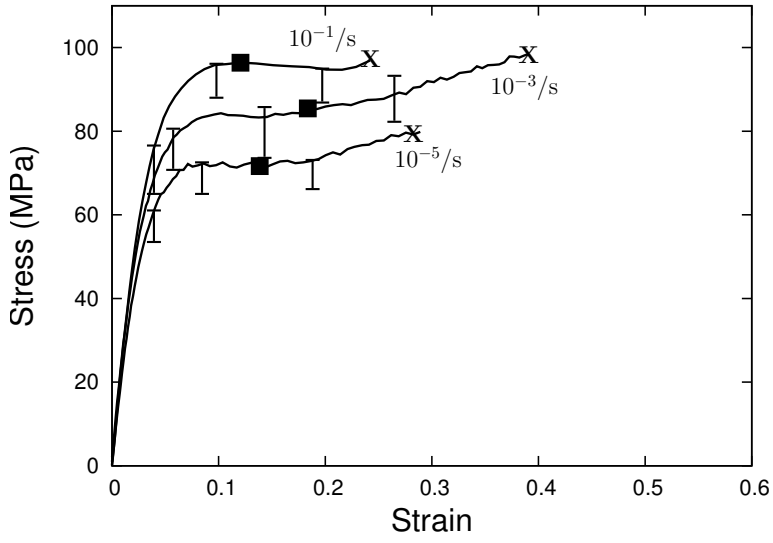

(b)

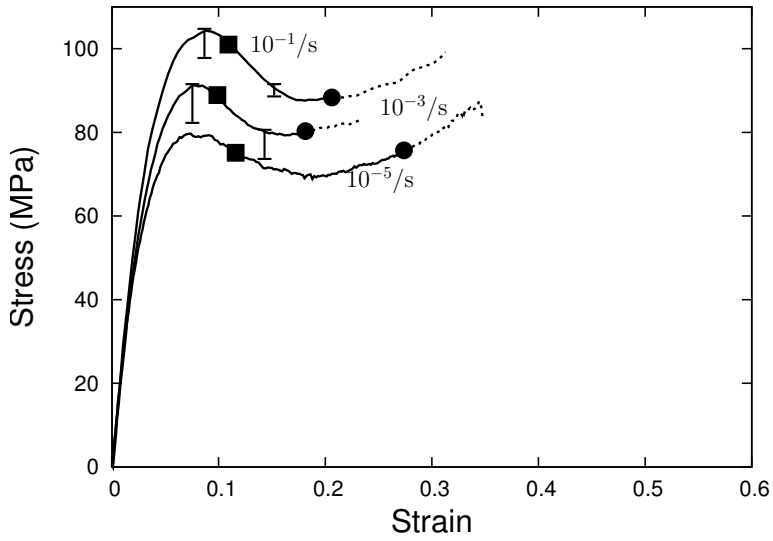

Fig. 9. Effect of nominal strain-rate at $T = 25°\text{C}$. True stress versus strain ($\bar{\epsilon}_{22}$) curves for (a) tension; and (b) compression.

CHAPTER III

MODELING OF THE VISCOPLASTIC BEHAVIOR OF A POLYMER EPOXY

A. Overview

Viscoplastic models are commonly used to assess and predict the complex behavior of glassy polymers under their glass transition temperature. Among the most sophisticated is the macromolecular model developed by Boyce et al. (1988). Here, we challenge the capabilities of a variant of this model against experimental results on epoxy resin Epon-862. Uniaxial tests in tension and compression were performed for temperatures varying from 25°C to 80°C and strain rates from 10^{-5}/s to 10^{-1}/s Poulain et al. (2010b). These experimental data were divided into two separate sets. The first set was used to assess the model material parameters whereas the model predictive capabilities were tested based on the second set of experimental data. We detail a procedure aiming at estimating those material parameters. The model encompasses several modifications from the original model of Boyce et al. in that (i) yielding is allowed to occur before peak stress; (ii) the pre-peak hardening is better captured; and (iii) the strain rate exponential factor which appears in the viscoplastic law is here considered as a free parameter m, as opposed to a fixed value (=5/6). The identification of the material parameters leads to $m = 0.5$. Excellent fitting is observed between computed versus experimental stress-strain responses for both calibration and prediction sets. In particular, the temperature, strain rate and pressure sensitivity are accurately captured.

B. Introduction

Glassy polymers commonly exhibit complex mechanical behaviors. Monotonic loading tests performed on polymers under their glass transition temperature result in stress-strain curves which display specific features. After an initial (nonlinear) elastic regime, the stress keeps increasing until it reaches a peak. It usually follows a strain softening stage which competes with a large strain rehardening regime. The characterization of the full range polymer response demands special precautions. For instance, optical testing methodologies capture the full deformation range of polymers (Poulain et al., 2010b) whereas some traditional characterization techniques such as strain gauges promote early fracture due to stress concentration (Goldberg et al., 2005). Moreover, the response of glassy polymers is time, temperature, rate and pressure dependent (Klompen et al., 2005; Hope et al., 1980a,b; Rabinowitz et al., 1970). In the past few decades, specific attention has been given to the development of models capable of assessing such mechanical behaviors. For instance, early models were built accounting for pressure-sensitivity plastic potential (Drucker and Prager, 1952), combined with isotropic strain hardening (Goldberg and Stouffer, 2002). However, two major classes of models emerged. The first category of polymer models is based on viscoelastoplastic constitutive relations. They benefited from the original work of Tervoort et al. (1998) who formulated a three dimensional constitutive framework based on a compressive modification of the Leonov's fluid model (Leonov, 1976). The corresponding rheological model is formed of a linear spring element and a 3-D Eyring dashpot. Later, following the work of Hasan et al. (1993) strain softening was included as well as pressure sensitivity (Govaert, 2000). Moreover, strain rehardening was accounted for through a neo-Hookean rubber spring (Tervoort and Govaert, 2000).

The second major class of models are based on viscoplastic formulations. They originated from the early work of Haward and Thackray (1968) who described the large strain mechanical behavior by the contribution of two processes. The first process captures the rate dependence of the flow stress with respect to the thermally activated motions of polymer chain segments. This molecular motion was characterized by an Eyring-like viscosity (Eyring, 1936). The second process reflects the progressive alignment of the molecular chains. It is modeled directly from the theory of rubber elasticity by a Langevin spring (Treloar, 1975). Boyce, Parks and Argon performed a three dimensional extension of this model (Boyce et al., 1988). This so-called *BPA* model includes a 3D generalization of the Argon plastic flow theory (Argon, 1973) and accounts for pressure and intrinsic softening. The representation of the large strain hardening builds on successive improvements. The initial three-chain model lead to a more realistic eight-chain model (Arruda and Boyce, 1993b) such that a full network model is usually preferred (Wu and Van der Giessen, 1996). It is worth emphasing that a close relationship exists between the strain rate and temperature sensitivity in this model. This temperature-rate interdependence is characterized by a specific viscoplastic law based on the thermoactivated production of local molecular kinks with yielding (Argon, 1973). In particular, an exponential factor m enters this law and was derived to take the value $m = 5/6$. This model was used to capture the mechanical response of several thermoplastics such as Polycarbonate (PC) (Boyce and Arruda, 1990; Boyce et al., 1994), Ultra-High Molecular Weight Polyethylene (UHMWPE) (Bergstrom et al., 2002), Polymethylmethacrylate (PMMA) (Boyce et al., 1988, 1992). However, little attempt has been made to capture and assess the response of thermosets for a large range of temperatures and strain-rates with this model (Wu et al., 2005). Recently, an extension of this model (Mulliken and Boyce, 2006) was used to assess the response of Epon 826/DEA epoxy (Jordan

et al., 2008).

In this chapter, a modified version of the BPA model is used to characterize the mechanical behavior of thermosetting resin EPON-862. The experimental data of this epoxy were collected from (Poulain et al., 2010b,a). The original model is amended to better represent the prepeak hardening and to allow for yielding to occur before peak stress, as observed in experiments. Also, the parameter m is here taken as a free parameter instead of a fixed value of 5/6. A procedure to assess each material parameter is fully described. This calibration is carried out from a limited set of experimental data. The model predictive capabilities are illustrated from comparisons of stress-strain curves between experiments and numerical simulations at other conditions.

C. Macromolecular Model

This part of the model has been developed in Chowdhury et al. (2006); Chowdhury (2007); Chowdhury et al. (2008b). We assume additive decomposition of the total rate of deformation $\mathbf{D}$. A hypoelastic law is used to specify the elastic part $\mathbf{D}^{\mathrm{e}}$ in terms of the co-rotational rate of Cauchy stress as:

$$\mathbf{D}^{\mathrm{e}} = \mathbf{L}^{-1} : \overset{\triangledown}{\boldsymbol{\sigma}} \tag{3.1}$$

where $\mathbf{L}$ is the point-wise tensor of elastic moduli given in terms of Young's modulus and Poisson's ratio.

In the polymer matrix, the flow rule is specified such that plastic deformation is incompressible, i.e.,

$$\mathbf{D}^{\mathrm{p}} = \dot{\bar{\epsilon}}\,\mathbf{p}, \quad \mathbf{p} = \frac{3}{2\sigma_{\mathrm{e}}}\boldsymbol{\sigma}'_{\mathrm{d}} \tag{3.2}$$

where $\dot{\bar{\epsilon}}$ is the effective strain rate defined as:

$$\dot{\bar{\epsilon}} = \sqrt{\frac{2}{3}\,\mathbf{D}^{\mathrm{p}\prime} : \mathbf{D}^{\mathrm{p}\prime}} \tag{3.3}$$

with $\mathbf{X}'$ referring to the deviator of second-rank tensor $\mathbf{X}$, and σ_{e} is an effective stress defined by:

$$\sigma_{\mathrm{e}} = \sqrt{\frac{3}{2}\boldsymbol{\sigma}'_{\mathrm{d}} : \boldsymbol{\sigma}'_{\mathrm{d}}}, \qquad \boldsymbol{\sigma}_{\mathrm{d}} = \boldsymbol{\sigma} - \mathbf{b} \tag{3.4}$$

with $\boldsymbol{\sigma}_{\mathrm{d}}$ the driving stress and $\mathbf{b}$ the back stress tensor that describes the orientation hardening of the material. It evolves following:

$$\overset{\triangledown}{\mathbf{b}} = \mathbf{R} : \mathbf{D} \tag{3.5}$$

$\mathbf{R}$ being a fourth-order tensor, which is specified here by using a non-Gaussian network model (Wu and Van der Giessen, 1996) that combines the classical three-chain rubber elasticity model (Boyce et al., 1988) and the eight-chain model (Arruda and Boyce, 1993b), such that

$$\mathbf{R} = (1-\kappa)\,\mathbf{R}_{\text{3-ch}} + \kappa \mathbf{R}_{\text{8-ch}} \tag{3.6}$$

where $\kappa = 0.85\bar{\lambda}/\sqrt{N}$, N is a material constant and $\bar{\lambda}$ is the maximum principal stretch, which is calculated based on the left Cauchy–Green tensor $\mathbf{B} = \mathbf{F}\cdot\mathbf{F}^T$, and

$$R^{ijkl}_{8-\mathrm{ch}} = \frac{1}{3}C^R\sqrt{N}\left[\left(\frac{\xi_c}{\sqrt{N}} - \frac{\beta_{\mathrm{c}}}{\lambda_c}\right)\frac{B^{ij}B^{kl}}{B^{mm}} + \frac{\beta_{\mathrm{c}}}{\lambda_c}\left(\delta^{ik}B^{jl} + B^{ik}\delta^{jl}\right)\right] \tag{3.7}$$

where C^R and N are material constants known as the rubbery modulus and average number of links between entanglements, respectively, and

$$\lambda_c^2 = \frac{1}{3}\mathrm{tr}\mathbf{B}, \quad \beta_{\mathrm{c}} = \mathcal{L}^{-1}\left(\frac{\lambda_c}{\sqrt{N}}\right), \quad \xi_c = \frac{\beta_{\mathrm{c}}^2}{1-\beta_{\mathrm{c}}^2\mathrm{csch}^2\beta_{\mathrm{c}}} \tag{3.8}$$

where $\mathcal{L}^{-1}$ is the inverse Langevin function defined as $\mathcal{L}(x) = \coth x - \frac{1}{x}$. The three-

chain model reads:

$$R^{ijkl}_{3-\mathrm{ch}} = \begin{cases} \frac{1}{3}C^R\sqrt{N}\lambda_i^2\left(\frac{\xi_i}{\sqrt{N}}+\frac{\beta_i}{\lambda_i}\right)\delta^{ik}\delta^{jl} & \text{if } \lambda_i = \lambda_j \\ \frac{1}{3}C^R\sqrt{N}\frac{\lambda_i^2+\lambda_j^2}{\lambda_i^2-\lambda_j^2}(\lambda_i\beta_i-\lambda_j\beta_j)\delta^{ik}\delta^{jl} & \text{if } \lambda_i \neq \lambda_j \end{cases} \tag{3.9}$$

Strain rate effects are accounted for through a viscoplastic law giving the effective plastic strain rate $\dot{\bar{\epsilon}}$ in (3.2) as (Argon, 1973; Boyce et al., 1988):

$$\dot{\bar{\epsilon}} = \dot{\epsilon_0}\exp\left[-\frac{A\left(s-\alpha\sigma_h\right)}{T}\left(1-\left(\frac{\sigma_{\mathrm{e}}}{s-\alpha\sigma_h}\right)^m\right)\right] \tag{3.10}$$

where $\dot{\epsilon}_0$, m and A are material parameters, α is a factor describing pressure sensitivity, T is the absolute temperature, $\sigma_h = \mathrm{tr}\boldsymbol{\sigma}$ is the trace of Cauchy stress and s is a micro-scale athermal shear strength. Boyce et al. (1988) introduced strain softening effects through the state variable s. The evolution law for s (from its initial value s_0 to its current value s) is given by the following law:

$$\dot{s} = H_1(\bar{\epsilon})\left(1-\frac{s}{s_1}\right)\dot{\bar{\epsilon}} + H_2(\bar{\epsilon})\left(1-\frac{s}{s_2}\right)\dot{\bar{\epsilon}} \tag{3.11}$$

where s_1 and s_2 are adjustable parameters and $h_1(\bar{\epsilon})$ and $h_2(\bar{\epsilon})$ are smooth, Heaviside-like functions given by:

$$H_1(\bar{\epsilon}) = -h_1\left\{\tanh\left(\frac{\bar{\epsilon}-\bar{\epsilon}_p}{f\bar{\epsilon}_p}\right)-1\right\}; \quad H_2(\bar{\epsilon}) = h_2\left\{\tanh\left(\frac{\bar{\epsilon}-\bar{\epsilon}_p}{f\bar{\epsilon}_p}\right)+1\right\} \tag{3.12}$$

The updating of the back stress $\mathbf{b}$ is obtained using $\mathbf{b}_{t+\triangle t} = \mathbf{b}_t + \triangle t\dot{\mathbf{b}}$ with

$$\dot{\mathbf{b}} = \overset{\nabla}{\mathbf{b}} - \mathbf{b}\mathbf{D} - \mathbf{D}\mathbf{b} \tag{3.13}$$

This constitutive model has been implemented in a user-defined routine (UMAT) for ABAQUS-Standard. Here, large strains are modeled within objective space frames.

Implementation of the macromolecular model as a UMAT thus requires to recast the constitutive equations using a co-rotational formulation. For details about the general structure of the implementation method see Kweon and Benzerga (2010).

D. Material Parameter Identification

This section provides some background on the method for determining model parameters and outlines the procedure that should be followed in their identification, irrespective of what experimental data is available.

1. Background

The material parameters entering the model are the elastic constants (E, ν), and s_0, s_1, s_2 (Eq. (3.11)), h_1, h_2, f, $\bar{\epsilon}_{\mathrm{p}}$ (Eq. (3.12)), A, m, $\dot{\epsilon}_0$, α (Eq. (3.10)) and C^R, N (Eq. (3.7)).

Apart from elastic constants, there are ten (10) main constant parameters involved in the deformation model. Table I contains a listing of these constants. Parameters h_1, f and $\bar{\epsilon}_{\mathrm{p}}$ have secondary effects because heuristic functions H_1 and H_2 behave like step functions but are smooth.

Arruda et al. (1995) introduced a temperature dependence of the elastic shear modulus μ through Young's modulus, with Poisson's ratio ν taken as constant. Their equation is:

$$\log \frac{E_{\mathrm{ref}}}{E(T)} = \beta(T - T_{\mathrm{ref}}) \tag{3.14}$$

where T_{ref} and $E_{E_{\mathrm{ref}}} \equiv E(T_{\mathrm{ref}})$ are reference values and β is a parameter. This equation involves two independent parameters. The above equation was also used by Chowdhury et al. (2008c) and has been followed in this work as well.

With this temperature dependence of elastic constants as basis, an apparent

dependence of the athermal shear resistance parameters upon temperature emerges. Thus, the initial shear strength is obtained using the following equation (Argon, 1973; Boyce et al., 1988):

$$\frac{s_0}{\mu} = \frac{0.077}{(1-\nu)}, \qquad \mu(T) = \frac{E(T)}{2(1+\nu)} \tag{3.15}$$

In the original macromolecular model, s_0 is associated with the peak stress at which inelastic deformation is assumed to set in. In the modified model, s_0 is associated with a "yield point" which occurs well before the peak. On the true stress–strain curve, this yield point is characterized by a yield stress σ_{y}, defined as that level of stress beyond which unloading reveals a permanent strain after unloading[1]. Similarly, two references stress levels are defined on the true stress-strain curve: the peak stress, σ_{p}, and the dip stress, σ_{d}. The true stress reaches σ_{p} then σ_{d} when the state variable s is roughly equal to s_1 and s_2, respectively. When the initial shear strength s_0 is known from (3.15) the ratios s_1/s_0 and s_2/s_0 may be estimated using the ratios $\sigma_{\mathrm{p}}/\sigma_{\mathrm{y}}$ and $\sigma_{\mathrm{d}}/\sigma_{\mathrm{y}}$, respectively. A slightly better accuracy is obtained when accounting for the pressure coefficient α through $\bar{s_1}$ and $\bar{s_2}$. The connection between the true (flow) stress σ and the athermal shear strength s is described with further details in Appendix .

The identification of the pressure-sensitivity parameter α supposes that the amount of superposed hydrostatic pressure is varied in the laboratory. Experiments where an actual fluid pressure is superimposed on, say a tensile stress state have been carried out in the literature, e.g. on PMMA (Rabinowitz et al., 1970), but remain scarce. A more efficient method consists of using tension–compression asymmetry, the amount of pressure being different between the two. The data set can be made more discriminating by adding one or more of the following tests: (i) a shear test

[1]Time-dependent recovery is ignored.

(zero pressure); (ii) plane strain tension or compression; (iii) tests on round notched bars. Since α is considered as constant throughout deformation, it can be determined at any stage of the deformation at fixed temperature and strain rate. Recasting the viscoplastic law (3.10) as

$$\sigma_{\mathrm{e}} = (s - \alpha\sigma_h)\left[1 - \frac{T}{A(s - \alpha\sigma_h)} \ln \frac{\dot{\epsilon}_0}{\dot{\epsilon}}\right]^{\frac{1}{m}} \tag{3.16}$$

the easiest way to identify α is to consider values of σ_{e} at yield. Then, (3.16) simplifies into:

$$\sigma_{\mathrm{e}}|_{\mathrm{yield}} = (s - \alpha\sigma_h)|_{\mathrm{yield}}.$$

This simplification does not rigorously apply at the peak stress, based on our interpretation of plastic flow taking place before the peak. Depending on the material and the magnitude of pressure-sensitivity, the following approximation may suffice to determine α:

$$\sigma_{\mathrm{e}}|_{\mathrm{peak}} = (s - \alpha\sigma_h)|_{\mathrm{peak}} \tag{3.17}$$

With this approximation in mind, α can be determined by plotting values of the von Mises effective stress at peak flow against those of σ_h. Parameter α is then the slope of that plot.

The effects of temperature and strain rate are most important and, for certain materials, are the most difficult to represent with high fidelity. The fundamental premise of the viscoplastic constitutive law (3.10) is that temperature and strain-rate effects are coupled. Fundamentally, this results from the view that plastic flow commences when intermolecular resistance is overcome through a thermally activated process of segment rotation. As a practical consequence, the rate-sensitivity parameters m, $\dot{\epsilon}_0$ and A may be identified either by fixing the temperature and varying the strain rate or vice versa, the loading mode being tension or compression. For

PMMA, Boyce et al. (1988) have used $m = 5/6$ based on an earlier derivation by Argon (1973). Our experience with model assessment against various experimetal data is that this value is not universal. In particular, two observations were made: (i) neither the original model nor the modified one have previously been used to model the thermomechanical behavior of polymeric epoxies; (ii) challenges arise in representing both the low-to-moderate strain-rate regime and high strain-rate regime with a single value of m, even for thermoplastic materials

However, making material constant m a free parameter complicates the identification of the three rate-sensitivity parameters, which are linked. When m is fixed, $\dot{\epsilon}_0$ and A are determined by reducing data from a series of tests at fixed temperature and varying strain rate. Specifically, the viscoplastic law (3.10) is rearranged to be the equation of a line:

$$\ln \dot{\bar{\epsilon}} = B + C \left(\frac{\sigma_{\mathrm{e}}}{s - \alpha\sigma_h} \right)^m \tag{3.18}$$

where

$$\begin{aligned} B &= \ln \dot{\epsilon_0} - \frac{A}{T} (s - \alpha\sigma_h) \\ C &= \frac{A}{T} (s - \alpha\sigma_h) \end{aligned} \tag{3.19}$$

For a series of tensile or compressive test data, at peak flow stress, the above equations are specialized using $\sigma_{\mathrm{e}} = |\sigma_h| = \sigma_{\mathrm{p}}$ and $s = s_1$. At this stage of identification, s_1 and α must already be known. Data is then gathered as $\ln \dot{\bar{\epsilon}}$ versus $\left(\dfrac{\sigma_{\mathrm{p}}}{s_1 \pm \alpha\sigma_{\mathrm{p}}} \right)^m$ plots[2]. A straight line is then drawn to fit the data. The slope and intercept of the resulting line are the values of C and B from which the constants $\dot{\epsilon}_0$ and A are extracted by solving the system of equations (3.19).

[2]The sign in the denominator is a minus in tension and a plus in compression.

Thus, if m is known (from theory or a lower-scale molecular analysis) the triplet (m, $\dot{\epsilon}_0$, A) is unique. This is no longer true if m is considered as an additional parameter. For any m, one can find by regression a given set of ($\dot{\epsilon}_0$, A) that best represents the strain rate sensitivity. Hence, in the proposed identification procedure, we supplement the series of tests at constant temperature with a second series of tests at constant strain rate and varying temperature. From the second series, the relative difference between peak stresses $\Delta\sigma_{\rm p}/\Delta T$ is used as a target[3] to discriminate among all possible triplets (m, $\dot{\epsilon}_0$, A) that emerge from the first series of data.

It is worth noting that while the $\Delta\sigma_{\rm p}/\Delta T$ criterion is robust and quite effective, its variation with m is rather weak. Elements of that are included in Appendix under "Sensitivity Analysis" and further elaborated upon in Section

Next, the parameters entering the small-strain hardening/softening involve s_0, s_1, s_2, h_1, h_2, f and $\bar{\epsilon}_{\rm p}$. The first three have already been discussed in the context of temperature dependence. Parameter h_1 controls the amount of hardening prior to peak flow whereas h_2 controls the rate of yield drop post-peak. Straighforward estimates of these parameters may be inferred from:

$$h_2 \approx \frac{s_2 - s_1}{\Delta\bar{\epsilon}} \left(\frac{1}{1 - \dfrac{s_1}{s_2}} \right); \qquad h_1 \approx \frac{s_1 - s_0}{\Delta\bar{\epsilon}} \left(\frac{1}{1 - \dfrac{s_0}{s_1}} \right) \tag{3.20}$$

where $\Delta\bar{\epsilon}$ corresponds to the plastic strain over which there is a yield drop (first equation) or a pre-peak yield increase (second equation). These equations obviously take a simpler form but are written so as to exhibit the temperature-independent ratios s_0/s_1 and s_1/s_2. Although these equations suggest that the h_i values vary with temperature, here they are taken as independent of temperature. Parameter

[3]This target value is a robust criterion because the measure $\Delta\sigma_{\rm p}/\Delta T$ of temperature sensitivity is nearly independent of strain rate and of the testing mode, tension or compression.

$\bar{\epsilon}_{\mathrm{p}}$ corresponds to the effective plastic strain at peak flow and is extracted from the stress–strain curve as simply the total strain minus the elastic strain, the latter being estimated as σ_{p}/E. The last parameter in this group is f which is generally unimportant. It affects the strain window over which the small strain behavior goes from hardening to softening.

Finally, the parameters affecting the strain hardening at larger strains are the rubbery modulus C^R and the number of rigid links between entanglements, N. Theorically, C^R is estimated from birefringence measurements as:

$$C^R = nkT \tag{3.21}$$

where n is the number of chain segments per unit volume, k the Boltzmann's constant ($= 1.4 * 10^{-23} JK^{-1}$) and T the absolute temperature. Alternatively, an approximate value of C^R may be directly measured in tension or compression at a test temperature T_{test} slightly above T_{g}. The test should be conducted at a moderately rapid rate to minimize entanglement drift. The value of C^R at T_{test} is the initial slope of the stress–strain curve thus obtained. Values of C^R at other temperatures in the glassy regime may be obtained by rescaling, i.e.,

$$C^R(T) = C^R(T_{\mathrm{test}})\,\frac{T}{T_{\mathrm{test}}}. \tag{3.22}$$

When experimental measurements of n and $C^R(T_{\mathrm{test}})$ are not available or when the values inferred from Eq. (3.21) are inconsistent with the measured rate of strain hardening, C^R is determined directly by matching the slopes of computed and experimental stress-strain curves at large strains.

The parameter N represents the average number of links between entanglements. In polymers undergoing large-strain locking, N is estimated from the locking strain ϵ_{lock} through $\sqrt{N} = \exp \epsilon_{\mathrm{lock}}$. However, thermoset epoxies do not typically exhibit

such behavior. In this case, N is either left free or refined to fit experimental data at high strains, depending on how C^R is obtained. Also note that since the constitutive formulation involves a back stress the material undergoes significant hardening of the kinematic type. Therefore, C^R and N can be, in principle, identified based on cyclic loading experiments, if available.

2. Procedure

Details aside, the identification procedure is straightforward. The temperature dependence of the elastic modulus is first determined. Thus, one series of data must correspond to various temperatures at fixed strain rate. From a uniaxial stress–strain response at reference temperature and strain rate, the set (s_0, s_1, s_2, h_2) is fairly well estimated through a fit to the response near the peak yield while C_R and N are estimated based on the large strain response. Next, the pressure-sensitivity parameter α is determined based, for example, on tension–compression asymmetry. Finally, $\dot{\epsilon}_0$, m and A are determined based on two series of data where strain rate and temperature are varied independently.

A standard procedure has been developed in order to identify all parameters following specific guidelines. The steps below need to be followed:

1. A series of data (tension or compression) where temperature is varied at fixed strain rate should be available. The initial slopes of the stress–strain curves resulting from multiple realizations should be collected and averaged. $\log E$–T plots are thus generated from which the slope β in Eq. (3.14) can be extracted. The other constants involved are E_{ref} and T_{ref}. T_{ref} is usually taken to be room temperature and thus E_{ref} is the corresponding elastic modulus. The outcome of this step is to determine the temperature dependence of Young's modulus

using Eq. (3.14). Take Poisson's ratio to be constant.

2. Determine the initial shear resistance s_0 using Eq. (3.15). This step must come after step 1 above. Since the ratio s_0/E is independent of temperature, this step may be done for one value of T within the series of data of step 1.

3. A series of tests at fixed temperature and strain rate but varying amounts of hydrostatic stress should be available, e.g., tension, compression and shear. Flow stress values at the peak should be extracted and plots of $\sigma_{\rm e}|_{\rm peak}$ versus $\sigma_h|_{\rm peak}$ can be used to extract the slope α of a linear fit to the data; see Eq. (3.17). This determines the pressure sensitivity parameter α.

4. Determine the flow resistances s_1/s_0 (peak) and s_2/s_0 (saturation) based on the ratios $\sigma_{\rm p}/\sigma_{\rm y}$ and $\sigma_{\rm d}/\sigma_{\rm y}$, which are directly extracted from a stress-strain curve for one test condition[4]. A more accurate estimate consists of using Eqs. (A.2) and (A.3) of the Appendix. If the latter method is used, this step must come after step 3 above.

5. Determine the parameters h_1 and h_2 using Eq. (3.20) for the same test condition used in steps 2 and 4. This is achieved by recording the windows of plastic strain over which there is hardening (from $\sigma_{\rm y}$ to $\sigma_{\rm p}$) and softening (from $\sigma_{\rm p}$ to $\sigma_{\rm d}$).

6. A series of data (tension or compression) should be available where temperature is fixed and the strain rate $\dot\epsilon$ is varied. Take a record of peak flow stresses from this data and make plots of $\ln\dot\epsilon$ versus $\left(\dfrac{\sigma_{\rm p}}{s_1 \pm \alpha\sigma_{\rm p}}\right)^m$ using the values of s_1 and α determined in steps 3 and 4. Make as many such plots at there are trial values of m. The exponent m may be sought in the interval 0.1–0.83 with increments

[4]To each value of the temperature will correspond actual values of s_1 and s_2. However, the ratios s_1/s_0 and s_2/s_0 are independent of T as is the ratio s_0/E.

of 0.1. For each value of m, parameters $\dot{\epsilon}_0$ and A can be uniquely obtained by data reduction following Eqs. (3.18)–(3.19).

7. From the series of data where temperature is varied (step 1) extract the relative difference between peak stresses, $\Delta\sigma_{\mathrm{p}}/\Delta T$. Use that value as a criterion to discriminate among all possible triplets (m, $\dot{\epsilon}_0$, A) that have come out of the previous step. This completes the determination of the rate-sensitivity parameters.

8. Obtain from the literature the number of chain segments per unit volume, n, then estimate the rubbery modulus C^R using Eq. (3.21). Alternatively, a single test at T just above T_{g} and a moderately high loading rate should be available. C^R is then extracted as the initial slope of the stress–strain curve. Its dependence upon temperature is inferred from Eq. (5.23). If none of this data is available, calibrate C^R on the large strain hardening of a stress–strain curve in tension.

9. Use the average number of rigid links between entanglements, N, as a free parameter if the locking stretch is not reached in the experiments. If C^R is obtained from measurements, calibrate N based on the large strain hardening of a stress–strain curve in tension.

10. Fine-tune the parameters f and $\bar{\epsilon}_p$ to improve the quality of the fit to the stress–strain curve around the peak stress. This can only be done by running actual simulations using material parameters from the previous steps. The default value of f is 0.1. The default value of $\bar{\epsilon}_p$ is the amount of plastic strain at peak flow; see text after Eq. (3.20).

E. Model Calibration and Assessment

The standard procedure outlined in Section D above has been followed to identify the material parameters of the macromolecular model in the case of epoxy resin EPON 862. The characterization of this thermosetting resin has been carried out for a large range of temperatures and strain rates. These data, which result from a previous study (Littell et al., 2008), can be found in (Poulain et al., 2010b). Here, we use these experimental data and group them in two broad sets of data: a calibration set and an assessment set. The first set was used for model calibration, i.e., for the identification of material parameters. The second set was used to make an assessment of the predictive capabilities of the model when the same material parameters resulting from the calibration step are used.

The following experimental data belongs to the "calibration set":

- A series of data in tension at a fixed strain rate ($\dot{\epsilon} = 10^{-3}$/s) over a range of temperatures (three values of T: 25°C, 50°C and 80°C).
- A series of data in compression at a fixed temperature (25°C) at various levels of strain rate (10^{-5}/s, 10^{-3}/s and 10^{-1}/s).
- Data in shear and tension at $T = 25$°C and $\dot{\epsilon} = 10^{-1}$/s.

Using this calibration data set, the values obtained for the main material parameters are reported in Table I. Two sets of parameter values are included: set 'Modified' comprises the values obtained when the material parameter m is a free parameter while set 'Original' refers to the values obtained using the original value for m ($m = 5/6$) (Boyce et al., 1988). To derive these values, the steps of the standard procedure were specialized as follows:

1. The first series of data in tension was used to determine the temperature dependence of the elastic modulus. The values obtained for parameters E_{ref}, T_{ref} and β involved in Eq. (3.14) are as shown in Table I. The parameter β being the slope of a line in a semi-log plot, the uncertainty on it is quite large. Mean values of the elastic modulus for all three values of temperature in this data set were provided by Littell (2008). However, the dispersion of data was not provided. To determine the uncertainty on E we have proceeded as follows. First, the mean on E was re-evaluated. This led to differences of up to 200 MPa in comparison with values supplied in Littell (2008). The actual mean was then averaged over the two estimates by the two independent operators. Also, the scatter around the mean was determined. With that as basis, the final values that are consistent with Table I are as follows. At the lowest temperature ($T = 25°\text{C}$) we used the mean minus one dispersion. At the highest temperature ($T = 80°\text{C}$) we used the mean plus one dispersion. At the intermediate temperature ($T = 50°\text{C}$) we used the mean value. These values determine bounds and were found to lead to the best representation of temperature dependence of the flow stress. E was determined as the slope of a line which best fits with the experimental stress-strain curve in the range of strain 0 to 0.01. The fit was observed to be good, but the accuracy was not precisely investigated.

2. The initial shear resistance s_0 at T_{ref} was evaluated by using the value of $E_{\text{ref}} = E(T_{\text{ref}})$ in Eq. (3.15). The same ratio s_0/E was used at other temperatures.

3. The third series of data in the calibration set was used to determine α. The value reported in Table I was obtained without accounting for any shear test data.

4. A variant of this step of the standard procedure had to be implemented. The

stress–strain curves in tension exhibit a plateau post-peak whereas in compression they exhibit a clear post-peak strain softening. Therefore, the corresponding ratios of $\sigma_{\rm p}/\sigma_{\rm y}$ and $\sigma_{\rm d}/\sigma_{\rm p}$ are different (Table II). For the identification of s_1 and s_2, we have used average values. Note that the data reported in Table II correspond to $T = 25°$C and $\dot{\epsilon} = 10^{-1}$/s. For tension this data are part of the third series in the calibration set. For compression, this data is part of the second series in that set.

5. Parameters h_1 and h_2:

   As in step 4, we have used averaging between tension data and compression data to determine these parameters. The values of $\Delta\bar{\epsilon}$ for use in Eq. (3.20) are reported in Table II with superscripts 1 and 2 for h_1 and h_2, respectively.

6. Parameters m, A and $\dot{\epsilon}_0$ (iteration 1):

   The second series of data of the calibration set (compression at various levels of strain rate) was used to implement the first iteration in the identification of rate-sensitivity parameters. For each value of m, the couple (A , $\dot{\epsilon}_0$) was obtained by data reduction on plots of $\ln\dot{\epsilon}$ versus $\left(\dfrac{\sigma_{\rm p}}{s_1 \pm \alpha\sigma_{\rm p}}\right)^m$. Details on the outcome of this step are included in Appendix . Examples of such a plot are depicted in Fig. 10 in the cases of $m = 0.5$ and $m = 0.83$. The resulting values of A and $\dot{\epsilon}_0$ are those shown in Table I.

Table I. The material parameters entering the deformation model. * relative uncertainty.

Material parameter	Units	Description	Eqns	Set Modified	Set Original	Uncertainty
E_{ref}	GPa	modulus at T_{ref}	(3.14)	2.6	2.6	0.1
T_{ref}	K	reference temperature	(3.14)	298	298	5
β	1/K	temperature dependence	(3.14)	0.002	0.002	0.38*
ν	—	Poisson's ratio	(3.15)	0.4	0.4	0.01
s_0/E	—	initial shear strength	(3.11)	0.046	0.046	0.06*
s_1/s_0	—	pre-peak strength	(3.11),(3.20)	1.19	1.19	0.1*
s_2/s_0	—	saturation strength	(3.11),(3.21)	1.09	1.09	0.08*
h_1	MPa	pre-peak hardening	(3.12),(3.20)	3000	3000	0.31*
h_2	MPa	rate of yield drop	(3.12),(3.20)	900	900	0.29*
$\bar{\epsilon}_{\text{p}}$	—	peak plastic strain	(3.12)	0.054	0.054	0.21*
f	—		(3.12)	0.1	0.1	0.05
α	—	pressure-sensitivity	(3.10),(3.17)	0.05	0.05	0.01
m	—	rate-sensitivity	(3.10),(3.18)	0.5	0.83	0.05
$\dot{\epsilon}_0$	s^{-1}	rate-sensitivity	(3.10),(3.19)	4.3E5	2.0E6	0.54*
A	1/K	rate-sensitivity	(3.10),(3.19)	173.8	122.1	0.27*
C^R	MPa	rubbery modulus	(3.7),(3.21),(5.23)	15	15	3
N	—	number of rigid links	(3.7),(3.8)	7	7	1*

(a)

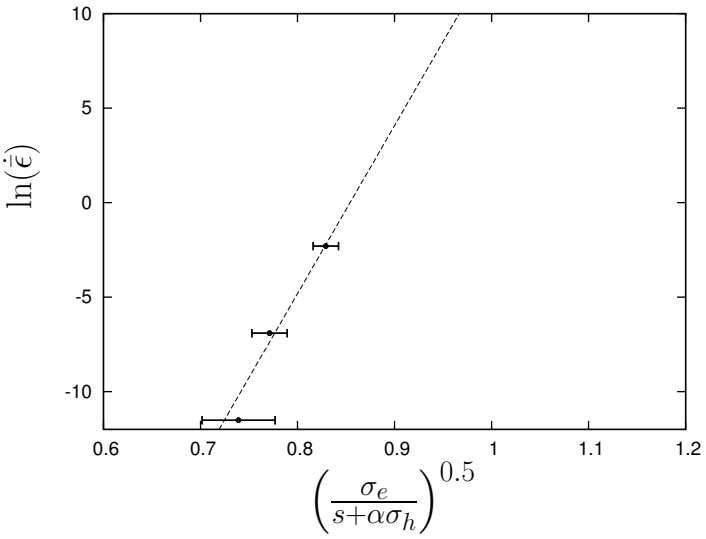

(b)

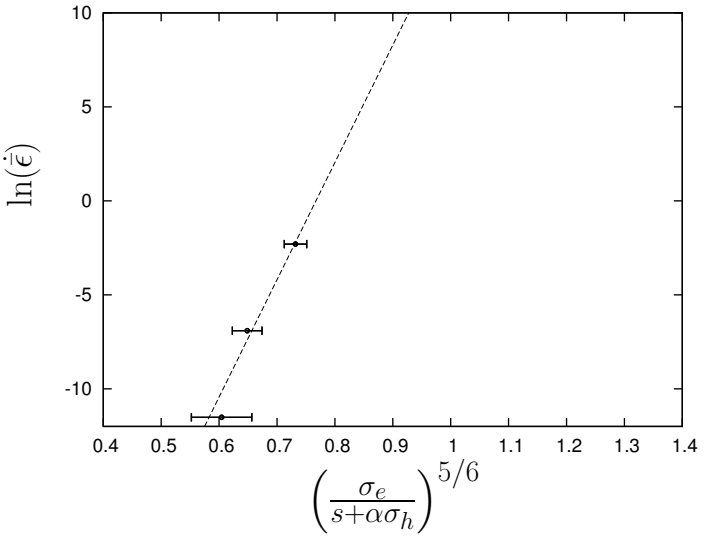

Fig. 10. Strain rate versus intermolecular resistance plots used to determine the rate-sensitivity parameters A and $\dot{\epsilon}_0$ using compression data at 25C with (a) m=0.5; (b) m=5/6

Table II. Experimental values used in steps 4 and 5 for the determination of small-strain hardening/softening parameters. Data at $T = 25°\mathrm{C}$ and $\dot{\epsilon} = 10^{-1}/\mathrm{s}$.

	σ_y	$\sigma_\mathrm{p}/\sigma_\mathrm{y}$	$\sigma_\mathrm{d}/\sigma_\mathrm{p}$	s_1/s_0	s_2/s_1	$\Delta\bar{\epsilon}^{(1)}$	$\Delta\bar{\epsilon}^{(2)}$	h_1	h_2
Tension	74.4	1.23	0.98	1.23	0.98	0.0506	0.1	2800	1300
Compression	88.8	1.14	0.85	1.14	0.85	0.0445	0.263	3200	500
Average	81.6	1.19	0.92	1.19	0.92	0.0476	0.1815	3000	900

7. Parameters m, A and $\dot{\epsilon}_0$ (iteration 2):

   From the first series of data (see step 1 above), we find $\Delta\sigma_{\rm p} \approx 35$ MPa for $\Delta T = 55$ K[5]. At this point, simulations were carried out using material parameters from steps 1–6 and the default values of $f = 0.1$ and $\bar{\epsilon}_{\rm p} = 0.054$. The objective of these simulations is to compare the difference in peak flow stresses at the two extreme temperatures with the experimental value of 35 MPa. Therefore, values assigned in these simulations to C^R and N, which are not known yet, do not affect the outcome of this comparison. From this analysis we found that the value of $m = 0.5$ provides the best result (see Appendix for details.).

8. The number of chain segments per unit volume is not known for E862 material. Since no experiment was carried out at a temperature slightly above $T_{\rm g}$, we have obtained C^R by calibration of the large strain hardening. Here again, the final value of $C^R = 15$ was averaged out over tension and compression data at $T = 25°$C and $\dot{\epsilon} = 10^{-1}$/s. This value is consistent with data found in the literature. A storage modulus $G' \approx$10 MPa was obtained at 200°C in Zhu et al. (2010). However, a higher values of G' ($\approx$500 MPa) was observed with a different curing agent Case et al. (2005).

9. Parameter N:

   Experiments on Epon 862 do not exhibit clear evidence of strain locking in the studied range of strains. Therefore, assuming that locking would occur at a stretch around $\lambda_{\rm lock} = 1$, $N = 7$.

10. It was found that the standard value for parameter $f = 0.1$ was appropriate and $\bar{\epsilon}_{\rm p} = 0.054$.

---

[5]Remarkably, this difference is nearly the same at other strain rates, both in tension and compression.

(a)

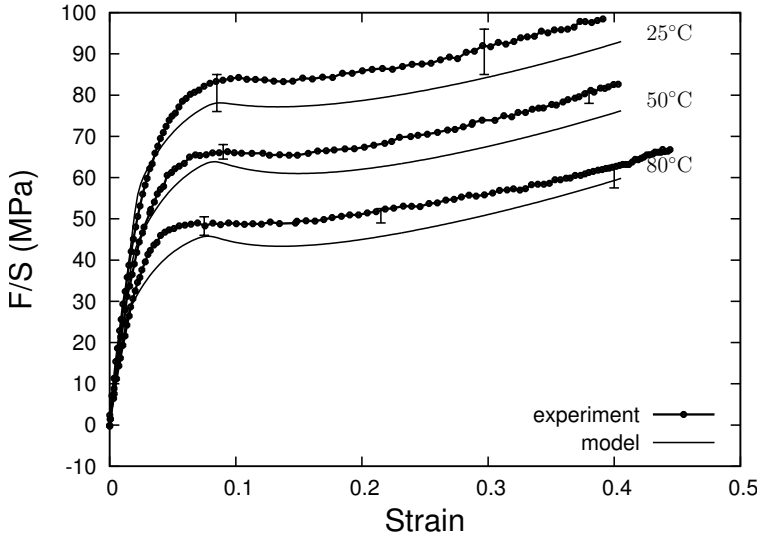

(b)

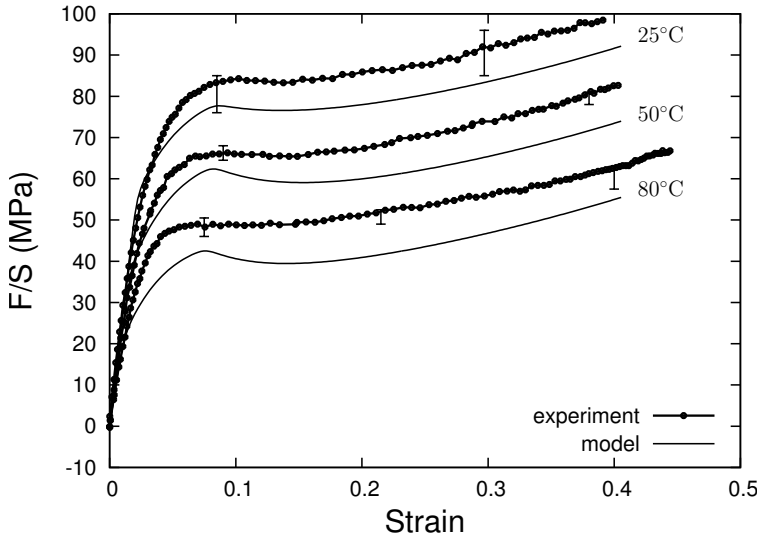

Fig. 11. Verification of the model identification procedure. Computed versus experimental stress–strain responses. Effect of temperature in tension at $\dot{\epsilon} = 10^{-3}/\text{s}$ using calibration set with (a) $m = 0.5$ and (b) $m = 5/6$.

The outcome of this procedure is the set of parameters reported in Table I. The table also contains uncertainty and relative uncertainty[6] estimates. The background for the determination of the latter are provided in Appendix .

Using the material parameters thus identified, simulations were carried out and their results compared with experimental data of the calibration set. This task was undertaken to check that the identification procedure outlined above delivers the expected results. The quality of the calibration of temperature-sensitivity, rate-sensitivity and pressure-sensitivity can be appreciated from Figs. 11, 12 and 13, respectively. The comparison is shown for the set of data 'Modified', which is based on the modified value for m ($m = 0.5$) as well as the set 'Original', which results from the original value for m ($m = 5/6$). Scatter bars on measured stresses are included in all subsequent comparisons.

Consider first calibration using the Modified data set. The effect of temperature is very well calibrated, as quantified by a peak stress shift of about 35 MPa (Fig. 11a)[7]. The same calibration obtained with the Original data set (Fig. 11b) is qualitatively acceptable but overestimates the temperature sensitivity. Indeed, although the two data sets give similar results at 25°C, the Original set exhibits lower strengths than the Modified set at higher temperatures. These numerical results justify the choice for a lower value of m in comparison with its original one. The effect of strain-rate sensitivity is also very well represented in the low-to-moderate strain rate regime for both the Modified data set (Fig. 12a) and Original set (Fig. 12b). Indeed, the same difference in strength at peak between 10^{-1}/s and 10^{-5}/s is obtained for simulations

[6]Uncertainty normalized by the parameter's value

[7]The computed curves exhibit some amount of post-peak softening, unlike the data. This is due to the fact that compression data was also considered in the identification procedure.

and experiments. Simulations do not exhibit as much softening in experiments since the calibration procedure was based on the averaged response between tension (post-peak plateau) and compression (post-peak softening). Stress-strain curves resulting from these two sets are almost indistinguishable. Indeed, as observed in Fig. 10, although a modification of m rescales the x axis, it does not modify the general feature of the plotted line (e.g. the line passes through similar locations within the error bars). Finally, the effect of pressure-sensitivity (more precisely, tension–compression asymmetry) is also well captured, Fig. 13. Simulations in both tension (Fig. 13a) and compression (Fig. 13b) slightly underestimates the flow strength at peak stress with a similar amount (a few MPa). It is worth recalling that regarding this third series for calibration, the identification of α is independent of m.

Using the material parameters thus identified, the model predictions can now be compared with additional data not used for model calibration. The following experimental data belongs to the "assessment set":

- A second series of data in tension at a fixed strain rate ($\dot{\epsilon} = 10^{-1}$/s) over a range of temperatures (three values of T: 25°C, 50°C and 80°C).
- Data in tension at $\dot{\epsilon} = 10^{-5}$/s and $T = 25$°C.
- A second series of data in compression at a fixed temperature (50°C) at two levels of strain rate (10^{-3}/s and 10^{-1}/s).
- A third series of data in compression at a fixed temperature (80°C) at two levels of strain rate (10^{-3}/s and 10^{-1}/s).

Figure 14 shows that the prediction of temperature sensitivity is excellent with the set Modified (Fig. 14a) but slightly less accurate for the set Original (Fig. 14b).

Recall that temperature sensitivity was calibrated using data at the lower strain rate of 10^{-3}/s (see Fig. 11).

Figure 15 shows the model prediction using parameter set Modified for the only tension data available at $\dot{\epsilon} = 10^{-5}$/s. The prediction is excellent.

Next, consider the compression data. Figures 16 and 17 show that the strain-rate sensitivity is extremely well predicted using parameter set Modified.

F. Conclusion

In this chapter, a macromolecular model initially developed by Boyce et al. (1988) was used to model the mechanical response of thermosetting epoxy resin EPON-862 in tension and compression, for temperatures varying from 25°C to 80°C and strain rates ranging from 10^{-5}/s to 10^{-1}/s. All the experimental data presented in this chapter were gathered from a previous study in which the epoxy behavior was characterized Poulain et al. (2010b). A limited set among these experiments was used in order to assess the material parameters on which the polymer model builds. The identification of each parameter entering the model was precisely detailed in a procedure. This procedure has some specificities: (i) it accounts for the possibility for yielding to occur before the peak stress is reached; (ii) it enables a better representation of prepeak hardening; (iii) it considers the exponential factor 5/6 present in the viscoplastic law of the original macromolecular model (Boyce et al. Boyce et al. (1988)) as a free parameter m which can take values ranging from 0.1 to 5/6. Such a modification originated from the observation that the initial model overestimated the temperature sensitivity for EPON-862 while well capturing the strain rate sensitivity. The calibration procedure leads to the value $m = 0.5$ for the best representation of temperature sensitivity. A modification of m does not significantly affect the quality

of the strain rate sensitivity nor the pressure sensitivity. As a direct result of the calibration of material parameters, comparisons between experimental stress-strain curves and numerical simulations showed that strain rate and pressure sensitivity are very well captured for both $m = 0.5$ and $m = 5/6$ whereas temperature sensitivity is precisely acquired only in the case of $m = 0.5$. Finally, the predictive capabilities of the model were positively tested. Indeed, an excellent fit was observed between numerical simulations and experimental stress-strain curves which were not used in the calibration procedure. The same conclusions as for calibration were drawn. In particular, besides keeping a good representation of the rate sensitivity, the modification of the value for $m = 5/6$ to $m = 0.5$ improves the quality of the fit at all temperatures. Therefore, this set of material parameters can be confidently used to model the behavior of EPON-862 for any condition in the range of temperatures and rates studied. More generally, such a modified model and procedure may be used to investigate the large strain mechanical response of glassy polymers under their glass transition temperature regardless of their temperature and rate sensitivity dependence.

(a)

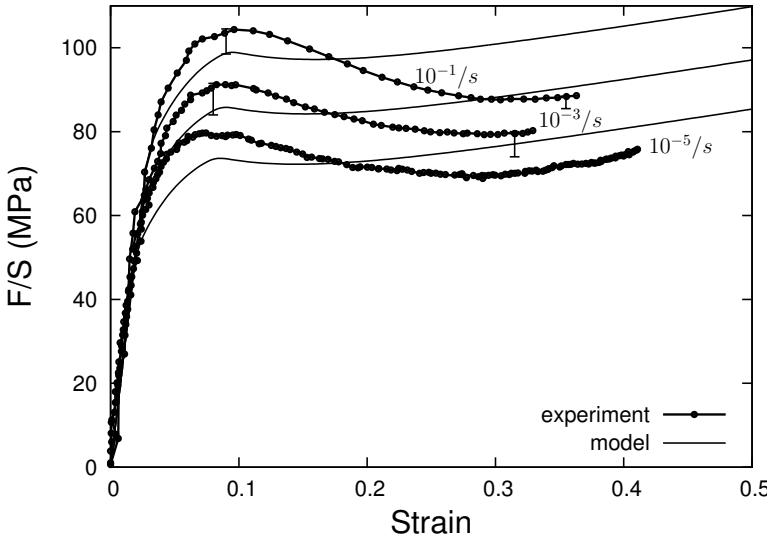

(b)

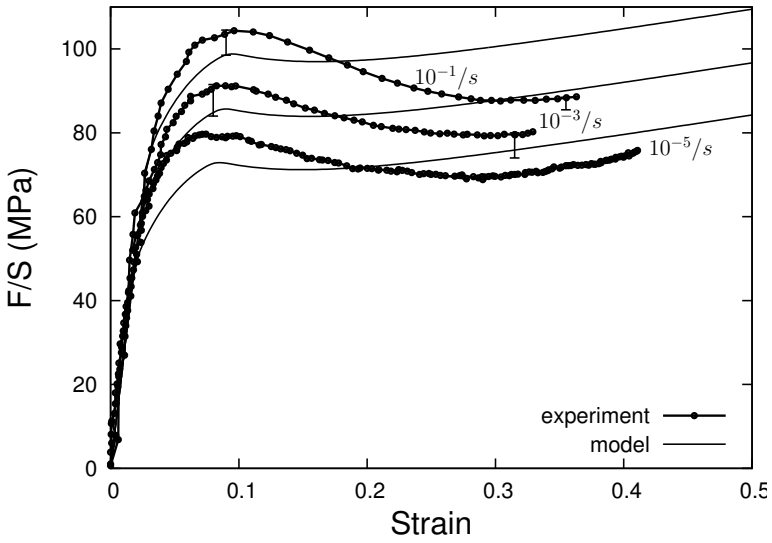

Fig. 12. Verification of the model identification procedure. Computed versus experimental stress–strain responses. Effect of strain rate in compression at $T = 25°\mathrm{C}$ using calibration set with (a) $m = 0.5$ and (b) $m = 5/6$.

(a)

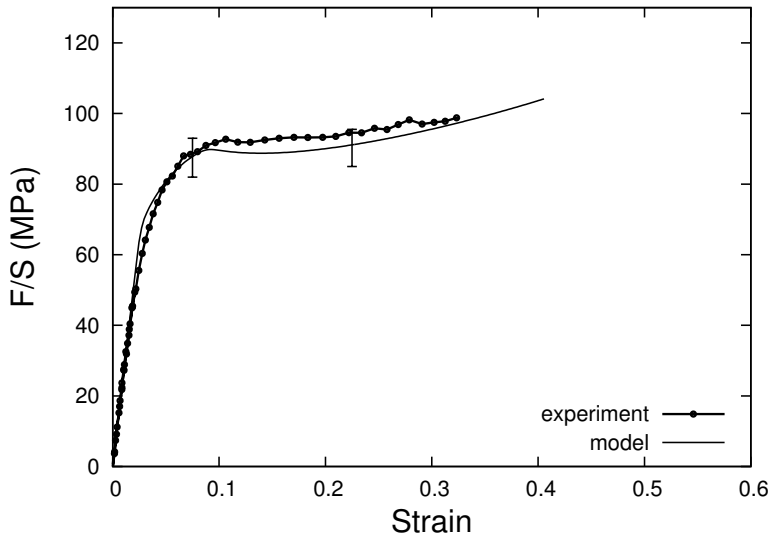

(b)

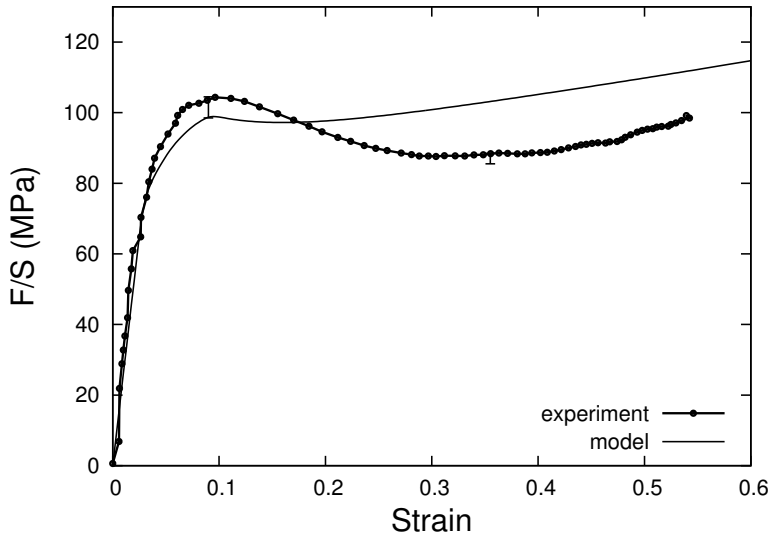

Fig. 13. Verification of the model identification procedure. Computed versus experimental stress–strain responses. Effect of pressure at $T = 25°\text{C}$ and $10^{-1}/\text{s}$ using calibration set with $m = 0.5$ in (a) tension and (b) compression.

(a)

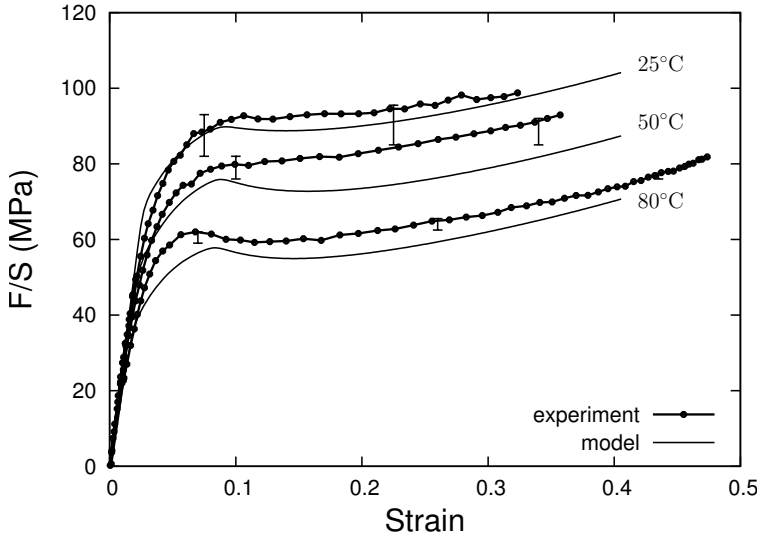

(b)

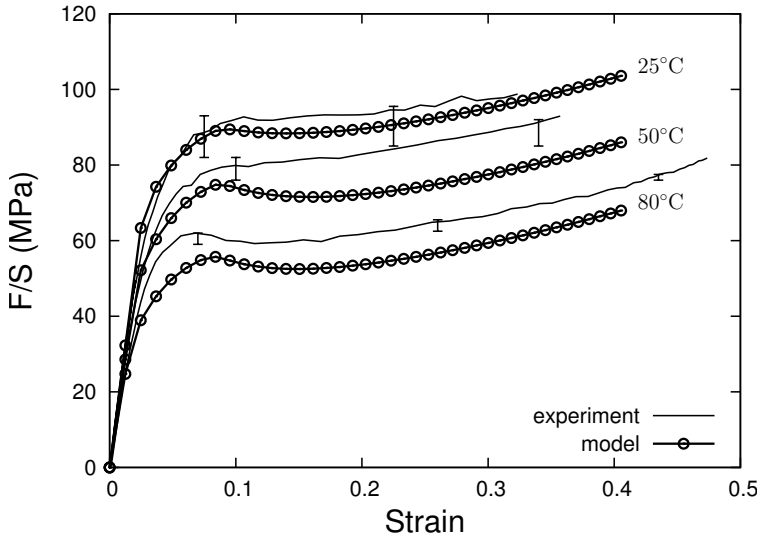

Fig. 14. Predicted versus experimental stress–strain responses. Effect of temperature in tension at $\dot{\epsilon} = 10^{-1}$/s using calibration set with (a) $m = 0.5$ and (b) $m = 5/6$.

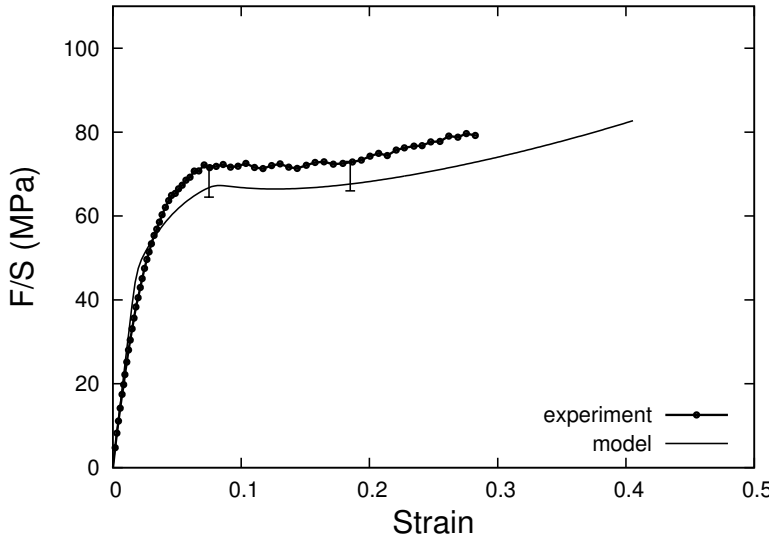

Fig. 15. Predicted versus experimental stress–strain responses. Tension at 25°C and $\dot{\epsilon} = 10^{-5}$/s using calibration set with $m = 0.5$.

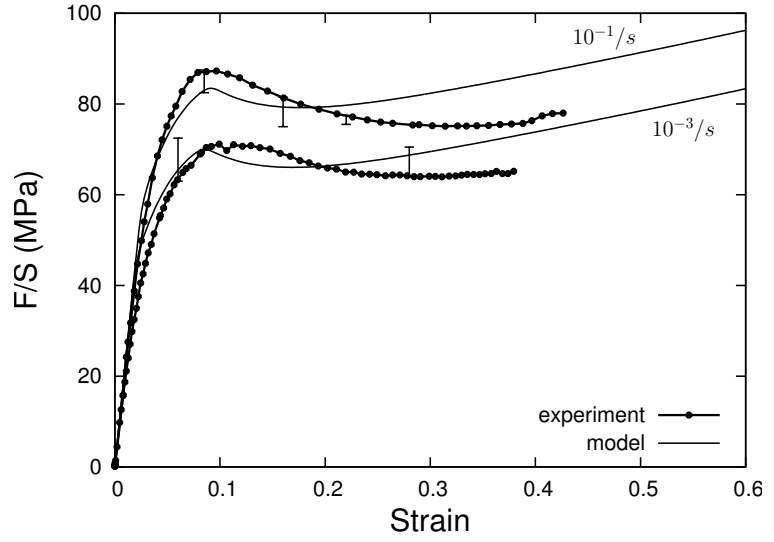

Fig. 16. Predicted versus experimental stress–strain responses. Effect of strain rate in compression at $T = 50$°C using calibration set with $m = 0.5$.

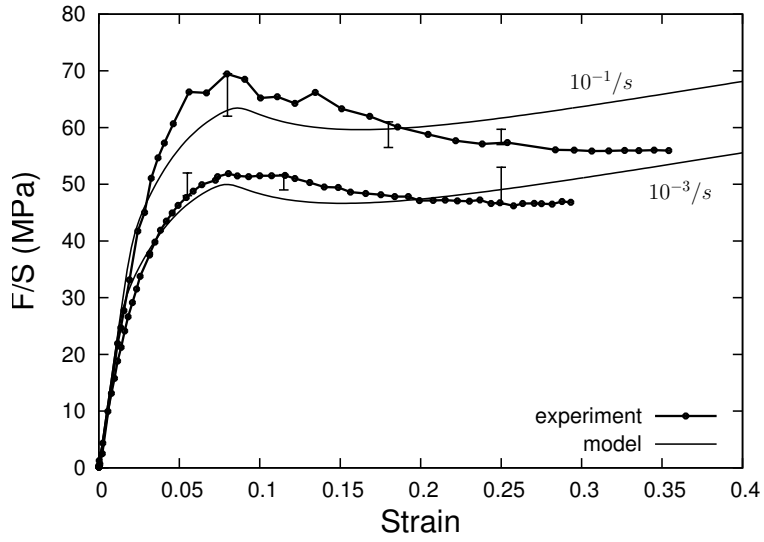

Fig. 17. Predicted versus experimental stress–strain responses. Effect of strain rate in compression at $T = 80°\mathrm{C}$ using calibration with $m = 0.5$.

CHAPTER IV

MECHANICAL AND AGING BEHAVIOR OF A POLYMER EPOXY OVER A WIDE RANGE OF TEMPERATURES AND STRAIN RATES

A. Introduction

Thermoset resins are currently considered as potential materials to use as matrix in new designs of composite blade containment cases (BCCs) for turbofans. Among other design requirements, these BCCs need to sustain the impact of a failed blade and maintain its structural integrity during the subsequent engine shut down. Throughout their service life, these BCCs experience large variations of temperature and operate with different moisture conditions. High temperatures and moisture are both known to accelerate the aging process of glassy polymers, through an evolution of their structure from a metastable state. The response of glassy polymers is also known to be highly dependent on temperature, strain rate and pressure. In a case of such a blade-out event, damage is localized in a limited zone around the impacted area. Therein, complex triaxial states of stress exist with the development of high gradients of stress, strain and strain rates. Knowledge of the mechanical response of polymer candidates for conditions relevant to damage tolerant BCC is fundamental. In particular, an experimental methodology should be developed and used to capture the full mechanical response of tested polymers, and provide reliable input regarding their dependence on strain rate, temperature, pressure and aging. In this chapter we describe the mechanical behavior of a thermosetting polymer epoxy, a potential candidate for BCC matrix, tested in tension and compression for low, moderate and high strain rates at various temperatures below the glass transition temperature. The effect of hygrothermal aging on the yield behavior has also been investigated. The low-to-moderate strain-rate

experiments allowed for the determination of the true stress versus strain response and its temperature dependence thanks to a new experimental methodology. The latter is based on full-field strain measurements by digital image correlation combined with video-monitored extensometry. The high-rate response was determined using Kolsky bar testing.

B. Experimental Methods

1. Material

The material used in this study is a commercial untoughened thermosetting epoxy resin EPON 862. Because of its wide availability, low viscosity and high glass transition temperature (T_g=133°C (Gilat et al., 2007)), this highly crosslinked resin has been recently selected as potential candidate for advanced designs of composite jet engine fan containment cases. It results from the curing reaction (at 176°C) of epoxide resin EPON Resin 862 (Diglycidyl ether of bisphenol F -DGEBF-) with the aromatic amine curing agent Epicure W which is mainly composed of diethyltoluenediamine (DETDA) (Tack, 2006).

2. Quasi-static Experiments

a. Direct Characterization

In a previous study (Littell et al., 2008), the quasi-static response of EPON 862 was investigated using round smooth bars. These specimens, smaller than ASTM standard tensile specimens (D638, 2004), were tested in tension and compression at various temperatures below T_{g} (T = 25°C, 50°C and 80°C) and at various nominal strain-rates (defined as the crosshead speed divided by the initial gauge length) in quasi-static conditions ($\dot{\epsilon}$ = 10^{-5}/s, 10^{-3}/s and 10^{-1}/s). For each test condition,

between three and seven realizations (with one exception), which encompass both monotonic and unloading–reloading tests, were performed. Details regarding the specimen geometry and the experimental procedure may be found in Littell et al. (2008).

In that study, all experimental data were reported in terms of the engineering stress defined as:

$$\sigma^{\text{eng}} = \frac{F}{S_0} \tag{4.1}$$

versus a local strain. The latter, which will be precisely defined below, is inferred by averaging from full field measurements collected by a precise digital image correlation (DIC) technique[1]. This apparatus enables to capture pointwise dilatational and shear strains on the specimen surface. In (4.1), F is the force given by the load cell and S_0 is the initial cross sectional area. Unfortunately, the experimental data as presented in Littell et al. (2008) cannot be used directly in any constitutive model. As a consequence, these data were re-analyzed to obtain the true stress–strain behavior of EPON 862.

The main difficulty in assessing the intrinsic response of polymers resides in accounting for the evolution of the specimen geometry at large deformations. This task is further complicated with the development of heterogenous deformations as a result of plastic instabilities such as necking in tension and barreling in compression. Such issues regarding the characterization of EPON-862 are resolved with the use of the DIC system.

In what follows, we will work with two strain measures. The first measure is that

[1]ARAMIS$^{\text{TM}}$, GOM, Braunschweig, Germany

used in Littell et al. (2008) and is defined as:

$$\bar{\epsilon}_{22} = \langle \frac{\partial u_2}{\partial x_2} \rangle_{\text{five points}} \tag{4.2}$$

where u_2 denotes the axial displacement and $\langle \cdot \rangle$ stands for averaging over five locations (material points) located in the current region where the highest strains are expected, i.e, in the central region of the gauge section. Precisely, the first point is located between four other points equally distributed along the radial and axial directions. Averaging over a limited set of points allows to smear out pointwise fluctuations while keeping the "local" character of the measurement. However, this measurement presents the inconvenients of being averaged from strains which are collected at the specimen *surface* and which may substantially vary among points once necking or barreling occurs. Indeed, when these plastic instabilities occur, strain gradients are commonly observed in the axial direction such that points located above the neck (or section of maximum diameter under compression) become further apart (or closer to each other) as deformation proceeds. For each experiment on EPON 862, the values of $\bar{\epsilon}_{22}$ as measured by Littell et al. (2008) was communicated to us by NASA GRC.

The second measure of strain is thus defined based on the reduction of cross-sectional area within the neck:

$$\varepsilon = \ln \frac{S_0}{S} = 2 \ln \frac{\Phi_0}{\Phi} \tag{4.3}$$

where S is the current cross-sectional area at the neck (or section of maximum diameter under compression), Φ is the diameter and the subscript 0 refers to initial values. Besides being an approximation of the Hencky strain if any compressibility and radial strain gradients are neglected, ε presents the additional advantage of confining the measurement to the most deformed section. A domestic Texas A&M undergraduate was sent to NASA to measure the evolution of Φ using the tangent circle method.

The true stress can be evaluated as

$$\sigma = \frac{F}{S} = \frac{4F}{\pi\Phi^2} \tag{4.4}$$

In what follows, curves of the above measure of true stress, σ, versus an approximate measure of true strain (either $\bar{\epsilon}_{22}$ or ε) will be referred to as the (true) stress–strain curves of the material.

In order to gain some insight into the nature of the inelastic strains that accumulate beyond the domain of reversibility, unloading tests were also carried out by Littell et al. (2008). Precisely, between two and four unloading-reloading experiments were carried out for each condition of strain rate (10^{-1}/s and 10^{-3}/s), temperature (room temperature, 50°C and 80°C) and loading mode (tension and compression). Such experiments were not performed at 10^{-5}/s. Each specimen was loaded, unloaded once then reloaded up to large strains (compression) or fracture (tension). The levels of total strain at which the specimens were unloaded varied from about 0.02 to 0.11 with strain increments generally of about 0.02–0.03. Yielding was characterized by a yield stress $\sigma_{\rm y}$ determined with an offset of 0.022± (average value with minimum and maximum values of 0.010 and 0.039 respectively) total strain. It was generally found that unloading past the yield point so defined leads to a permanent strain. In most cases, partial or total time recovery took place but that was not considered in the definition of $\sigma_{\rm y}$

b. Simplified Method for Characterization

Determination of the true stress in (4.4) requires the monitoring of the current cross-sectional area, which can be tedious. An alternative procedure has also been developed which is based on the full field strain measurements, analysis and a set of approximations. Assuming that the radial strain ϵ_{11} is uniform (i.e., independent of

x_1) at a given height x_2 along the specimen axis[2], one may write

$$\epsilon_{11} \approx \frac{\Delta\Phi}{\Phi_0}$$

where $\Delta\Phi = \Phi - \Phi_0$. Therefore, assuming incompressibility of the material[3], the true stress may be estimated using:

$$\sigma = \frac{F}{S_0}\frac{S_0}{S} = \sigma^{\text{eng}}\left(\frac{\Phi_0}{\Phi}\right)^2 = \sigma^{\text{eng}}\left(\frac{1}{1+\epsilon_{11}}\right)^2$$

In principle, the radial strain ϵ_{11} may be estimated at any location within the neck (or apex of the barrel). Ideally, one could take the average of ϵ_{11} values within that section. Since the latter average was not made available, in what follows we will use the following average measure:

$$\bar{\epsilon}_{11} = \langle\frac{\partial u_1}{\partial x_1}\rangle_{\text{five points}} \tag{4.5}$$

where the same five points defined in (4.2) have been used. Thus, in the simplified procedure, the true stress is estimated using the following formula:

$$\sigma = \frac{F}{S_0}\left(\frac{1}{1+\bar{\epsilon}_{11}}\right)^2 \tag{4.6}$$

where $\bar{\epsilon}_{11}$ constitutes direct output from the DIC apparatus. For each experiment on EPON 862, the values of $\bar{\epsilon}_{11}$ as measured by Littell et al. (2008) was communicated to us by NASA GRC.

To sum up, for every test conducted in Littell et al. (2008) the following tasks have been accomplished to obtain the true stress–strain response of EPON 862:

1. Visualize the recording of the test using two videos: (i) the deformed specimen;

[2]This is exactly true before the onset of plastic instability.

[3]Just like strain measure (4.3), the assumption of incompressibility is rough in the elastic regime.

and (ii) the superposed surface strain field.

2. Identify the cross-section where deformation localizes, i.e., the section of minimal diameter under tension and the section of maximum diameter under compression.

3. Measure the diameter Φ at the location identified in step 2 above.

4. Obtain ε by (4.3) and σ by (4.4). This is the *direct* method.

5. Obtain an estimate of axial strain as $2\bar{\epsilon}_{11}$ from (4.5) and an estimate of true stress σ by (4.6). This is the *simplified* method. Compare with results from step 4.

6. Determine the stage at which plastic localization (necking or barreling) has become visually evident. In all stress-strain curves to be presented below, this stage will be indicated by a full square.

7. Determine the stage, if any, beyond which the data based on the first strain measure $\bar{\epsilon}_{22}$ becomes questionable leading sometimes to inconsistencies and serrations in the stress–strain curve. This is due to a loss of local information. This stage will be indicated by a full circle.

8. In tension, record the final strain measured. The latter is presumed to correspond to material separation and failure, although the movies did not always explicitly include that stage.

3. Dynamic Response of EPON 862

The impact performance of advanced composites used in engine fan blade containment cases can only be assessed if the dynamic behavior of all constituents is well

understood. Since the reinforcement entities, i.e., the fibers, remain elastic essentially all the way to failure, it is the dynamic behavior of the polymeric resin that needs to be characterized.

Under dynamic loading, the stress levels attained in any structure are much higher than under quasi-static loading. It is important to separate two contributions to this increase in local stresses. The first contribution is purely dynamic and is associated with the inertial terms in the statement of conservation of linear momentum. Physically, these terms manifest through stress waves propagating throughout the material, component or structure. The second contribution to the stress increase comes from the intrinsic rate-sensitivity of the constituent material.

In general, it is assumed that tests conducted under quasi-static conditions are isothermal. This approximation becomes increasingly crude as the rate of loading increases. Under dynamic loading, only a small protion of the energy dissipated in plastic deformation is fluxed out of the specimen. The main portion of that energy contributes to heating up the material. Thus, the dynamic response is thermomechanical and one should bear this in mind when interpreting the data.

The dynamic behavior was characterized by Prof. A. Gilat from the Ohio State University who used Kolsky bar experiments. The apparatus was used for high strain rate ($10^2/s < \dot{\epsilon} < 10^3/s$) testing in tension and compression at ambient temperature. The specimens used present the same geometry as for testing in quasi-static conditions. Contrary to the quasi-static case, optical and traditional methods are not adequate. Instead, the tested specimen is cemented (glue to two adapters) between an incident and a transmitter aluminum bar. The incident bar is clamped and loaded in tension. When the clamp is release, a wave is generated in the incident bar. This wave is partially transmitted in the transmitter bar through the specimen and partially reflected in the incident bar. The deformation in the bars remain elastic. Two

strain gauges are placed on two locations on the incident bar, and one on the transmitter bar such that strain rate, strain and stress are determined from the recorded waves using SHB equations. More details can be found in (Gilat et al., 2007).

4. Aging Behavior of EPON 862

In the experiments presented above on pristine resin, it was tacitly assumed that the material properties are not altered and are time-invariant during the test or simulation. This is usually a good assumption when the initial age of the material exceeds the experimental or simulation time. However, for long-term loading conditions or under circumstances where accelerated aging may occur, e.g., at high temperatures, the above assumption no longer holds. By way of consequence, the material properties are expected to change during the experiment.

The issue of how aging would affect the mechanical integrity and impact performance of a fan blade containment case is of paramount importance. This is so because a blade-out event (i.e., the separation of a blade from the rotating fan) is rare and thus might not happen until a late stage in the life of the engine. In fact, in the special case of a jet engine fan containment case we are faced with both conditions of progressive aging mentioned above: long-term loading and conditions of relatively high temperatures.

Focus is on the aging behavior of pristine EPON 862 in bulk form[4]. More specifically, what is at stake is the physical aging of the material, i.e., after a quench from above the glass transition temperature T_g to slightly below it.

By convention, physical aging in amorphous polymers refers to the change in their mechanical properties after they are quenched from above to below T_g and then

[4]The issue of how the aging process would change when the epoxy is embedded in the braided composite is out of the scope of this project.

aged isothermally in the glassy state (Struik, 1978; McKenna, 1989). It is to be distinguished from chemical aging, which involves some degree of chemical degradation of the material. Mechanical properties that are typically altered by physical aging include the isochronal viscoelastic modulus, the creep rate, the strength (G'Sell et al., 1992) and to a lesser extent the impact fracture energy (Mininni et al., 1973; McKenna et al., 1988).

There is indication from the specialized literature that many aspects of physical aging are common to both thermoplastic and thermosetting materials (Struik, 1978; G'Sell et al., 1992; O'Connell and McKenna, 2002; Engels et al., 2009; Belbachir et al., 2010). Macroscopic aspects are uncovered through a quantitative characterization of materials and the monitoring of changes to macroscopic, measurable properties imparted by well-controlled aging or annealing programs. The microscopic mechanisms that control the observed property evolution are usually hypothesized and are seldom characterized quantitatively.

Several phenomena occur because of physical aging. This includes the aging of viscoelastic relaxation (McKenna, 1989), the aging of volume recovery (Santore et al., 1991) and that of the yield behavior (G'Sell et al., 1992). These three are evidently related but they seem to be controlled by different time scales. Because of this inherent complexity in the processes involved in aging, it is still difficult to paint a complete picture especially for composite applications where phenomena such as microcracking (Leveque et al., 2005) add to the complexity of the problem. Yet, some trends emerge which will be summarized below. Focus is laid on the aging of the yield behavior. Also, its connection to volume recovery and viscoelasticity is briefly highlighted.

1. The upper yield stress σ_{p} increases with aging time.

2. The aging rate of σ_p is initially fast then slows down before tending to a presumed asymptotic limit at very long aging times. That limit is presumed to correspond to the polymer network evolving toward thermodynamic equilibrium[5].

3. The transition time t^* from fast to slow aging is shifted to higher values as the aging temperature is decreased.

4. The lower yield stress σ_d is not so much affected by the aging time, unlike σ_p.

5. The physical aging seems to affect the viscoelastic response and the yield behavior in different ways since the t^* of the upper yield point is measured to be one order of magnitude larger than the t^* from viscoelastic measurements.

6. The aging of the yield response is closely related to the evolution of the specific volume. However, the transition time t^* is longer than that required to reach equilibrium in volume recovery experiments.

An experimental plan has been defined and performed at NASA GRC in order to investigate the effects of aging on the deformation of EPON 862. It consisted of the following tasks, listed in chronological order:

1. Aging program : Panels were subjected to a complex aging program where a combination of temperature and moisture was prescribed. This hygrothermal aging program was carried out using a sophisticated aging chamber. It consisted of a large number of cycles[6]. Each cycle consisted of a 5 h soak at 85F and 85%

[5]It is established that quenched amorphous polymers are far from thermodynamic equilibrium (e.g. McKenna (1989)). One consequence is that their specific volume is larger than is expected based on extrapolations from the rubbery state. Thus, densification occurs on aging.

[6]The total aging time has not been communicated by NASA.

humidity, a ramp to -65F and 1 h soak, then a ramp to 250F (i.e., $T_g - 12$) and 2 h soak and finally a ramp. The total time for one cycle was 12 h, including ramps.

2. About 10 cylindrical samples were cut out of the aged panels and smooth bars were machined. The specimens were tested in compression and tension following the same procedure as in Section 2.

3. Anticipating on possible changes in the material behavior among the two batches of pristine and aged EPON 862 (more than a year apart), a series of tension and compression tests were carried out on unaged specimens machined from the material subjected to the aging program.

C. Results

1. Quasi-static Behavior

In Littell et al. (2008) only "engineering" curves have been provided. In Fig. 18 such engineering stress σ^{eng} (4.1) and true stress σ (4.4) are plotted versus the true strain $\bar{\epsilon}_{22}$ (4.2) on two examples. This figure shows that the engineering stress is significantly greater (resp. smaller) than the true stress under compression (resp. tension). For example, at the peak stress in compression the difference between the two measures is a little over 20 MPa and increases to about 50 MPa at larger strains whereas in tension it does not exceed 20 MPa. As will be illustrated below, the difference is higher in compression due to a more pronounced barreling in comparison with necking in tension. Contrary to previous investigations in which premature fracture of epoxy E-862 was reported to be caused by strain gauges (Goldberg et al., 2005), this epoxy is instead able to sustain very large strains, even in tension.

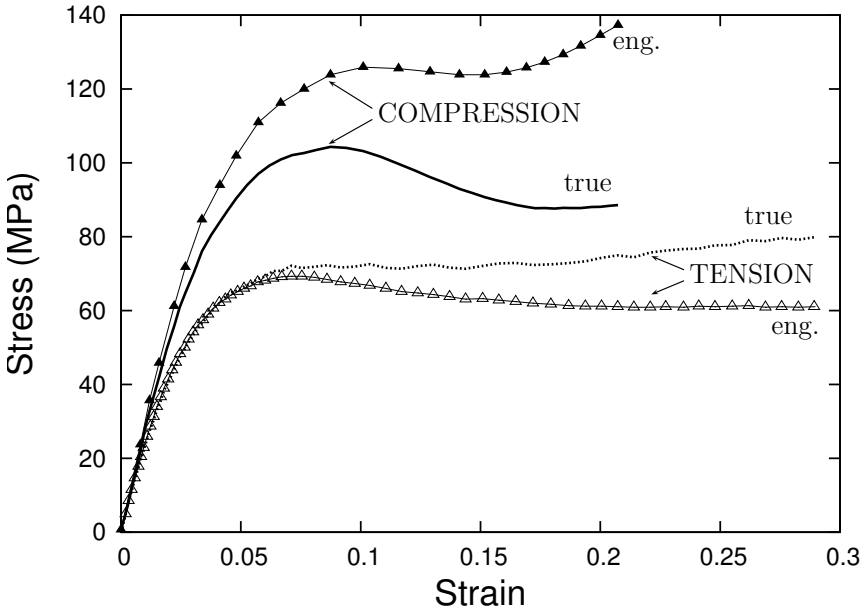

Fig. 18. Comparison between the true stress–strain response of EPON 862 (σ in (4.4) versus $\bar{\epsilon}_{22}$ in (4.2)) with the engineering response ($\sigma^{\rm eng}$ in (4.1) versus $\bar{\epsilon}_{22}$). Example 1: compression at $T = 25°$C and nominal strain-rate $\dot{\epsilon} = 10^{-1}$/s; Example 2: tension at $T = 25°$C and $\dot{\epsilon} = 10^{-5}$/s.

Results of unloading tests have indicated that inelastic strains begin to build up well before the peak stress. An example is given in Fig. 19, which depicts the definition of the "yield" stress, the upper yield stress and the lower yield stress. Tables III, IV and V contain some key parameters inferred from the stress-strain curves at 25°C, 50°C and 80°C, respectively, for various levels of strain rate.

Table III. At room temperature, mechanical properties of EPON 862 for various strain rates ($\dot{\bar{\epsilon}}$) : Young's Modulus E, yield stress σ_{y}, stress at peak σ_{p}, lower yield stress σ_{d}, strain at peak ϵ_{p} and strain at fracture ϵ_{f}. Each compressive (C) and tensile (T) property is given under the format "C / T". Note that the value for Poisson's ratio $\nu = 0.4$ is considered independent of temperature and strain rate.

$\dot{\bar{\epsilon}}$ (/s)	E (MPa)	σ_{y} (MPa)	σ_{p} (MPa)	σ_{d} (MPa)	ϵ_{p} (%)	ϵ_{f} (%)
10^{-1}	2800/2600	89/74	102/92	86/89	8.7/12.0	–/25.8
10^{-3}	2500/2500	72/73	86/80	74/78	7.8/9.4	–/31.0
10^{-5}	2500/2300	–/–	80/69	69/68	7.4/9.2	–/25.7

Table IV. At 50°C, mechanical properties of EPON 862

$\dot{\bar{\epsilon}}$ (/s)	E (MPa)	σ_{y} (MPa)	σ_{p} (MPa)	σ_{d} (MPa)	ϵ_{p} (%)	ϵ_{f} (%)
10^{-1}	2400/2300	83/75	85/79	75/79	8.9/10.5	–/34.5
10^{-3}	2100/2200	70/62	73/66	64/65	8.5/10.0	–/33.1

Table V. At 80°C, mechanical properties of EPON 862

$\dot{\bar{\epsilon}}$ (/s)	E (MPa)	σ_{y} (MPa)	σ_{p} (MPa)	σ_{d} (MPa)	ϵ_{p} (%)	ϵ_{f} (%)
10^{-1}	1900/2000	64/60	66/61	54/60	7.3/7.3	–/36.4
10^{-3}	1700/1800	48/46	52/48	48/48	8.8/7.0	–/41.4

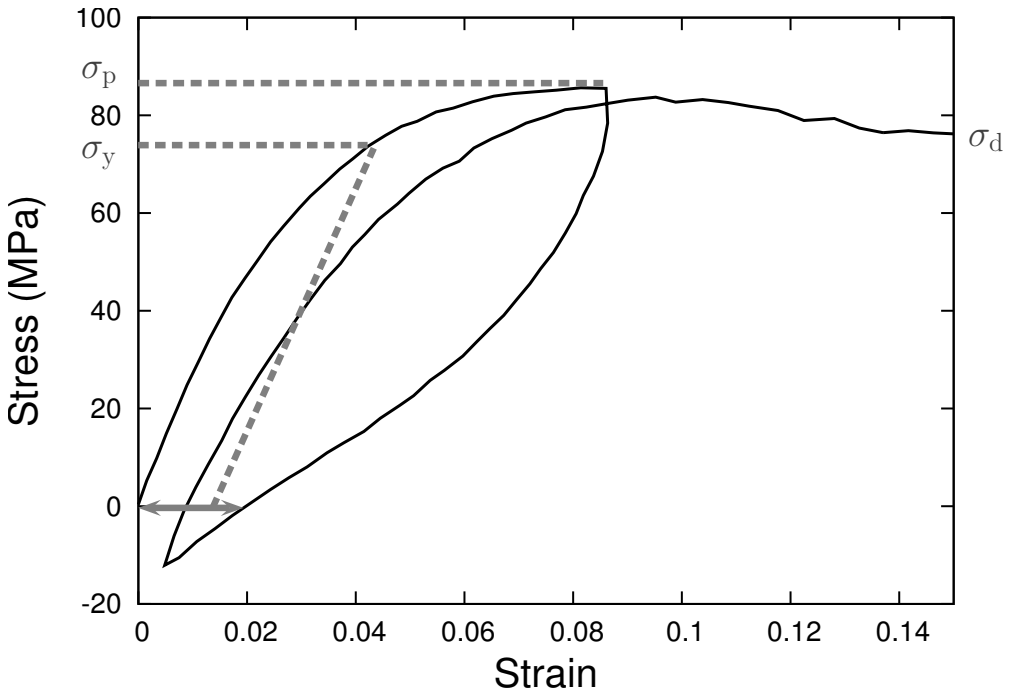

Fig. 19. Loading-unloading response in compression at 25°C at a nominal strain-rate of 10^{-3}/s showing the amount of inelastic strain after unloading.

A comparison between the two measures of "true strain" $\bar{\epsilon}_{22}$ in (4.2) and ε in (4.3) is illustrated in Fig. 20 at room temperature and 80°C, in tension and compression. At room temperature, despite the fact that $\bar{\epsilon}_{22}$ has more of a local character, this strain measure was observed to be systematically[7] smaller than ε: in compression, the difference grows considerably subsequent to strain localization whereas the two measures are almost indistinguishable in tension. As indicated above, the strain measure ε is more reliable post-localization. Nonetheless, at higher temperatures (50°C and 80°C) $\bar{\epsilon}_{22}$ is found to be greater than ε. In tension, differences are small. In compression, in the extreme case the strain difference is over 0.1.

[7]There is only one exception among all experiments at 25C: one case of tension at $\dot{\epsilon} = 10^{-3}$/s shows end-of-test values of $\varepsilon = 0.32$ and $\bar{\epsilon}_{22} = 0.38$.

Figure 21 illustrates the correlation between the full-field strain mapping and the overall stress–strain response in the case of tension at $T = 50°\text{C}$ and $\dot{\epsilon} = 10^{-1}/\text{s}$. After the initially linear elastic response the material behavior becomes nonlinear. At a strain of $\varepsilon = 0.13$, the strain distribution is essentially homogeneous within the gauge area, Snapshot (A). Shortly thereafter, deformation localizes concurrently to the development of a shallow neck. Difficult to visualize with the naked eye, the onset of necking is ascertained based on two observations: (i) the drop in the force, as seen for example in the engineering curve of Fig. 18; and (ii) the deformation becomes nonunifom along the x_2-axis (Snapshot (B) in Fig. 21). The filled square at (B) means that at this stage it has become visually evident that localization took place. Localization, which is visually evident at (B) as denoted by the filled square, is likely to have set earlier. Strains $\bar{\epsilon}_{22}$ reach values around 0.19 and decrease down to about 0.11 near the ends of the specimen gauge section. Subsequent deformation is characterized by a hardening stage. Consequently, material in the vicinity of the incipient neck hardens again and deformation becomes more uniform going from snapshot (B) to (D) through (C). Finally, fracture takes place at a strain ε of about 0.36. The corresponding snapshot (D), taken right before fracture, exhibits some strain concentration at the center with most of the gauge section experiencing strains $\bar{\epsilon}_{22}$ higher than 0.25.

(a)

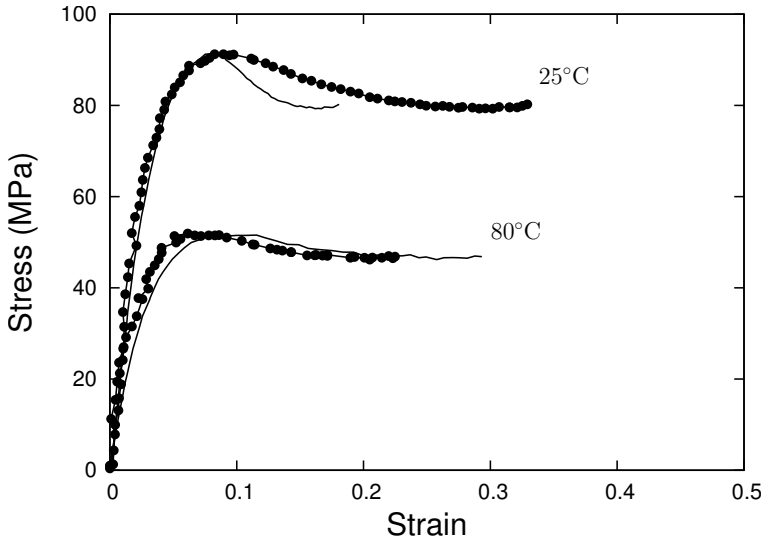

(b)

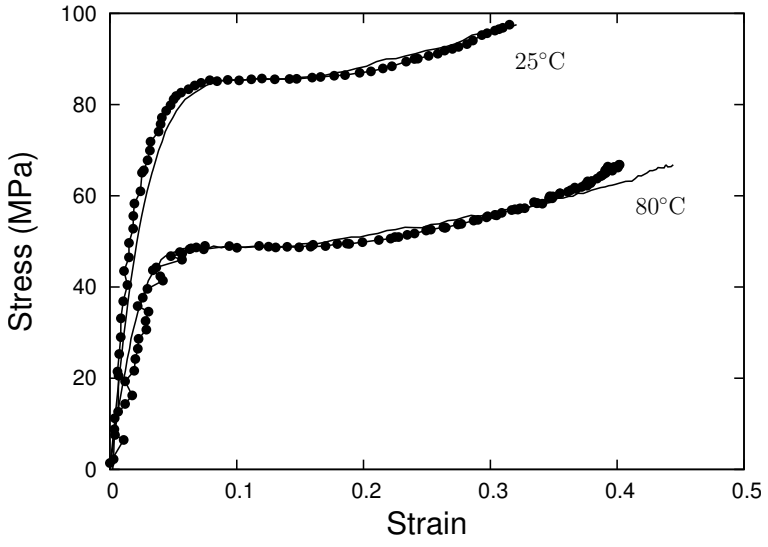

Fig. 20. True stress versus strain curves for $T = 25°\mathrm{C}$ and $T = 80°\mathrm{C}$ and two definitions of the "true" strain: $\bar{\epsilon}_{22}$ in (4.2) (solid lines) or ε in (4.3) (filled circles). (a) compression at $\dot{\epsilon} = 10^{-3}/\mathrm{s}$; (b) tension under the same conditions.

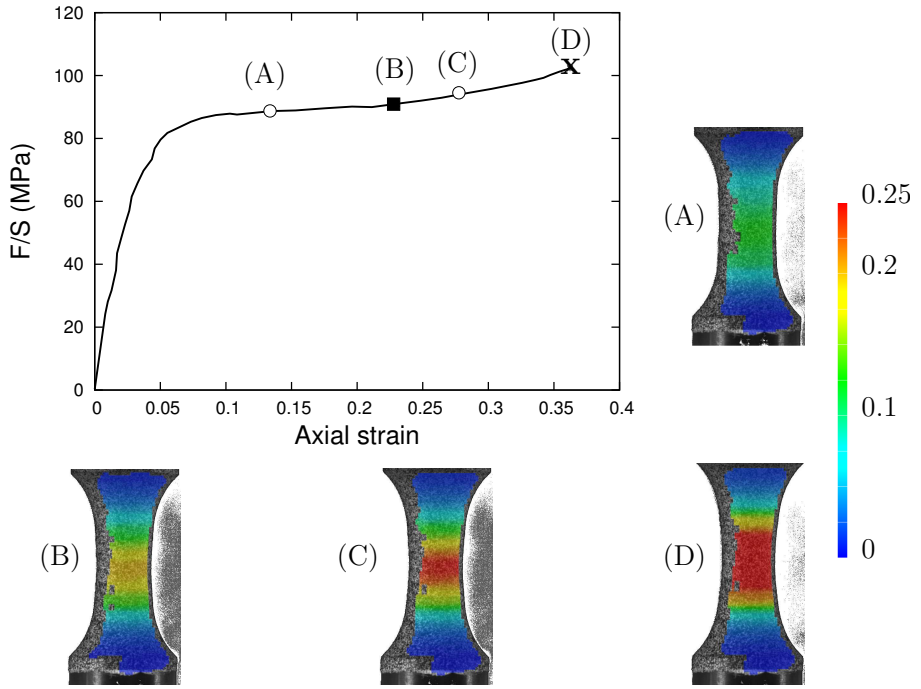

Fig. 21. True stress versus true strain ε and corresponding select snapshots of Aramis strain contours ($\bar{\epsilon}_{22}$) in tension at $T = 50°\text{C}$ and $\dot{\epsilon} = 10^{-1}/\text{s}$. The circles on the curve correspond to stages before and after the onset of necking (resp. (A) and (C)), which is clearly observable at (B). The cross indicates fracture which occurs slightly after stage (D).

Figure 22 depicts a typical response in uniaxial compression as well as snapshots of strain contours at various stages of deformation. The strains at peak stress (σ=92 MPa) are rather homogeneous (about 0.08), snapshot (A). During the softening regime, which is more pronounced than in tension, barreling becomes clear within the specimen gauge, snapshot (B). A subtle discoloration in the strain contours is observed in the neighborhood of the center, which marks the onset of strain gradient therein. Further deformation is accompanied by a growing barreling instability as well as strain concentrations. The minimal stress, also called lower yield stress or dip stress (σ=80 MPa), is obtained at ε= 0.25, snapshot (C). Contrary to the symmetric

distribution of strains in tension, an asymmetric strain distribution pattern develops within the specimen which induces a macroscopically visible asymmetry between the top and bottom parts of the specimen. In this particular case, the maximum compressive strains are obtained in the higher half of the gauge section. It is likely that the non-standard specimen geometry is the cause of this strain distribution asymetry. Moreover, the DIC software may not be capable of capturing and calculating strains in highly deformed regions (dark spots in Fig. 22 at stage (D)). When such problems occur in the center of the specimen, where strain values are used for post-processing the measure $\bar{\epsilon}_{22}$, the software calculates the strain at a nearby location, which is problematic for consistency. In the example shown, as indicated by a filled circle, this data capturing problem occurred at a strain ε of about 0.31. The data acquired beyond this point is plotted as dotted line, simply to indicate that it may not be as reliable as data before that stage. At ε= 0.325, the strain distribution is heterogeneous with a maximum value for $\bar{\epsilon}_{22}$ of about 0.45 concentrated at the top of the gauge section, Snapshot (D).

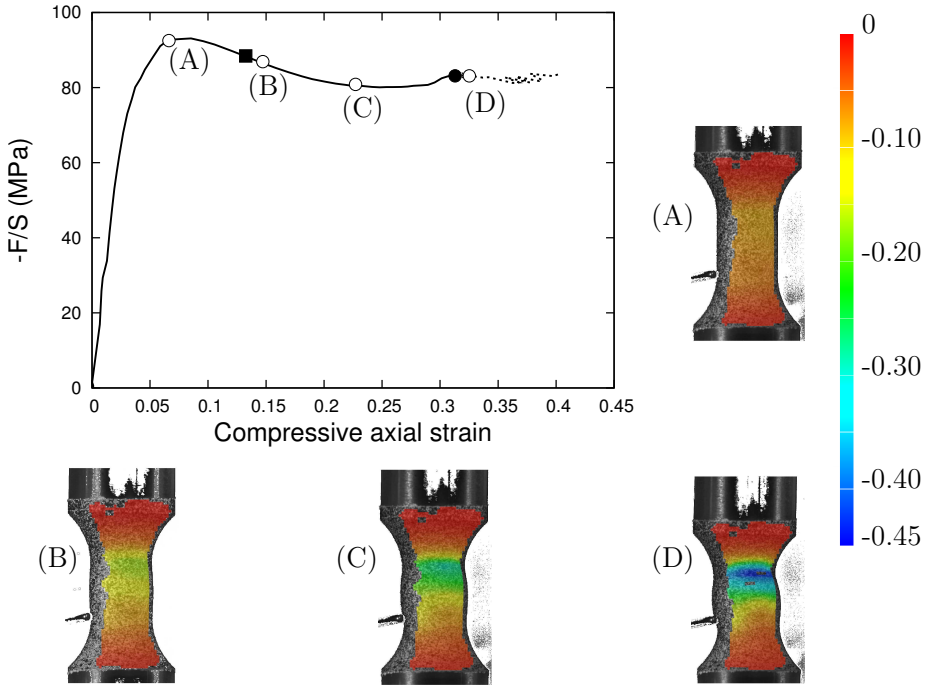

Fig. 22. True stress versus true strain ε and corresponding select snapshots of Aramis strain contours ($\bar{\epsilon}_{22}$) in compression at $T = 50°\text{C}$ and $\dot{\epsilon} = 10^{-1}/\text{s}$. The circles on the curve correspond to stages before and after the onset of barreling (resp. (A) and (C)), which is clearly observable at (B). The full circle indicates the loss of consistency of Aramis data. At (D) the dark spot in the highly deformed region is an example of the absence of calculated strains.

The results of Figs. 21 and 22 bring a new light on the difference between the two strain measures $\bar{\epsilon}_{22}$ in (4.2) and ε in (4.3) (see Fig. 20). In particular, resulting from barreling in compression, an asymmetric strain distribution with respect to the horizontal x_1-axis is usually observed. Since the strain measure $\bar{\epsilon}_{22}$ includes some material points above and below the section of maximum diameter, $\bar{\epsilon}_{22}$ ends up being smaller than the maximum value. Therefore, ε is expected to be greater than $\bar{\epsilon}_{22}$. This is observed at room temperature although at elevated temperatures, in many instances $\bar{\epsilon}_{22}$ is reported to be greater than ε. One possible explanation of this trend is that, for the high temperature testing, surfaces are hotter than the interior of the

specimen. Because the DIC system measured surface strains, there may be a greater gradient in strain in the radial direction than at $T = 25°\text{C}$. If that is the case, then the measure ε would be once again more appropriate to work with since it averages out the radial gradient of strains associated with a nonuniform temperature distribution. In tension, similar differences are noted although less dramatic than under compression loading.

Although the strain measure ε is in principle more reliable than $\bar{\epsilon}_{22}$, it is in practice more difficult to acquire. The measurement of the current minimum or maximum diameter, which is a necessary step for determining the true stress and true strain by the direct procedure in (4.4) and (4.3), requires post-mortem examination of videos for each test. This can be tedious and may lead to inefficient data acquisition, especially if multiple materials and test conditions are to be considered. In addition, some challenges arise in measuring the diameter with sufficient accuracy in the early stages of deformation, particularly for testing at high temperatures. Some stress–strain curves (σ–ε) illustrating this are showed in Fig. 23 in tension at 10^{-1}/s and compression at 10^{-3}/s. In both cases, the full range response is rather smooth at room temperature whereas at 50°C and 80°C serrations are observed in the initial elastic stage and pre-peak hardening regime. However, the smoothness of the stress–strain curves beyond peak stress indicates a higher efficiency in the assessment of the large strain behavior for all testing conditions in comparison with the acquisition of the small strain response.

(a)

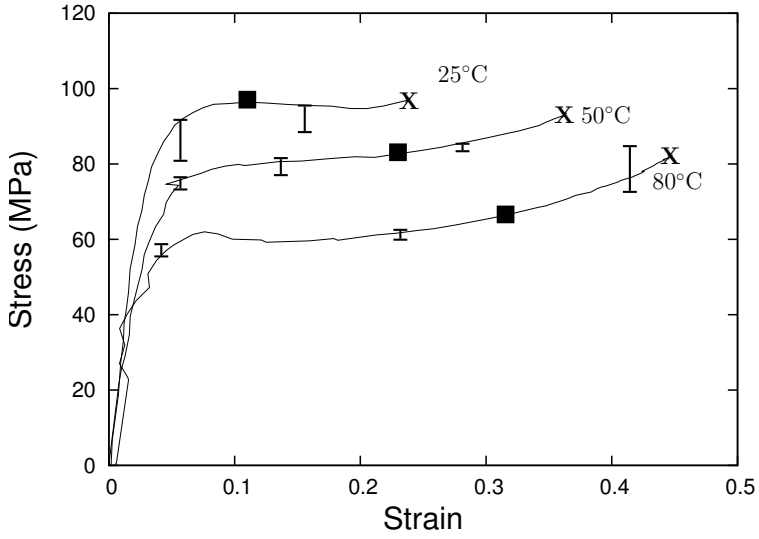

(b)

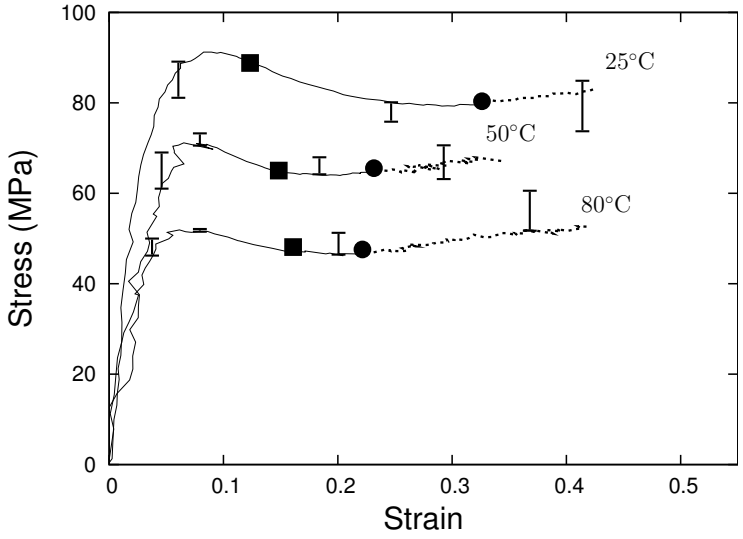

Fig. 23. Effect of temperature on the true stress–strain behavior of EPON 862 (σ versus ε). (a) Under tension at a nominal strain-rate of 10^{-1}/s and (b) under compression at a nominal strain-rate of 10^{-3}/s.

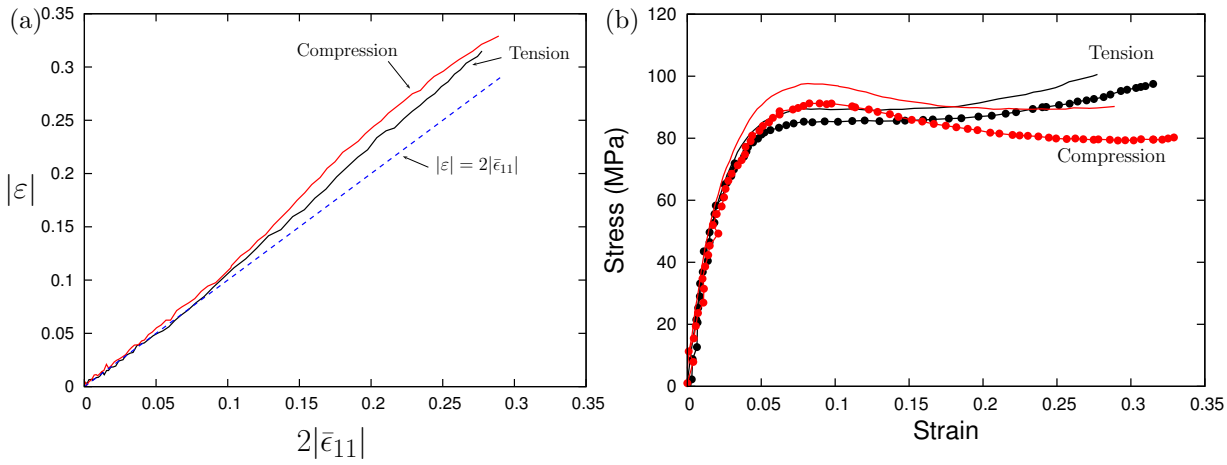

Fig. 24. Comparison of the direct and simplified methods for the determination of true stress versus strain behavior in tension and compression at $T = 25°C$ and $\dot{\epsilon} = 10^{-3}/s$. (a) Logarithmic measure $|\varepsilon|$ versus $2|\bar{\epsilon}_{11}|$. (b) Stress–strain curves corresponding to the direct method (equations (4.4) and (4.3); filled circles) and the simplified method (equations (4.6) and (4.5); solid lines).

In what follows, we briefly describe results obtained using the alternative simplified procedure, i.e., using equations (4.6) and (4.5) to estimate the true stress and true strain ($2\bar{\epsilon}_{11}$), respectively. Typical results obtained with this simplified method are compared with those obtained using the direct method in Fig. 24. The test conditions are the same as in Fig. 20 for T=25°C. Fig. 24a shows that the two strain measures ε and $2\bar{\epsilon}_{11}$ take identical values before plastic instability. Subsequent to that, the logarithimic measure ε is found to be greater. As discussed in the context of comparing ε with $\bar{\epsilon}_{22}$, this difference is due to strain localization so that (i) the local strain varies significantly among the five locations used to post-process $2\bar{\epsilon}_{11}$; and (ii) the location of the maximum of $2\bar{\epsilon}_{11}$ may be far from the neck (tension) or barrel's apex (compression). Fig. 24b shows the corresponding stress–strain curves. What is encouraging in this figure is that the two curves are close to each other, both

under tension and compression. The stress estimated using the simplified method is greater than the actual stress and this is due to the approximations used in the analysis. Within such approximations and with appropriate care, it may be convenient in general to work with true stress–strain curves obtained using this simplified procedure.

The temperature-sensitivity of Epon 862 in tension at a strain-rate of 10^{-1}/s (top) and in compression at a strain-rate of 10^{-3}/s (bottom) is summarized in Fig. 23. ε is used as the true strain measure. The bars on the stress–strain curves indicate the extent of scatter in experimental data collected for multiple realizations of the same test condition. As explained above, a filled square refers to that stage at which necking or barreling has become evident to the naked eye; in tension a cross represents the failure of specimens and in compression full circles with following dotted lines denote questionable data due to data collection problems.

The amount of thermal softening of E862 epoxy, as inferred from Fig. 23, is significant over the temperature range investigated. In tension, for example, the peak stress reaches about 95 MPa at room temperature, and decreases down to 60 MPa at 80°C. In compression, the peak stress decreases from 90 MPa at 25°C down to 50 MPa at 80°C. It is worth noting that thermal softening does not affect the shape of the stress–strain curve. In tension, the true stress–strain curve is characterized by a hardening stage at small strains, followed by a plateau then a rehardening stage at larger strains. In compression, the amount of post-peak softening is noticeable. Further details on temperature sensitivity at other conditions, as well as effects of strain-rate, may be inferred from Fig. 25 and Fig. 26.

2. Dynamic Response

Figure 27 compares true stress–strain ($\bar{\epsilon}_{22}$) curves obtained at low-to-moderate strain rates with those determined from the SHB tests. For low to moderate rates, the strain rates were assumed constant even though the displacement rate was prescribed. At high rates, besides oscillations, the strain rate was observed to increase then rather quickly stabilize from which an average value for strain rate was determined. In tension, the reliability of the SHB data is questionable in view of the unrealistic initial stiffnesses measured. In addition, the test is prematurely terminated because of failure of the specimen. In compression, however, the data is of excellent quality. In the subsequent discussion only the compression SHB data in Fig. 27b will be considered. As expected, the higher the strain rate the greater the flow stress. For low to moderate strain rates in both tension and compression, the peak stress increases by about 25 MPa when the strain rate increases from 10^{-5}/s to 10^{-1}/s. Hence, a variation of the strain rate by four orders of magnitude leads to a variation of the flow stress smaller than that effected by a 55K variation in the temperature (see Fig. 20a above where the peak-stress difference was about 40 MPa). These results indicate that the material is weakly rate-sensitive within the regime of low to moderate strain rates. However, assuming that the variation in flow stress is the sole signature of the material rate-sensitivity, it is remarkable that the peak stress increases by almost 100 MPa when the strain rate increases from 10^{-1}/s to about 10^{3}/s. That is a much higher variation in the flow stress measured at high strain rates within a comparable interval of four orders of magnitude in $\dot{\epsilon}$. The results in Fig. 27b indicate that the effect of strain rate on the flow stress is strongly nonlinear, consistent with theories of thermally activated processes. It is likely, however, that the magnitude of the strain-rate sensitivity at high rates of loading inferred from these results is

exaggerated. Indeed, some contribution to the measured stresses may have come from purely dynamic effects. The equilibrium reads:

$$div(\sigma) + \rho \mathrm{B} = \rho \frac{\partial^2 \mathrm{u}}{\partial t^2} \tag{4.7}$$

where σ is the Cauchy stress tensor, ρ the density, B the volumetric body force vector and u the displacement vector. At low strain rates, the inertial term of the right hand-side can be neglected. However, in dynamic conditions, inertia has a strengthening effect on the polymer response. It is also more important with increasing specimen size. the natural outcome is that stress-strain curves of high rate loadings exhibit higher levels of strength as compared with static conditions. Also, the transient feature of the equilibrium equation induces the generation of stress waves which propagate into the specimen. These stress waves manifest themselves under the form of oscillations in stress-strain curves. These oscillations progressively die out, aided by the damping effect of the polymer response. A possible explanation to the high strengthening at large strain rates is that a secondary (β) thermo-activated relaxation process is allowed to occur. This β transition has been observed in other polymers (PC, PMMA) and has been associated with the restriction of molecular group rotations (Hutchinson, 1995). However, the interpretation of the Kolsky experiments is complicated since these experiments are essentially adiabatic. At low strain rates, isothermal assumptions are usually accepted. However, at higher rates, the heat generated by the conversion of plastic dissipation is assumed to not flux out through conduction or convection process. Therefore, the material is expected to soften as a consequence of its thermal sensitivity. These opposite effects (strenghtening and softening) are difficult to decouple in such experiments, especially since the surface temperature of the specimens tested has not been recorded.

(a)

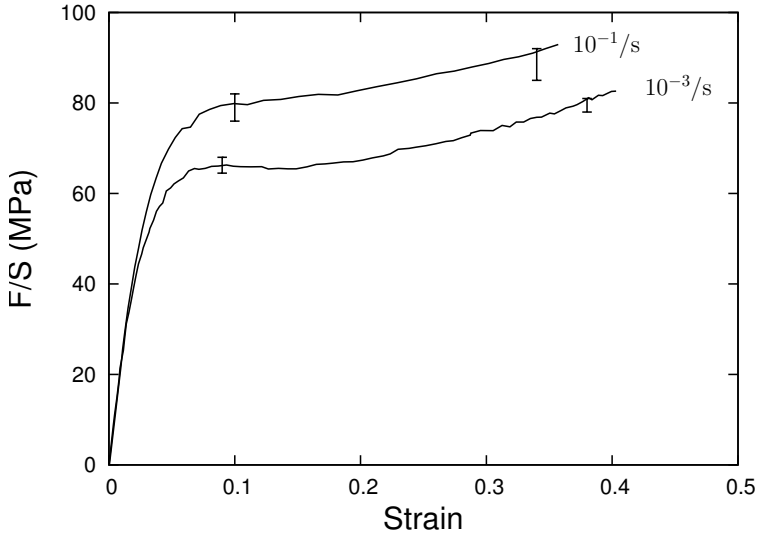

(b)

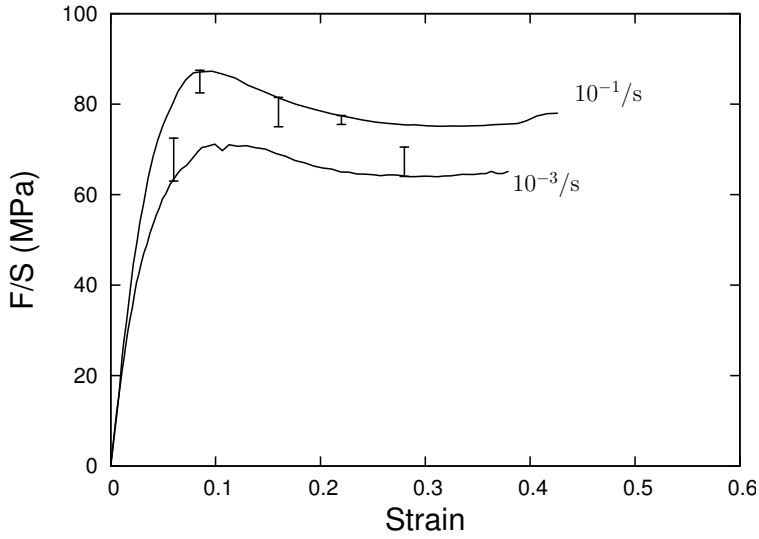

Fig. 25. Effect of nominal strain-rate at $T = 50°$C. True stress versus strain ($\bar{\epsilon}_{22}$) curves for (a) tension; and (b) compression.

(a)

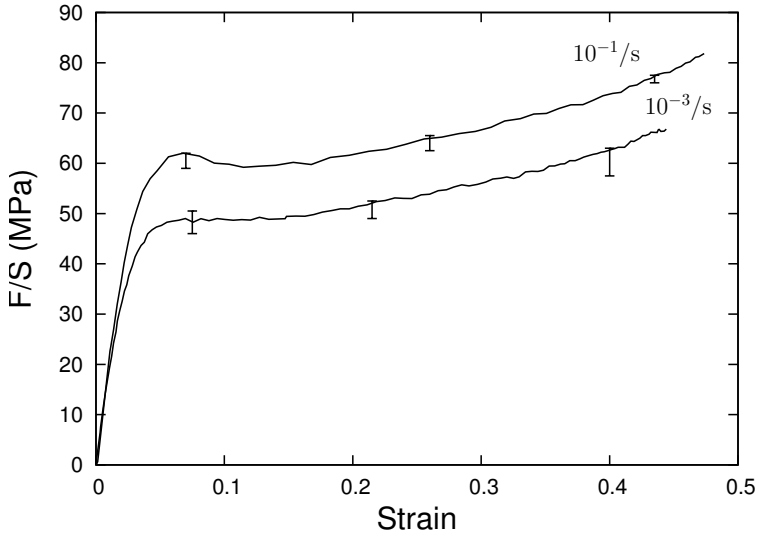

(b)

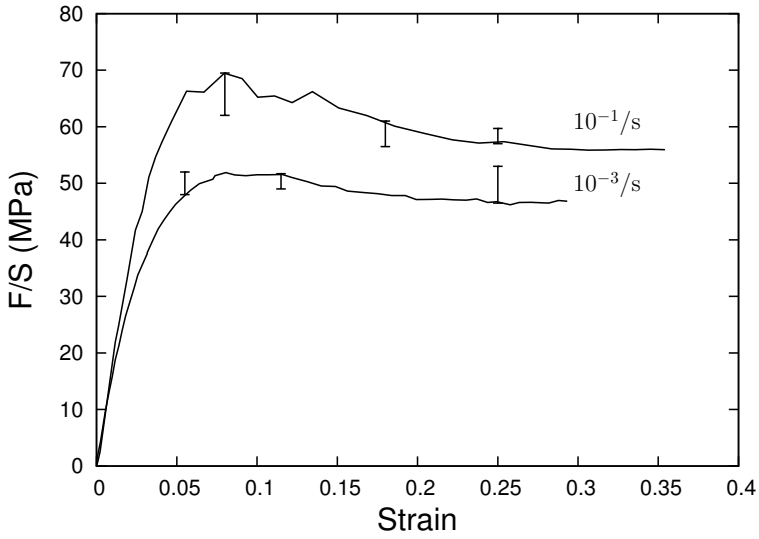

Fig. 26. Effect of nominal strain-rate at $T = 80°$C. True stress versus strain ($\bar{\epsilon}_{22}$) curves for (a) tension; and (b) compression.

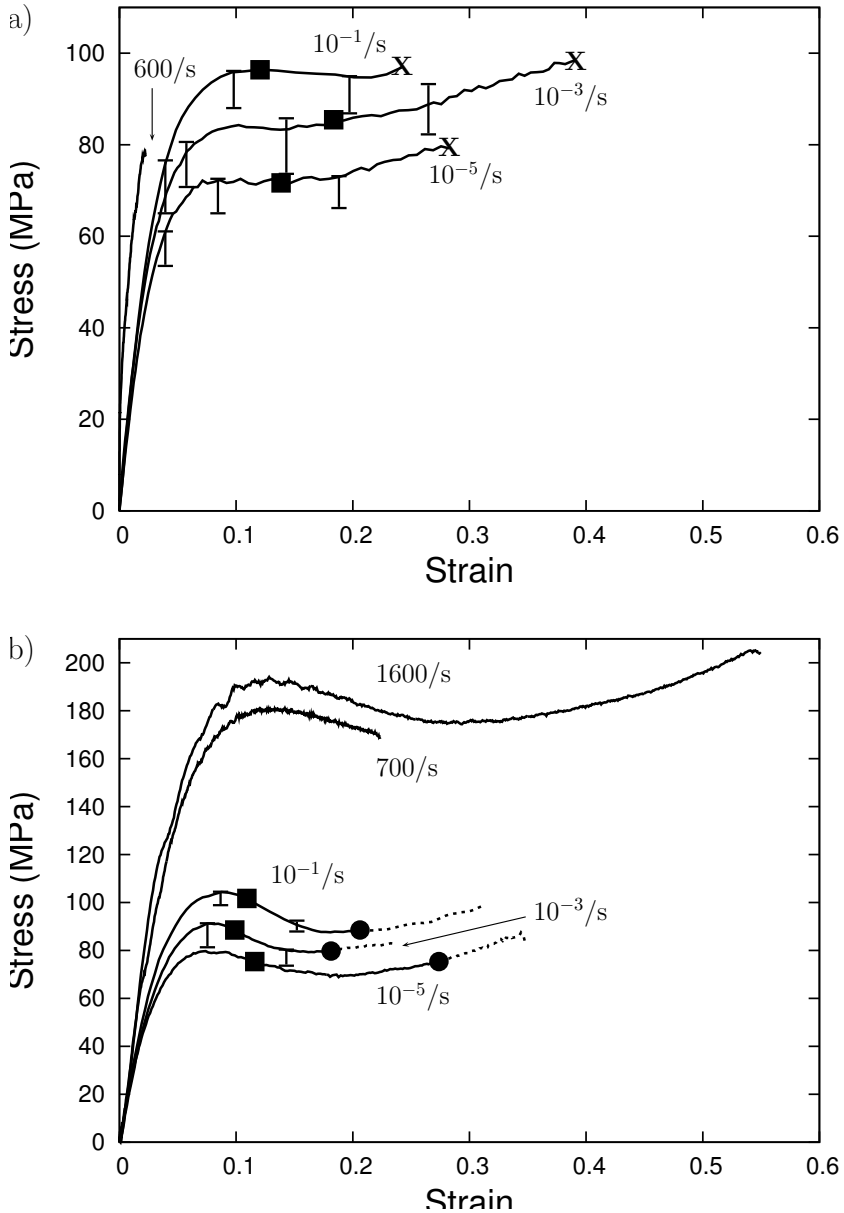

Fig. 27. Strain-rate and dynamic effects at $T = 25°$C. (a) Tension. (b) Compression.

3. Aging Effects

The mechanical response of aged specimens was characterized at room temperature only. The smooth bars were tested in tension at two strains rates $\dot{\epsilon} = 10^{-3}s/$ and 10^{-1}/s and in compression at two strain rates $\dot{\epsilon} = 10^{-5}$/s and 10^{-3}/s. Two realizations of the same test condition were carried out. The experimental procedure follows exactly the methodology outlined in Sections 2 and 4, including the procedure for determining true stress versus true strain behavior. Eight (8) additional bars from the same panels but before aging were also tested (batch 2). This allows comparison with the aged bars as well as with unaged specimens taken from different panels tested by Littell et al. Littell et al. (2008) (batch 1).

The stress–strain response in tension of specimens of batch 2 is shown in Fig. 28 (all realizations). There are some significant differences between the behavior of these specimens with those from batch 1; see Fig. 27a. In both cases, curves of the true stress (σ in (4.4)) versus the true strain ($\bar{\epsilon}_{22}$ in (4.2)) are plotted. Qualitatively, specimens of batch 1 did not exhibit post-peak softening. Instead, the flow stress reached a plateau after which some clear strain hardening took place (Fig. 27a). By way of contrast, specimens of batch 2 seem to exhibit a significant yield drop at the strain rate of 10^{-1}/s (Fig. 28a) and at 10^{-3}/s (Fig. 28b). In addition, specimens of batch 2 do not re-harden at larger strains.

Quantitatively, from Fig. 27a the peak yield stress σ_{p} is about 80 ± 5 MPa at 10^{-3}/s and 92 ± 5 MPa at 10^{-1}/s. These values are in very good agreement with values of σ_{p} from the second batch. However, there are some quantitative differences between the two batches. Higher levels of strength at peak are observed for batch 2: 87 MPa at 10^{-3}/s and 100 MPa at 10^{-1}/s. Even though the newer experiments were

interrupted[8] at strains smaller than those for batch 1 (compare 0.33 with 0.45), the expectation was that specimens of batch 2 would harden at strains of about 0.2. As a consequence yield stresses beyond the peak are greater in batch 1 than those from batch 2.

Explanations for the observed differences among specimens of EPON 862 belonging to the two different batches include (i) a difference in the procedure followed to extract true stress data; (ii) a difference in the material (chemistry, synthesis method, etc..); and (iii) an effect of aging at room temperature. The differences cannot be rationalized based on hypothesis (i) above because for both batches of experiments the true stress was generated using the same method. Differences based on (ii) are likely but no information was received regarding how the second material differed from the first batch. Finally, hypothesis (iii) seems somewhat reasonable upon examination of the data in that aging leads to more pronounced softening (with due reference to the common trends summarized in Section 4). Note that specimens of batch 1 also exhibited some softening in tension when tested at a higher temperature (80C) at 10^{-1}/s.

The compression response of specimens of batch 2 is shown in Fig. 29 (all realizations). There are some significant differences between the behavior of these specimens with those from batch 1; see Fig. 27b. As in tension, some differences are observed in compression as well. The post-peak softening is clear in both series of experiments. However, the amount of softening was greater in specimens of batch 1. Also, quantitative differences in peak yield stresses are noted. From Fig. 27b the peak yield stress $\sigma_{\rm p}$ is about 77 MPa at 10^{-5}/s and 85 ± 5 MPa at 10^{-3}/s. These values are smaller than the values of $\sigma_{\rm p}$ from the second batch (about 89 MPa and 103 MPa,

[8]The specimens fractured.

respectively). This increase of over 10 MPa in peak yield is also consistent with the hypothesis that specimens from batch 2 may have undergone some long-term aging at room temperature before they were actually tested[9]. In conclusion, it is very likely that the specimens labeled "unaged" in this section have actually aged at room temperature. According to this hypothesis, the specimens labeled "aged" in the figures are simply characterized by a greater aging time. The results in tension and compression of batch 1 and batch 2 indicate a strenghtening effect of aging (10 MPa increase at peak stress). It is important to notice that the aging cycle performed at NASA on EPON 862 incorporates accelerated aging at a temperature close to T_g. However, the curing process, which affects the epoxy chemistry (increase of percentage crosslinks) as well as its physical properties (e.g. increase of strength), is also accelerated at high temperatures. Therefore, both aging induced molecular rearrangements and curing could explain the observed strengthening.

As shown in Figs. 28 and 29, the stress-strain curves for aged and "unaged" EPON 862 specimens exhibit qualitatively similar responses. The initial stiffness does not seem to be affected by aging. This does not mean that the viscoelastic properties were not altered, as the type of mechanical tests conducted here does not permit to measure the relaxation response. However, the strength observed at peak stress on aged specimens is slightly higher than on unaged specimens. Also, the amount of softening between the peak stress and dip stress seems slightly more pronounced for aged specimens. Both of these trends are consistent with expectations based on the common trends obtained for the aging of epoxies.

It appears that the macromolecular model can be enhanced to account for the effects of physical aging. indeed, the physical basis of the model makes it potentially

[9]Not fully consistent though since the amount of softening has decreased in specimens of batch 2.

and ideal candidate for accounting of aging effects. Evidently, our focus has been on the physical aging of the yield behavior, as opposed to that of volume recovery or viscoelastic relaxation.

The aging kinetics is incorporated into the macromolecular constitutive equations. In the enhanced model, a phenomenological description for the of kinetics aging is introduced through a logarithmic increase of peak stress with aging, as well as the use of master curves for time-temperature and time-stress superpositions. The yield drop is modeled as a state parameter which depends on time, temperature, stress and plastic strain. It is decoupled into two opposite contributions: aging and rejuvenation. The model incorporates shift functions which capture the temperature and stress accelerating aging kinetics. Thus, the viscoplastic law (Eq. 3.10) is amended such that:

$$\dot{\bar{\epsilon}} = \dot{\epsilon_0} \exp\left[-\frac{A\,(s-\alpha\sigma_h)}{T}\left(1-\left(\frac{\sigma_{\mathrm{e}}}{s-\alpha\sigma_h}\right)^m\right)\right]\exp(-S_a) \tag{4.8}$$

where

$$S_a(t_{eff}) = c_0 + c_1 \log\frac{t_{eff}(t,T,\sigma_{\mathrm{e}})+t_a}{t_0} \tag{4.9}$$

with c_0, c_1 are parameters and the effective time t_{eff}, which describes the thermomechanical history of the aging material, is defined as :

$$t_{eff}(t,T,\sigma_{\mathrm{e}}) = \int_0^t \frac{d\xi}{a_T(T(\xi))a_\sigma(\sigma_{\mathrm{e}}(\xi))} \tag{4.10}$$

with the temperature shift factor a_T is defined from a master curve (Arrhenius relation) such that :

$$a_T(T) = \exp\left[\frac{\Delta U_a}{R}(\frac{1}{T}-\frac{1}{T_{ref}})\right] \tag{4.11}$$

in which ΔU_a denotes the activation energy, R the universal gas constant, T the annealing temperature, and T_{ref} a reference temperature. The stress shift factor is

calculated from a stress activated shift of Eyring type :

$$a_\sigma(\sigma_e) = \frac{\sigma_e/\sigma_a}{sinh(\sigma_e/\sigma_a)} \qquad \sigma_a = \frac{RT}{\nu_a} \tag{4.12}$$

where ν_a is an aging activation volume fitted from master annealing time-stress superposition curve. More details can be found in Klompen et al. (2005).

D. Conclusion

This chapter discussed results regarding the mechanical behavior of a thermoset epoxy tested in tension and compression for low, moderate and high rates of strain at various temperatures below the glass transition temperature and for two conditions of aging ("as-received" and accelerated aged states). The characterization of the mechanical response at low to moderate rate of deformations was carried out using a new experimental technique. This methodology based on digital image correlation enables to capture the evolution of the displacement fields on the surface of the deformed specimen and to calculate surface strains after post processing. Similarly to video-monitored extensometry techniques, the evolution of the diameter in the minimal/maximal cross section was also determined such that the intrinsic response of the polymer was presented by means of true stress-strain curves. A simplified method for a rapid characterization of the mechanical response of polymers is also presented. This method was showed to give a good estimate of the polymer behavior, with true stress-strain curves plotted from the sole surface strains data. The response of the epoxy at high strain rates was determined from experiments performed by Prof. A. Gilat from O.S.U who used Kolsky bar experiments. These SHB tests are essentially adiabatic, which complicates the interpretation of results. The measurements showed that the material is able to sustain large inelastic strains, in excess of 0.4, including

under tensile loading. The deformation takes place in stages with a short visco-elastic region followed by a rounded yield point. Systematic unloading experiments in the neighborhood of the peak yield were carried out to probe the onset of inelastic behavior. The amount of strain softening was found to be independent of strain rate or temperature. The amount of thermal softening and the strain-rate sensitivity of the polymer were quantified. The experiments led to a comprehensive data base that can be used for developing a physics-based constitutive model for the polymer and in higher scale finite-element analyses of epoxy-based advanced composites for jet engine fan containment cases.

(a)

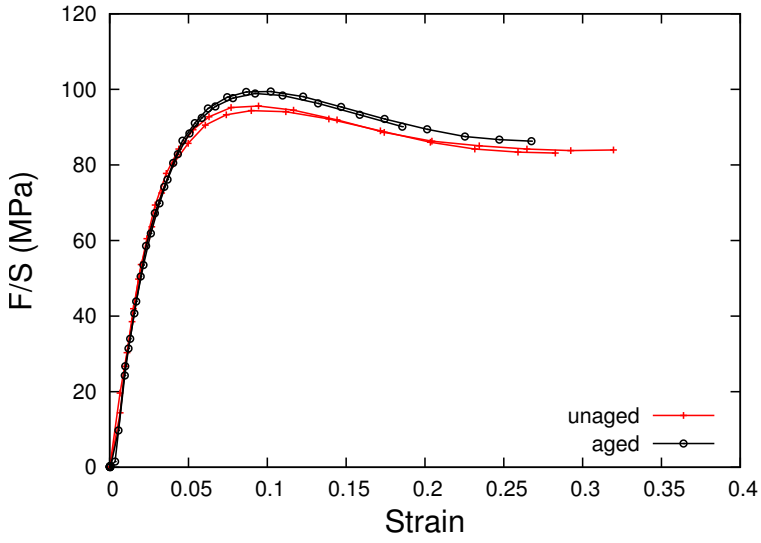

(b)

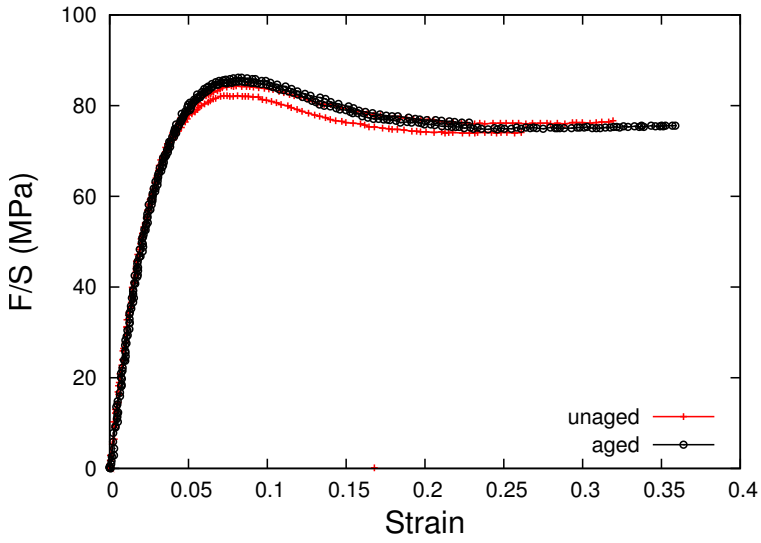

Fig. 28. Effect of aging program 2 on the tensile response at room temperature. True stress versus strain curves at a nominal strain rate: (a) $\dot{\epsilon} = 10^{-1}$/s; and (b) $\dot{\epsilon} = 10^{-3}$/s.

(a)

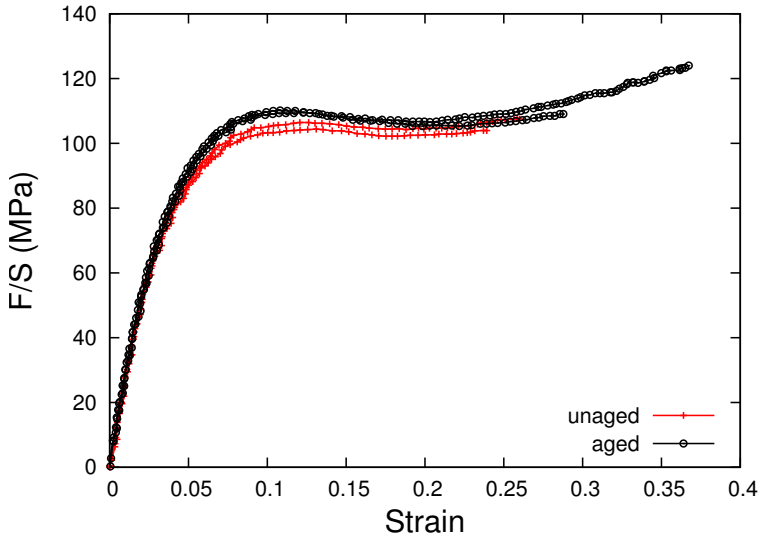

(b)

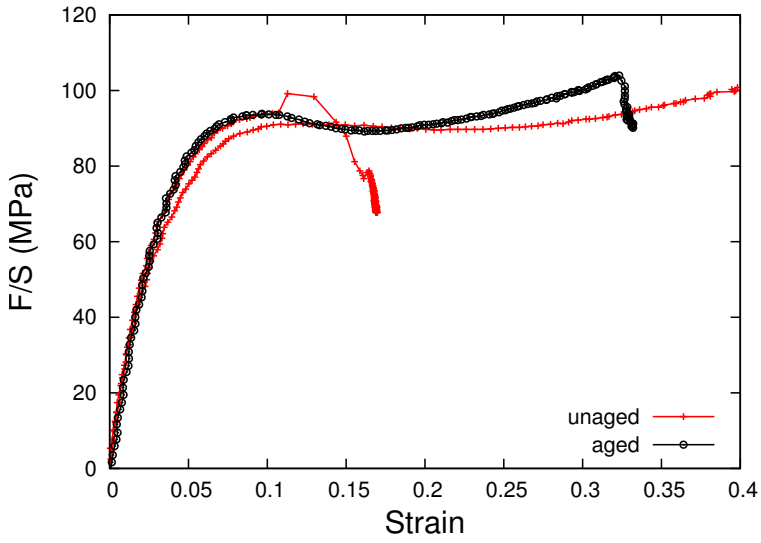

Fig. 29. Effect of aging program 2 on the compression response at room temperature. True stress versus strain curves at a nominal strain rate: (a) $\dot{\epsilon} = 10^{-3}/\text{s}$; and (b) $\dot{\epsilon} = 10^{-5}/\text{s}$.

CHAPTER V

MODELING OF THE RESPONSE OF AN EPOXY RESIN USED AS MATRIX IN IMPACT RESISTANT FAN BLADE COMPOSITES

A. Introduction

Viscoplastic models are commonly used to assess and predict the complex behavior of glassy polymers under their glass transition temperature. Among the most sophisticated is the macromolecular model developed by Boyce et al. (1988). Here, we challenge the capabilities of a variant of this model against experimental results on epoxy resin Epon-862. This glassy polymer is considered as a potential candidate for matrix constituent for new designs for turbofan composite blade containment cases (BCC). BCCs have to contain a failed blade in case of a blade-out event and maintain its structural integrity while the jet engine is powered down. Such a catastrophic event may originate from a mechanical failure of from the ingestion of foreign objects, such as birds. When a blade impacts the can casing, complex triaxial states of stress and strains are expected in the area around the impacted site. Therein, strong gradients of thermomechanical fields, large deformations and damage are likely to take place. In particular, within the composite structure, both highly compressed regions and tensile dominant regions could be observed. Also, large deformations and strain localization may induce local variations of deformation rates with ballistic (dynamic) conditions at the location of impact. This blade-out event may occur any time during a BCC's life service and during a flight, during which variations of temperature in the BCCs are observed. Moreover, exposed to moisture and temperature cycles as well as other harsh environmental conditions, these BCCs are prone to aging.

NASA is developing a multiscale modeling methodology aiming at the design of

optimized composite structures. Experimentally verified physics-based models should be used in order to accurately predict the complex inelastic response observed in glassy polymers. Applied to the design of damage tolerant composite BCCs, the polymer model should capture the intrinsic response of the epoxy resin used as matrix. The intrinsic response of this epoxy resin, EPON 862, was characterized for conditions representatives of the ones in the case of a blade out event Poulain et al. (2010b,a). In this chapter, the capabilities of the model are challenged in light of experimental results and discuss the implications brought by the considerations of high strain rate conditions.

B. Macromolecular Model

The macromolecular model, detailed in this section, has been developed in (Chowdhury et al., 2006; Chowdhury, 2007; Chowdhury et al., 2008b). The total rate of deformation $\mathbf{D}$ is calculated from the addition of elastic and inelastic contributions $\mathbf{D}^{\mathrm{e}}$ and $\mathbf{D}^{\mathrm{p}}$ respectively. In particular, $\mathbf{D}^{\mathrm{e}}$ is represented in terms of the co-rotational rate of Cauchy stress through a hypoelastic law as:

$$\mathrm{D}^{\mathrm{e}}_{ij} = \mathrm{L}^{-1}_{ijkl} \overset{\nabla}{\sigma}_{kl} \tag{5.1}$$

where $\mathbf{L}$ is the point-wise tensor of elastic moduli given in terms of Young's modulus and Poisson's ratio. The flow rule is specified such that plastic deformation is incompressible, i.e.,

$$\mathrm{D}^{\mathrm{p}}_{ij} = \dot{\bar{\epsilon}}\, \mathrm{p}_{ij}, \quad \mathrm{p}_{ij} = \frac{3}{2\sigma_{\mathrm{e}}} \sigma'_{\mathrm{d}_{ij}} \tag{5.2}$$

where $\dot{\bar{\epsilon}}$ is the effective strain rate defined as:

$$\dot{\bar{\epsilon}} = \sqrt{\frac{2}{3} \left(\mathrm{D}^{\mathrm{p}'}_{ij} \right)^2} \tag{5.3}$$

with $\mathbf{X}'$ referring to the deviator of second-rank tensor $\mathbf{X}$, and σ_{e} is an effective stress defined by:

$$\sigma_{\mathrm{e}} = \sqrt{\frac{3}{2}\left(\sigma'_{\mathrm{d}_{ij}}\right)^2}, \qquad \sigma_{\mathrm{d}_{ij}} = \sigma_{ij} - \mathrm{b}_{ij} \tag{5.4}$$

in which $\boldsymbol{\sigma}_{\mathrm{d}}$ is the driving stress tensor and $\mathbf{b}$ the back stress tensor that describes the orientation hardening of the material. It evolves following:

$$\overset{\triangledown}{\mathrm{b}}_{ij} = \mathrm{R}_{ijkl}\mathrm{D}_{kl} \tag{5.5}$$

with $\mathbf{R}$ a fourth-order tensor, which is specified here by using a non-Gaussian network model (Wu and Van der Giessen, 1996) that combines the classical three-chain rubber elasticity model (Boyce et al., 1988) and the eight-chain model (Arruda and Boyce, 1993b), such that

$$\mathrm{R}_{ijkl} = (1-\kappa)\,\mathrm{R}^{\text{3-ch}}_{ijkl} + \kappa \mathrm{R}^{\text{8-ch}}_{ijkl} \tag{5.6}$$

where $\kappa = 0.85\bar{\lambda}/\sqrt{N}$, N is a material constant describing the average number of links between entanglements and $\bar{\lambda}$ is the maximum principal stretch, which is calculated based on the left Cauchy–Green tensor $\mathbf{B} = \mathbf{F}\cdot\mathbf{F}^T$, and

$$\mathrm{R}^{\text{8-ch}}_{ijkl} = \frac{1}{3}C^R\sqrt{N}\left[\left(\frac{\xi_c}{\sqrt{N}} - \frac{\beta_{\mathrm{c}}}{\lambda_c}\right)\frac{\mathrm{B}_{ij}\mathrm{B}_{kl}}{\mathrm{B}_{mm}} + \frac{\beta_{\mathrm{c}}}{\lambda_c}\left(\delta_{ik}\mathrm{B}_{jl} + \mathrm{B}_{ik}\delta_{jl}\right)\right] \tag{5.7}$$

where C^R is a material constant known as the rubbery modulus and

$$\lambda_c^2 = \frac{1}{3}\mathrm{tr}\mathbf{B}, \quad \beta_{\mathrm{c}} = \mathcal{L}^{-1}\left(\frac{\lambda_c}{\sqrt{N}}\right), \quad \xi_c = \frac{\beta_{\mathrm{c}}^2}{1-\beta_{\mathrm{c}}^2\mathrm{csch}^2\beta_{\mathrm{c}}} \tag{5.8}$$

where $\mathcal{L}^{-1}$ is the inverse Langevin function defined as $\mathcal{L}(x) = \coth x - \frac{1}{x}$.

The components of the three-chain model are given in terms of the principal total stretches λ_I with respect to axes pointing onto the principal stretch directions :

$$\mathrm{R}^{\text{3-ch}}_{IJKL} = \begin{cases} \frac{1}{3}C^R\sqrt{N}\lambda_I^2\left(\frac{\xi_I}{\sqrt{N}}+\frac{\beta_I}{\lambda_I}\right)\delta_{IK}\delta_{JL} & \text{if } \lambda_I = \lambda_J \\ \frac{1}{3}C^R\sqrt{N}\frac{\lambda_I^2+\lambda_J^2}{\lambda_I^2-\lambda_J^2}(\lambda_I\beta_I-\lambda_J\beta_J)\delta_{IK}\delta_{JL} & \text{if } \lambda_I \neq \lambda_J \end{cases} \tag{5.9}$$

where

$$\beta_I = \mathcal{L}^{-1}\left(\frac{\lambda_I}{\sqrt{N}}\right), \quad \xi_I = \frac{\beta_I^2}{1-\beta_I^2\mathrm{csch}^2\beta_I} \tag{5.10}$$

Strain rate effects are accounted for through a viscoplastic law giving the effective plastic strain rate $\dot{\bar{\epsilon}}$ in (5.2) as (Argon, 1973; Boyce et al., 1988):

$$\dot{\bar{\epsilon}} = \dot{\epsilon_0}\exp\left[-\frac{A\left(s-\alpha\sigma_h\right)}{T}\left(1-\left(\frac{\sigma_{\mathrm{e}}}{s-\alpha\sigma_h}\right)^m\right)\right] \tag{5.11}$$

where $\dot{\epsilon}_0$, m and A are material parameters, α is a factor describing pressure sensitivity, T is the absolute temperature, $\sigma_h = \mathrm{tr}\boldsymbol{\sigma}$ is the trace of Cauchy stress and s is a micro-scale athermal shear strength. Boyce et al. (1988) introduced strain softening effects through the state variable s. The evolution law for s (from its initial value s_0 to its current value s) is given by the following law:

$$\dot{s} = H_1(\bar{\epsilon})\left(1-\frac{s}{s_1}\right)\dot{\bar{\epsilon}} + H_2(\bar{\epsilon})\left(1-\frac{s}{s_2}\right)\dot{\bar{\epsilon}} \tag{5.12}$$

where s_1 and s_2 are adjustable parameters and $H_1(\bar{\epsilon})$ and $H_2(\bar{\epsilon})$ are smooth, Heaviside-like functions given by:

$$H_1(\bar{\epsilon}) = -h_1\left\{\tanh\left(\frac{\bar{\epsilon}-\bar{\epsilon}_p}{f\bar{\epsilon}_p}\right)-1\right\}; \quad H_2(\bar{\epsilon}) = h_2\left\{\tanh\left(\frac{\bar{\epsilon}-\bar{\epsilon}_p}{f\bar{\epsilon}_p}\right)+1\right\} \tag{5.13}$$

The updating of the back stress $\mathbf{b}$ is obtained using $\mathbf{b}_{t+\triangle t} = \mathbf{b}_t + \triangle t\dot{\mathbf{b}}$ with

$$\dot{\mathrm{b}}_{ij} = \overset{\triangledown}{\mathrm{b}}_{ij} - \mathrm{b}_{im}\mathrm{D}_{mj} - \mathrm{D}_{im}\mathrm{b}_{mj} \tag{5.14}$$

These constitutive equations have been implemented in a user-defined routine (UMAT) for ABAQUS-Standard. Objective space frames were used to model large

strains. As such, this macromolecular constitutive model had to be recast using a co-rotational formulation. Kweon and Benzerga (2010) details the general structure of the implementation method.

C. Material Parameter Identification

In this section, we provide some background on the method aiming at determining the material parameters entering the model, we depict the influence of these parameters on a typical stress–strain curve and we outline the procedure to be followed for their identification.

1. Background

Besides the mass density ρ and the elastic constants (E, ν), the material parameters to be identified are C^R, N (Eq. (5.7)), A, m, $\dot{\epsilon}_0$, α (Eq. (5.11)), s_0, s_1, s_2 (Eq. (5.12)), and h_1, h_2, f, $\bar{\epsilon}_{\rm p}$ (Eq. (5.21)). Since the functions H_1 and H_2 (Eq. (5.21)) behave like smooth step functions, the parameters h_1, f and $\bar{\epsilon}_{\rm p}$ have secondary effects.

Arruda et al. (1995) modeled the temperature dependence of the Young's modulus as:

$$\log \frac{E_{\rm ref}}{E(T)} = \beta(T - T_{\rm ref}) \tag{5.15}$$

where $T_{\rm ref}$ and $E_{\rm ref} \equiv E(T_{\rm ref})$ are reference values and β is a parameter. This equation involves two independent parameters. The above equation was also used by Chowdhury et al. (2008c) and has been adopted in this work as well.

The effects of temperature on the Young's modulus (the Poisson's ratio ν is taken as constant) is transferred to the athermal shear resistance parameters through the

shear modulus (Argon, 1973; Boyce et al., 1988):

$$\frac{s_0}{\mu} = \frac{0.077}{(1-\nu)}, \qquad \mu(T) = \frac{E(T)}{2(1+\nu)} \tag{5.16}$$

In the original macromolecular model, s_0 is associated with the peak stress at which inelastic deformation is assumed to set in. In the modified model, s_0 is associated with a "yield point" which occurs well before the peak. On the true stress–strain curve, this yield point is characterized by a yield stress $\sigma_{\rm y}$, defined as that level of stress beyond which unloading reveals a permanent strain after unloading[1]. On the true stress-strain curve, the true stress reaches successively the peak stress $\sigma_{\rm p}$ before the dip stress or lower yield stress $\sigma_{\rm d}$ when the state variable s is roughly equal to s_1 and s_2, respectively. The ratios s_1/s_0 and s_2/s_0 may be estimated from the ratios $\sigma_{\rm p}/\sigma_{\rm y}$ and $\sigma_{\rm d}/\sigma_{\rm y}$, respectively, and from α for a slightly better accuracy (Appendix 2).

The pressure-sensitivity parameter α is assessed based on experiments in which the amount of superposed hydrostatic pressure is varied. Experiments where an actual fluid pressure is superimposed on, say a tensile stress state have been carried out in the literature, e.g. on PMMA (Rabinowitz et al., 1970), but remain scarce. A more efficient method consists of using tension–compression asymmetry, the amount of pressure being different between the two. The assessment of α can be refined by adding one or more of the following tests: (i) a shear test (zero pressure); (ii) plane strain tension or compression; (iii) tests on round notched bars. α can be assessed at any stage of the deformation at fixed strain rate and temperature since α is considered

[1]Time-dependent recovery is ignored.

as constant throughout deformation. Writing the viscoplastic law (5.11) as

$$\sigma_{\mathrm{e}} = (s - \alpha\sigma_h)\left[1 - \frac{T}{A(s - \alpha\sigma_h)} \ln \frac{\dot{\epsilon}_0}{\dot{\epsilon}}\right]^{\frac{1}{m}} \tag{5.17}$$

the identification of α becomes straightforward at yield where (5.17) simplifies into:

$$\sigma_{\mathrm{e}}|_{\mathrm{yield}} = (s - \alpha\sigma_h)|_{\mathrm{yield}}$$

However, depending on the material and the magnitude of pressure-sensitivity, α may be estimated at the peak stress:

$$\sigma_{\mathrm{e}}|_{\mathrm{peak}} = (s - \alpha\sigma_h)|_{\mathrm{peak}} \tag{5.18}$$

Note that this approximation is not strictly rigorous regarding our interpretation of plastic flow taking place before the peak. Parameter α is the slope of the plot "von Mises effective stress" versus "σ_h" at peak. The more predominant effects of strain rate and temperature are, for some materials, more difficult to accurately represent. The viscoplastic constitutive law (5.11) encompasses coupling between temperature and strain-rate effects through a thermally activated process of segment rotation, as plastic flow starts when intermolecular resistance is overcome. Therefore, the rate-sensitivity parameters m, $\dot{\epsilon}_0$ and A may be assessed in tension or compression either by fixing the strain rate and varying the temperature or vice versa. The value $m = 5/6$ was derived by Argon (1973) and later used by Boyce et al. (1988) for PMMA. Our experience with model assessment against various experimental data indicates that this value is not universal. In particular, two observations were made: (i) the thermomechanical behavior of polymeric epoxies has not been modeled by the original model nor the modified one; (ii) representing both the low-to-moderate strain-rate and high strain-rate regimes with a single value of m is challenging even for thermoplastic materials.

However, considering m as a free parameter complicates the identification of the three related rate-sensitivity parameters. In the case of a fixed m, reducing data from a series of tests varying strain rate and at constant temperature is used to determine A and $\dot{\epsilon}_0$. Specifically, the viscoplastic law (5.11) is rearranged to be the equation of a line:

$$\ln \dot{\bar{\epsilon}} = B + C \left(\frac{\sigma_{\mathrm{e}}}{s - \alpha\sigma_h} \right)^m \tag{5.19}$$

where

$$\begin{aligned} B &= \ln \dot{\epsilon_0} - \frac{A}{T}(s - \alpha\sigma_h) \\ C &= \frac{A}{T}(s - \alpha\sigma_h) \end{aligned} \tag{5.20}$$

These equations in compression or tension are specialized at peak flow stress with $\sigma_{\mathrm{e}} = |\sigma_h| = \sigma_{\mathrm{p}}$ and $s = s_1$.

At this stage of identification, s_1 and α must already be known. Data is then gathered as $\ln \dot{\bar{\epsilon}}$ versus $\left(\frac{\sigma_{\mathrm{p}}}{s_1 \pm \alpha\sigma_{\mathrm{p}}} \right)^m$ plots[2] from which a fitting straight line is then drawn. The parameters A and $\dot{\epsilon}_0$ are calculated from the slope and intercept of this line, which are given by C and B, respectively (see Eq (5.20)).

Therefore, the triplet (m, A and $\dot{\epsilon}_0$) is unique only if m is known (from theory or a lower-scale molecular analysis). However, for any m when considered as an additional parameter, one can find by regression a given set of ($\dot{\epsilon}_0$, A) that best represents the strain rate sensitivity.

Thus, in the proposed identification procedure, besides the series of tests at constant temperature we also carry out a second series of tests at constant strain

[2]The sign in the denominator is a minus in tension and a plus in compression.

rate and varying temperature. From the second series, the relative difference between peak stresses $\Delta\sigma_{\rm p}/\Delta T$ is used as a target[3] to discriminate among all possible triplets (m, $\dot{\epsilon}_0$, A) that emerge from the first series of data.

Next, besides s_0, s_1 and s_2 which have been already discussed, the parameters h_1, h_2, f and $\bar{\epsilon}_{\rm p}$ enter the small-strain hardening/softening regime. Parameter h_1 determines the amount of hardening prior to peak stress whereas h_2 controls the rate of post-peak yield drop.

These parameters may be directed estimated from:

$$h_2 \approx \frac{s_2 - s_1}{\Delta\bar{\epsilon}} \left(\frac{1}{1 - \dfrac{s_1}{s_2}} \right); \qquad h_1 \approx \frac{s_1 - s_0}{\Delta\bar{\epsilon}} \left(\frac{1}{1 - \dfrac{s_0}{s_1}} \right) \tag{5.21}$$

where $\Delta\bar{\epsilon}$ corresponds to the plastic strain over which there is a yield drop (first equation) or a pre-peak yield increase (second equation). These equations, written so as to exhibit the temperature-independent ratios s_0/s_1 and s_1/s_2, suggest that the h_i values vary with temperature although they are here taken as independent of temperature.

Parameter $\bar{\epsilon}_{\rm p}$ corresponds to the effective plastic strain at peak flow and is extracted from the stress–strain curve as simply the total strain minus the elastic strain, the latter being estimated as $\sigma_{\rm p}/E$. The last parameter in this group, f, slightly adjusts the strain range over which the polymer behavior transition from hardening to softening.

Finally, the parameters N (number of rigid links between Entanglements) and C^R (rubbery modulus) affect the strain hardening at larger strains. The latter is

[3]This target value is a robust criterion because the measure $\Delta\sigma_{\rm p}/\Delta T$ of temperature sensitivity is nearly independent of strain rate and of the testing mode, tension or compression.

theoretically estimated from birefringence measurements(Boyce et al., 1988) as:

$$C^R = nkT \tag{5.22}$$

where T is the absolute temperature, k the Boltzmann's constant ($= 1.4{*}10^{-23} JK^{-1}$) and n is the number of chain segments per unit volume.

Alternatively, C^R may be approximated as the initial slope of the stress–strain curve resulting from a tensile or compression test conducted at a temperature T_{test} slightly above T_{g} and at a moderately rapid rate to minimize entanglement drift.

Values of C^R may be obtained at other temperatures in the glassy regime by rescaling, i.e.,

$$C^R(T) = C^R(T_{\text{test}})\,\frac{T}{T_{\text{test}}}. \tag{5.23}$$

Note that C^R may be directly assessed by fitting the slopes of experimental and computed stress-strain curves at large strains when the values inferred from Eq. (5.22) are inconsistent with the measured rate of strain hardening or when experimental measurements of $C^R(T_{\text{test}})$ and n are not available.

The parameter N represents the average number of links between entanglements. In polymers undergoing large-strain locking, N is estimated from the locking strain ϵ_{lock} through $\sqrt{N} = \exp \epsilon_{\text{lock}}$. However, thermosetting epoxies do not typically exhibit such behavior. In this case, depending on how C^R is obtained, N is either refined to fit experimental data at high strains or left free.

Theoretically, cyclic loading experiments may be used to identify N and C^R since the material undergoes significant kinematic hardening represented as back stress in the constitutive formulation.

The individual effects of parameters, which have already been introduced, are summarized in Fig. 30. The elastic constant E (as well as ν in plane strain conditions)

determines the initial slope of the elastic regime. The initial value of the athermal shear strength parameter s_0 controls yielding whereas s_1 and s_2 govern the peak stress and the saturation stress (or dip stress), respectively. $\bar{\epsilon}_p$ controls the strain at which the peak stress is reached. The parameters h_1 and h_2 determine the rate at which the peak stress and dip stress are reached, respectively. f affects the shape of the curve around peak. At large strains, C^R controls the hardening rate whereas N govern the strain locking beyond which the deformation remains elastic. The overall flow strength beyond yielding is affected by A, m, $\dot{\epsilon}_0$ and α.

2. Procedure

The identification procedure is rather straightforward. We first determine the temperature dependence of the elastic modulus. Thus, one series of data must correspond to various temperatures at a fixed strain rate. From a uniaxial stress–strain response at reference strain rate and temperature, a fit to the response near the peak yield determines $(s_0, s_1, s_2, h_1, h_2)$ whereas the large strain response is used to estimate N and C_R. Next, the pressure-sensitivity parameter α is determined based, for example, on tension–compression asymmetry[4]. Finally, A, $\dot{\epsilon}_0$ and m are assessed based on two series of data where temperature and strain rate are varied independently.

A detailed procedure must be followed to identify each parameter:

1. First, multiple realizations of tension or compression tests where temperature is varied at fixed strain rate should be carried out. The initial slopes of the resulting stress–strain curves should be collected and averaged from which the slope β (Eq. (5.15)) of $\log E$–T plots are extracted. The temperature dependence

[4]The mechanical behavior of a polymer loaded in tension is different than in compression (e.g. the peak stress is greater in compression than in tension)

of Young's modulus is specified using T_{ref} usually taken as room temperature and the corresponding elastic modulus E_{ref} (Eq. (5.15)). The Poisson's ratio is considered as constant.

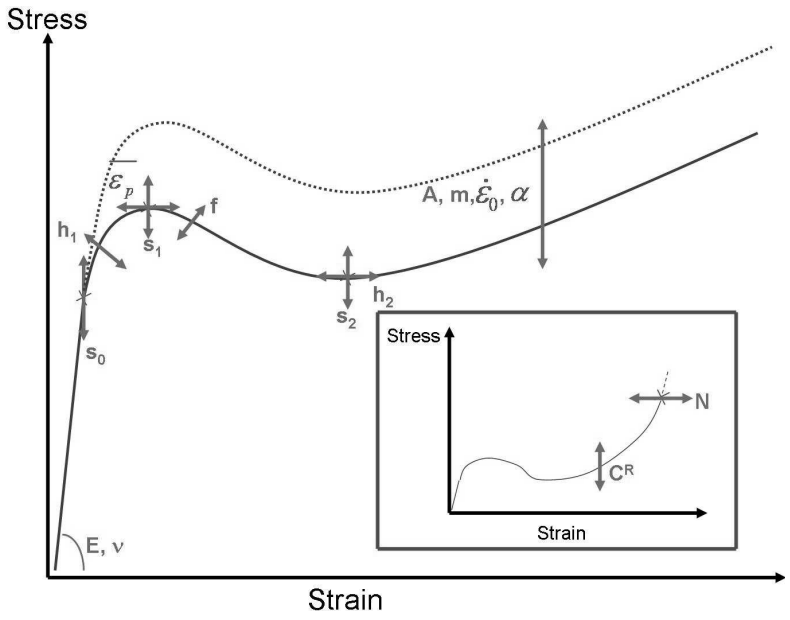

Fig. 30. Representation of the effect of individual material parameter on the material response

2. Determine the initial shear resistance s_0 using Eq. (5.16). Since the ratio s_0/E is temperature independent, this step, which must come after step 1 above, may be done for one value of T within the series of data of step 1.

3. A series of tests varying the amounts of hydrostatic stress should be carried out, e.g., compression, tension, and shear at fixed strain rate and temperature. Flow stress values at the peak should be extracted and α is extracted from the slope of a linear line fitting to the plots of $\sigma_{\text{e}}|_{\text{peak}}$ versus $\sigma_h|_{\text{peak}}$.

4. The flow resistances s_1/s_0 (peak) and s_2/s_0 (saturation) are determined based on the ratios $\sigma_{\text{p}}/\sigma_{\text{y}}$ and $\sigma_{\text{d}}/\sigma_{\text{y}}$, which are directly extracted from a stress-

strain curve for one test condition[5]. A more accurate estimate is obtained from Eqs. (A.2) and (A.3) (see Appendix). If the latter method is used, this step must come after step 3 above.

5. Determine h_1 and h_2 (Eq. (5.21)) by recording the range of plastic strain over which there is hardening (from σ_{y} to σ_{p}) and softening (from σ_{p} to σ_{d}) in the same test condition used in steps 2 and 4.

6. A series of data (compression or tension) should be available where the strain rate $\dot{\epsilon}$ is varied while temperature is fixed. Make plots of $\ln \dot{\epsilon}$ versus $\left(\dfrac{\sigma_{\mathrm{p}}}{s_1 \pm \alpha \sigma_{\mathrm{p}}} \right)^m$ using data at peak stress and the values of s_1 and α assessed in steps 3 and 4. The exponent m may be sought in the interval 0.1–0.83 with increments of 0.1. For each value of m, Eqs. (5.19)–(5.20) are used to extract the parameters A and $\dot{\epsilon}_0$.

7. The relative difference between peak stresses, $\Delta\sigma_{\mathrm{p}}/\Delta T$ is extracted from the series of data where temperature is varied (step 1). Use that value as a criterion to discriminate among all possible rate-sensitivity parameters triplets (m, $\dot{\epsilon}_0$, A) that emerge from the previous step.

8. Estimate the rubbery modulus C^R from the number of chain segments per unit volume n obtained in the literature using Eq. (5.22). Alternatively, a single test at T just above T_{g} and a moderately high loading rate should be available. C^R is then extracted as the initial slope of the stress–strain curve. Its temperature dependence is inferred from Eq. (5.23). Otherwise, C^R should be calibrated on the large strain hardening of a stress–strain curve in tension.

---

[5]To each value of the temperature will correspond actual values of s_1 and s_2. However, the ratios s_1/s_0 and s_2/s_0 are independent of T as is the ratio s_0/E.

9. If the locking stretch is not reached in the experiments take the average number of rigid links between entanglements N as a free parameter. If C^R is obtained from measurements, calibrate N based on the large strain hardening of a tensile stress–strain curve.

10. Improve the quality of the fit to the stress–strain curve around the peak stress by adjusting the parameters $\bar{\epsilon}_p$ and f. This can only be done by running actual simulations using material parameters from the previous steps. The default value of $\bar{\epsilon}_p$ is the amount of plastic strain at peak flow; see text after Eq. (5.21). The default value of f is 0.1.

D. Model Calibration and Assessment Applied to EPON 862

The material parameters of the macromolecular model have been identified for EPON 862 following the standard procedure detailed in Section C. The experimental data for this thermosetting epoxy, which are reported in Poulain et al. (2010b) and Poulain et al. (2010a) (based on a previous study by Littell et al. (Littell et al., 2008)), were divided into (i) a calibration set and (ii) an assessment set. The former set was used to identify the material parameters whereas the latter was used to estimate the model predictive capabilities. Specifically, the material parameters were identified based on the following experiments (from the "calibration set"):

- A series of data in tension at a fixed strain rate ($\dot{\epsilon} = 10^{-3}$/s) over a range of temperatures (three values of T: 25°C, 50°C and 80°C).

- A series of data in compression at various levels of strain rate (10^{-5}/s, 10^{-3}/s, 10^{-1}/s, and $\approx 10^{3}$/s) at a fixed temperature (25°C).

- Data in shear and tension at $\dot{\epsilon} = 10^{-1}$/s and $T = 25$°C.

The resulting values for the main material parameters are gathered in Table VI. Two sets of parameter values are included: set QS comprises the values obtained when test data at high loading rates is ignored while set D refers to the values obtained using all data in the calibration set. These values were derived from a specialization of each step of the standard procedure:

1. The first series of data in tension was used to assess the temperature dependence of the elastic modulus. E was determined as the slope of a line which best fits with the experimental stress-strain curve in the range of strain 0 to 0.01. The resulting values for E_{ref}, T_{ref} and β (see Eq. (5.15)) are reported in Table VI. Since the parameter β is the slope of a line in a semi-log plot, the uncertainty on it is quite important. Littell (2008) did not provide the dispersion around the mean values of the elastic modulus at the three temperatures studied. Here, differences up to 200 MPa were observed between a re-estimate of the mean value of E and values given by Littell. The actual mean was then averaged over the two estimates by the two independent operators and the scatter around the mean was determined (see Fig. 31). With that as basis, the final values that are consistent with Table VI are as follows. At the highest temperature ($T = 80°\text{C}$) we used the mean plus one dispersion. At the intermediate temperature ($T = 50°\text{C}$) we used the mean value. At the lowest temperature ($T = 25°\text{C}$) we used the mean minus one dispersion. The temperature dependence of the flow stress was best represented by these bounds.

2. The initial shear resistance s_0 at T_{ref} was inferred from the value of $E_{\text{ref}} = E(T_{\text{ref}})$ (Eq. (5.16)). The same ratio s_0/E was used at other temperatures.

3. α was identified from the third series of data in the calibration set (Figure 32). The value reported in Table VI does not included shear test data.

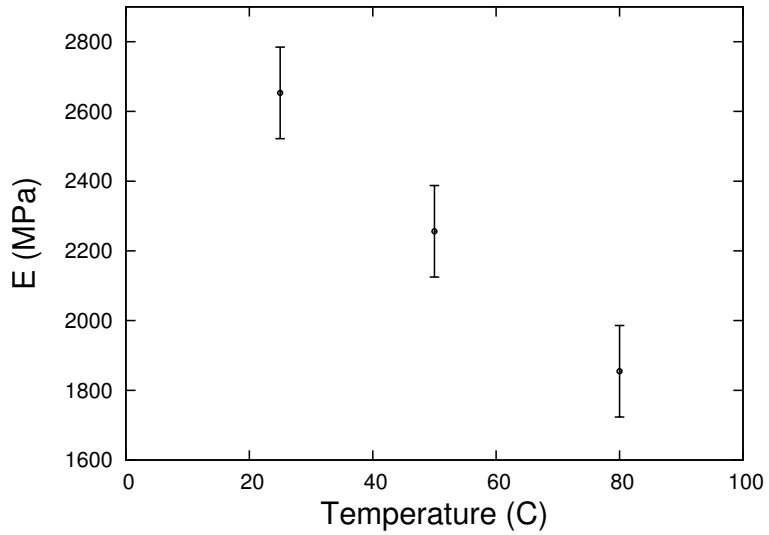

Fig. 31. Experimental values of Young's modulus versus the test temperature. All measurements correspond to the first series of data in the calibration set (tension at $\dot{\epsilon} = 10^{-3}/\mathrm{s}$).

4. A variant of this step of the standard procedure had to be implemented. Indeed, stress–strain curves in compression exhibit a clear post-peak strain softening whereas a plateau is observed in tension. Since the corresponding ratios $\sigma_\mathrm{p}/\sigma_\mathrm{y}$ and $\sigma_\mathrm{d}/\sigma_\mathrm{p}$ depend on the loading mode (Table VII), s_1 and s_2 were identified based on average values. For compression (respectively tension) the data reported in Table VII are part of the second (respectively third) series in the calibration set at $T = 25°\mathrm{C}$ and $\dot{\epsilon} = 10^{-1}/\mathrm{s}$.

5. As in the previous step, the parameters h_1 and h_2 are determined from averaged values between compression and tension and the values of $\Delta\bar{\epsilon}$ for use in Eq. (5.21) are reported in Table VII with superscripts 1 and 2 for h_1 and h_2, respectively.

6. Rate-sentivity parameters m, $\dot{\epsilon}_0$ and A (iteration 1):

   Their identification is based on the second series of data of the calibration set

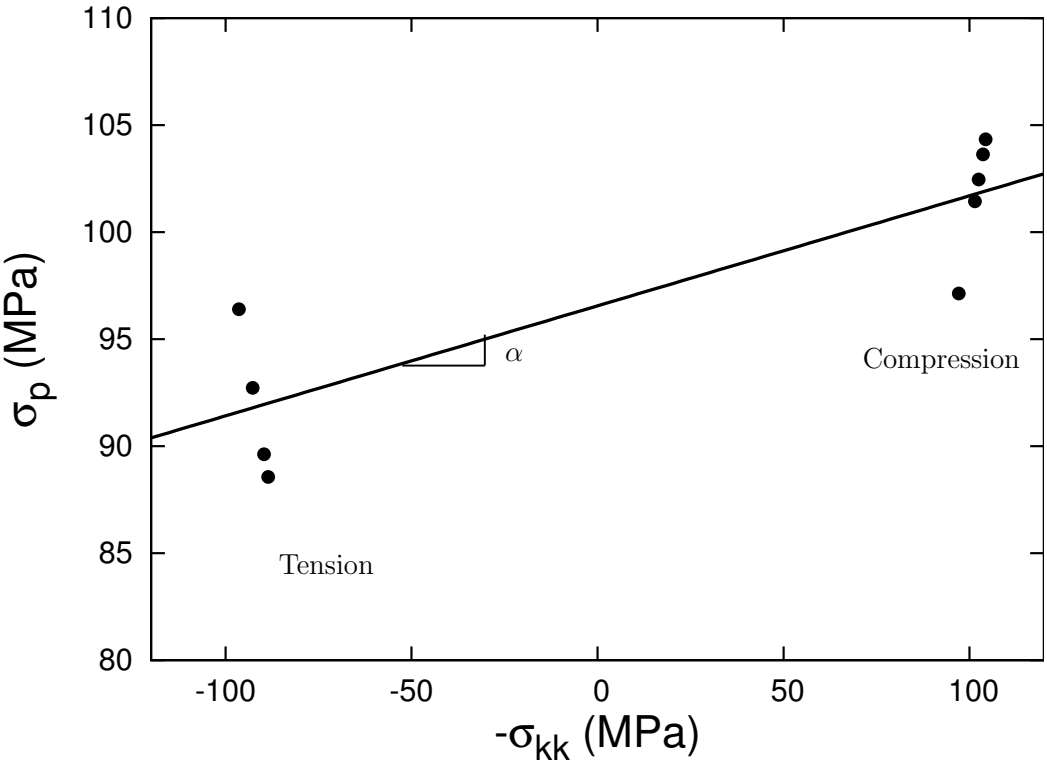

Fig. 32. Experimental plots of $\sigma_{\mathrm{e}}|_{\mathrm{peak}}$ versus $\sigma_h|_{\mathrm{peak}}$ used to determine α.

(compression at various levels of strain rate). For each value of m, the couple ($\dot{\epsilon}_0$, A) was obtained by data reduction on plots of $\ln \dot{\epsilon}$ versus $\left(\dfrac{\sigma_{\mathrm{p}}}{s_1 \pm \alpha\sigma_{\mathrm{p}}}\right)^m$. Such a plot is depicted in Fig. 33 in the case of $m = 0.5$ for both parameter sets QS and D. The resulting values of $\dot{\epsilon}_0$ and A are reported in Table VI.

7. Parameters m, $\dot{\epsilon}_0$ and A (iteration 2):

   From the first series of data (see step 1 above), we find $\Delta\sigma_{\rm p} \approx 35$ MPa for $\Delta T = 55$ K[6] at the two extreme temperatures. Here, numerical simulations were carried out to find the value m which leads to the best representation of this difference in peak stresses. These simulations, which were performed with values for material parameters deduced from steps 1–6, default values for $f = 0.1$ and $\bar{\epsilon}_{\rm p} = 0.054$, and pre-assigned values for C^R and N[7] result in an optimal value for m found as $m = 0.5$.

8. Since the number of chain segments per unit volume is not known for EPON 862 and no experiment was carried out at a temperature slightly above $T_{\rm g}$, C^R was calibrated based on the large strain hardening response, averaged from compression and tension data at $\dot{\epsilon} = 10^{-1}$/s and $T = 25°$C.

9. Parameter N:

   For E862 material, strain locking was not clearly observed in the range of strains studied. A value for $N = 7$ was taken, based on the assumption that locking would occur at a stretch around $\lambda_{\rm lock} = 1$.

10. A standard value for parameter $f = 0.1$ and $\bar{\epsilon}_{\rm p} = 0.054$ were used.

[6]Remarkably, this difference is nearly the same at other strain rates, both in tension and compression.

[7]The influence of both N and C^R at peak stress is secondary.

Table VI. The material parameters entering the deformation model.

Material parameter	Units	Description	Eqns	Set QS	Set D
ρ	kg/m^3	mass density	(–)	1200	1200
E_{ref}	GPa	modulus at T_{ref}	(5.15)	2.6	2.6
T_{ref}	K	reference temperature	(5.15)	298	298
β	1/K	temperature dependence	(5.15)	0.002	0.002
ν	—	Poisson's ratio	(5.16)	0.4	0.4
s_0/E	—	initial shear strength	(5.12)	0.046	0.046
s_1/s_0	—	pre-peak strength	(5.12),(5.21)	1.19	1.19
s_2/s_0	—	saturation strength	(5.12),(5.22)	1.09	1.09
h_1	MPa	pre-peak hardening	(5.21),(5.21)	3000	3000
h_2	MPa	rate of yield drop	(5.21),(5.21)	900	900
$\bar{\epsilon}_{\text{p}}$	—	peak plastic strain	(5.21)	0.054	0.054
f	—		(5.21)	0.1	0.1
α	—	pressure-sensitivity	(5.11),(5.17)	0.05	0.05
m	—	rate-sensitivity	(5.11),(5.19)	0.5	0.5
$\dot{\epsilon}_0$	s^{-1}	rate-sensitivity	(5.11),(5.20)	4.3E5	1.7E1
A	1/K	rate-sensitivity	(5.11),(5.20)	173.8	74.0
C^R	MPa	rubbery modulus	(5.7),(5.22),(5.23)	15	15
N	—	number of rigid links	(5.7),(5.8)	7	7

(a)

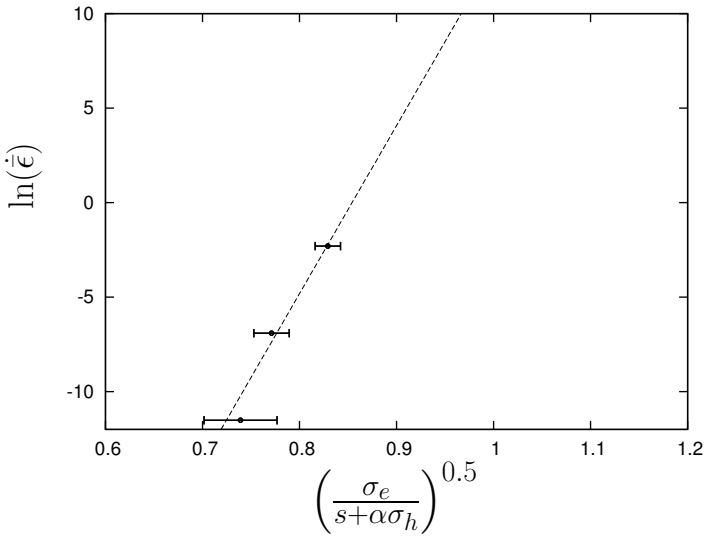

(b)

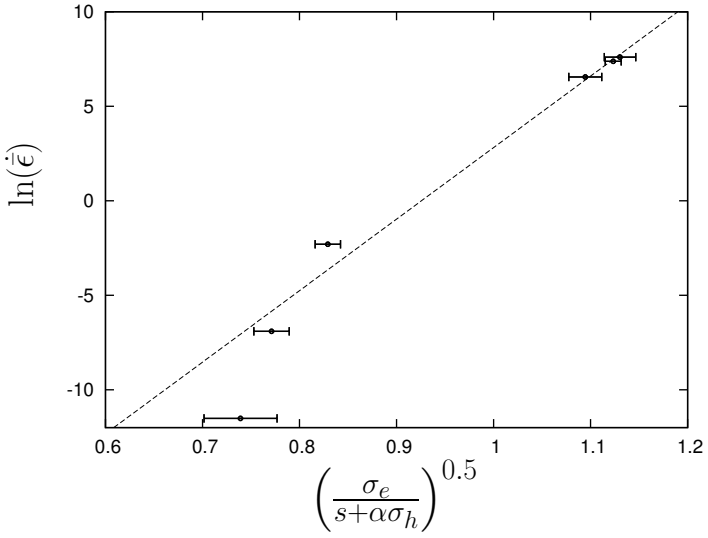

Fig. 33. Strain rate versus intermolecular resistance plots used to determine the rate-sensitivity parameters A and $\dot{\epsilon}_0$ for $m = 0.5$ using compression data at 25C. (a) using low-rate data only (set QS); (b) using all data (set D).

Table VII. Experimental values used in steps 4 and 5 for the determination of small--strain hardening/softening parametrs. Data at $T = 25°\mathrm{C}$ and $\dot{\epsilon} = 10^{-1}/\mathrm{s}$.

	σ_y	$\sigma_\mathrm{p}/\sigma_\mathrm{y}$	$\sigma_\mathrm{d}/\sigma_\mathrm{p}$	s_1/s_0	s_2/s_1	$\Delta\bar{\epsilon}^{(1)}$	$\Delta\bar{\epsilon}^{(2)}$	h_1	h_2
Tension	74.4	1.23	0.98	1.23	0.98	0.0506	0.1	2800	1300
Compression	88.8	1.14	0.85	1.14	0.85	0.0445	0.263	3200	500
Average	81.6	1.19	0.92	1.19	0.92	0.0476	0.1815	3000	900

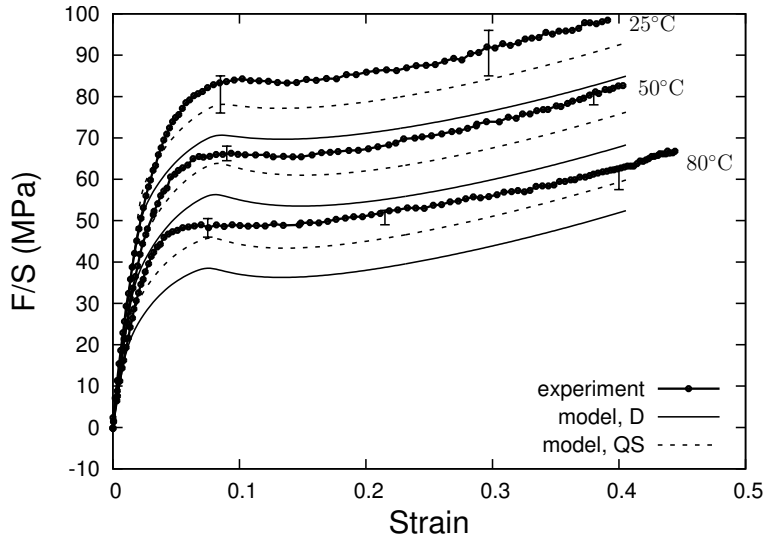

Fig. 34. Verification of the model identification procedure. Computed versus experimental stress–strain responses. Effect of temperature in tension at $\dot{\epsilon} = 10^{-3}/\mathrm{s}$ using calibration sets QS and D.

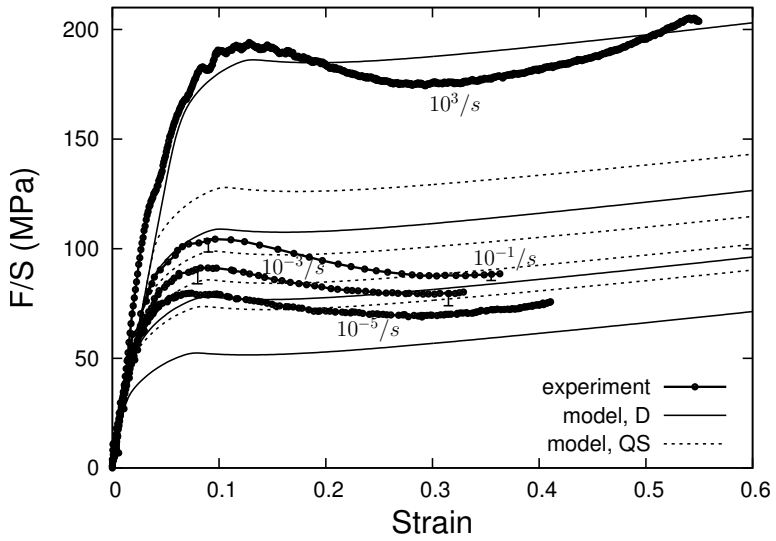

Fig. 35. Verification of the model identification procedure. Computed versus experimental stress–strain responses. Effect of strain rate in compression at $T = 25°\text{C}$ using calibration sets QS and D.

The outcome of this procedure is the set of parameters reported in Table VI. The use of the high strain-rate experimental data for the identification of material parameters results in different values for A and $\dot{\epsilon}_0$ for set D in comparison with set QS. Among all material parameters, the identification of m, f, $\bar{\epsilon}_{\text{p}}$, N and C^R was based on the fit of stress-strain curves between experiments and numerical simulations although the two latter parameters can be theoretically determined from experiments, when available.

In order to verify the efficiency of the identification procedure, numerical simulations were performed with the assessed material parameters and their results were compared with experimental data of the calibration set.

The quality of the calibration of temperature-sensitivity, rate-sensitivity and pressure-sensitivity can be appreciated from Figs. 34, 35 and 36, respectively. The comparison is shown for both the set of data 'D', which includes data at all strain

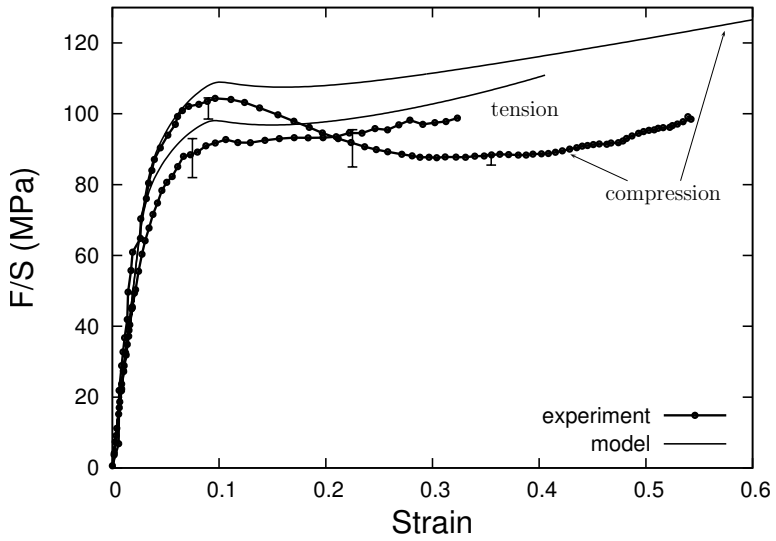

Fig. 36. Verification of the model identification procedure. Computed versus experimental stress–strain responses. Effect of pressure at $T = 25°\text{C}$ and $10^{-1}/\text{s}$ using calibration set D.

rates, and set 'QS', which excludes the high strain-rate data. All comparisons include scatter bars on measured stresses.

First, consider calibration using data set QS. A peak stress shift of about 35 MPa (Fig. 34) suggests a very good calibration of the temperature sensitivity[8]. As illustrated in Fig. 35, the strain-rate sensitivity is also very well represented in the low-to-moderate strain rate regime. However, the simulations underestimate the stresses at the high loading rate.

Next, consider calibration using the D data set. As for QS data set, the temperature effect on the peak stress shift is very well captured; however, all stress levels are shifted down, Fig. 34. This can be explained by analyzing Fig. 35. When the high rate data is accounted for in calibrating the model, the predictions of the lower

[8]Since the identification procedure was also performed based on compression data, the computed curves exhibit some amount of post-peak softening.

strain rate data deteriorate. If the high rate data were only revealing the strain-rate sensitivity of the material, then this discrepancy would uncover an inherent limitation of the viscoplastic flow rule used in the model. It is not possible to capture strain rate effects over 8 decades with the same set of material parameters, unless part of the stress increase in the high rate data results from purely dynamic effects, and not solely from intrinsic rate-sensitivity. As shown in Fig. 35 the stresses measured at strain rates lower than 10^{-3}/s are underestimated. On the other hand, stress levels are very well calibrated for strain rates between 10^{-1}/s and 10^{3}/s. Practically, this finding suggests that the set of material parameters QS may be used in quasi-static calculations whereas the set D can be used in impact or other high-rate calculations. Finally, the effect of pressure-sensitivity (more precisely, tension–compression asymmetry) is also well captured, Fig. 36.

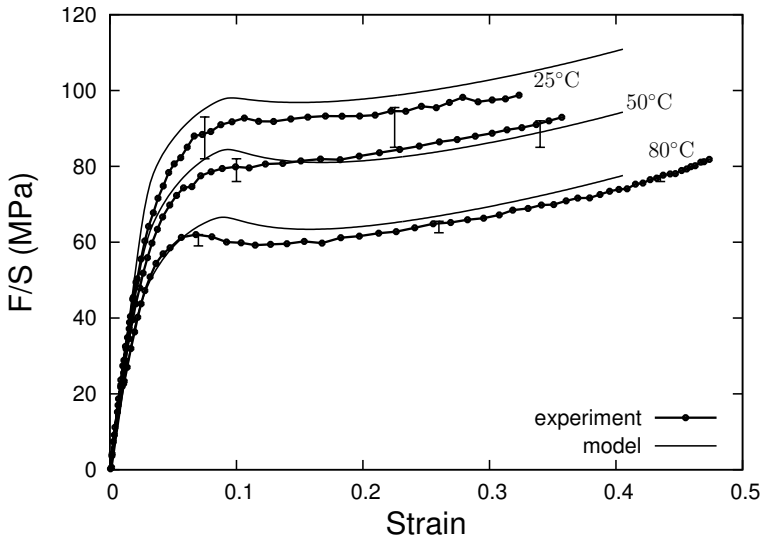

Fig. 37. Predicted versus experimental stress–strain responses. Effect of temperature in tension at $\dot{\epsilon} = 10^{-1}$/s using calibration set D.

Now, the model predictions can be compared with experimental data which have not been used for the material parameters calibration. The following experimental

data belong to the "assessment set":

- A second series of data in tension at a fixed strain rate ($\dot{\epsilon} = 10^{-1}$/s) over a range of temperatures (three values of T: 25°C, 50°C and 80°C).
- Data in tension at $T = 25$°C and $\dot{\epsilon} = 10^{-5}$/s.
- A second series of data at two levels of strain rate (10^{-3}/s and 10^{-1}/s) in compression at a fixed temperature (50°C).
- A third series of data at two levels of strain rate (10^{-3}/s and 10^{-1}/s) in compression at a fixed temperature (80°C).

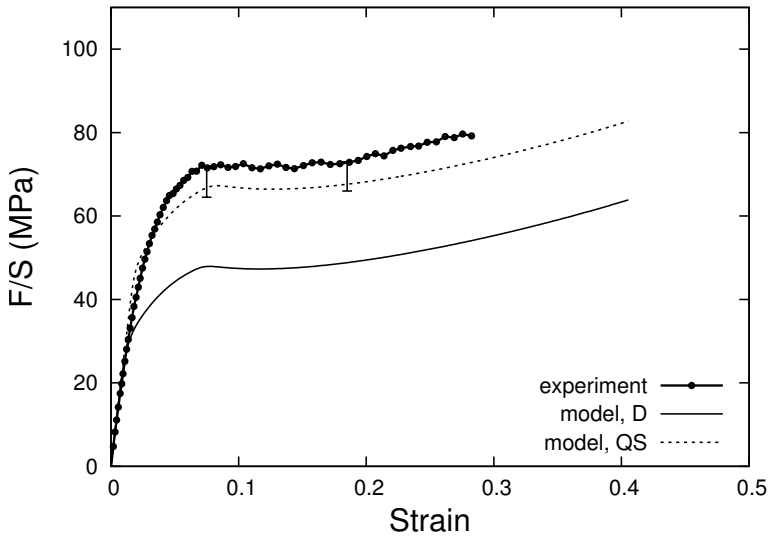

Fig. 38. Predicted versus experimental stress–strain responses. Tension at 25°C and $\dot{\epsilon} = 10^{-5}$/s using calibration sets QS and D.

As illustrated in Figure 37, the prediction of temperature sensitivity is excellent with the set of material parameters D. Not shown here, a similar temperature sensitivity is obtained with set QS but the stress levels are slightly shifted down. Note that data at the lower strain rate of 10^{-3}/s were used to calibrate temperature sensitivity

(see Fig. 34). Since the strain rate is higher, the set D provides better predictions than in Fig. 34.

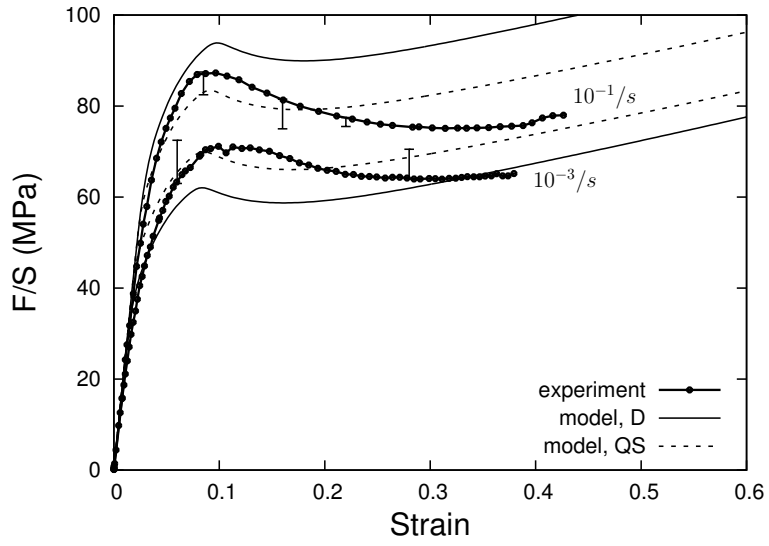

Fig. 39. Predicted versus experimental stress–strain responses. Effect of strain rate in compression at $T = 50°$C using calibration sets QS and D.

Figure 38 shows the model prediction for the only tension data available at $\dot{\epsilon} = 10^{-5}$/s. The prediction is excellent using parameter set QS. With set D the stresses are underestimated, as expected. Once again, that is the tradeoff for representing well the high strain-rate data with parameter set D.

Next, consider the compression data. Figures 39 and 40 show that the strain-rate sensitivity is extremely well predicted using parameter set QS and fairly well represented using set D for both temperatures 50C and 80C.

E. Conclusion

The capabilities of a variant of the macromolecular model was tested based on experimental results on an epoxy resin. These tests were performed in tension and compression, at temperatures varying from room temperature to 80°C, and strain

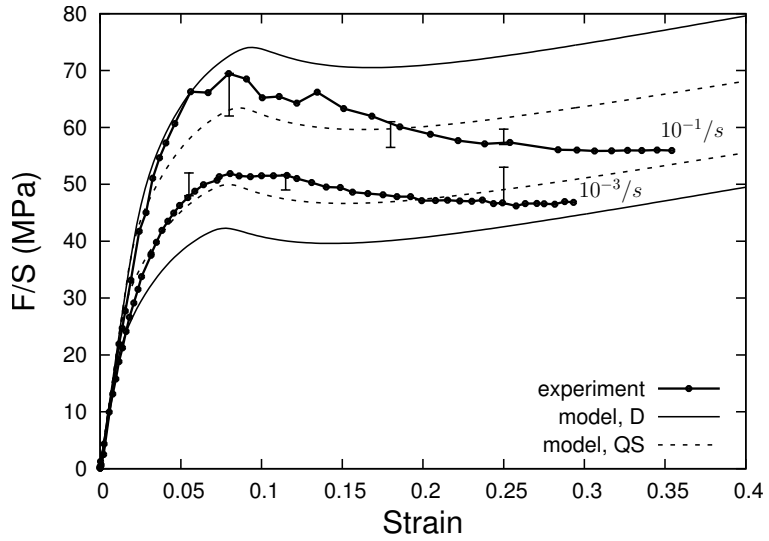

Fig. 40. Predicted versus experimental stress–strain responses. Effect of strain rate in compression at $T = 80°C$ using calibration sets QS and D.

rates ranging from 10^{-5}/s (quasi-static conditions) to 10^{3}/s (dynamic conditions). The identification of material parameters entering the polymer model was discussed in a previous chapter. Here, the same procedure was followed although two sets of experiments for parameter identification were considered. The first set of experiments (QS) corresponds to experiments performed at low to moderate strain rates. This is the same case as discussed in a previous chapter. For this case, experiments at high strain rates enable to test the predictive capabilities of the model. The second set (D) encompasses experiments at all strain rates. For this case, the efficiency of the calibration can be tested, and consequences regarding the model predictive capabilities may be discussed. Results showed that with the set (QS), the model captures well the epoxy response in quasi-static conditions, as discussed in a previous chapter. However, the response at high strain rate is largely underestimated. The model does not capture the high strenghtening associated with the transition from low to high strain rates. With the set (D), all trends are captured since the material parameters

was identified based on the whole range of strain rates. However, a degradation of calibration is observed for low strain rates data. due to the high strengthening in dynamic conditions. Indeed, the model consistently underestimates the strength at low rates. The temperature sensitivity is not affected. Therefore, the model does not have all the ingredients to model the response of polymer glasses for a strain rate range of 8 decades. Parameter identification based a large range of strain rates would favor good predictions at larger strain rates, which would be adequate for impacting problems. However, an identification limited on low rate data would enhance accuracy in predictions at low strain rates and underestimate the strength for polymers dynamically loaded.

CHAPTER VI

FLOW LOCALIZATION IN POLYMERS AT FINITE STRAINS

A. Introduction

In interpreting the experimental data, the best care was taken to extract the assumely intrinsic behavior of the material through an appropriate choice of specimen-level and/or local stress and strain measures. To that end use of DIC and video-based extensometry was quite helpful. Another approach to the problem of material parameter identification consists of formulating an inverse problem. Once implemented in a finite-element software, the macromolecular model can be used to simulate the behavior of complex specimen geometries, including the tensile and compressive response of full, initially smooth bars. This enables a detailed analysis of possible localization patterns associated with both geometric and material nonlinearities, as well as the dynamic versus quasi-static behavior. Once the full specimen is simulated, mechanical fields can be analyzed just like in the experiments. Thus, in principle, one could optimize the identification of material parameters based on the structural response obtained in the experiments and simulations. This constitutes an inverse problem.

While this method is in general appealing, this chapter does not focus on the inverse indentification procedure as much as it does on general features of the localized response, as it is affected by boundary conditions, type of loading and choice of material parameters. Some comparisons with experimental data are offered for the sake of discussion. The localized response under plane strain conditions is investigated in detail using a fully transient formulation first initiated in Chowdhury (2007) and further developed here to account for thermal softening effects. The plane strain

results are compared with those obtained using a quasi-static formulation which was implemented in Abaqus as a user defined subroutine (UMAT) developed by Kweon and Benzerga (2010). Finally, some analyses are carried out under axisymmetric conditions using the same quasi-static formulation.

Accounting for geometric nonlinearities requires a finite strain framework. The material nonlinearity is readily accounted for using the macromolecular model. Thus, this framework has the necessary ingredients to investigate the onset and propagation of flow localization. Bifurcation phenomena such as necking and shear banding have been investigated in the past decades, mainly in the context of ductile fracture of metals Benzerga et al. (2002). The loss of stability of the plastic flow with J_2 flow theory may originate from porosity induced softening. Hadamard (1903); Hill (1962); Mandel (1966) showed that bifurcation into a localized shear band initiates concurrently with the loss of ellipticity of the equations which govern equilibrium. Bifurcation analysis were performed on porous plastic materials which exhibit isotropic behavior (Leblond, 1994) and anisotropic response (Kailasam and PonteCastaneda, 1998). In view of these results, and considering the post-peak softening and large strain anisotropic hardening which has been implemented in the intrinsic response of EPON 862 from the identification procedure, simulations of experiments on full specimen are expected to show some level of localization.

B. Description of the Numerical Simulations

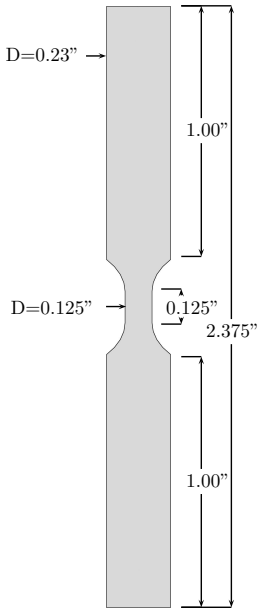

Fig. 41. Geometry and dimensions of the cylindrical specimen used by Littel et al. Littell et al. (2008) in tension and compression testing.

This constitutive model has been implemented in two separate finite-element codes. The first one is a dynamic code for transient, two-dimensional analyses (plane strain or plane stress). Large strain behavior is modeled using a convected representation of finite-strain plasticity. The general structure of the code and implementation details may be found in Appendix Sec. ; also see Ref. Chowdhury et al. (2008b) for numerous examples of boundary-value problem solutions. This code has been augmented to account for thermomechanical couplings, which are relevant to high rate loadings such as impact. In the augmented code, temperature is treated as a field variable. The constitutive updating associated with this modification is reported in Appendix Sec. . The second code is a user-defined routine (UMAT) for ABAQUS-Standard. It can only be used for quasi-static analyses but can be used to solve a

variety of three-dimensional problems. The general structure of the implementation method is provided in Appendix Sec. ; also see Ref. Kweon and Benzerga (2010). Here, large strains are modeled within objective space frames. Implementation of the macromolecular model as a UMAT thus requires to recast the constitutive equations using a co-rotational formulation (Appendix Sec.).

1. Quasi-static Calculations in Plane Strain Conditions

These computations cannot be compared quantitatively with experimental results from the previous section since the calculations have been carried out using a dynamic formulation (see Appendix) under assumed plane strain conditions. Finite element simulations were performed based on the geometry of the test specimen (Fig. 41). First, a quadrant was discretized. Then, a double folded symmetry was performed to generate the full meshed geometry. In order to simulate testing in tensile and compressive conditions, a constant vertical displacement rate was prescribed to the nodes located at the top surface. No vertical displacement of nodes at the bottom surface was allowed. Traction free conditions were enforced for lateral surfaces such that deformation induced contraction (in tension) and expansion (in compression) were permitted. Finally, all rigid body motions were suppressed. Figure 42 depicts the finite element mesh used in the computations.

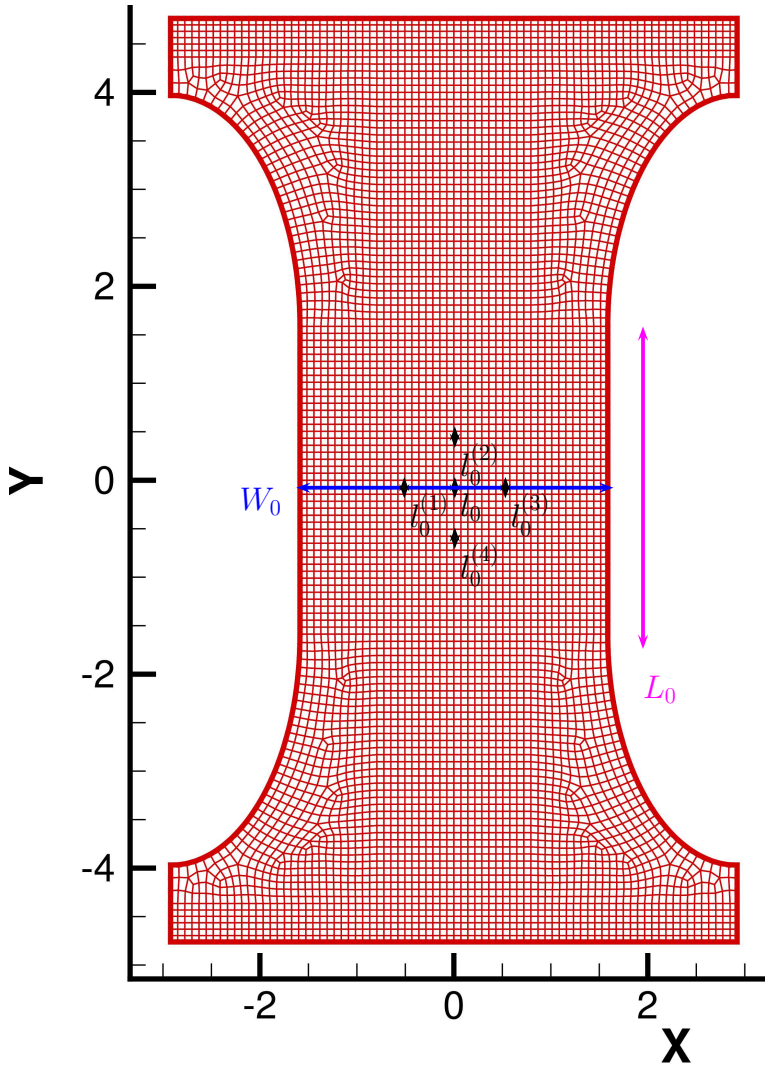

Fig. 42. Undeformed mesh of the specimen used in the experiments.

When plastic instabilities (necking and barrelling) are simulated, the same care taken in analyzing experimental data has to be taken here in extracting meaningful measures of specimen-level stresses and strains (see Figure 42). Let L and W denote the current gauge length and current width of the minimal (or maximal) section. Also, let l denote the current length of an element located at the center of the specimen. The following logarithmic strain measure is defined as the counterpart of measure ε in Eq. (2.3)[1]:

$$\varepsilon = \ln \frac{S_0}{S} = \ln \frac{W_0}{W} \tag{6.1}$$

In addition, a local strain may be defined over an element located at the center of the specimen:

$$\epsilon_{22}^{\text{local}} = \ln \frac{l}{l_0}, \tag{6.2}$$

As the counterpart of the experimental measure, $\bar{\epsilon}_{22}$ is defined as:

$$\bar{\epsilon}_{22} = \frac{1}{5}\left(\ln \frac{l}{l_0} + \ln \frac{l^{(1)}}{l_0^{(1)}} + \ln \frac{l^{(2)}}{l_0^{(2)}} + \ln \frac{l^{(3)}}{l_0^{(3)}} + \ln \frac{l^{(4)}}{l_0^{(4)}} \right) \tag{6.3}$$

For comparison purposes, we also define an axial strain defined as

$$\epsilon_{22}^{\text{global}} = \ln \frac{L}{L_0}, \tag{6.4}$$

The true stress in the minimal/maximal cross section is defined as

$$\sigma = \frac{F}{W}, \tag{6.5}$$

In all of these definitions, the subscript 0 refers to initial values. All simulations and experiments correspond to $T = 50°\text{C}$ and a strain rate of $10^{-1}/\text{s}$.

---

[1]Note that the factor 2 is dropped here because the out-of-plane deformation is nil.

2. Dynamic Calculations in Plane Strain Conditions

In a previous chapter it was concluded that it is impossible to calibrate the constitutive model so that it represents low strain-rate data and high strain-rate data equally well. Two hypotheses can be formulated to explain this discrepancy. Hypothesis 1 consists of associating the discrepancy with an inherent limitation of the model. It would be fully justified if the stress increase observed in the high loading rate experiment is solely due to an intrinsic strain-rate sensitivity. However, such data are obtained from a split hopkinson bar (SHB) test, which is by no means an isothermal test. In addition, a contribution to the stresses may come from purely dynamic effects, i.e., due to stress waves. Furthermore, the SHB test is quite difficult to conduct in the laboratory. For example, the errors on the initial stiffnesses can be huge, as is the case under tensile loading (see Fig. 27a). Thus, Hypothesis 2 consists of associating the above mentioned discrepancy with dynamic effects, including possible experimental errors caused by them.

In such experiments, the inertial term is no longer negligible. Instead, it induces dynamic effects which manifest in the polymer response in the form of stress waves. The onset of plasticity leads to a rapid damping of the waves so that the load versus displacement curve may not exhibit strong oscillations. However, at small strains, the apparent stiffness is higher than the actual one. Figure 43 illustrates this behavior for the compression data already shown in Fig. 12 but within a narrower strain window. Clearly, if the initial stiffness is reduced to that of the simulations, the discrepancy between calibrated and measured stress–strain curves would be significantly reduced.

In principle, these dynamic effects can be quantified using a transient analysis of the SHB test. Since the large deformations measured in polymers loaded at high strain rates are accompanied by a substantial rise of temperature, a full thermome-

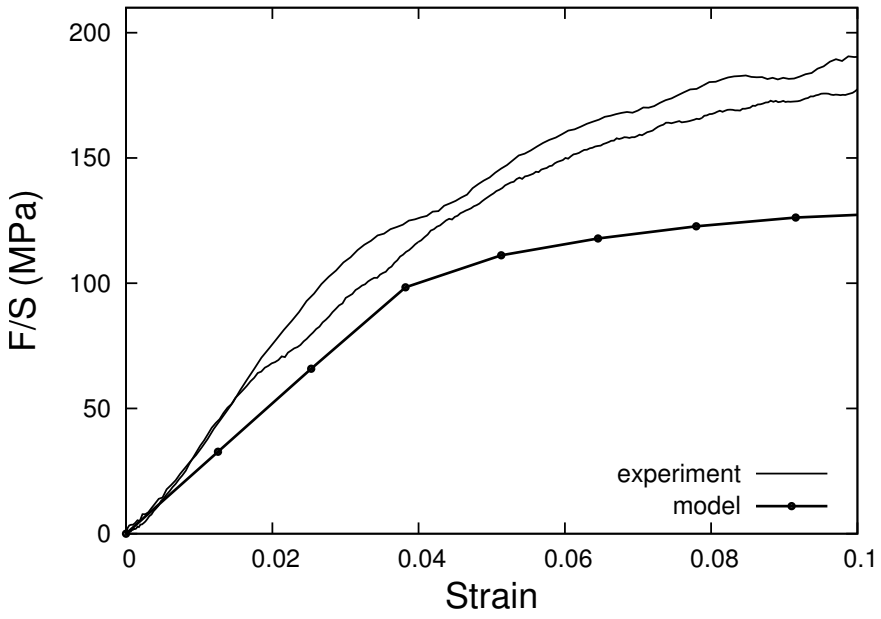

Fig. 43. Close up at low strains of computed (set QS) versus experimental stress–strain responses in compression at $T = 25°\mathrm{C}$ at $10^3/\mathrm{s}$.

chanical analysis is in order. To simply the problem, we have developed a formulation whereby specimen heating is assumed to take place in some adiabatic conditions. This assumption is very reasonable under high loading rates. The response observed from experiments on polymers results from competitive hardening and softening effects. Indeed, although the strain-rate sensitivity induces a higher strength at high rates compared to quasi-static conditions, the subsequent heating tends to soften the response as a consequence of temperature sensitivity. The macromolecular model has been modified to include this thermal softening (see Appendix) but all simulations here have been performed in isothermal conditions. Precisely, these simulations have been performed on EPON 862, in the same conditions as for static calculations but in dynamic conditions, i.e. at higher strain rates. Loading was prescribed as follows. A linear ramping function was used. From time $t = 0$ to $t = t_{rise}$ the displacement rate prescribed at the top of the specimen linearly increases such that at the "rising

time" (t_{rise}), the displacement rate corresponds to a prescribed nominal strain rate. In these calculations, the nominal strain rate is 10/s.

3. Quasi-static Calculations in Axisymmetric Conditions

In these simulations, only half of the geometry of the specimen is modeled, Fig. 44. Axisymmetric conditions are applied and axisymmetric finite elements are choosen. Boundary conditions are the same as for plane strain calculations. Specifically, in the x-y plane, the vertical displacement at the nodes located at the bottom is prescribed to zero; the vertical velocity at the nodes located at the top is prescribed to be constant and the radial displacement at the nodes located along the center of the specimen is prescribed to zero. A detail of the meshed undeformed gauge section is supplied, with details of locations where strains are calculated.

C. Results

1. Quasi-static Calculations in Plane Strain Conditions

Configurations after large deformations are shown in Fig. 45 for tension and compression, In tension (Figs. 45a-b), the amount of necking seems a little exagerated than what was observed experimentally (e.g., see Fig. 21). One explanation is that plane strain conditions promote greater localization in the plane of analysis since material flow is precluded out of plane. The meshed region in the neck shows regular rectangular elements with limited distorsion, which illustrates rather uniform deformations therein. In compression, the formation of a barrel (Fig. 45c-d) is in qualitative agreement with experimental observations (Fig. 22). Simulations show shear banding formations, which are commonly observed in plane strain calculations.

Figure 46 shows a comparison between the three measures of "true strain": $\epsilon_{22}^{\text{local}}$

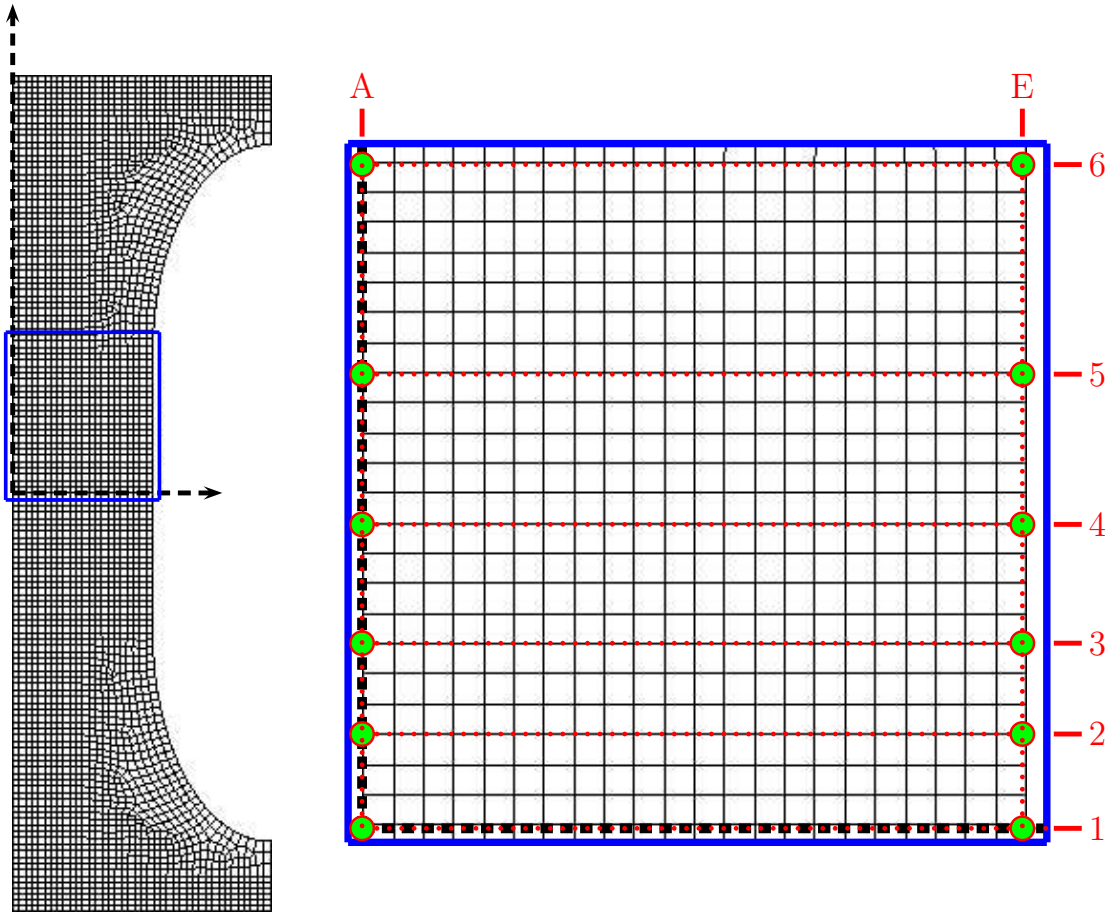

Fig. 44. Meshed undeformed specimen for axisymmetric calculations, with details of strain measurements

in (6.2), $\bar{\epsilon}_{22}$ in (6.3) and ε in (6.1). In tension and compression, the $\epsilon_{22}^{\text{local}}$ and $\bar{\epsilon}_{22}$ are found to be higher than the measure ε. The difference in strain measure occurs subsequent to strain localization. As indicated in the experimental section, the strain measure ε is more reliable post-localization. In tension, the three measures are very close to each other. This is reminiscent of what was observed experimentally, see Fig. 5.

Consider the initial middle cross section. Initially, strains are homogenous therein. Rapidly, heterogenous deformations set in, as a consequence of the formation of a neck.

Since the formation of a neck modifies the stress traxiality, it can be determined from the departure of stress-strain curves plotted from single element calculations (which exhibit uniform deformations) and from full specimen calculations (in which localization may occur). For EPON 862 and the geometry considered, the departure of stress-strain curves and thus the formation of a neck occurs around the peak stress ($\bar{\epsilon}_{22}$ of about 0.07), see Fig. 47a. For the one element calculation, softening immediatly follows whereas additional hardening is observed for the full specimen. However, direct comparison is difficult since in the cross section of the full specimen (i) the development of the neck accentuates the stress triaxiality and (ii) the normal stress within the cross section is no longer uniform. As a consequence of the neck, strains localize at the center of the cross section. Indeed, it is observed that $\varepsilon < \bar{\epsilon}_{22} < \epsilon_{22}^{\text{local}}$, with moderate differences between these strain measures, see (Fig. 46). Therefore, at a given macroscopic deformation, the elements at the center of the specimen are moderately more deformed than the elements at the free surface. The presence of this small strain gradient within the neck as demonstrated by the strain measures is confirmed by the meshed deformed geometry where elements in the necking region present rather similar size and shape (Fig. 45a-b).

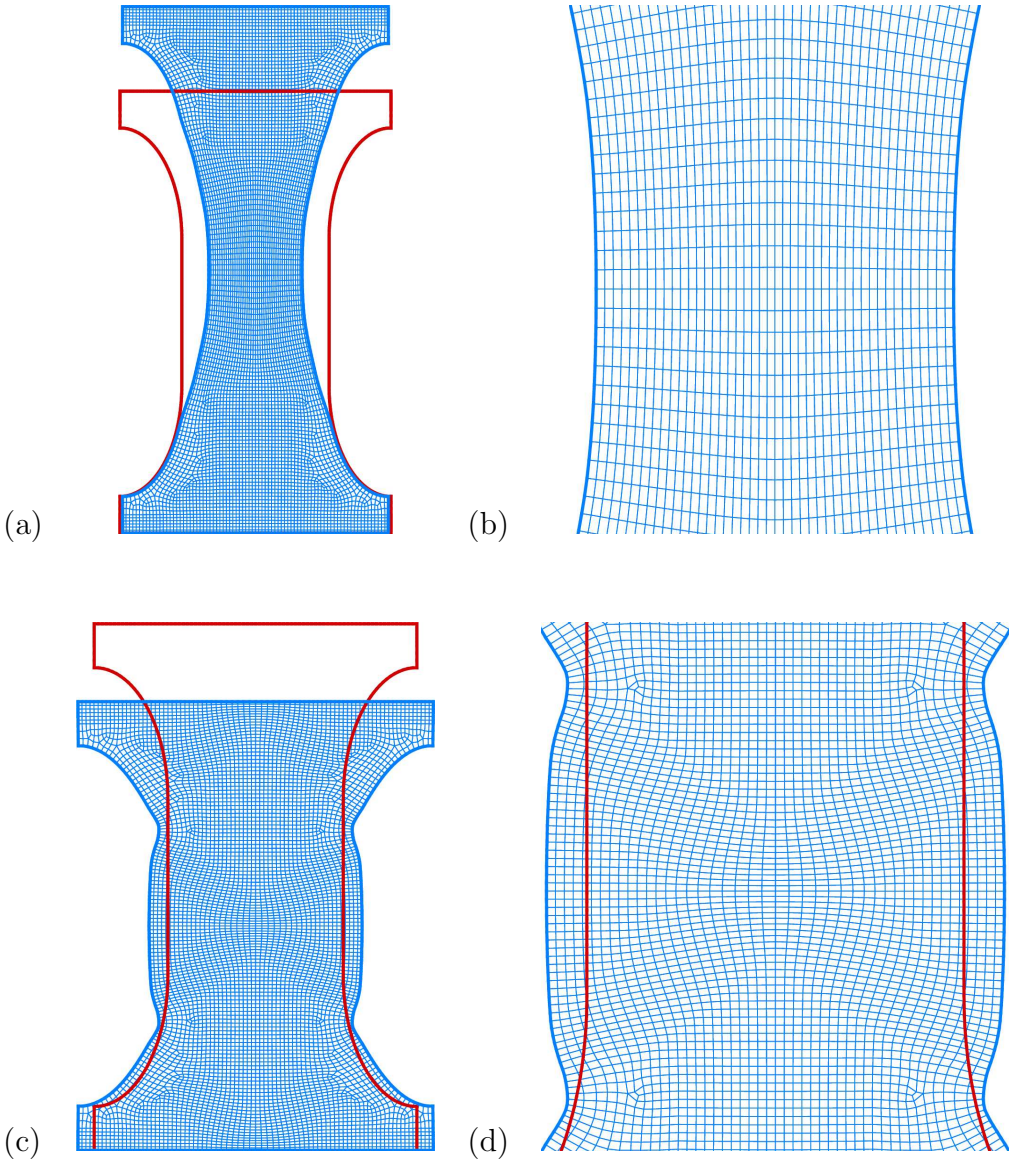

Fig. 45. (a) deformed mesh in tension showing necking; (b) zoom-in of the necking region; (c) deformed mesh in compression illustrating barrel formation; (d) zoom-in in the region where barelling takes place

(a)

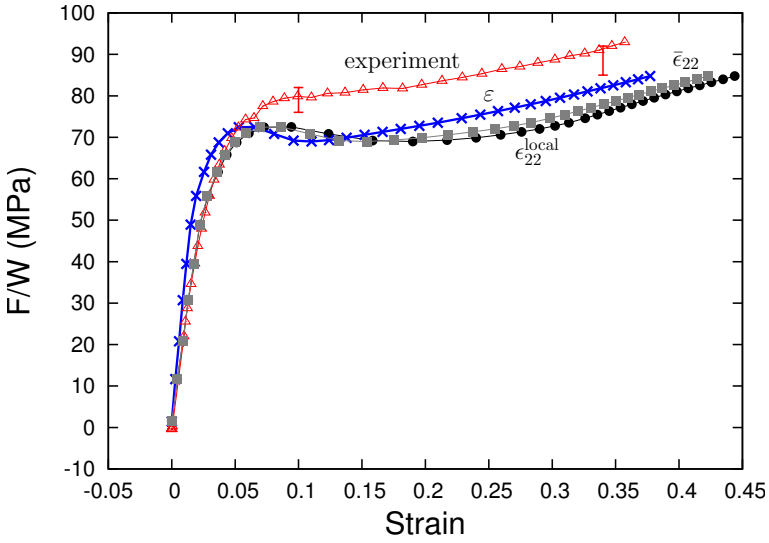

(b)

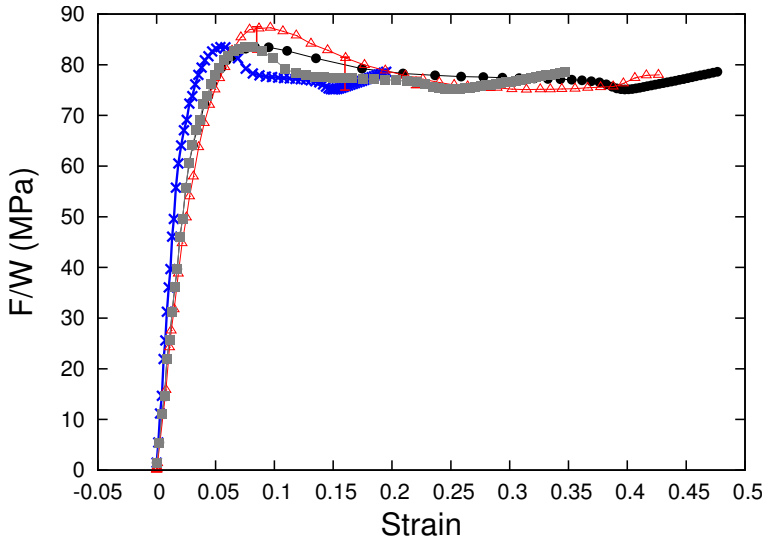

Fig. 46. Computed true stress versus strain curves for $T = 50°\text{C}$, at $10^{-1}/\text{s}$ and for three definitions of the "true" strain: $\epsilon_{22}^{\text{local}}$ in (6.2) or $\bar{\epsilon}_{22}$ in (6.3) or ε in (6.1). (a) Tension. (b) Compression. **Note:** The computed stress has been multiplied by a coefficient of 0.84 to accomodate the initial stiffness between experiments on EPON 862 (axisymmetric conditions) and simulations (plane strain conditions).

(a)

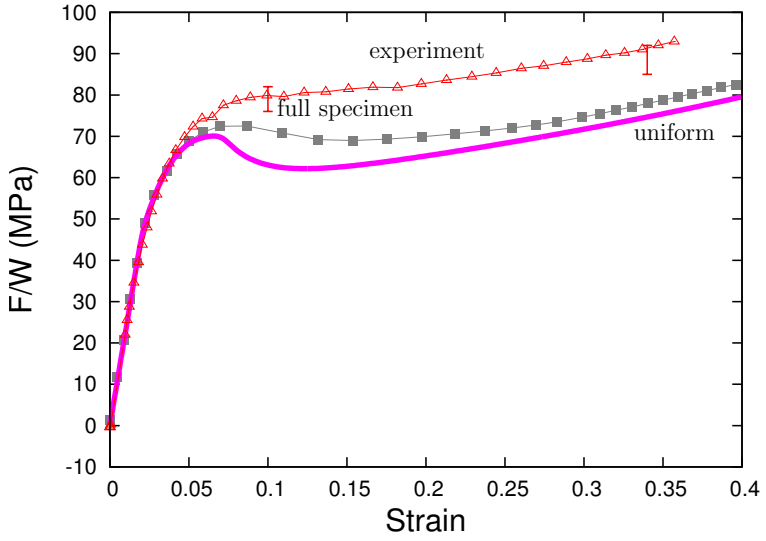

(b)

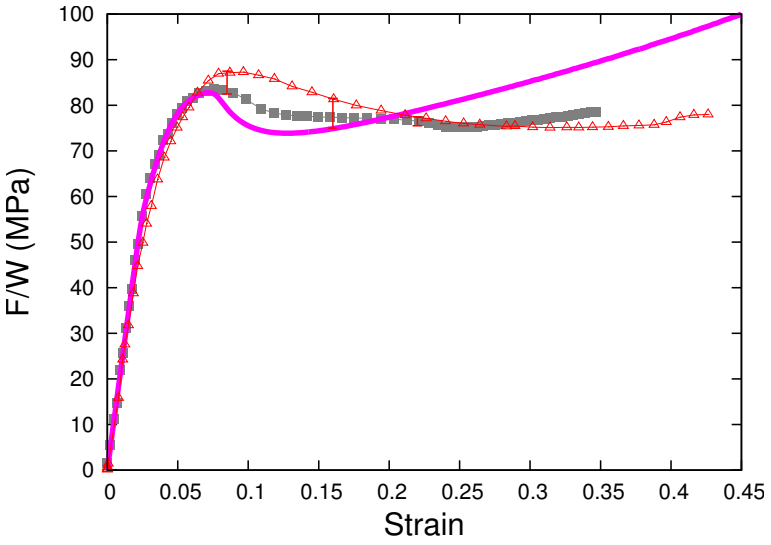

Fig. 47. Computed true stress versus strain curves for $T = 50°\text{C}$, at $10^{-1}/\text{s}$ for full specimen response ($\bar{\epsilon}_{22}$ in (6.3)) and single element uniform response. (a) Tension. (b) Compression. **Note:** The computed stress has been multiplied by a coefficient of 0.84 to accomodate the initial stiffness between experiments on EPON 862 (axisymmetric conditions) and simulations (plane strain conditions).

(a)

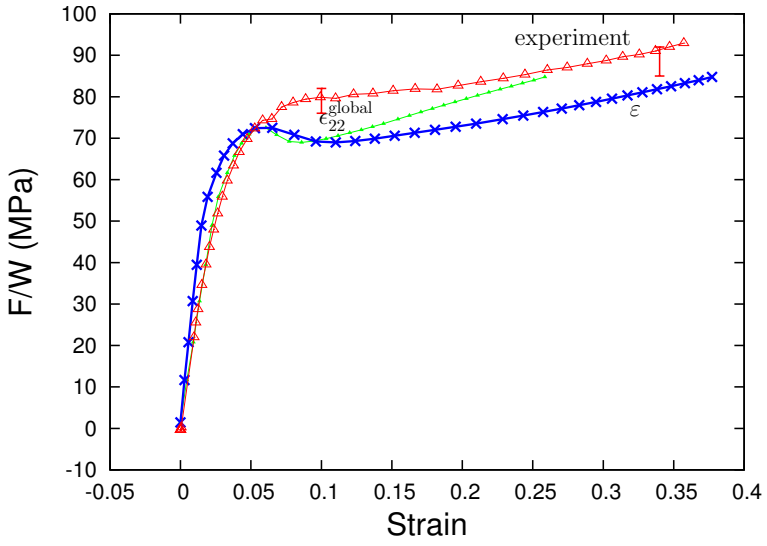

(b)

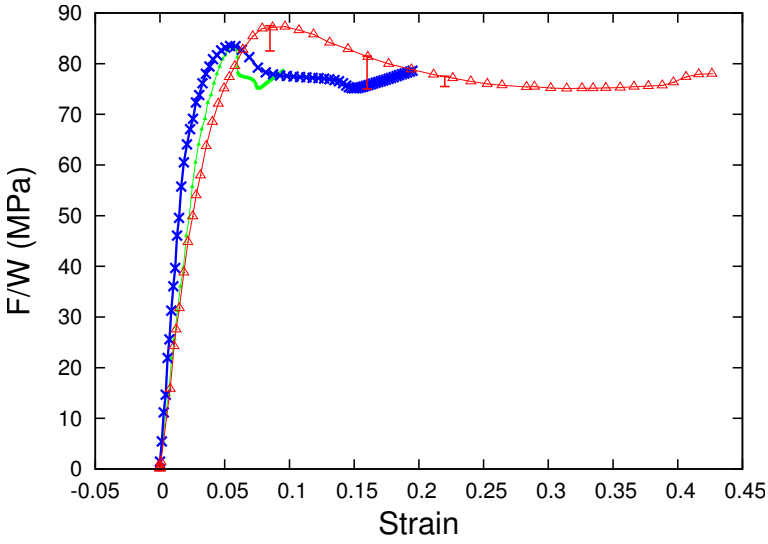

Fig. 48. Computed true stress versus strain curves for $T = 50°\text{C}$, at $10^{-1}/\text{s}$ and two definitions of measure of strains: $\epsilon_{22}^{\text{global}}$ in (6.4) or ε in (6.1). (a) Tension. (b) Compression. **Note:** The computed stress has been multiplied by a coefficient of 0.84 to accomodate the initial stiffness between experiments on EPON 862 (axisymmetric conditions) and simulations (plane strain conditions).

During the softening regime, , the higher rapid increase of deformation at the center of the specimen ($\epsilon_{22}^{\text{local}}$) in comparison with the entire minimal cross section (ε) confirms that strain localization initiated at the center of the specimen, Fig. 46. Very shortly follows the rapid increase of $\bar{\epsilon}_{22}$, which shows that the localization is spreading away from the center of the specimen. One explanation regarding the "temporal" and "spatial" evolution of strain localization follows. At the onset of necking, the region at the center of the specimen starts to soften and localization starts therein. Localization tends to quickly accentuate since the intrinsic response of Epon 862 exhibits an important rate of softening (see the curve "uniform" in Fig. 47a). However, with the rapid onset of the hardening regime, the localization is not exacerbated and tends to die therein to, instead, propagate to the neighborhood, which explains the "smoothness" of the deformed specimen. Consequently, deformations become more homogenous within the minimum cross section (and cross sections nearby) with higher strain levels at its center. Concurrently, the severity of necking tends to decrease with indications of drawing of the minimum cross section (and neighbooring cross sections), such as: (i) the deformed geometry at large strain, in particular around the minimum cross section (Fig. 45a-b); (ii) the similar trend at large strains for ε, $\bar{\epsilon}_{22}$ and $\epsilon_{22}^{\text{local}}$ (Fig. 46) (iii) the linear relationship at large strains between $\epsilon_{22}^{\text{global}}$ and ε (Fig. 48) and (iv) the similar trend for the response at large strain for both uniform and full specimen simulations (Fig. 47a). In the latter figure, the higher strength for the full specimen is due to the stress triaxiality.

Both in tension and compression the measure $\epsilon_{22}^{\text{global}}$ is found to be considerably smaller than ε (Fig. 48). The strain measure $\epsilon_{22}^{\text{global}}$ is in fact totally inadequate once plastic instability sets in, especially in the case of extreme localization. In compression, in compression the strain measures $\epsilon_{22}^{\text{local}}$ and $\bar{\epsilon}_{22}$ are found to be somewhat larger than the measure ε (Fig. 46b). This difference occurs subsequent to strain localiza-

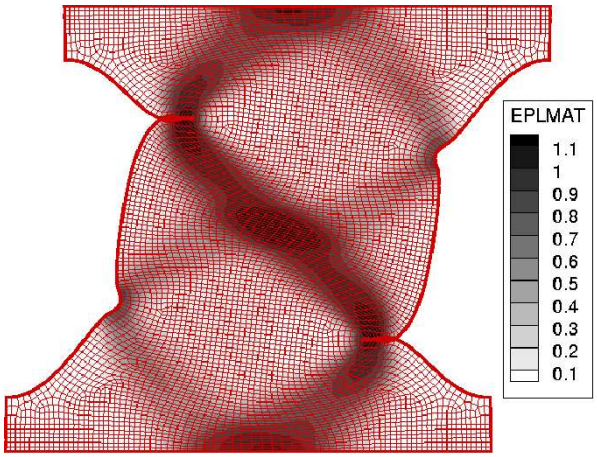

Fig. 49. Contours of effective plastic strains and deformed mesh. Barreling and folding is also observed.

tion. As indicated in the experimental section, the strain measure ε is more reliable post-localization. In compression, $\varepsilon < \bar{\epsilon}_{22} < \epsilon_{22}^{\text{local}}$. As in tension, it indicates that the center of the specimen deforms more than the free surface. In tension, this results correlates with the onset and propagation of a neck. In compression, barreling is the macroscopic localization mode and is associated with the formation of shear band patterns which pass through the center of the specimen (Fig. 45c-d). Therein, the elements are compressed. The strain gradients within the maximum cross section are more prononced than in tension. Indeed, the difference between ε and $\epsilon_{22}^{\text{local}}$ is more important in compression than in tension (Fig. 46b), and the elements at the specimen center show a high level of compression (Fig. 45c-d).

In Appendix , the same type of analysis has been performed on a fictitious material which exhibits a smoother softening regime and no large strain hardening. As expected for that case, flow localization is more severe (necking, barreling) and more concentrated.

The above results demonstrate that the response of a polymer clearly depends on the specimen geometry and the method choosen to characterize it, especially when strain localization occurs due to necking, barreling or shear banding. In some instances, extreme localization is observed in numerical simulations. This is illustrated in Fig. 49 where specimen "folding" is observed due to barrelling. This type of pattern is reminiscent of some experimental observations (see e.g. Fig. 22 at stage D).

2. Dynamic Calculations in Plane Strain Conditions

Simulations in compression, at a nominal rate of 10/s, for two ramping times (t=0.01s and t=0.005s) are presented in Fig. 50. These values for the ramping times were choosen such that they are not too low (which could generate numerical problems and a too high stiffness) neither too high (which could delay the dynamic regime to large strains). Several general observations are made.

First, a nomimal rate of deformation of 10/s is sufficient to generate dynamic effects, as illustrated by the oscillations in the stress-strain curves. These oscillations are generated in the early stages of deformation and rapidly die out. The strain measure $\epsilon_{22}^{\text{local}}$ is much higher than ε, suggesting a high concentration of strains in the center of the specimen. The difference between these strain measures increase with deformation, which illustrates strain localization at the center of the specimen. Simulations in compression in quasi-static conditions already showed the presence of shear bands wich results in high strain concentrations at the specimen center. The presence of shear bands in dynamic conditions are confirmed, see Fig. 51.

(a)

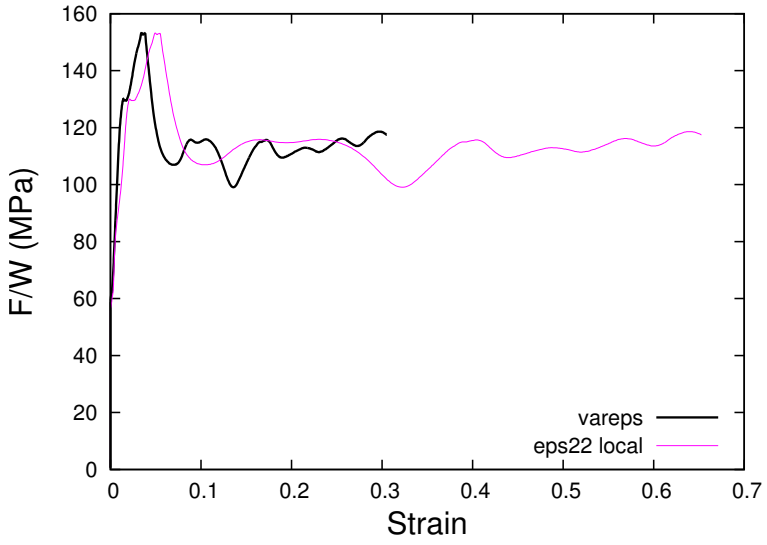

(b)

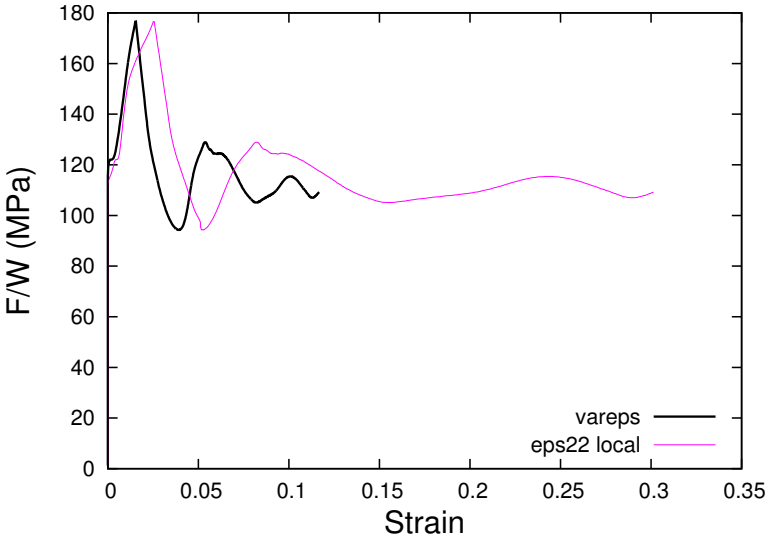

Fig. 50. Computed true stress versus strain curves for $T = 50°C$, at 10/s in compression and two definitions of measure of strains $\epsilon_{22}^{\text{local}}$ and ε corresponding to two ramping time: (a) 0.01s and (b) 0.005s

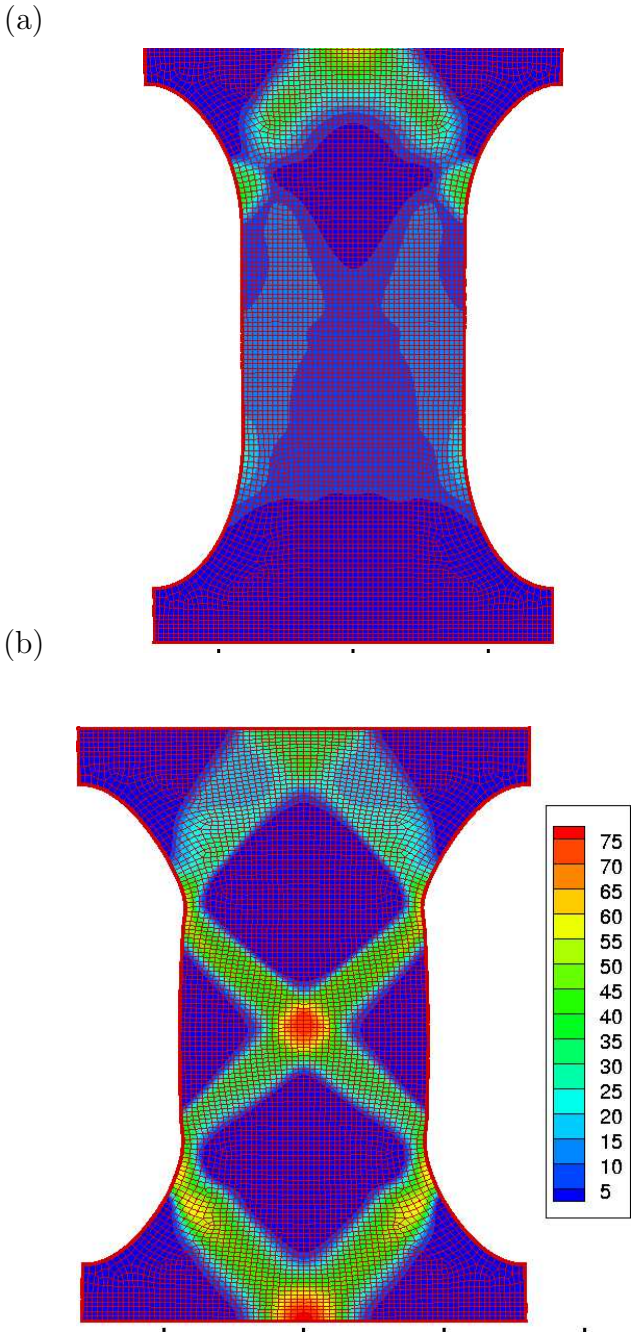

Fig. 51. Contours of plastic strain rate in dynamic response corresponding to a rising time of 0.005s, at (a) ε=0.0358 and (b)ε=0.1080

In comparing the stress-strain curves corresponding to different rising time in Fig. 50, the following observations are made. First, a lower rising time induces an increase of the initial slope. The apparent infinite initial stiffness of the curves in dynamic conditions is reminiscent to what is observed in experiments (Fig. 43). Also, high levels of strength at low strains are observed, before the peak stress in quasi-static conditions. As expected, the maximum of stress is higher with a lower rising time. Right after, the sudden drop in strength corresponds to the transition from the ramping loading function to a constant displacement rate.

Going back to Fig. 51, dynamic conditions results in stress wave propagation, which is illustrated by disymmetric contours between the top and bottom of the specimen. Starting from the location of prescribed displacement rate (top of the speciment), strains propagate through a preferred shear banding mode down to the bottom and intensify concurrently to barreling.

3. Quasi-static Calculations in Axisymmetric Conditions

To further analyze the localization of flow, simulations using a quasi-static formulation (UMAT in Abaqus) have been performed. First, the dynamic code previously employed was compared with the quasi-static implementation in the plane strain conditions, Fig. 52. The single element calculations (Fig. 52a) show overall a satisfactory match although discrepancies begin to appear around the peak stress and become more important in the softening regime to finally be small at large strains. The low amount of softening which is exhibited by the curves from the quasi-static code could be of concern since softening drives strain localization. At the time of the redaction of this dissertation, the origin of these discrepancies are under investigation. The response from the full specimen calculations are compared in Fig. 52b. In comparison with Fig. 52a, the differences are smeared out (especially in the softening regime)

due to strain localization. Contours of axial strains for both quasi-static and dynamic codes are plotted in Fig. 52c-d. The similarity of contours, of severity of the neck, and of overall deformation between these two cases bring some confidence in the interpretation of data corresponding to the quasi-static code in light of the results from the dynamic code which have been discussed earlier. Special attention should be taken in the interpretation of data regarding the neck formation and propagation since the softening regime is less important. Specifically, a little less localized necking migh be expected for calculations performed with the quasi-static code (also, plane strain calculations are known to favor localization).

Axisymmetric calculations were performed on the full specimen. Stress-strain curves corresponding to measures ε and $\epsilon_{22}^{\text{local}}$ are plotted in Fig. 53. These two measures of strain are almost identical for the whole range of deformatio, which suggests that localization of strain has not taken place or only slightly.

Next, in Fig. 54a, the evolution of the axial strain with deformation is plotted for various locations of the free surface. Initially for $\epsilon_{22}^{\text{local}} < 0.1$, all the curves are identical, which denotes that the free surface along the whole gauge section exhibits the same (uniform) deformation. Then, deformations concentrate in a band delimited by the locations "1" to "3" in Fig. 44. Moving away from this band decreases the level of deformation ("5" and "6"), such that the rate of deformation in the upper part of the gauge length is actually smaller than observed initially. At $t = 2s$, strains exceed 0.5 in the band of localized deformations whereas they barely reach 0.2 at the upper part of the gauge section. Beyond that time, the rate of deformation in the band slowly decreases to reach a constant value, while deformations progressively accelerate in the upper section "6". The rate of deformation at location "5" remains rather constant. At $t = 5.5s$ all cross sections have similarly deformed at the free surface.

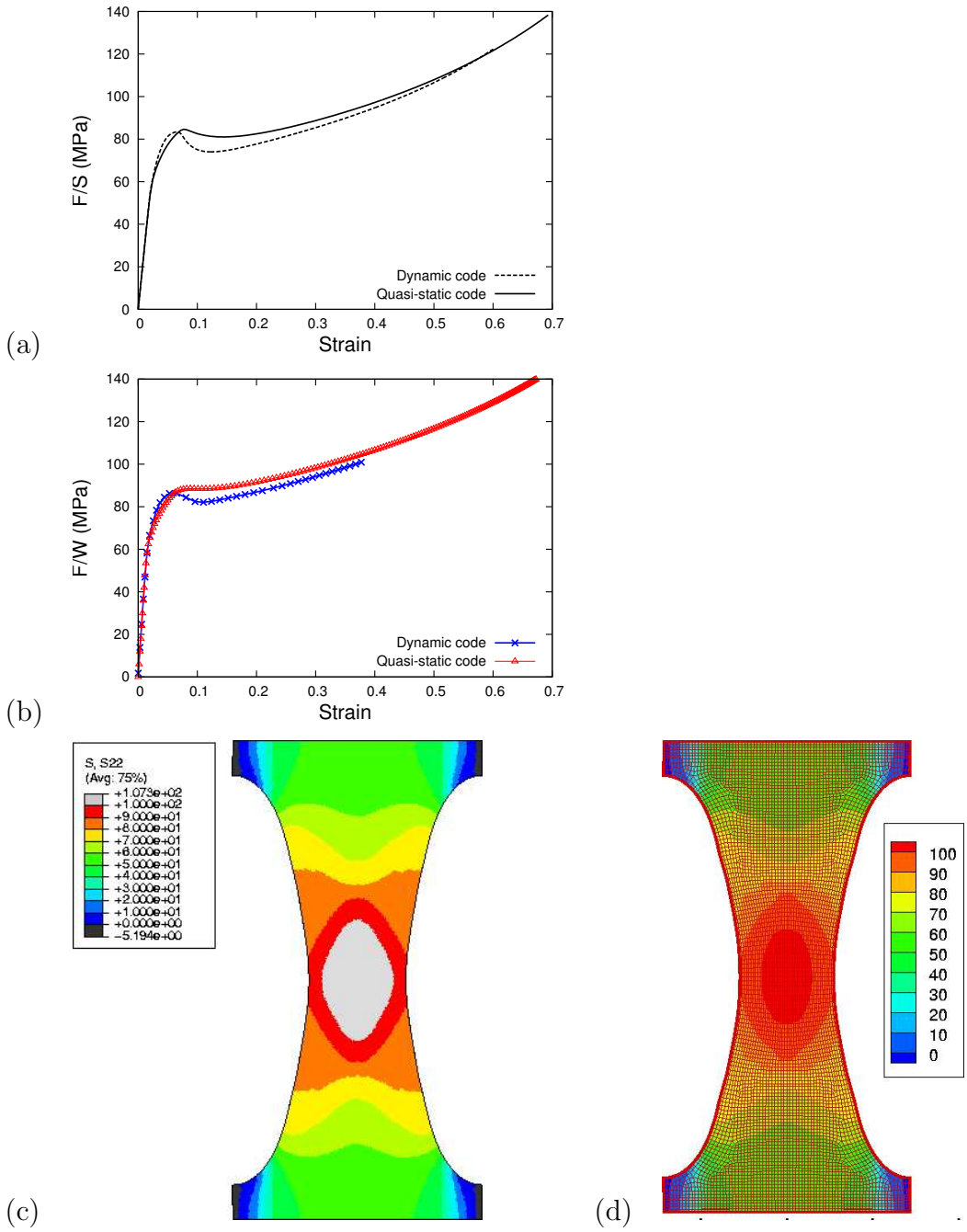

Fig. 52. Response of EPON 862 computed from quasi-static formulation and dynamic code based on: (a) a single element calculation; (b) the full specimen calculation. Axial stress contour plotted at $\varepsilon = 0.36$ from (c) quasi-static code; (d) dynamic formulation

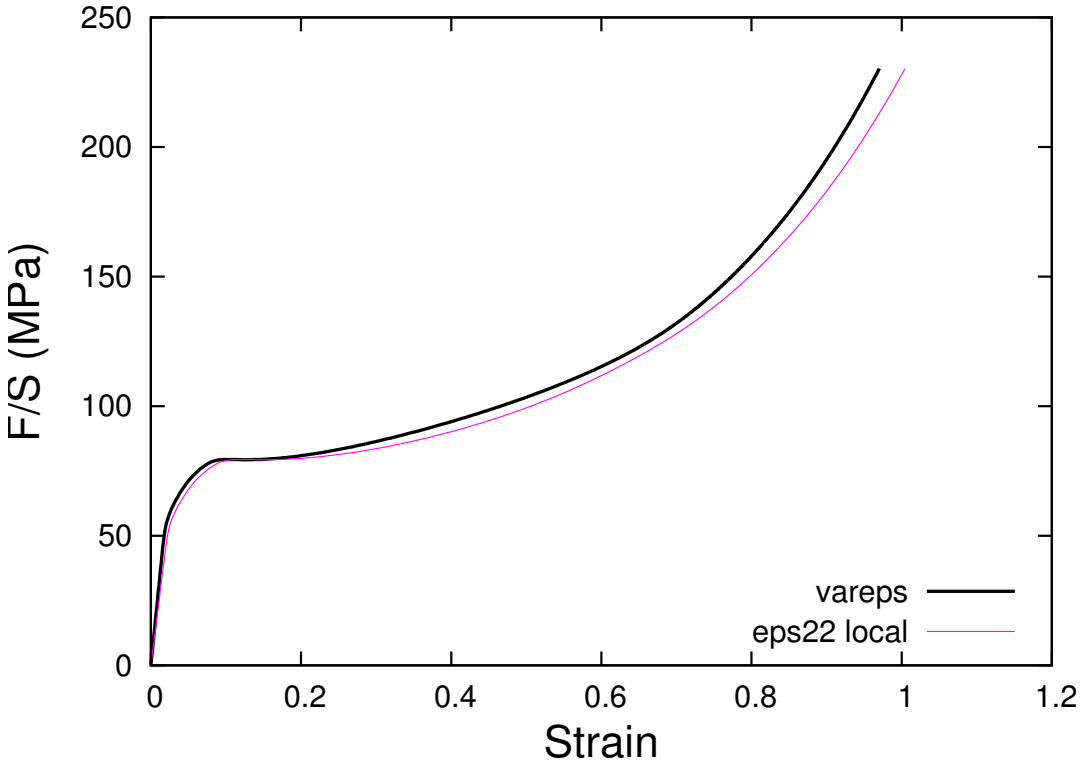

Fig. 53. Response in axisymmetric conditions for strain measures ε and $\epsilon_{22}^{\text{local}}$

Beyond, the whole free surface of the gauge deforms at the same rate, which denotes a complete drawing of the cross section. This mode of deformation started before for the location "1" to "3", at around $t = 3.5s$.

Fig. 54b compares the evolution of axial strains at the center of the specimen and at the free surface (already discussed in Fig. 54a). At any time of the deformation, deformations at the center and at the free surface are rather equal for locations "1" to "5", with values little higher at the center. At location "6" (top of the gauge section) the free surface deformes first, followed by the center. Then this cross section deforms homogenously before the free surface resumes deforming at a faster pace than the center. The trends of all these curves at large strains follows the curve describing the evolution of the macroscopic response, which demonstrates drawing of the whole specimen gauge.

The results of Fig. 54a-b are confirmed in Fig. 55 where the contours of the effective plastic strains are plotted at various stages of deformation. This figure supports the assumption that at the initial stages of deformation, strains localized in a rather large band at the center of the gauge section. Therein, strains are rather uniform with slight higher strains at the center. This could be explained by the little softening of the intrinsic response, which results in slightly larger deformations in a rather large area around the center of the specimen. Then, this area draws, rapidly followed by cross section away from the center such that the whole gauge draws with little observed necking.

These observations are also captured with the strain measure ε, Fig. 56a. Initially, the diameter of the whole gauge decreases uniformly. Then, a whole band around the center of the specimen contracts ("1" to "3") more than the rest ("4" to "6"). It follows a more rapid contraction of the cross sections around that the neck at the center of the center stabilizes and spreads to the neighborhood. At $t = 6s$, the

neck has disappeared since the whole gauge section has the same radius. Fig. 56b demonstrates the uniformity of strains within each cross section of the gauge section (except at its extremity).

Finally, in Fig. 57 are plotted the rate of deformation of various cross sections. It is confirmed that the cross section "1" to "3" deforms at the same rate, about a maximum of about 4 times the macroscopic rate. The cross sections deform slower as they are located away from the center. Then, the rate of deformation at the center of the specimen rapidly decreases as opposed to the cross sections away. At $t = 4s$, most of the deformation occurs at cross section "6", then the rate of deformation decreases. At $t = 8s$, the whole gauge section deforms uniformily, with a rate smaller than the macroscopic one, which demonstrates that the materials outside the gauge section is prone to deform.

D. Conclusion

This chapter detailed the onset and propagation of flow localization in tension and compression. Simulations based on two formulations (quasi-static and dynamic) were performed, in plane strain, and axisymmetric conditions. With the help of these numerical simulations based on single element and full specimen calculations, the close relationship between the intrinsic response and the flow localization was examined through various strain measures.

(a)

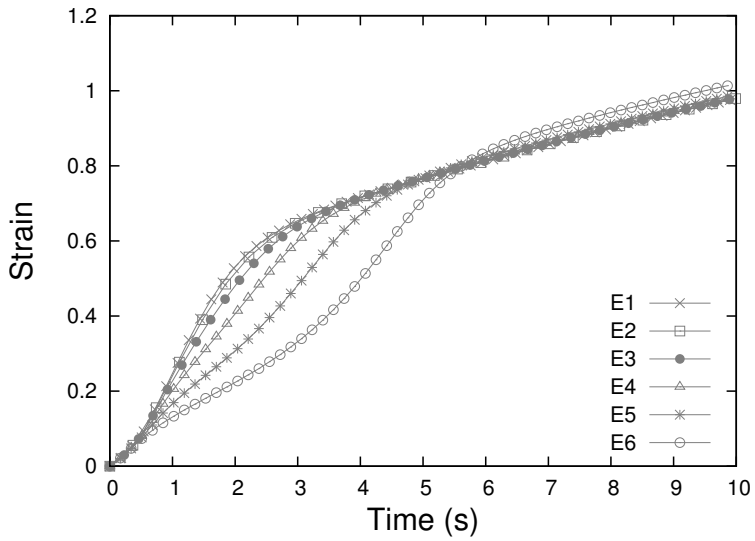

(b)

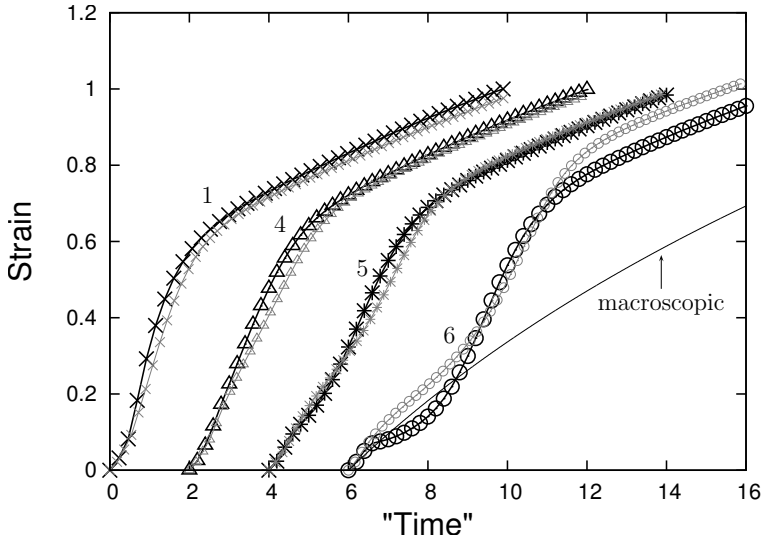

Fig. 54. (a) Evolution of axial strain at various locations of the free surface. (b) Direct comparison between the evolution of axial strain at various locations along the specimen axis (bigger labels) and along the free surface (smaller labels). Also is plotted the evolution of the macroscopic strain. Note a shift of time scale for clarity.

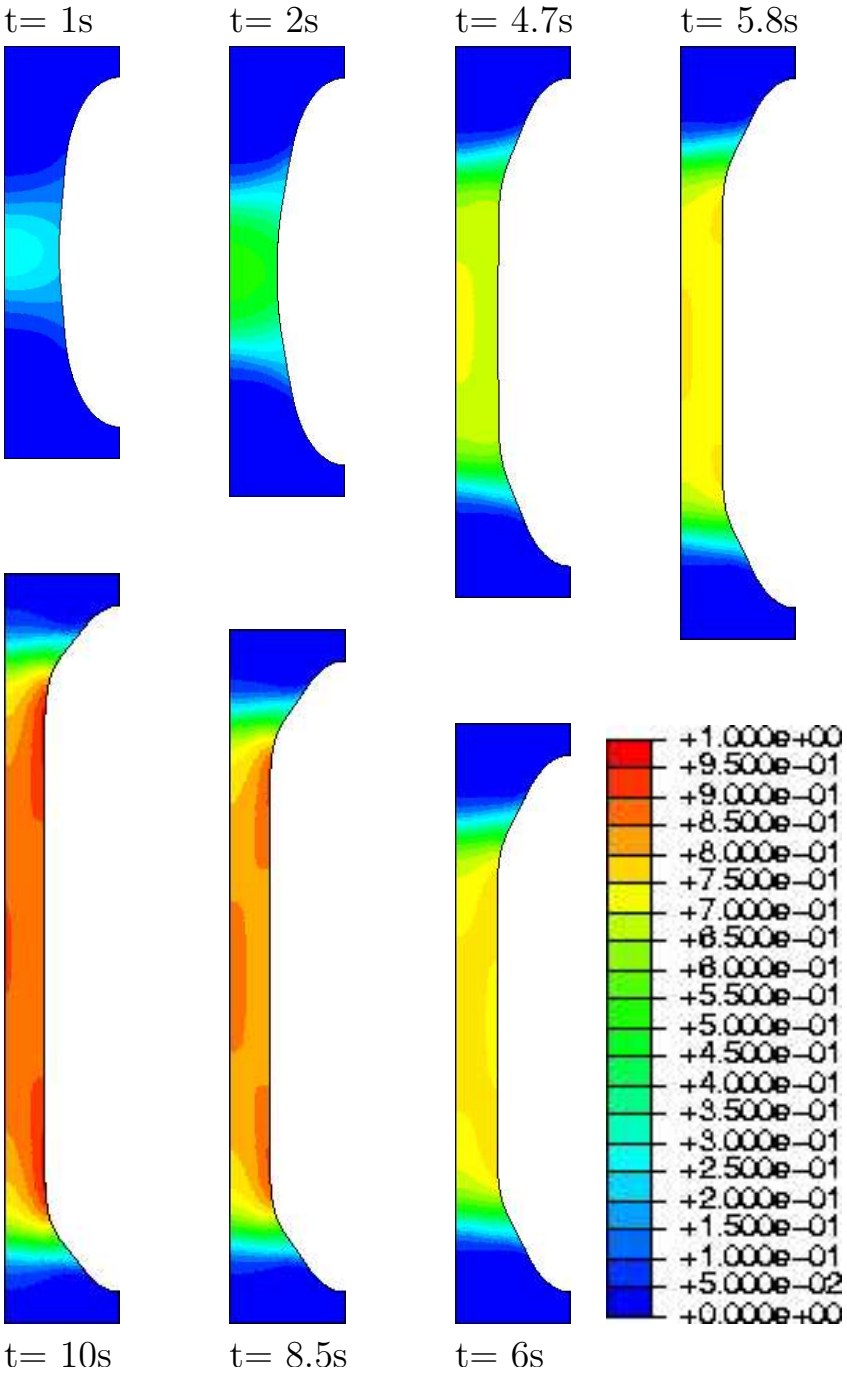

Fig. 55. Contours of effective plastic strains

(a)

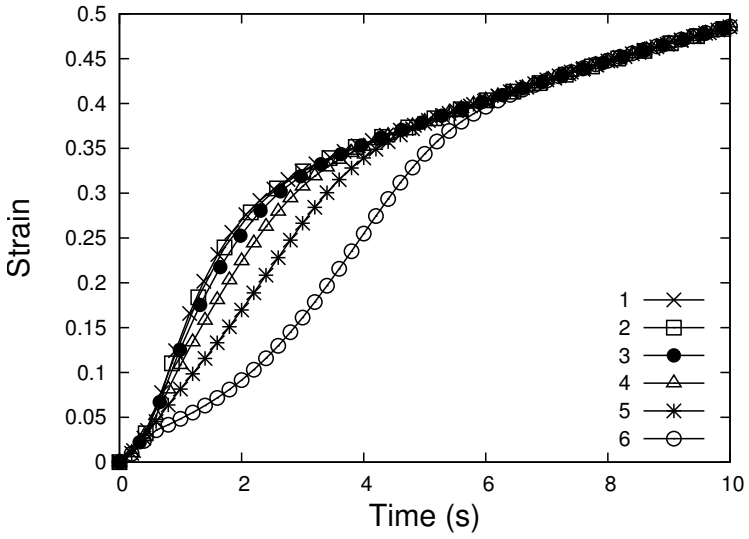

(b)

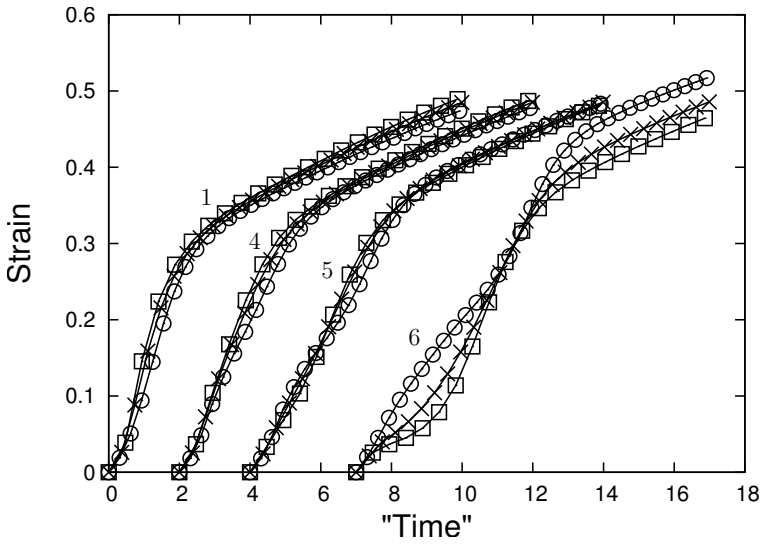

Fig. 56. (a) Evolution of macroscopic radial strain (ε) of various cross sections. (b) Evolution of measures of radial strain at various cross sections: macroscopic (crosses), local at the axis of the specimen (rectangles) and local at the free surface (circles). Note a shift of time scale for clarity.

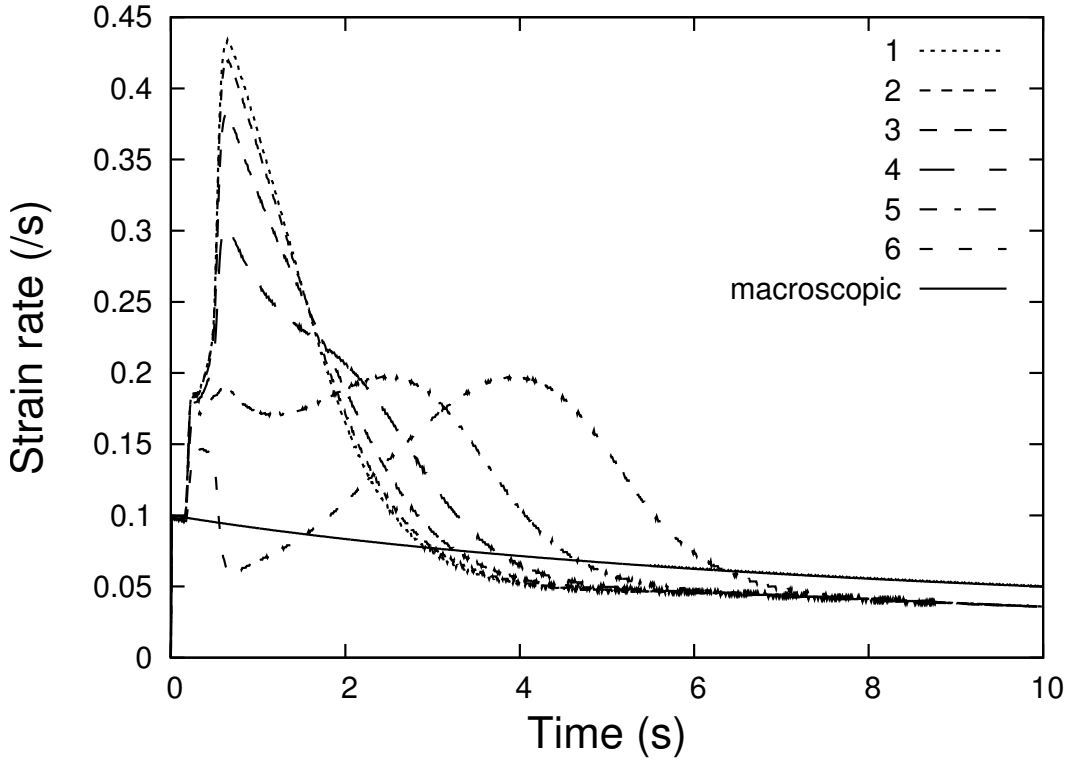

Fig. 57. Instantaneous strain rate ($\dot{\varepsilon}$) in various cross sections

CHAPTER VII

CONCLUSIONS

The goal of this research was to provide input into the design process of composites through a methodology aiming at the characterization and modeling of the mechanical response of polymers. The following research objectives of this work were to: (a) Characterize experimentally the intrinsic thermomechanical behavior of a polymer epoxy under quasi-static loading conditions; (b) Develop an experimentally validated macromolecular model that represents the mechanical behavior of amorphous polymers; (c) Analyze the effects of high rate loadings and physical aging on the behavior of polymers as is relevant to the impact and ballistic performance of composite structures; (d) Develop a robust procedure for model parameter identification with due respect to both quasi-static and dynamic conditions, and (e) Analyze plastic flow localization in epoxies using full boundary-value problem solutions and compare with experiments.

All these objectives were met.

– The engineering stress–strain response of EPON 862 was showed to be significantly different from the true response (Fig. 4). Differences were greater under compression loading. In all cases, the amount of post-peak softening changed depending on the stress measure. Two approximate measures of true strain were used: The first measure was the axial surface strain $\bar{\epsilon}_{22}$, averaged value between limited locations in the neighborhood of the highest deformed region; The second measure, ε, described the contraction of the most strained cross section, and could be interpreted as a logarithmic measure of axial strain if the polymer were incompressible. In tension, the two measures are very close to each other. In compression, however, $\bar{\epsilon}_{22}$ was found to be considerably smaller than ε at room temperature. This differ-

ence occured because of the onset of a plastic instability (necking or barreling) and subsequent strain localization. The essential conclusions remain the same for testing at higher temperatures. Nonetheless, in most cases $\bar{\epsilon}_{22}$ is found to be greater than ε, probably due to higher temperatures at the surfaces of the specimen in comparison with the interior of the specimen. ε is more reliable than $\bar{\epsilon}_{22}$ both at room temperature and at elevated temperatures, albeit for different reasons. A simplified procedure for determining the true stress–strain behavior was proposed to alleviate difficulties associated with the direct method based on monitoring the current extremal diameter of the specimen. It may be convenient to apply the simplified procedure to avoid inefficient data acquisition, especially if multiple materials and test conditions are to be considered. However, extra care should be taken in some cases. Moreover the amount of thermal softening of EPON 862 is significant over the temperature range investigated. The thermal softening does not affect the shape of the true stress–strain curve provided that the measure ε is used. In tension, the true stress–strain curve is characterized by a hardening stage at small strains, followed by a plateau then a rehardening stage at larger strains. The amount of softening, if any, is very small. In compression, the amount of post-peak softening is noticeable.

–A macromolecular model initially developed by Boyce et al. (1988) was used to model the mechanical response of thermosetting epoxy resin EPON-862 in tension and compression, for temperatures varying from 25°C to 80°C and strain rates ranging from 10^{-5}/s to 10^{-1}/s. A limited set among these experiments was used in order to assess the material parameters on which the polymer model builds. The identification of each parameter entering the model was precisely detailed in a procedure. This procedure has some specificities: (i) it accounts for the possibility for yielding to occur before the peak stress is reached; (ii) it enables a better representation of prepeak hardening; (iii) it considers the exponential factor 5/6 present in

the viscoplastic law of the original macromolecular model (Boyce et al. Boyce et al. (1988)) as a free parameter m which can take values ranging from 0.1 to 5/6. Such a modification originated from the observation that the initial model overestimated the temperature sensitivity for EPON-862 while well capturing the strain rate sensitivity. The calibration procedure leads to the value $m = 0.5$ for the best representation of temperature sensitivity. A modification of m does not significantly affect the quality of the strain rate sensitivity nor the pressure sensitivity. As a direct result of the calibration of material parameters, comparisons between experimental stress-strain curves and numerical simulations showed that strain rate and pressure sensitivity are very well captured for both $m = 0.5$ and $m = 5/6$ whereas temperature sensitivity is precisely acquired only in the case of $m = 0.5$. Finally, the predictive capabilities of the model were positively tested. Indeed, an excellent fit was observed between numerical simulations and experimental stress-strain curves which were not used in the calibration procedure. The same conclusions as for calibration were drawn. In particular, besides keeping a good representation of the rate sensitivity, the modification of the value for $m = 5/6$ to $m = 0.5$ improves the quality of the fit at all temperatures. Therefore, this set of material parameters can be confidently used to model the behavior of EPON-862 for any condition in the range of temperatures and rates studied. More generally, such a modified model and procedure may be used to investigate the large strain mechanical response of glassy polymers under their glass transition temperature regardless of their temperature and rate sensitivity dependence.

– The mechanical behavior of the thermoset epoxy was characterized in tension and compression for high rates using Split Hopkinson bars experiments at room temperature and for two conditions of aging ("as-received" and accelerated aged states). A simplified method for a rapid characterization of the mechanical response of polymers was presented. This method was showed to give a good estimate of the polymer

behavior, with true stress-strain curves plotted from the sole surface strains data. The measurements showed that the material is able to sustain large inelastic strains, in excess of 0.4, including under tensile loading. The deformation takes place in stages with a short visco-elastic region followed by a rounded yield point. Systematic unloading experiments in the neighborhood of the peak yield were carried out to probe the onset of inelastic behavior. The amount of strain softening was found to be independent of strain rate or temperature. The amount of thermal softening and the strain-rate sensitivity of the polymer were quantified. The experiments led to a comprehensive data base that can be used for developing a physics-based constitutive model for the polymer and in higher scale finite-element analyses of epoxy-based advanced composites.

–The capabilities of a variant of the macromolecular model was tested based on experimental results on the epoxy resin. The tests considered were the ones performed in tension and compression, at temperatures varying from room temperature to 80°C, and strain rates ranging from 10^{-5}/s (quasi-static conditions) to 10^{3}/s (dynamic conditions). The material parameter identification procedure was followed although two sets of experiments for parameter identification were considered. The first set of experiments (QS) corresponds to experiments performed at low to moderate strain rates. For this case, experiments at high strain rates enable to test the predictive capabilities of the model. The second set (D) encompasses experiments at all strain rates. For this case, the efficiency of the calibration can be tested, and consequences regarding the model predictive capabilities may be discussed. Results showed that with the set (QS), the model captures well the epoxy response in quasi-static conditions, as discussed in a previous chapter. However, the response at high strain rate is largely underestimated. The model does not capture the high strenghtening associated with the transition from low to high strain rates. With the set (D), all

trends are captured since the material parameters was identified based on the whole range of strain rates. However, a degradation of calibration is observed for low strain rates data. due to the high strengthening in dynamic conditions. Indeed, the model consistently underestimates the strength at low rates. The temperature sensitivity is not affected. Therefore, the model does not have all the ingredients to model the response of polymer glasses for a strain rate range of 8 decades. Parameter identification based a large range of strain rates would favor good predictions at larger strain rates, which would be adequate for impacting problems. However, an identification limited on low rate data would enhance accuracy in predictions at low strain rates and underestimate the strength for polymers dynamically loaded.

– The onset and propagation of flow localization was investigated in tension and compression. Simulations based on two formulations (quasi-static and dynamic) were performed, in plane strain, and axisymmetric conditions. With the help of these numerical simulations based on single element and full specimen calculations, the close relationship between the intrinsic response and the flow localization was examined through various strain measures.

A few directions for future work: (a) perform relevant aging experiments in order to permit the identification of material parameters; (b) analyze flow localization under dynamic simulations in adiabatic conditions; (c) investigate reverse problem for identification of material parameters.

REFERENCES

ABAQUS, 2009. ABAQUS Version 6.7 Documentation. ABAQUS, Inc. and Dassault Systemes, Providence, RI.

Aboudi, J., 2003. Micromechanical analysis of the finite elastic-viscoplastic response of multiphase composites. International Journal of Solids and Structures 40 (11), 2793–2817.

Adam, G., Gibbs, J. H., 1965. On the temperature dependence of cooperative relaxation properties in glass-forming liquids. The Journal of Chemical Physics 43 (1), 139–146.

Adolf, D. B., Chambers, R. S., Caruthers, J. M., 2004. Extensive validation of a thermodynamically consistent, nonlinear viscoelastic model for glassy polymers. Polymer 45, 4599–4621.

Ahmed, S., Jones, F. R., 1990. A review of particulate reinforcement theories for polymer composites. Journal of the Materials Science 25, 4993–4942.

Airbus, 2010. Airbus a350 xwb factsheet. http://www.airbus.com/en/aircraftfamilies/a350. Accessed 09-23-10.

Anand, L., Gurtin, M. E., 2003. A theory of amorphous solids undergoing large deformations, with application to polymeric glasses. International Journal of Solids and Structures 40, 1465–1487.

Argon, A. S., 1973. A theory for the low temperature plastic deformation of glassy polymers. Philosophical Magazine 15, 28–39.

Arruda, E. M., Boyce, M. C., 1993a. Evolution of plastic anisotropy in amorphous polymers during finite straining. International Journal of Plasticity 9, 697–720.

Arruda, E. M., Boyce, M. C., 1993b. A three-dimensional constitutive model for the large stretch behavior of rubber elastic materials. Journal of the Mechanics and Physics of Solids 41, 389–412.

Arruda, E. M., Boyce, M. C., Jayachandran, R., 1995. Effects of strain rate, temperature and thermomechanical coupling on the finite strain deformation of glassy polymers. Mechanics of Materials 19, 193–212.

Arruda, E. M., Boyce, M. C., Quintus-Bosz, H., 1993. Effects of initial anisotropy on the finite strain deformation behavior of glassy polymers. International Journal of Plasticity 9, 783–811.

Bakis, C. E., Bank, L. C., Brown, V. L., Cosenza, E., Davalos, J. F., Lesko, J. J., Machida, A., Rizkalla, S. H., Triantafillou, T. C., 2002. Fiber-reinforced polymer composites for construction– state-of-the-art review. Journal of Composites for Construction 6, 73–87.

Bauwens, J. C., 1980. Attempt to correlate the formation of free volume and the plastic deformation process in glassy polymers. Polymer 21, 699–705.

Belbachir, S., Zairi, F., Ayoub, G., Maschke, U., Nait-Abdelaziz, M., Gloaguen, J. M., Benguediab, M., Lefebvre, J., 2010. Modelling of photodegradation effect on elastic-viscoplastic behavior of amorphous polyactic acid films. Journal of the Mechanics and Physics of Solids 58 (2), 241–255.

Benzerga, A. A., Besson, J., Batisse, R., Pineau, A., 2002. Synergistic effects of

plastic anisotropy and void coalescence on fracture mode in plane strain. Modelling Simulation in Materials Science and Engineering 10, 73–102.

Benzerga, A. A., Besson, J., Pineau, A., 2004. Anisotropic ductile fracture. Part I: experiments. Acta Materialia 52, 4623–4638.

Beremin, F. M., 1981. Experimental and numerical study of the different stages in ductile rupture: application to crack initiation and stable crack growth. In: Nemat-Nasser, S. (Ed.), Three-Dimensional Constitutive Relations of Damage and Fracture. Pergamon Press, North Holland, pp. 157–172.

Bergstrom, J., Boyce, M. C., 1998. Constitutive modeling of the large strain time-dependent behavior of elastomers. Journal of the Mechanics and Physics of Solids 46 (5), 931–954.

Bergstrom, J. S., Kurtz, S. M., Rimnac, C. M., Edidin, A. A., 2002. Constitutive modeling of ultra-high molecular weight polyethylene under large deformation and cyclic loading conditions. Biomaterials 23, 2329–2343.

Bigg, D. M., 1996. A review of positron annihilation lifetime spectroscopy as applied to the physical aging of polymers. Polymer Engineering and Science 36 (6), 737–743.

Bjerke, T., Li, Z., Lambros, J., 2002. Role of plasticity in heat generation during high rate deformation and fracture of polycarbonate. International Journal of Plasticity 18, 549–567.

Bodner, S. R., 2002. Unified Plasticity for Engineering Applications. Kluwer Academic/Plenum, New York.

Bodner, S. R., Partom, Y., 1975. Constitutive equations for elastic-viscoplastic strain-hardening materials. Journal of Applied Mechanics 42, 385–389.

Boeing, 2010. 787 dreamliner fact sheet. http://www.boeing.com/commercial/787family/programfacts.html. Accessed 09-08-10.

Bowden, P. B., 1973. The Yield Behavior of Glassy Polymers: The Physics of Glassy Polymers. Applied Sci. Publishers, Essex, England.

Bowden, P. B., Raha, S., 1970. The formation of micro-shear bands in polystyrene and polymethylmethacrylate. Philosophical Magazine 22, 463–482.

Boyce, M. C., Arruda, E. M., 1990. An experimental and analytical investigation of the large strain compressive and tensile response of glassy polymers. Polymer Engineering and Science 30 (20), 1288–1298.

Boyce, M. C., Arruda, E. M., Jayachandran, R., 1994. The large strain compression, tension, and simple shear of polycarbonate. Polymer Engineering and Science 34, 716–725.

Boyce, M. C., Montagut, E. L., Argon, A. S., 1992. The effects of thermomechanical coupling on the cold drawing process of glassy polymers. Polymer Engineering and Science 32, 1073–1085.

Boyce, M. C., Parks, D. M., Argon, A. S., 1988. Large inelastic deformation of glassy polymers, Part I: Rate dependent constitutive model. Mechanics of Materials 7, 15–33.

Brereton, M. G., Duckett, R. A., Joseph, S. H., Spence, P. J., 1977. An interpretation of the yield behaviour of polymers in terms of correlated motion. Journal of the Mechanics and Physics of Solids 25 (2), 127–136.

Brinson, L. C., Gates, T. S., 1995. Effects of physical aging on long term creep of polymers and polymer matrix composites. International Journal of Solids and Structures 32, 827–846.

Brodnyan, J. G., 1959. The concentration dependence of the newtonian viscosity of prolate ellipsoids. Journal of Rheology 3 (1), 61–68.

Brondsted, P., Lilholt, H., Lystrup, A., 2005. Composite materials for wind power turbine blades. Annual Review of Materials Research 35, 505–538.

Buckley, C., Harding, J., Hou, J., Ruiz, C., Trojanowski, A., 2001. Deformation of thermosetting resins at impact rates of strain. Part I: Experimental study. Journal of the Mechanics and Physics of Solids 49, 1517–1538.

Buisson, G., Ravi-Chandar, K., 1990. On the constitutive behavior of polycarbonate under large deformation. Polymer 31, 2071–2076.

Caruthers, J. M., Adolf, D. B., Chambers, R. S., Shrikhande, P., 2004. A thermodynamically consistent, nonlinear viscoelastic approach for modeling glassy polymers. Polymer 45, 4577–4597.

Case, S. L., O'Brien, E. P., Ward, T. C., 2005. Cure profiles, crosslink density, residual stresses, and adhesion in a model epoxy. Polymer 46, 10831–10840.

Cavaille, J. Y., Etienne, S., Perez, J., Monnerie, L., Johari, G. P., 1986. Dynamic shear measurements of physical ageing and the memory effect in a polymer glass. Polymer 27, 686–692.

Chang, W. J., Pan, J., 1997. Effects of yield surface shape and round-off vertex on crack-tip fields for pressure-sensitive materials. International Journal of Solids and Structures 34, 3291–3320.

Chen, K., Schweizer, K. S., 2008. Theory of physical aging in polymer glasses. Physical Review E. 78, 031802–1–031802–15.

Chow, T. S., 1978. Effect of particle shape at finite concentration on the elastic moduli of filled polymers. Journal of Polymer Science: Polymer Physics 17, 959–965.

Chowdhury, K., Benzerga, A. A., Talreja, R., 2006. A numerical study of impact-induced deformation modes in amorphous glassy polymers. In: Besson, J., Moinereau, D., Steglich, D. (Eds.), 9$^{\text{th}}$ European Mechanics of Materials Conference. Les Presses, Paris, pp. 421–426.

Chowdhury, K. A., 2007. Damage initiation, progression and failure of polymer based composites due to manufacturing induced defects. Ph.D. dissertation, Texas A&M University, College Station, TX.

Chowdhury, K. A., Benzerga, A. A., Talreja, R., 2008a. An analysis of impact-induced deformation and fracture modes in amorphous glassy polymers. Engineering Fracture Mechanics 75, 3328–3342.

Chowdhury, K. A., Benzerga, A. A., Talreja, R., 2008b. A computational framework for analyzing the dynamic response of glassy polymers. Computer Methods in Applied Mechanics and Engineering 197, 4485–4502.

Chowdhury, K. A., Talreja, R., Benzerga, A. A., 2008c. Effects of manufacturing-induced voids on local failure in polymer-based composites. Journal of Engineering Materials and Technology 130, 021010–1–021010–9.

Christman, T., Needleman, A., Suresh, S., 1989. An experimental and numerical study of deformation in metal-ceramic composites. Acta Metallurgica 11, 3029–3050.

Counto, U. J., 1964. The effect of the elastic modulus of the aggregate on the elastic modulus, creep and creep recovery of concrete. Magazine of Concrete Research 16, 129–138.

Cox, H. L., 1952. The elasticity and strength of paper and other fibrous materials. British Journal of Applied Physics 3, 72–79.

Curro, J. J., Roe, R., 1984. Isothermal relaxation of specific volume and density fluctuation in poly(methyl methacrylate) and polycarbonate. Polymer 25, 1424–1430.

D638, A., 2004. Section 6.3-rigid rods, standard test method for tensile properties of plastics. ASTM International. SAI GLOBAL, Paramus, NJ.

Das, S., 2001. The cost of automobile polymer composites: a review and assessment of doe's lightweight materials composites research. Energy Division, Oak Ridge National Laboratory.

Dickie, R. A., 1973. On the modulus of three–component particulate–filled composites. Journal of Applied Polymer Science 17, 2509–2517.

Drucker, D. C., Prager, W., 1952. Soil mechanics and plastic analysis or limit design. Quarterly of Applied Mathematics 10 (2), 157–165.

Duckett, R. A., Rabinowitz, S., Ward, I. M., 1970. The strain-rate, temperature and pressure dependence of yield of isotropic poly(methylmethacrylate) and poly(ethylene terephthalate). Journal of Materials Science 5, 909–915.

Engels, T. A. P., Govaert, L. E., Peters, G. W. M., Meijer, H. E. H., 2006. Processing-induced properties in glassy polymers: application of structural relaxation to yield

stress development. Journal of Polymer Science: Part B: Polymer Physics 44, 1212–1225.

Engels, T. A. P., Schrauwen, B. A. G., Govaert, L. E., 2009. Improvement of the long-term performance of impact-modified polycarbonate by selected heat treatments. Macromolecular Materials and Engineering 294, 114–121.

Eyring, H., 1936. Viscosity, plasticity and diffusion as examples of absolute reaction rate. Journal of Chemical Physics 4, 283–291.

FAA, 1984. Federal Aviation Regulation FAR Part 33 Section 94: Blade Containment and Rotor Unbalance Tests. Federal Aviation Administration, Washington DC.

Fang, Q.-Z., Wang, T. J., Beom, H. G., Zhao, H. P., 2009. Rate-dependent large deformation behavior of pc/abs. Polymer 50, 296–304.

Ferry, J. D., 1962. Viscoelastic Properties of Polymers. Wiley, New York.

Frigione, M., Lettieri, M., 2008. Procedures conditioning the absorption/desorption behavior of cold-cured epoxy resins. Journal of Polymer Science, Part B: Polymer Physics 46, 1320–1336.

Gallouze, N., Belhaneche-Bensemra, N., 2008. Influence of polluted atmospheres on the natural aging of poly(vinyl chloride) stabilized with epoxidized sunflower oil. Journal of Applied Polymer Science 110, 1973–1978.

Garces, J. M., Moll, D. J., Bicerano, J., Fibiger, R., Mc Leod, D., 2000. Polymeric nanocomposites for automotive applications. Advanced Materials 12, 1835–1839.

Garg, M., Mulliken, A., Boyce, M., 2008. Temperature rise in polymeric materials during high rate deformation. Journal of Applied Mechanics 75, 011009–1–8.

Gilat, A., Goldberg, R. K., Roberts, G. D., 2002. Experimental study of strain-rate-dependent behavior of carbon/epoxy composite. Composites Science and Technology 62, 1469–1476.

Gilat, A., Goldberg, R. K., Roberts, G. D., 2007. Strain rate sensitivity of epoxy resin in tensile and shear loading. Journal of Aerospace Engineering 20, 75–89.

Gloaguen, J. M., Lefebvre, J. M., 2001. Plastic deformation behavior of thermoplastic/clay nanocomposites. Polymer 42, 5841–5847.

Goldberg, R. K., Roberts, G. D., Gilat, A., 2005. Implementation of an associative flow rule including hydrostatic stress effects into the high strain rate deformation analysis of polymer matrix composites. Journal of Aerospace Engineering 18, 18–27.

Goldberg, R. K., Stouffer, D. C., 2002. Strain rate dependent analysis of a polymer matrix composite utilizing a micromechanics approach. Journal of Composite Materials 36, 773–793.

Gonzalez, C., LLorca, J., 2007. Mechanical behavior of unidirectional fiber-reinforced polymers under transverse compression: microscopic mechanisms and modeling. Composites Science and Technology 67, 2795–2806.

Govaert, L. E., 2000. The influence of intrinsic strain softening on strain localization in polycarbonate: modeling and experimental validation. Journal of Engineering Materials and Technology 122, 177–185.

Green, A. E., Zerna, W., 1954. Theoretical Elasticity. Clarendon Press, Oxford.

Grytten, F., Daiyan, H., Polanco-Loria, M., Dumoulin, S., 2009. Use of digital image correlation to measure large-strain tensile properties of ductile thermoplastics. Polymer Testing 28, 653–660.

G'Sell, C., 1986. Plastic deformation of glassy polymers: constitutive equations and macromolecular mechanisms. In: McQueen, H. J., Bailon, J. P., Dickson, J. I., Jonas, J. J., Akben, M. G. (Eds.), Strength of Metals and Alloys. Pergamon Press, New York, pp. 1943–1982.

G'Sell, C., Gopez, A. J., 1981. Plastic banding in glassy polycarbonate under plane simple shear. Journal of Material Science 20, 3462–3478.

G'Sell, C., Hiver, J. M., Dahoun, A., 2002. Experimental characterization of deformation damage in solid polymers under tension, and its interrelation with necking. International Journal of Solids and Structures 39, 3857–3872.

G'Sell, C., Hiver, J. M., Dahoun, A., Souahi, A., 1992. Video-controlled tensile testing of polymers and metals beyond the necking point. Journal of Material Science 27, 5031–5039.

G'Sell, C., Jonas, J. J., 1979. Determination of the plastic behavior of solid polymers at constant true strain rate. Journal of Materials Science 14, 583–591.

Guth, E., 1945. Theory of filler reinforcement. Journal of Applied Physics 16, 20–25.

Hadamard, J., 1903. Lecons sur la propagation des ondes et les equations de l'hydrodynamique. Chap. 6. Librairie Scientifique. Hermann, Paris.

Hasan, O. A., Boyce, M. C., 1993. Energy storage during inelastic deformation of glassy polymers. Polymer 34, 5085–5092.

Hasan, O. A., Boyce, M. C., Li, X. S., Berko, S., 1993. Investigation of the yield and postyield behavior and corresponding structure of poly(methyl methacrylate). Journal of Polymer Science, Part B: Polymer Physics 31 (2), 185–197.

Hashin, Z., Shtrikman, S., 1963. A variational approach to the theory of the elastic behaviour of multiphase materials. Journal of the Mechanics and Physics of Solids 11, 127–140.

Haward, R. N., Thackray, G., 1968. The use of a mathematical model to describe isothermal stress-strain curves in glassy thermoplastics. Proceedings of the Royal Society of London. Series A. Mathematical and Physical Sciences 302, 453–472.

Hermann, A., Chaudhuri, T., Spagnol, P., 2005. Bipolar plates for pem fuel cells: a review. International Journal of Hydrogen Energy 30, 1297–1302.

Hild, F., Roux, S., 2006. Digital image correlation: from displacement measurement to identification of elastic properties– a review. Strain 42, 69–80.

Hill, A. J., Katz, I. M., Jones, P. L., 1990. Isothermal volume relaxation in aged polycarbonate measured by positron annihilation lifetime spectroscopy. Polymer Engineering and Science 30, 762–768.

Hill, R., 1962. Acceleration waves in solids. Journal of the Mechanics and Physics of Solids 10, 1–16.

Hirsch, T. J., 1962. Modulus of elasticity of concrete affected by elastic moduli of cement paste matrix and aggregate. Journal of the American Concrete Institute 59, 427–452.

Hojo, H., Toyoshima, W., Tamura, M., Kawamura, N., 1977. Short- and long-term strength characteristics of particulate-filled cast epoxy resin. Polymer Engineering and Science, 163–167.

Holbery, J., Houston, D., 2006. Natural-fiber-reinforced polymer composites in auto-

mobile applications. JOM Journal of the Minerals, Metals and Materials Society 58, 80–86.

Hope, P. S., Duckett, R. A., Ward, I. M., 1980a. Effect of free monomer content on the drawing behavior of poly(methyl-methacrylate). Journal of Applied Polymer Science 25, 1373–1379.

Hope, P. S., Ward, I. M., Gibson, A. G., 1980b. The hydrostatic extrusion of polymethylmethacrylate. Journal of Materials Science 15, 2207–2220.

Hsu, S. Y., Vogler, T. J., Kyriakides, S., 1999. Inelastic behavior of an AS4/PEEK composite under combined transverse compression and shear. Part II: modeling. International Journal of Plasticity 15, 807–836.

Huang, Y., Paul, D. R., 2006. Physical aging of thin glassy polymer films monitored by optical properties. Macromolecules 39, 1554–1559.

Hutchinson, J. M., 1995. Physical aging of polymers. Progress in Polymer Science 20, 703–760.

Hutchinson, J. W., Neale, K. W., 1983. Neck propagation. Journal of the Mechanics and Physics of Solids 31, 405–426.

Iannucci, L., Willows, M. L., 2006. An energy based damage mechanics approach to modelling impact onto woven composite materials- Part I: numerical models. Composites: Part A 37, 2041–2056.

Ishai, O., Cohen, L. J., 1967. Elastic properties of filled and porous epoxy composites. International Journal of Mechanical Sciences 9, 539–546.

Janssen, R. P. M., De Kanter, K., Govaert, L. E., Meijer, H. E. H., 2008. Fatigue life predictions for glassy polymers: a constitutive approach. Macromolecules 41, 2520–2530.

Jiang, Y., Tabei, A., Simitses, G. J., 2000. A novel micromechanics-based approach to the derivation of constitutive equations for local/global analysis of a plain-weave fabric composite. Composites Science and Technology 60, 1825–1833.

Jones, J., 2006. Damage-tolerant fan casings for jet engines. http://www.sti.nasa.gov/tto/Spinoff2006/T_1.html. Accessed 09-27-10.

Jordan, J. L., Foley, J. R., Siviour, C. R., 2008. Mechanical properties of epon 826/dea epoxy. Mechanics of Time-Dependent Materials 12, 249–272.

Kailasam, M., PonteCastaneda, P., 1998. A general constitutive theory for linear and nonlinear particulate media with microstructure evolution. Journal of Mechanics and Physics of Solids 46, 427–465.

Kim, J., Lee, W., Tsai, S. W., 2002. Modeling of mechanical property degradation by short-term aging at high temperatures. Composites: Part B 33, 631–543.

Klompen, E. T. J., Engels, T. A. P., Govaert, L. E., Meijer, H. E. H., 2005. Modeling of the postyield response of glassy polymers: influence of thermomechanical history. Macromolecules 38, 6997–7008.

Knauss, W. G., Emri, I. J., 1981. Non-linear viscoelasticity based on free volume consideration. Computers & Structures 13, 123–128.

Kovacs, A. J., 1963. Glass transition in amorphous polymers. Fortschritte der Hochpolymeren -Forschung 30, 394–507.

Kovacs, A. J., Aklonis, J. J., Hutchinson, J. M., Ramos, A. R., 1979. Isobaric volume and enthalpy recovery of glasses- 2. a transparent multiparameter theory. Journal of Polymer Science: Polymer Physics Edition 17 (7), 1097–1162.

Kovacs, A. J., Stratton, R. A., Ferry, J. D., 1963. Dynamic mechanical properties of polyvinyl acetate in shear in the glass transition temperature range. Journal of Physical Chemistry 67, 152–161.

Kozlov, G. V., Dolbin, I. V., Zaikov, G. E., 2004. Theoretical description of physical aging of amorphous polymers. Russian Journal of Applied Chemistry 77, 267–270.

Krieg, R. O., Key, S. W., 1973. Transient shell response by numerical time integration. International Journal for Numerical Methods in Engineering 7, 273–286.

Kweon, S., Benzerga, A. A., 2010. Unpublished manuscript. Dept of Aerospace Engineering, Texas A&M University.

Kyriakides, S., 1994. Propagating instabilities in structures. Advances in Applied Mechanics 30, 67–189.

Lamarre, L., Sung, C. S. P., 1983. Studies of physical aging and molecular motion by azochromophoric labels attached to the main chains of amorphous polymers. Macromolecules 16, 1729–1736.

Laraba-Abbes, F., Ienny, P., Piques, R., 2003. A new 'tailor–made' methodology for the mechanical behavior analysis of rubber–like materials: I. Kinematics measurements using a digital speckle extensometry. Polymer 44, 807–820.

Leblond, J. B., 1994. Bifurcation effects in ductile metals with nonlocal damage. Journal of Applied Mechanics 61, 236–242.

Legrand, D. G., 1969. Crazing, yielding, and fracture of polymers. I. Ductile brittle transition in polycarbonate. Journal of Applied Sciences 13 (10), 2129–2147.

Leidner, J., Woodhams, R. T., 1974. Strength of polymeric composites containing spherical fillers. Journal of Applied Polymer Science 18, 1639–1654.

Leonov, A. I., 1976. Nonequilibrium thermodynamics and rheology of viscoelastic polymer media. Rheologica Acta 15, 85–98.

Leveque, D., Schieffer, A., Mavel, A., Maire, J., 2005. Analysis of how thermal aging affects the long-term mechanical behavior and strength of polymer-matrix composites. Composites Science and Technology 65 (3-4), 395–401.

Li, F. Z., Pan, J., 1990. Plane-strain crack-tip fields for pressure-sensitive dilatant materials. Journal of Applied Mechanics 57, 40–49.

Liang, Y.-M., Liechti, K. M., 1996. On the large deformation and localization behavior of an epoxy resin under multiaxial stress states. International Journal of Solids and Structures 33, 1479–1500.

Lim, C. T., Shim, V. P. W., Ng, Y. H., 2003. Finite-element modeling of the ballistic impact of fabric armor. International Journal of Impact Engineering 26, 13–31.

Littell, J. D., 2008. The experimental and analytical characterization of the macromechanical response for triaxial braided composite materials. Ph.D. dissertation, University of Akron, Akron, OH.

Littell, J. D., Ruggeri, C. R., Goldberg, R. G., Roberts, G. R., Arnold, W. A., Binienda, W. K., 2008. Measurement of epoxy resin tension, compression, and shear stress–strain curves over a wide range of strain rates using small test specimens. Journal of Aerospace Engineering 21, 162–173.

Llorca, J., Needleman, A., Suresh, S., 1991. An analysis of the effects of matrix void growth on deformation and ductility in metal ceramic composites. Acta Metallurgica et Materialia 39, 2317–2335.

Lu, J., Ravi-chandar, K., 1999. Inelastic deformation and localization in polycarbonate under tension. International Journal of Solids and Structures 36, 391–425.

Lucintel, 2010. Aerospace market research survey. http://www.lucintel.com /is_aerospace.asp. Accessed 09-23-10.

Lustig, S. R., Shay, R. M., Caruthers, J. M., 1995. Thermodynamic constitutive equations for materials with memory on a material time scale. Journal of Rheology 40 (1), 69–106.

Lyulin, A. V., Michels, M. A. J., 2006. Simulation of polymer glasses: from segmental dynamics to bulk mechanics. Journal of Non-Crystalline Solids 352, 5008–5012.

Lyulin, A. V., Michels, M. A. J., 2007. Time scales and mechanisms of relaxation in the energy landscape of polymer glass under deformation: direct atomistic modeling. Physical Review Letters 99, 085504–1–085504–4.

Ma, Z., Ravi-Chandar, K., 2000. Confined compression: a stable homogeneous deformation for constitutive characterization. Experimental Mechanics 40, 38–45.

Mandel, J., 1966. Conditions de stabilite et postulat de Drucker. In: Krautchenko, J., Sirieys, P. M. (Eds.), Rheology and Soil Mechanics. Springer, Berlin, pp. 55–68.

Matsuoka, S., Bair, H. E., Bearder, S. S., Kern, H. E., Ryan, J. T., 1978. Analysis of non-linear stress relaxation in polymeric glasses. Polymer Enginneering and Science 18, 1073–1080.

Mazumder, S. K., 2002. Composites Manufacturing, Materials, Product and Process Engineering. CRC Press LLC, Boca Raton, FL.

McClung, A. J. W., Ruggles-Wrenn, M. B., 2009. Effects of prior aging at 288C in argon environment on time-dependent deformation behavior of a thermoset polymer at elevated temperature, Part 2: modeling with viscoplasticity theory based on overstress. Journal of Applied Polymer Science 114, 3389–3395.

McConnell, V., 2005. Composites in the sky with dreamliner. http://www.aviationtoday.com/am/categories/commercial/Composites-in-the-Sky-with-Dreamliner_256.html. Accessed 09-26-10.

McKenna, G. B., 1989. Polymer Properties. Pergamon, Oxford.

McKenna, G. B., Crissman, J. M., Lee, A., 1988. Relationships between failure and other time dependent processes in polymeric materials. American Chemical Society, Polymer Preprints, Division of Polymer Chemistry 29, 128–129.

McLoughlin, J. R., Tobolsky, A. V., 1952. The viscoelastic behavior of polymethyl methacrylate. Journal of Colloid Science 7, 555–568.

Mecham, M., 2006. Genx development emphasizes composites, combustor technology. http://www.aviationweek.com/aw/generic/story_channel.jsp?channel=comm&id=news/aw041706p1.xml. Accessed 09-26-10.

Michel, J. C., Moulinec, H., Suquet, P., 1999. Effective properties of composite materials with periodic microstructure: a computational approach. Computer Methods in Applied Mechanics and Engineering 172, 109–143.

Mininni, R. M., Moore, R. S., Flick, J. R., Petrie, S. E. B., 1973. The effect of excess

volume on molecular mobility and on the mode of failure of glassy poly(ethylene terephthalate). Journal of Macromolecular Science, Part B 8, 343–359.

Miravetea, A., Bielsab, J., Chiminellia, A., Cuarteroa, J., Serranoa, S., Tolosanaa, N., Guzman de Villoria, R., 2006. 3D mesomechanical analysis of three-axial braided composite materials. Composites Science and Technology 66, 2954–2964.

Mohanraj, J., Barton, D. C., Ward, I. M., Dahoun, A., Hiver, J. M., G'Sell, C., 2006. Plastic deformation and damage of polyoxymethylene in the large strain range at elevated temperatures. Polymer 47, 5852–5861.

Morales, A., Escolano, C., Keles, Y., 2009. ObservatoryNANO, economic assessment, aeronautics and automotive sectors. Final report, Bax & Willems Consulting Venturing.
http://www.observatorynano.eu/project/filesystem/files/ObservatoryNANO_Economic_assessment_automotive_aeronautics_final_report.pdf. Accessed 09-08-10.

Moynihan, C. T., Easteal, A. J., DeBolt, M. A., 1976. Dependence of the fictive temperature of glass on cooling rate. Journal of the American Ceramic Society 59 (1-2), 12–16.

Muliana, A., Kim, J. K., 2007. A concurrent micromechanical model for predicting nonlinear viscoelastic responses of composites reinforced with solid spherical particles. International Journal of Solids and Structures 44, 6891–6913.

Mulliken, A. D., Boyce, M. C., 2006. Mechanics of the rate-dependent elastic-plastic deformation of glassy polymers from low to high strain rates. International Journal of Solids and Structures 43, 1331–1356.

Muzeau, E., Vigier, G., Vassoille, R., 1994. Physical aging phenomena in an amorphous polymer at temperatures far below the glass transition. Journal of Non-Crystalline Solids 172–174, 575–579.

Needleman, A., 1989. Dynamic shear band development in plane strain. Journal of Applied Mechanics 56, 1–9.

Needleman, A., Tvergaard, V., 1983. Finite element analysis of localization in plasticity. In: Oden, J. T., Carey, G. F. (Eds.), Finite Elements–Special Problems in Solid Mechanics. Vol. 5. Prentice–Hall, Englewood Cliffs, NJ, pp. 94–157.

Newmark, N. M., July 1959. A method of computation for structural dynamics. Journal of the Engineering Mechanics Division. ASCE 85, 67–94.

Nicolais, L., Narkis, M., 1971. Stress-strain behavior of styrene- acrylonitrile/glass bead composites in the glassy region. Polymer Engineering and Science 11 (3), 194–199.

Nielsen, L. E., 1970. Generalized equation for the elastic moduli of composite materials. Journal of Applied Physics 41, 4626–4627.

O'Connell, P. A., McKenna, G. B., 2002. The non-linear viscoelastic response of polycarbonate in torsion: an investigation of time-temperature and time-strain superposition. Mechanics of Time-Dependent Materials 6, 207–229.

Owens, B. C., Whitcomb, J. D., Varghese, J., 2010. Effect of finite thickness and free edges on stresses in plain weave composites. Journal of Composite Materials 44, 675–992.

Parsons, E., Boyce, M. C., Parks, D. M., 2004. An experimental investigation of the

large–strain tensile behavior of neat and rubber–toughened polycarbonate. Polymer 45, 2665–2684.

Pavlov, P. A., Ogorodov, L. I., 1992. Long-time resistance of polymer and composite materials with a view to the time of long-time natural aging. Mechanics of Composite Materials 27, 454–457.

Peirce, D., Shih, C. F., Needleman, A., 1984. A tangent modulus method for rate dependent solids. Computers & Structures 18, 875–887.

Piggott, M. R., Leidner, J., 1974. Misconceptions about filled polymers. Journal of Applied Polymer Science 18, 1619–1623.

Poulain, X., Gilat, A., Roberts, G. D., Goldberg, R. K., Benzerga, A. A., 2010a. Mechanical and aging behavior of a polymer epoxy over a wide range of temperatures and strain rates. Unpublished manuscript. Dept of Aerospace Engineering, Texas A&M University.

Poulain, X., Kohlman, L., Binienda, W., Roberts, G. D., Goldberg, R. K., Benzerga, A. A., 2010b. Determination of the intrinsic behavior of polymers using digital image correlation combined with video–monitored testing. Unpublished manuscript. Dept of Aerospace Engineering, Texas A&M University.

Powers, J. M., Caddell, R. M., November 1972. The macroscopic volume changes of selected polymers subjected to uniform tensile deformation. Polymer Engineering and Science 12 (6), 432–436.

Rabinowitz, S., Ward, I. M., Perry, J. S. C., 1970. The effect of hydrostatic pressure on the shear yield behavior of polymers. Journal of Materials Science 5, 29–39.

Ramakrishna, S., Mayer, J., Wintermantel, E., Leaong, K. W., 2001. Biomedical applications of polymer-composite materials: a review. Composites Science and Technology 61, 1189–1224.

Ravi-Chandar, K., Ma, Z., 2000. Inelastic deformation in polymers under multiaxial compression. Mechanics of Time-Dependent Materials 4, 333–357.

Red, C., 2008. Aviation outlook: Composites in commercial aircraft jet engines. http://www.compositesworld.com/articles/aviation-outlook-composites-in-commercial-aircraft-jet-engines. Accessed 09-27-10.

Rittel, D., 1999. On the conversion of plastic work to heat during high strain rate deformation of glassy polymers. Mechanics of Materials 31, 131–139.

Roberts, G. D., Pereira, J. M., Braley, M. S., Arnold, W. A., Dorer, J. D., Watson, W. R., 2009. Design and testing of braided composite fan case materials and components. NASA/TM–2009-215811, 1–11.

Robertson, R. E., 1966. Theory for the plasticity of glassy polymers. Journal of Chemical Physics 44 (10), 3950–3956.

Roman, J. C. S., 2005. Experiments on epoxy, polyurethane and adp adhesives. Technical Report CCLab2000. 1b/1, Ecole Polytechnique, France.

Rottler, J., Robbins, M. O., November 2001. Yield conditions for deformation of amorphous polymer glasses. Physical Review E 64 (5), 1–8.

Rottler, J., Robbins, M. O., 2005. Unified description of aging and rate effects in yield of glassy solids. Physical Review Letters 95, 225504–1–225504–4.

Royal, J. S., Torkelson, J. M., 1993. Physical aging effects on molecular-scale polymer relaxations monitored with mobility-sensitive fluorescent molecules. Macromolecules 26, 5331–5335.

Ruggles-Wrenn, M. B., Broeckert, J. L., 2009. Effects of prior aging at 288c in air and in argon environments on creep response of pmr-15 neat resin. Journal of Applied Polymer Science 111, 228–236.

Rush, K. C., Beck, R. H. J., 1969. Yielding of glassy polymers. Journal of Macromolecular Science B3, 365–375.

Sahu, S., Broutman, L. J., 1972. Mechanical properties of particulate composites. Polymer Engineering and Science 12, 91–100.

Santore, M. M., Duran, R. S., McKenna, G. B., 1991. Volume recovery in epoxy glasses subjected to torsional deformations: the question of rejuvenation. Polymer 32, 2377–2381.

Sarva, S., Mulliken, A. D., Boyce, M. C., 2006. The mechanics of large-strain inhomogeneous deformation of polymeric materials under dynamic loading conditions. Journal de Physique IV 134, 95–101.

Sarva, S. S., Boyce, M. C., 2007. Mechanics of polycarbonate during high-rate tension. Journal of Mechanics of Materials and Structures 2 (10), 1853–1880.

Sato, Y., Furukawa, J., 1963. A molecular theory of filler reinforcement based on the concept of internal deformation (a rough approximation of internal deformation). Rubber Chemistry and Technology 36, 1081–1106.

Sauer, J. A., Pae, K. D., Bhateja, S. K., 1973. Influence of pressure on yield and fracture in polymers. Journal of Macromolecular Science B8, 631–654.

Schapery, R. A., 1997. Nonlinear viscoelastic and viscoplastic constitutive equations based on thermodynamics. Mechanics of Time-Dependent Materials 1, 209–240.

Shapery, R. A., 1969. On the characterization of nonlinear viscoelastic materials. Polymer Engineering and Science 9, 295–310.

Shay Jr, R. M., Caruthers, J. M., 1990. A predictive model for the effects of thermal history on the mechanical behavior of amorphous polymers. Polymer Engineering and Science 30, 1266–1280.

Shield, T. W., Kim, K. S., 1991. Diffraction theory of optical interference moire and a device for production of variable cirtual reference gratings. a moire microscope. Experimental Mechanics 31, 126–134.

Simo, J. C., Hughes, T. J. R., 1998. Computational Inelasticity. Springer, New York.

Simo, J. C., Tarnow, N., Wong, K. K., 1992. Exact energy-momentum conserving algorithms and symplectic schemes for nonlinear dynamics. Computer Methods in Applied Mechanics and Engineering 100, 63–116.

Singh, C. V., Talreja, R., 2008. Analysis of multiple off-axis ply cracks in composite laminates. International Journal of Solids and Structures 45, 4574–4589.

Song, S., Waas, A., Shahwan, K., Xiao, X., Faruque, O., 2007. Braided textile composites under compressive loads: modeling the response, strength and degradation. Composites Science and Technology 67, 3059–3070.

Spanoudakis, J., Young, R. J., 1984a. Crack propagation in a glass particle-filled epoxy resin - part 1 effect of particle volume fraction and size. Journal of Materials Science 19, 473–486.

Spanoudakis, J., Young, R. J., 1984b. Crack propagation in a glass particle-filled epoxy resin - part 2 effect of particle-matrix adhesion. Journal of Materials Science 19, 487–496.

Spitzig, W. A., Richmond, O., 1979. Effect of hydrostatic pressure on the deformation behavior of polyethylene and polycarbonate in tension and compression. Polymer Engineering and Science 19, 1129–1139.

Stachurski, Z. H., 1986. Yield strength and anelastic limit of amorphous ductile polymers. I. Amorphous structure and deformation. Journal of Materials Science 21, 3231–3236.

Stahlecker, Z., Mobasher, B., Rajan, S. D., Pereira, J. M., 2009. Development of reliable modeling methodologies for engine fan blade out containment analysis. Part II: Finite element analysis. International Journal of Impacting Engineering 36, 447–459.

Struik, L. C. E., 1977. Physical aging in plastics and other glassy materials. Polymer Engineering and Science 17, 165–173.

Struik, L. C. E., 1978. Physical Aging in Amorphous Polymers and Other Materials. Elsevier, Amsterdam.

Tabei, A., Jiang, Y., 1999. Woven fabric composite material model with material nonlinearity for nonlinear finite element simulation. International Journal of Solids and Structures 36, 2757–2771.

Tack, J. L., 2006. Thermodynamic and mechanical properties of Epon 862 with curing agent DETDA by molecular simulation, M.S. Thesis. Texas A&M University, College Station, TX.

Talreja, R., 2006. Damage analysis for structural integrity and durability of composite materials. Fatigue & Fracture of Engineering Materials & Structures 29, 481–506.

Tan, P., Tong, L., Steven, G. P., 1997. Modelling for predicting the mechanical properties of textile composites- a review. Composites Part A 28, 903–922.

Tant, M. R., Wilkes, G. L., 1981. Physical aging studies of semicrystalline poly(ethylene terephthalate. Journal of Applied Polymer Science 26, 2813–2825.

Tervoort, T. A., Govaert, L. E., 2000. Strain hardening of polycarbonate in the glassy state. Journal of Rheology 44, 1263–1277.

Tervoort, T. A., Smit, R. J. M., Brekelmans, W. A. M., Govaert, L. E., 1998. A constitutive equation for the elasto-viscoplastic deformation of glassy polymers. Mechanics of Time-Dependent Materials 1, 269–291.

Totry, E., Gonzalez, C., Llorca, J., 2008. Prediction of the failure locus of c/peek composites under transverse compression and longitudinal shear through computational micromechanics. Composites Science and Technology 68, 3128–3136.

Treloar, L. R. G., 1975. The Physics of Rubber Elasticity. Clarendon Press, Oxford.

Trojanowski, A., Ruiz, C., Harding, J., 1997. Thermomechanical properties of polymers at high strain rates of strain. Journal de Physique IV 7, C3–447–452.

Tvergaard, V., Needleman, A., 1988. An analysis of the temperature and rate dependence of charpy v-notch energies for a high nitrogen steel. International Journal of Fracture 37, 197–215.

Tvergaard, V., Needleman, A., 2008. An analysis of thickness effects in the izod test. International Journal of Solids and Structures 45, 3951–3966.

van Breemen, L. C. A., Engels, T. A. P., Pelletier, C. G. N., Govaert, L. E., den Toonder, J. M. J., 2009. Numerical simulation of flat-tip micro-indentation of glassy polymers: influence of loading speed and thermodynamic state. Philosophical Magazine 89, 677–696.

van Melicka, H. G. H., Govaert, L. E., Raasa, B., Nautab, W. J., Meijer, H. E. H., 2003. Kinetics of ageing and re-embrittlement of mechanically rejuvenated polystyrene. Polymer 44, 1171–1179.

Varna, J., Krasnikovs, A., Kumar, R. S., Talreja, R., 2004. A synergistic damage mechanics approach to viscoelastic response of cracked cross-ply laminates. International Journal of Damage Mechanics 13, 301–334.

Vogler, T., Kyriakides, S., 1999. Inelastic behavior of an AS4/PEEK composite under combined transverse compression and shear. Part I: experiments. International Journal of Plasticity 15, 783–806.

Volynskii, A. L., Efimov, A. V., Bakeev, N. F., 2007. Structural aspects of physical aging of polymer glasses. Polymer Science - Series C 49, 301–320.

Whitcomb, J., Srirengan, K., 1996. Effects of various approximations on predicted progressive failure in plain weave composites. Composite Structures 34, 13–20.

Williams, G., Watts, D. C., 1970. Non-symetrical dielectric behavior arising from a simple empirical decay function. Transactions of the Faraday Society 66, 80–85.

Woo, K., Whitcomb, J. D., 1996. Three-dimensional failure analysis of plain weave textile composites using a global/local finite element method. Journal of Composite Materials 30, 984–1003.

Wu, P. D., Van der Giessen, E., 1994. Analysis of shear band propagation in amorphous glassy polymers. International Journal of Solids and Structures 31, 1493–1517.

Wu, P. D., Van der Giessen, E., 1996. Computational aspects of localized deformations in amorphous glassy polymers. European Journal of Mechanics 15, 799–823.

Wu, T. T., 1966. The effect of inclusion shape on the elastic moduli of a two-phase material. International Journal of Solids and Structures 2, 1–8.

Wu, Z., Ahzi, S., Arruda, E. M., Makradi, A., 2005. Modeling the large inelastic deformation response of non-filled and silica filled sl5170 cured resin. Journal of Materials Science 40, 4605–4612.

Zhu, J., Wei, S., Ryu, J., Sun, L., Luo, Z., Guo, Z., 2010. Magnetic epoxy resin nanocomposites reinforced with core-shell structured fe@feo nanoparticles: fabrication and property analysis. ACS Applied Materials and Interfaces 2, 2100–2107.

Zhu, L., Chattopadhyay, A., Goldberg, R. K., 2006. Nonlinear transient response of strain rate dependent composite laminated plates using multiscale simulation. International Journal of Solids and Structures 43, 2602–2630.

APPENDIX

Connection between flow stress and athermal shear strength

The viscoplastic law (Eq. 3.10) is rearranged as :

$$\sigma_{\mathrm{e}} = (s - \alpha\sigma_h)\left[1 - \frac{T}{A(s-\alpha\sigma_h)}\ln\frac{\dot{\epsilon}_0}{\dot{\epsilon}}\right]^{\frac{1}{m}} \tag{A.1}$$

At yield, the shear strength s has not departed from its initial value s_0 and $\sigma_e = \sigma_h = \sigma_y$ (in uniaxial conditions). With further deformation, s gradually increases, which induces a departure of the stress-strain curve from its initial linear behavior. At peak stress $\sigma_e = \sigma_h = \sigma_p$ and s is assumed to reach its value s_1. Therefore, s_1 is estimated from Eq.(A.1) such as:

$$\frac{\sigma_{\mathrm{p}}}{\sigma_{\mathrm{y}}} \approx \frac{(s_1 - \alpha\sigma_{\mathrm{p}})}{(s_0 - \alpha\sigma_{\mathrm{y}})} \equiv \frac{\bar{s}_1}{\bar{s}_0} \tag{A.2}$$

In Eq.(A.2), equality only holds for absolute temperature. However, the approximation is assumed to be still valid at low temperatures and at moderate strain-rates (no sign of dynamic effects) such that if α is known, s_1 can be estimated directly from s_0 and the experimental values of σ_{y} and σ_{p}. However, if the pressure term is neglected, the ratio $f_s \equiv \frac{\sigma_{\mathrm{p}}}{\sigma_{\mathrm{y}}}$ simply reads $f_s \approx \frac{s_1}{s_0} = \frac{s_1/\mu(T)}{s_0/\mu(T)}$ and is taken as independent of temperature. Therefore, s_1 is approximated as $s_1 = s_1(T) = f_s s_0(T)$.

Further deformation after peak stress induces a decrease of s, which results in strain softening. At the dip stress $\sigma_e = \sigma_h = \sigma_d$ and s is assumed to reach its value s_2. Therefore, similarly as for Eq.(A.2) the viscoplastic law (Eq. 3.10) reads :

$$\frac{\sigma_{\mathrm{y}}}{\sigma_{\mathrm{d}}} \approx \frac{(s_0 - \alpha\sigma_{\mathrm{y}})}{(s_2 - \alpha\sigma_{\mathrm{d}})} \equiv \frac{\bar{s}_0}{\bar{s}_2} \tag{A.3}$$

from which s_2 is estimated with the ratio $\frac{s_0}{s_2}$ being temperature independent.

Sensitivity Analysis

One key objective of the identification of material parameters is a good representation of temperature sensitivity. The latter is closely connected to the rate-sensitivity of the material through the viscoplastic flow rule. Therefore, one would expect that the difference in the flow stress caused by a finite variation ΔT in temperature can be controlled by appropriate calibration of model parameters $\dot{\epsilon}_0$ and A. The objective of this section is to derive an analytical formula giving the change in peak flow stress, i.e., $\delta\sigma_{\mathrm{p}}$, effected by variations in model parameters $\dot{\epsilon}_0$ and A. The first question addressed is that of what relationship exists between $\delta\dot{\epsilon}_0$ and δA on one side and $\delta\sigma_{\mathrm{p}}$ on the other?

The equations defining the line Eq.(3.18) reads:

$$\ln\left(\ln\dot{\bar{\epsilon}} - B\right) = \ln C + m\ln\left(\frac{\sigma_{\mathrm{e}}}{\bar{s}}\right) \tag{A.4}$$

Consider variations in A and $\dot{\epsilon}_0$:

$$\frac{\delta\left(\ln\dot{\bar{\epsilon}} - B\right)}{\ln\dot{\bar{\epsilon}} - B} = \frac{\delta C}{C} + m\frac{\delta\sigma_{\mathrm{e}}}{\sigma_{\mathrm{e}}} \tag{A.5}$$

$$-\frac{\delta B}{\ln\dot{\bar{\epsilon}} - B} = \frac{\delta C}{C} + m\frac{\delta\sigma_{\mathrm{e}}}{\sigma_{\mathrm{e}}} \tag{A.6}$$

where from Eq.(3.19):

$$\delta B = \frac{\delta\dot{\epsilon}_0}{\dot{\epsilon}_0} - \frac{\bar{s}}{T}\delta A \tag{A.7}$$

$$\delta C = \frac{\bar{s}}{T}\delta A \tag{A.8}$$

$$\frac{\delta C}{C} = \frac{\delta A}{A} \tag{A.9}$$

such that

$$\frac{\delta\sigma_{\mathrm{e}}}{\sigma_{\mathrm{e}}} = -\frac{1}{m}\left(\frac{\delta B}{\ln\dot{\bar{\epsilon}} - B} + \frac{\delta C}{C}\right) \tag{A.10}$$

$$\frac{\delta\sigma_{\mathrm{e}}}{\sigma_{\mathrm{e}}} = -\frac{1}{m}\left(\frac{1}{\ln\dot{\bar{\epsilon}} - B}(\frac{\delta\dot{\epsilon}_0}{\dot{\epsilon}_0} - \frac{\bar{s}}{T}\delta A) + \frac{\delta A}{A}\right) \tag{A.11}$$

$$\frac{\delta\sigma_{\mathrm{e}}}{\sigma_{\mathrm{e}}} = -\frac{1}{m}\left(\frac{1}{\dot{\epsilon}_0(\ln\dot{\bar{\epsilon}} - B)}\delta\dot{\epsilon}_0 + (-\frac{\bar{s}}{T(\ln\dot{\bar{\epsilon}} - B)} + \frac{1}{A})\delta A\right) \tag{A.12}$$

With this analytical formula at hand, we have investigated the influence of large variations in A at fixed $\dot{\epsilon}_0$ or vice-versa on the variation of the peak flow stress shift caused by increasing the test temperature from 25C to 80C. The results obtained suggest that varying A or $\dot{\epsilon}_0$ is not an effective way of controlling the $\Delta\sigma_{\mathrm{p}}/\Delta T$. This is not a straightforward matter because temperature dependence also enters through the shear resistance parameters s_0, etc.. This calls for extra caution in the identification of the temperature dependence of the elastic modulus, of which the identification of flow resistance is strongly dependent. In fact, we have found that the shift $\Delta\sigma_{\mathrm{p}}/\Delta T$ is best represented when the function $E(T)$ is carefully determined.

Uncertainty Analysis

The uncertainty associated with each model parameter is estimated at the appropriate step of the proposed identification procedure. While there are several potential sources of uncertainty, we have mainly accounted for that associated with the scatter in experimental data. Also, some of the values given below are primitive (direct measurement) or derived (using standard uncertainty analysis).

1. ΔT_{ref} is estimated as 5K based on seasonal variations of ambient temperature and heat gradients between the surface of a heated specimen and its interior. ΔE_{ref} is estimated as 100 MPa based on the actual scatter found in the measurements of initial slopes in the stress–strain curves determined by two independent operators. Finally, $\Delta\beta$ was derived as follows.

   The variational form of Eq.(3.14) reads:

$$\frac{\Delta E}{E} = \ln(\log \frac{E_{ref}}{E}) = \ln \beta + \ln(T - T_{ref}) \tag{A.13}$$

$$\frac{\Delta \beta}{\beta} = \frac{\Delta \log(\frac{E_{ref}}{E})}{\log(\frac{E_{ref}}{E})} + \frac{\Delta T}{T - T_{ref}} \tag{A.14}$$

$$\frac{\Delta \beta}{\beta} = \frac{\log(\frac{E_{ref}}{E_{min}}) - \log(\frac{E_{ref}}{E_{max}})}{\log(\frac{E_{ref}}{E})} + \frac{\Delta T}{T - T_{ref}} \tag{A.15}$$

   with T_{ref}=25°C and at 80°C, E_{min}=1840 MPa and E_{max}=2040 MPa. Therefore,

$$\frac{\Delta \beta}{\beta} = 0.289 + 0.091 = 0.38 \tag{A.16}$$

2. Δs_0 is derived:

   The variational form of Eq.(3.15) reads:

$$\frac{\Delta s_0}{s_0} = \frac{\Delta E}{E} + \frac{2}{1 - \nu^2} \Delta \nu \tag{A.17}$$

   With ΔE=100 MPa, E=E_{ref}=2770 MPa, ν=0.4, $\Delta\nu$=0.01, $\frac{\Delta s_0}{s_0}$=0.06.

3. $\Delta\alpha$ is based on the experimental plots.

   A linear regression based on data in compression and tension at 25°C and 10^{-1}/s gives $\Delta\alpha$=0.01.

4. Δs_1 and Δs_2 are derived:

   From Eq.(A.2),

$$\frac{\Delta s_1}{s_1} = \frac{\Delta s_0}{s_0} + \frac{\Delta \sigma_{\mathrm{p}}}{\sigma_{\mathrm{p}}} + \frac{\Delta \sigma_{\mathrm{y}}}{\sigma_{\mathrm{y}}} \tag{A.18}$$

   At 25°C and 10^{-1}/s in compression, with $\Delta\sigma_{\mathrm{p}}$=4 MPa, σ_{p}=100 MPa, $\Delta\sigma_{\mathrm{y}}$=0.5 MPa and σ_{y}=88 MPa, $\frac{\Delta s_1}{s_1}$=0.10

   From Eq.(A.3),

$$\frac{\Delta s_2}{s_2} = \frac{\Delta s_0}{s_0} + \frac{\Delta \sigma_d}{\sigma_d} + \frac{\Delta \sigma_y}{\sigma_y} \tag{A.19}$$

   At 25°C and 10^{-1}/s in compression, with $\Delta\sigma_d$=1 MPa, σ_d=86 MPa, $\frac{\Delta s_2}{s_2}$=0.08.

5. $\Delta\bar{\epsilon}_{\mathrm{p}}$ is derived based on the scatter on the yield strain ϵ_{y} added to the scatter on the strain at peak flow ϵ_{p}:

$$\bar{\epsilon}_{\mathrm{p}} = \epsilon_{\mathrm{p}} - \epsilon_{\mathrm{y}} \tag{A.20}$$

$$\frac{\Delta\bar{\epsilon}_{\mathrm{p}}}{\bar{\epsilon}_{\mathrm{p}}} = \frac{\Delta(\epsilon_{\mathrm{p}} - \epsilon_{\mathrm{y}})}{\epsilon_{\mathrm{p}} - \epsilon_{\mathrm{y}}} = \frac{\Delta\epsilon_{\mathrm{p}} + \Delta\epsilon_{\mathrm{y}}}{\epsilon_{\mathrm{p}} - \epsilon_{\mathrm{y}}} \tag{A.21}$$

   With ϵ_{p}=0.092, ϵ_{y}=0.0474, $\Delta\epsilon_{\mathrm{p}}$=0.007, $\Delta\epsilon_{\mathrm{y}}$=0.0024, $\frac{\Delta\bar{\epsilon}_{\mathrm{p}}}{\bar{\epsilon}_{\mathrm{p}}}$=0.21

6. Δh_1 and Δh_2 are derived:

   From Eq.(3.20),

$$h_1 = \frac{s_1}{\Delta\bar{\epsilon}} = \frac{s_1}{\bar{\epsilon}_\mathrm{p}} \tag{A.22}$$

$$\frac{\Delta(\epsilon_\mathrm{p} - \epsilon_\mathrm{y})}{\epsilon_\mathrm{p} - \epsilon_\mathrm{y}} = \frac{\Delta\epsilon_\mathrm{p} + \Delta\epsilon_\mathrm{y}}{\epsilon_\mathrm{p} - \epsilon_\mathrm{y}} \tag{A.23}$$

$$\frac{\Delta h_1}{h_1} = \frac{\Delta s_1}{s_1} + \frac{\Delta\bar{\epsilon}_\mathrm{p}}{\bar{\epsilon}_\mathrm{p}} \tag{A.24}$$

$\frac{\Delta h_1}{h_1}$=0.10+0.21=0.31

Also, with ϵ_d the strain at dip stress,

$$h_2 = \frac{s_2}{\Delta\bar{\epsilon}} = \frac{s_2}{\epsilon_\mathrm{d} - \epsilon_\mathrm{p}} \tag{A.25}$$

$$\frac{\Delta h_2}{h_2} = \frac{\Delta s_2}{s_2} + \frac{\Delta(\epsilon_\mathrm{d} - \epsilon_\mathrm{p})}{\epsilon_\mathrm{d} - \epsilon_\mathrm{p}} = \frac{\Delta s_2}{s_2} + \frac{\Delta\epsilon_\mathrm{p} + \Delta\epsilon_\mathrm{d}}{\epsilon_\mathrm{d} - \epsilon_\mathrm{p}} \tag{A.26}$$

With ϵ_p=0.092, ϵ_d=0.27, $\Delta\epsilon_\mathrm{p}$=0.007, $\Delta\epsilon_\mathrm{d}$=0.03, $\frac{\Delta h_2}{h_2}$=0.29

7. $\Delta m = 0.05$ since increments of 0.1 were used.

8. ΔA

   From Eq.(3.19):

$$\frac{\Delta A}{A} = \frac{\Delta C}{C} + \frac{\Delta T}{T} + \frac{\Delta s_1}{s_1} \tag{A.27}$$

   With $\frac{\Delta C}{C}$=0.15 (given by linear regression from Fig.(10)), T=298, ΔT=5, $\frac{\Delta A}{A}$=0.27.

9. $\Delta\epsilon_0$

   From Eq.(3.19):

$$\frac{\Delta \ln \dot{\epsilon}_0}{\ln \dot{\epsilon}_0} = \frac{\Delta B}{B} + \frac{\Delta A}{A} + \frac{\Delta T}{T} + \frac{\Delta s_1}{s_1} \tag{A.28}$$

With $\frac{\Delta B}{B}$=0.15 (given by linear regression from Fig.(10)), $\frac{\Delta \ln \dot{\epsilon}_0}{\ln \dot{\epsilon}_0}$=0.54.

10. ΔC^R is estimated based on the scatter in large strain flow stresses.

    ΔC^R=3 MPa.

11. ΔN

    Locking has not been observed in experiments and a value of N=7.4 has been given. A 100% variation has been applied, Fig.(58). Therefore $\frac{\Delta N}{N}$=1.

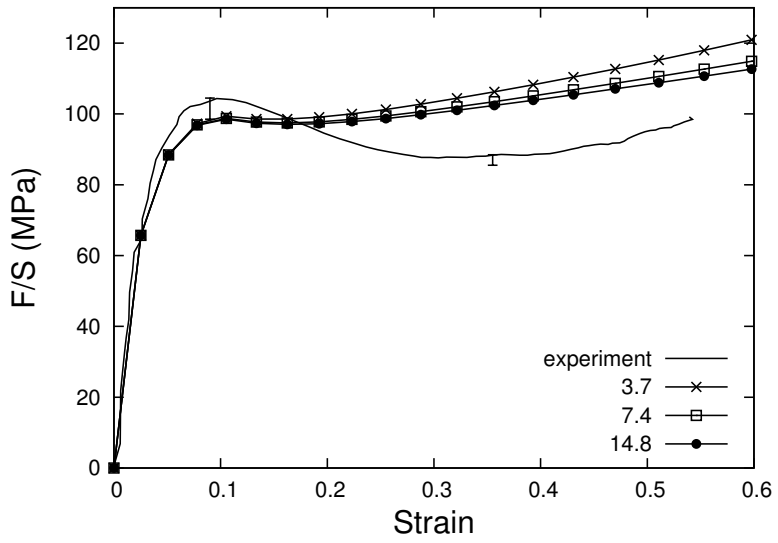

Fig. 58. Effect of 100% variation of N

Details for Step 6

Table VIII. Evolution of A and $\dot{\epsilon}_0$ with varying m

							25°C	80°C	25°C		
							10^{-1}/s	10^{-1}/s	10^{-5}/s		
m	B	ΔB	C	ΔC	A	$\dot{\epsilon}_0$	$\sigma_p^{(1)}$	$\sigma_p^{(2)}$	$\sigma_p^{(3)}$	$(\sigma_p^{(1)}$-$\sigma_p^{(2)})$	$(\sigma_p^{(1)}$-$\sigma_p^{(3)})$
0.1	-357.4	14.0	371	14.1	726.4	1.3E^6	104.90	54.36	80.20	50.55	24.71
0.3	-122.9	14.3	138.03	14.9	270.0	3.7E^6	104.96	53.01	80.77	51.96	24.19
0.5	-76.0	14.6	92.4	15.5	180.6	1.2E^7	105.03	51.48	80.74	53.55	24.29
0.83	-48.0	15.1	66.4	16.6	129.9	1.1E^8	105.15	48.35	80.69	56.80	24.46

Computational aspects

Dynamic code

A Lagrangian formulation of the field equations is employed whereby a field variable is considered as a function of convected coordinates, y^i, and time t; see Green and Zerna (1954); Needleman and Tvergaard (1983); Needleman (1989). The position of a material point in the initial configuration and current configuration, relative to the origin of a *fixed* Cartesian frame is denoted by $\mathbf{X}$ and $\mathbf{x}$, respectively. The displacement vector $\mathbf{u}$ and the deformation gradient $\mathbf{F}$ are given by,

$$\mathbf{u} = \mathbf{x} - \mathbf{X}, \quad \mathbf{F} = \frac{\partial \mathbf{x}}{\partial \mathbf{X}} \tag{A.29}$$

Denoting $\mathbf{G}_i$ and $\mathbf{g}_i$ the base vectors in the reference and current configurations, respectively, the relationships

$$\mathbf{G}_i = G^{ij}\mathbf{G}_j, \ \mathbf{g}_i = g^{ij}\mathbf{g}_j \tag{A.30}$$

define G^{ij} and g^{ij} as the inverse of the metric tensors $G_{ij} = \mathbf{G}_i \cdot \mathbf{G}_j$ and $g_{ij} = \mathbf{g}_i \cdot \mathbf{g}_j$, respectively.

In full transient analyses the dynamic principle of virtual work is written as:

$$\int_V \tau^{ij}\delta\eta_{ij}\mathrm{d}V = \int_S T^i\delta u_i\mathrm{d}S - \int_V \rho\frac{\partial^2 u^i}{\partial t^2}\delta u_i\mathrm{d}V \tag{A.31}$$

where τ^{ij} are the contravariant components of Kirchhoff stress, η_{ij} the covariant components of Green-Lagrange strain on the deformed, convected coordinate net, T^i the contravariant surface tractions and u_i the covariant displacements. Also, ρ is the mass density and V and S respectively denote the volume and surface of the body in

the reference configuration. Specifically,

$$\tau^{ij} = J\sigma^{ij}; \quad J = \sqrt{\det(g_{ij})/\det(G_{ij})} \tag{A.32}$$

$$\eta_{ij} = \frac{1}{2}\left(u_{i,j} + u_{j,i} + u^{k}_{,i}u_{k,j}\right) \tag{A.33}$$

$$T^{i} = \left(\tau^{ij} + \tau^{kj}u^{i}_{,k}\right)\nu_{j} \tag{A.34}$$

with σ^{ij} the components of Cauchy stress, J the ratio of current to reference volume and ν_j the covariant components of the reference surface normal. $()_{,i}$ denotes covariant differentiation in the reference frame.

Discretization of (A.31) in the reference configuration using a finite element grid results into equations of motion that take the form

$$\mathbf{M}\frac{\partial^2 \mathbf{U}}{\partial t^2} = \mathbf{R} \tag{A.35}$$

with $\mathbf{M}$ a symmetric definite-positive mass matrix, $\mathbf{U}$ the nodal displacement vector and $\mathbf{R}$ the nodal force vector. In the usual way, $\mathbf{U}$ results from substituting a suitable finite element approximation of the displacements u^i into (A.31) and from subsequent integration, and $\mathbf{R}$ is computed from the left hand side of (A.31) and from any applied boundary tractions, the surface integral in (A.31).

The discrete system (A.35) of equations of motion is integrated using a time stepping algorithm of the Newmark family Newmark (1959) . The sub-family of central difference schemes is written in the usual way. Let β be a real number, $0 \leq \beta \leq 1/2$, and $(\dot{})$ denote time differentiation $\partial(\ )/\partial t$, with components on appropriate base vectors. Given the nodal displacements and velocities $(\mathbf{U}_n, \dot{\mathbf{U}}_n)$ at time t_n, find

$(\mathbf{U}_{n+1}, \dot{\mathbf{U}}_{n+1})$ such that:

$$\mathbf{U}_{n+1} = \mathbf{U}_n + \Delta t \dot{\mathbf{U}}_n + \frac{1}{2}\Delta t^2[(1-2\beta)\mathbf{A}_n + 2\beta \mathbf{A}_{n+1}] \tag{A.36}$$

$$\dot{\mathbf{U}}_{n+1} = \dot{\mathbf{U}}_n + \Delta t \left(\frac{\mathbf{A}_{n+1} + \mathbf{A}_n}{2}\right) \tag{A.37}$$

with $\Delta t = t_{n+1} - t_n$ the time step and $\mathbf{A}$ the acceleration vector given by:

$$\mathbf{A}_n = \ddot{\mathbf{U}}_n = \mathbf{M}^{-1}\mathbf{R}_n \tag{A.38}$$

Central difference Newmark schemes are second-order accurate Simo et al. (1992). They are generally implicit but for $\beta = 0$ equation (A.36) is explicit for $\mathbf{U}_{n+1}$ in terms of $(\mathbf{U}_n, \dot{\mathbf{U}}_n)$, making the $\beta = 0$ case known as *explicit Newmark*. Unlike implicit members of the Newmark family, the explicit method is known to preserve momentum stricto sensu Simo et al. (1992). Here we shall use this method. In addition, a lumped mass matrix $\mathbf{M}$ is used in (A.38) instead of the consistent one. This is preferable for explicit integrators because a diagonal mass matrix offers computational accuracy as well as storage efficiency Krieg and Key (1973).

After computation of displacements and velocities at time t_{n+1} the deformation gradient, the strain rate and other kinematic quantities are directly computed. The constitutive updating is based on the rate tangent modulus method of Peirce et al. (1984) giving the Jaumann rate of Cauchy stress given as

$$\overset{\nabla}{\boldsymbol{\sigma}} = \mathbf{L}_{\tan}\dot{\boldsymbol{\eta}} + \dot{\mathbf{Q}} \tag{A.39}$$

where $\mathbf{L}_{\tan}$ and $\dot{\mathbf{Q}}$ are respectively fourth and second rank tensors. Also $\dot{\boldsymbol{\eta}}$ is the rate of Green-Lagrange strain defined after Eq. A.31; its covariant components are given by

$$\dot{\eta}_{ij} = \frac{1}{2}\left(F_i^k \dot{F}_{kj} + F_j^k \dot{F}_{kl}\right) \tag{A.40}$$

The updating of the Kirchhoff stress components in equilibrium equation (A.31) are then done by using $\tau^{ij}_{t+\triangle t} = \tau^{ij}_t + \triangle t \dot{\tau}^{ij}$ and a standard kinematic relation between the convected rate of Kirchhoff stress $\dot{\boldsymbol{\tau}}$ and the Jaumann rate of Cauchy stress $\overset{\nabla}{\boldsymbol{\sigma}}$, given by

$$\dot{\tau}^{ij} = J\left[\overset{\nabla}{\sigma}{}^{ij} + g^{kl}\dot{\eta}_{kl}\sigma^{ij} - g^{ik}\sigma^{jl}\dot{\eta}_{kl} - g^{jk}\sigma^{il}\dot{\eta}_{kl}\right] \tag{A.41}$$

Update of the back stress tensor, $\mathbf{b}$ in Eq. 3.4 is obtained using $b^{ij}_{t+\triangle t} = b^{ij}_t + \triangle t \dot{b}^{\ ij}$, where $\dot{b}^{ij}$ is obtained

$$\dot{b}^{ij} = \overset{\nabla}{b}{}^{ij} - g^{ik}b^{jl}\dot{\eta}_{kl} - g^{jk}b^{il}\dot{\eta}_{kl} \tag{A.42}$$

In Eq. 3.1, the tensor of elastic moduli $\mathbf{L}$ with components on the deformed coordinates reads

$$\mathbf{L}^{ijkl} = \frac{E}{1+\nu}\left[\frac{1}{2}\left(g^{ik}g^{jl} + g^{il}g^{jk}\right) + \frac{\nu}{1-2\nu}g^{ij}g^{kl}\right] \tag{A.43}$$

with E Young's modulus and ν Poisson's ratio.

Also, the contravariant components of the eight-chain model back stress moduli $\mathbf{R}_{8-\mathrm{ch}}$ (Eq. 3.6) is obtained as Wu and Van der Giessen (1996)

$$R^{ijkl}_{8-\mathrm{ch}} = \frac{1}{3}C^R\sqrt{N}\left[\left(\frac{\xi_c}{\sqrt{N}} - \frac{\beta_\mathrm{c}}{\lambda_c}\right)\frac{B^{ij}B^{kl}}{B^{mm}} + \frac{\beta_\mathrm{c}}{\lambda_c}\left(g^{ik}B^{jl} + B^{ik}g^{jl}\right)\right] \tag{A.44}$$

and the back stress moduli classical non Gaussian three-chain rubber elasticity model (Eq. 3.6) reads

$$R^{ijkl}_{3-\mathrm{ch}} = \begin{cases} \frac{1}{3}C^R\sqrt{N}\lambda_i^2\left(\frac{\xi_i}{\sqrt{N}} + \frac{\beta_i}{\lambda_i}\right)g^{ik}g^{jl} & \text{if } \lambda_i = \lambda_j \\ \frac{1}{3}C^R\sqrt{N}\frac{\lambda_i^2+\lambda_j^2}{\lambda_i^2-\lambda_j^2}(\lambda_i\beta_i - \lambda_j\beta_j)g^{ik}g^{jl} & \text{if } \lambda_i \neq \lambda_j \end{cases} \tag{A.45}$$

The update of mechanical fields is performed based on the rate tangent modulus method, Appendix .

The rate tangent modulus method is a one step forward gradient time integration scheme by which we have estimated the effective strain rate, $\dot{\bar{\epsilon}}$. In general $\dot{\bar{\epsilon}}$ is a function of effective plastic strain, $\bar{\epsilon}$, and a finite number of scalar variable, ψ_i. However, in our case $\bar{\epsilon}$ is not included in the functional form of effective plastic strain rate, $\dot{\bar{\epsilon}}(\psi_i)$ because $\bar{\epsilon}$ does not directly affect the strain rate hardening behavior (Eq. 3.10). Using the rate tangent method, $\bar{\epsilon}$ is obtained as a linear interpolation on the values between times t and $t + \triangle t$,

$$\triangle\bar{\epsilon} = \triangle t \left[(1-\theta)\,\dot{\bar{\epsilon}}_t + \theta\dot{\bar{\epsilon}}_{t+\triangle t}\right] \tag{A.46}$$

θ being a numerical factor between 0 and 1. Expressing the functional form of $\dot{\bar{\epsilon}}_{t+\triangle t}$ in equation(A.46) by Taylor-series-Expansion,

$$\dot{\bar{\epsilon}}_{t+\triangle t} = \dot{\bar{\epsilon}}_t + \triangle t \left(\sum_i \frac{\partial\dot{\bar{\epsilon}}}{\partial\psi_i}\dot{\psi}_i\right) \tag{A.47}$$

After substituting the rate form of the scalar variables and performing algebraic manipulation, following form of the effective strain rate at current time is obtained:

$$\dot{\bar{\epsilon}} = EP3(\frac{1}{1+\xi})\dot{\bar{\epsilon}}_t + \frac{\xi}{\sqrt{2}H(1+\xi)}\mathbf{P} : \mathbf{D} \tag{A.48}$$

where $\mathbf{P} = \mathbf{L} : \mathbf{p}$. Symmetry of $\mathbf{p}$ and $\mathbf{L}$ results in symmetric $\mathbf{P}$, which ultimately leads to symmetric tangent stiffness matrix, favorable for better convergence in solving nonlinear equations. ξ, $EP3$ and H are parameters, whose form dependent on particular material model.

After substituting $\dot{\bar{\epsilon}}$ and rate form of the internal state variables, the constitutive equation leads to the following expression,

$$\overset{\nabla}{\boldsymbol{\sigma}} = \mathbf{L}_{\tan} : \mathbf{D} + \dot{\mathbf{Q}} \tag{A.49}$$

where $\mathbf{L}_{\tan}$ and $\dot{\mathbf{Q}}$ have the following general form:

$$\mathbf{L}_{\tan} = \mathbf{L} - \frac{\xi}{\sqrt{2}H(1+\xi)}(\mathbf{P_{th}} \otimes \mathbf{P}) \tag{A.50}$$

and

$$\dot{\mathbf{Q}} = -EP3(\frac{1}{1+\xi})\dot{\bar{\epsilon}}_t\mathbf{P_{th}} \tag{A.51}$$

with

$$\mathbf{P_{th}} = \mathbf{P} + \frac{\gamma\chi\boldsymbol{\tau} : \mathbf{p}}{\rho C_p}\mathbf{L} : \mathbf{I} \tag{A.52}$$

in which γ is the coefficient of thermal expansion, C_p is the specific heat, and χ represents the fraction of plastic work converted into heat, deduced from the balance of energy.

An adaptive time stepping is used. First a conservative estimate of the stable time increment is given by the minimum dimension taken over all the elements.

$$\triangle t_{\text{dyn}} = (L_{\min}/c_{\text{d}}) \tag{A.53}$$

where $L_{\min}$ is the smallest element dimension in the mesh and c_{d} is the dilatational wave speed in terms of Young's moduli E and Poisson's ν , defined below:

$$c_{\text{d}} = \sqrt{\frac{E(1-\nu)(1-2\nu)}{\rho(1+\nu)}} \tag{A.54}$$

Then maximum allowable time steps, was further refined by using two more criteria from Wu and Van der Giessen (1994). First criteria is to ensure that effective plastic strain increment is lesser than the maximum effective plastic strain increment

$\bar{\epsilon}_{\max}$ during a time step $\triangle t$. The second criterion ensures that the drop of the athermal shear strength is lesser than a fraction f of current athermal shear strength s_t. For each increment, time step is taken to be the minimum of the three criteria, given by.

$$\triangle t = \min \left\{ \triangle t_{\text{dyn}}; \frac{\triangle \bar{\epsilon}_{\max}}{\dot{\bar{\epsilon}}}; f \frac{s}{\dot{s}_t} \right\} \tag{A.55}$$

Quasi-static code

The above constitutive model was implemented in the commercial code Abaqus as a user-defined subroutine. A rotational formulation is used which is described schematically in Fig. 59.

The formulation is based on the polar decomposition of the incremental deformation gradient ΔF, thus introducing the rotation tensor $\mathbf{R}^*$ through:

$$\mathbf{\Delta F} = \mathbf{R}^* \mathbf{U}^* \tag{A.56}$$

A rotated configuration is then obtained from the current configuration based on $\mathbf{R}^*$. All kinematic and stress-like quantities defined in the rotated configuration are indicated by the ($\hat{}$) symbol. Since the rotation part of the incremental deformation is already taken care of to reach the rotated configuration, the latter is rotation-free, *i.e.*, constitutive descriptions must be written only for the stretch part of deformations without taking account of the rotational part. Detailed derivations regarding the rotational description may be found in Simo and Hughes (1998). An important characteristic of the rotational formulation is that it preserves objectivity. Expressions for the constitutive relations of the macromolecular model in the rotated configuration are listed in another section (Sec.).

The material state in the rotated configuration is defined by a set of internal

state variables

$$[\mathbf{X}]^T = \left[\hat{\boldsymbol{\sigma}}',\ \hat{\mathbf{b}}',\ \hat{b}_{kk},\ \frac{\hat{\sigma}_{kk}}{3},\ s\right]. \tag{A.57}$$

The deviatoric-volumetric decomposition is applied to the Cauchy stress $\boldsymbol{\sigma}$ and the back stress $\mathbf{b}$ to facilitate convergence in the Newton-Raphson procedure, which is employed to obtain a converged state of the state variables at the end of a time increment Δt. The set of differential equations for the state variables includes Eq. (A.66), (A.73), and (A.75) . These differential equations are integrated with respect to time using an implicit time integration method. The full expressions of the integrated residual equations are given in the Appendix . These residual equations are solved using the Newton-Raphson method as

$$[\mathbf{R}]^T = \left[\mathbf{R}_{\hat{\boldsymbol{\sigma}}'},\ \mathbf{R}_{\hat{\mathbf{b}}'},\ R_{\hat{b}_{kk}},\ R_{\frac{\hat{\sigma}_{kk}}{3}},\ R_s\right] \tag{A.58}$$

$$\Delta[\mathbf{X}]^T = \left[\Delta\hat{\boldsymbol{\sigma}}',\ \Delta\hat{\mathbf{b}}',\ \Delta\hat{b}_{kk},\ \Delta\frac{\hat{\sigma}_{kk}}{3},\ \Delta s\right] \tag{A.59}$$

$$[\mathbf{X}] = [\mathbf{X}_0] + \Delta[\mathbf{X}] \tag{A.60}$$

$$[\mathbf{X}] = -\frac{\partial[\mathbf{R}]}{\partial\Delta[\mathbf{X}]}[\mathbf{R}] \tag{A.61}$$

, where $[\mathbf{X}_0]$ is the value of $[\mathbf{X}]$ at the beginning of a time increment Δt. To solve the residual equations (A.58), one needs to evaluate the Jacobian matrix $-\partial[\mathbf{R}]/\partial\Delta[\mathbf{X}]$. The components of the Jacobian matrix that are related to the back stress $\hat{\mathbf{b}}'$ and $\hat{b}_{kk}$ are given in the Appendix .

The consistent tangent matrix $\frac{\partial\Delta\hat{\boldsymbol{\sigma}}}{\partial\Delta\hat{\mathbf{D}}}$, which must be calculated inside an UMAT for ABAQUS to solve the boundary value problem, is computed as

$$\left[\frac{\partial\mathbf{X}}{\partial\hat{\mathbf{D}}}\right] = -\frac{\partial[\mathbf{R}]}{\partial\Delta[\mathbf{X}]}\left[\frac{\partial\mathbf{R}}{\partial\hat{\mathbf{D}}}\right] \tag{A.62}$$

$$\left[\frac{\partial\mathbf{X}}{\partial\hat{\mathbf{D}}}\right]^T = \left[\frac{\partial\hat{\boldsymbol{\sigma}}'}{\partial\hat{\mathbf{D}}},\ \frac{\partial\hat{\mathbf{b}}'}{\partial\hat{\mathbf{D}}},\ \frac{\partial\hat{b}_{kk}}{\partial\hat{\mathbf{D}}},\ \frac{\partial\frac{\hat{\sigma}_{kk}}{3}}{\partial\hat{\mathbf{D}}},\ \frac{\partial s}{\partial\hat{\mathbf{D}}}\right] \tag{A.63}$$

$$\left[\frac{\partial \mathbf{R}}{\partial \hat{\mathbf{D}}}\right]^T = \left[\frac{\partial \mathbf{R}_{\hat{\boldsymbol{\sigma}}'}}{\partial \hat{\mathbf{D}}}, \frac{\partial \mathbf{R}_{\hat{\mathbf{b}}'}}{\partial \hat{\mathbf{D}}}, \frac{\partial R_{\hat{b}_{kk}}}{\partial \hat{\mathbf{D}}}, \frac{\partial R_{\frac{\hat{\sigma}_{kk}}{3}}}{\partial \hat{\mathbf{D}}}, \frac{\partial R_s}{\partial \hat{\mathbf{D}}}\right] \tag{A.64}$$

$$\frac{\partial \Delta \hat{\boldsymbol{\sigma}}}{\partial \Delta \hat{\mathbf{D}}} = \frac{1}{\Delta t}\left(\frac{\partial \hat{\boldsymbol{\sigma}}'}{\partial \hat{\mathbf{D}}} + \mathbf{I} \otimes \frac{\partial \frac{\hat{\sigma}_{kk}}{3}}{\partial \hat{\mathbf{D}}}\right) \tag{A.65}$$

, where $\mathbf{I}$ is the second-rank identity tensor δ_{ij}. Note that the same Jacobian matrix $\partial[\mathbf{R}]/\partial\Delta[\mathbf{X}]$ in Eq. (A.61) is re-used in Eq. (A.62).

Co-rotational Formulation of Macromolecular Model

The hypoelastic constitutive law written in the current configuration in Eq. (3.1) is transformed to the equivalent form in the rotated configuration as

$$\hat{\mathrm{D}}^{\mathrm{e}} = \hat{C}^{-1} : \hat{\dot{\sigma}} \tag{A.66}$$

where the symbol on top of variables " ˆ " represents a rotated quantity following the transformation rules, $\hat{A} = \mathbf{R}^{*T} \cdot A \cdot \mathbf{R}^{*}$ and $\hat{B}_{ijpq} = R^{*}{}_{ki} R^{*}{}_{lj} R^{*}{}_{mp} R^{*}{}_{nq} B_{klmn}$. Note that $\hat{C} = C$ in case of the isotropic elasticity ; we assume the elastic response of polymeric materials to be isotropic, therefore using $\hat{D}^{\mathrm{e}} = C^{-1} : \hat{\dot{\sigma}}$. Also note that the transformed hypoelastic law does not have any objective rate such as the Jaumann rate, but it has a simple stress rate since the rotation part was already taken care of by pre-rotating the tensorial properties related to the rotation part, σ and D^{e}. This is the main advantage of utilizing the rotational formulation – calculation regarding constitutive updates are done without resort to any objective rate.

The plastic velocity gradient can be written more in general using the associative flow rule as

$$D^{\mathrm{p}} = \dot{\bar{\varepsilon}} \frac{\partial f}{\partial \sigma'} \tag{A.67}$$

$$f = \sigma_{\mathrm{e}} - \sigma_{\mathrm{y}} \tag{A.68}$$

where f is the Von-Mises yield function, σ_{y} is the yield (flow) stress, and σ_{e} is the effective stress. The corresponding equations to Eq. (3.1), (3.3), (3.4), (A.67) and (A.68) are obtained by simple algebras as

$$\hat{D} = \hat{D}^{\mathrm{e}} + \hat{D}^{\mathrm{p}} \tag{A.69}$$

$$\hat{D}^{\mathrm{p}} = \hat{\dot{\bar{\varepsilon}}} \frac{\partial \hat{f}}{\partial \hat{\sigma}'} = \hat{\dot{\bar{\varepsilon}}} \frac{3}{2\hat{\sigma}_{\mathrm{e}}} \hat{\sigma}'_{\mathrm{d}}, \quad \hat{\sigma}_{\mathrm{d}} = (\hat{\sigma} - \hat{b}) \tag{A.70}$$

$$\hat{\dot{\bar{\varepsilon}}} = \sqrt{\frac{2}{3}\hat{D}^{\mathrm{p}\prime} : \hat{D}^{\mathrm{p}\prime}}, \quad \hat{\sigma}_{\mathrm{e}} = \sqrt{\frac{3}{2}\hat{\sigma}'_{\mathrm{d}} : \hat{\sigma}'_{\mathrm{d}}} \tag{A.71}$$

$$\hat{f} = \hat{\sigma}_{\mathrm{e}} - \sigma_{\mathrm{y}} \tag{A.72}$$

The back stress evolution equation derived by Wu and Van der Giessen (1996) is also transformed to the rotated one in the same manner as to obtain Eq. (A.66) as

$$\dot{\hat{b}} = \hat{R} : \hat{D}^{\mathrm{p}}. \tag{A.73}$$

Note that the equation $\overset{\nabla}{b} = R : D^{\mathrm{p}}$ is derived utilizing the Jaumann rate, not the Green-McInnis-Naghdi rate, therefore $\overset{\nabla}{b}$ must be the Jaumann rate, while the equation $D^{\mathrm{e}} = C^{-1} : \overset{\nabla}{\sigma}$ can be obtained utilizing any objective rate, *i.e.*, $\overset{\nabla}{\sigma}$ could be the Jaumann or the Green-McInnis-Naghdi rate. To satisfy the constraint on $\overset{\nabla}{b}$, the Jaumann rate was chosen for $\overset{\nabla}{\sigma}$ – this fits the rotational framework utilizing $\mathbf{R}^*$ from the incremental deformation gradient ΔF in Fig. 59, not $\mathbf{R}$ from the total deformation gradient F.

The corresponding rotated equations to Eq. (3.10) to (3.12) are written as

$$\hat{\dot{\bar{\varepsilon}}} = \dot{\varepsilon}_0 \exp\left[- \frac{A(s - \alpha\hat{\sigma}_{\mathrm{h}})}{T}\left(1 - \left(\frac{\hat{\sigma}_{\mathrm{e}}}{s - \alpha\hat{\sigma}_{\mathrm{h}}}\right)^m\right)\right] \tag{A.74}$$

$$\dot{s} = h_1(\hat{\bar{\varepsilon}})\left(1 - \frac{s}{s_1(T, \hat{\dot{\bar{\varepsilon}}})}\right)\hat{\dot{\bar{\varepsilon}}} + h_2(\hat{\bar{\varepsilon}})\left(1 - \frac{s}{s_2(T, \hat{\dot{\bar{\varepsilon}}})}\right)\hat{\dot{\bar{\varepsilon}}} \tag{A.75}$$

$$h_1(\hat{\bar{\varepsilon}}) = -h_0\left[\tanh\left(\frac{\hat{\bar{\varepsilon}} - \bar{\varepsilon}_{\mathrm{p}}}{g\bar{\varepsilon}_{\mathrm{p}}}\right) - 1\right], \quad h_2(\hat{\bar{\varepsilon}}) = -h_3\left[\tanh\left(\frac{\hat{\bar{\varepsilon}} - \bar{\varepsilon}_{\mathrm{p}}}{g\bar{\varepsilon}_{\mathrm{p}}}\right) + 1\right] \tag{A.76}$$

This rotated description of the macromolecular model is derived specially for a user subroutine for ABAQUS, UMAT ABAQUS (2009) by utilizing the Jaumann rate.

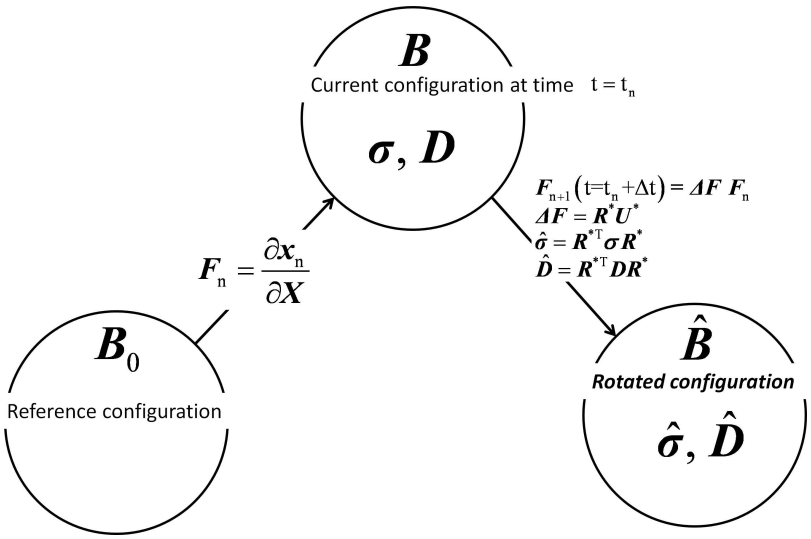

Fig. 59. Principle of co-rotational formulation.

Residual Equations and Jacobian Matrix

The expressions of R_i that are used in Eq. (A.58) are given:

$$\mathbf{R}_{\hat{\boldsymbol{\sigma}}'} = \frac{1}{2\mu}\left(\frac{\hat{\boldsymbol{\sigma}}' - \hat{\boldsymbol{\sigma}}'_0}{\Delta t}\right) + \dot{\bar{\varepsilon}}\frac{3}{2\sigma_{\mathrm{e}}}(\hat{\boldsymbol{\sigma}}' - \hat{\mathbf{b}}') - \hat{\mathbf{D}}' \tag{A.77}$$

$$\mathbf{R}_{\hat{\mathbf{b}}'} = \frac{1}{\Delta t}(\hat{\mathbf{b}}' - \hat{\mathbf{b}}'_0) - J : \hat{R} : \hat{\mathbf{D}} + J : \hat{R} : C^{-1} : \left(\frac{\hat{\boldsymbol{\sigma}}' + (\frac{\hat{\sigma}_{kk}}{3})\mathbf{I} - \hat{\boldsymbol{\sigma}}'_0 - (\frac{\hat{\sigma}_{kk}}{3})_0\mathbf{I}}{\Delta t}\right) \tag{A.78}$$

$$R_{\hat{b}_{kk}} = \frac{1}{\Delta t}(\hat{b}_{kk} - (\hat{b}_{kk})_0) - \mathbf{I} : \hat{R} : \hat{\mathbf{D}} + \mathbf{I} : \hat{R} : C^{-1} : \left(\frac{\hat{\boldsymbol{\sigma}}' + (\frac{\hat{\sigma}_{kk}}{3})\mathbf{I} - \hat{\boldsymbol{\sigma}}'_0 - (\frac{\hat{\sigma}_{kk}}{3})_0\mathbf{I}}{\Delta t}\right) \tag{A.79}$$

$$R_{\frac{\hat{\sigma}_{kk}}{3}} = \frac{1}{\Delta t}\left[\frac{\hat{\sigma}_{kk}}{3} - \left(\frac{\hat{\sigma}_{kk}}{3}\right)_0\right] - K\hat{D}_{kk} \tag{A.80}$$

$$R_s = \frac{s - s_0}{\Delta t} - h_1\left(1 - \frac{s}{s_1}\right)\dot{\bar{\varepsilon}} - h_2\left(1 - \frac{s}{s_2}\right)\dot{\bar{\varepsilon}} \tag{A.81}$$

where the subscript "$_0$" represents values at the beginning of a time increment Δt, J is the fourth-rank projector into the deviatoric hyperplane, *i.e.*, $\frac{1}{2}(\delta_{ik}\delta_{jl}+\delta_{il}\delta_{jk})-\frac{1}{3}\delta_{ij}\delta_{kl}$, $\mathbf{I}$ is the second-rank identity tensor δ_{ij} and K is the elastic bulk modulus $K = \frac{E}{3(1-2\nu)}$.

The components of the Jacobian matrix related to the back stress $\hat{\mathbf{b}}$ are given as

$$\mathbf{R}_{\hat{\mathbf{b}}',\hat{\boldsymbol{\sigma}}'} = \frac{1}{\Delta t}J : \hat{R} : C^{-1} \tag{A.82}$$

$$\mathbf{R}_{\hat{\mathbf{b}}',\hat{\mathbf{b}}'} = \frac{1}{\Delta t}J \tag{A.83}$$

$$\mathbf{R}_{\hat{\mathbf{b}}',\hat{b}_{kk}} = \mathbf{0} \tag{A.84}$$

$$\mathbf{R}_{\hat{\mathbf{b}}',\frac{\hat{\sigma}_{kk}}{3}} = \frac{1}{\Delta t}J : \hat{R} : C^{-1} : \mathbf{I} \tag{A.85}$$

$$\mathbf{R}_{\hat{\mathbf{b}}',s} = \mathbf{0} \tag{A.86}$$

$$R_{\hat{b}_{kk},\hat{\boldsymbol{\sigma}}'} = \frac{1}{\Delta t}\mathbf{I} : \hat{R} : C^{-1} \tag{A.87}$$

$$R_{\hat{b}_{kk},\hat{\mathbf{b}}'} = \mathbf{0} \tag{A.88}$$

$$R_{\hat{b}_{kk},\hat{b}_{kk}} = \frac{1}{\Delta t} \tag{A.89}$$

$$R_{\hat{b}_{kk},\frac{\hat{\sigma}_{kk}}{3}} = \frac{1}{\Delta t}\mathbf{I} : \hat{R} : C^{-1} : \mathbf{I} \tag{A.90}$$

$$R_{\hat{b}_{kk},s} = 0 \tag{A.91}$$

where $\mathbf{0}$ is the second-rank zero tensor.

Complementary analysis on flow localization

In this section, flow localization has been studied with numerical simulations performed on a full specimen on a fictitious material. The material parameters used in these simulations are listed in Table IX under 'Material E'.

Stress-strain curves defined with different strain measures, considering single element and full specimen calculations, are plotted in Fig.60. The intrinsic response of this fictitious material exhibits low softening, low rate of softening and little large strain hardening. The stress-strain curves plotted with strain measures $\bar{\epsilon}_{22}$ and ε are very similar, whereas $\epsilon_{22}^{\text{local}}$ is much higher after peak stress. This observation suggests that flow localization initiated at the center of the specimen, and intensified therein without propagating to the neighoring regions. As a consequence, a more pronounced and more localized neck are expected in comparison with EPON 862. These features are actually observed, Fig.61.

Table IX. Material parameters used in the finite-element calculations for material "E".

Material parameter	Units	Description	Material E
ρ	kg/m^3	mass density	1100
E_r	GPa	modulus at T_r	2.2
T_r	K	reference temperature	323
β	1/K	temperature dependence	0
ν	—	Poisson's ratio	0.36
s_0/E	—	initial shear strength	62
s_1/s_0	—	pre-peak strength	1.5
s_2/s_0	—	saturation strength	1.4
h_1	MPa	pre-peak hardening	3000
h_2	MPa	rate of yield drop	3000
$\bar{\epsilon}_p$	—	peak plastic strain	0.2
f	—		0.3
α	—	pressure-sensitivity	0.001
m	—	rate-sensitivity	5/6
$\dot{\epsilon}_0$	s^{-1}	rate-sensitivity	1.10^{13}
A	1/K	rate-sensitivity	250
C^R	MPa	rubbery modulus	0.5
N	—	number of rigid links	5.1

(a)

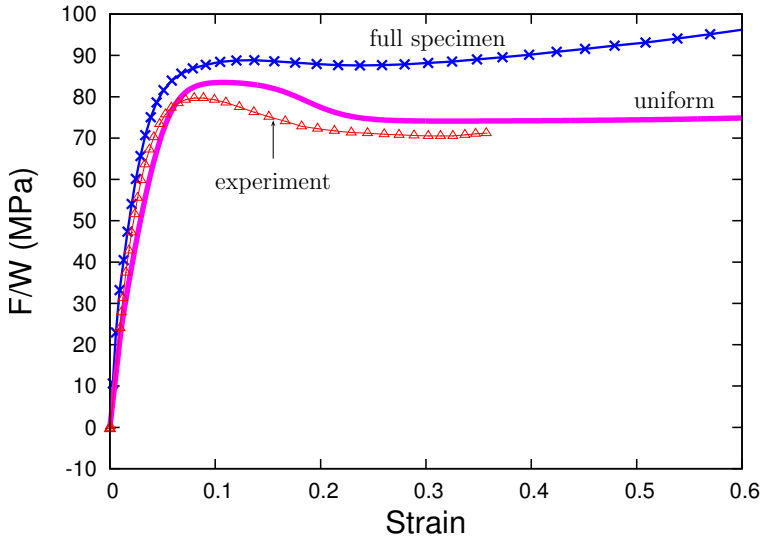

(b)

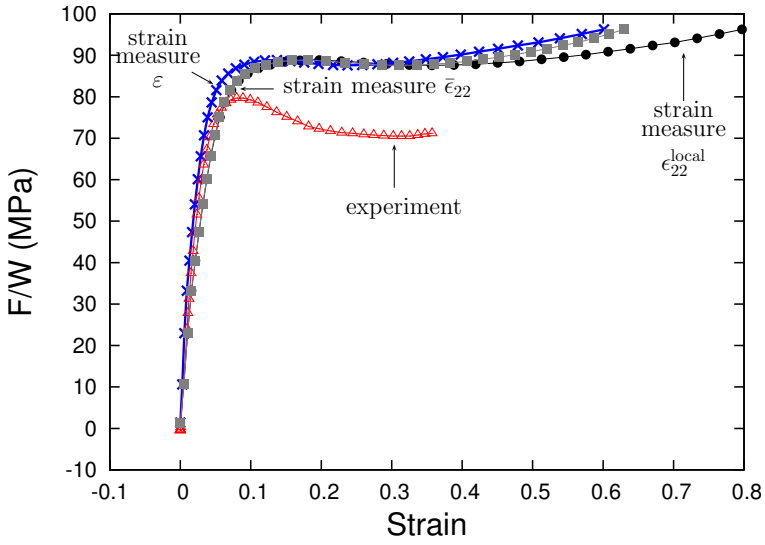

Fig. 60. Material 'E', in tension: (a) computed true stress versus strain curves for $T = 50°\text{C}$, at 10^{-1}/s for full specimen response (ε) and single element uniform response and (b) computed true stress versus strain curves for $T = 50°\text{C}$, at 10^{-1}/s and for three definitions of the "true" strain: $\epsilon_{22}^{\text{local}}$ in (6.2) or $\bar{\epsilon}_{22}$ in (6.3) or ε in (6.1). **Note:** The computed stress has been multiplied by a coefficient of 0.87 to accomodate the initial stiffness between experiments on EPON 862 (axisymmetric conditions) and simulations (plane strain conditions).

(a)

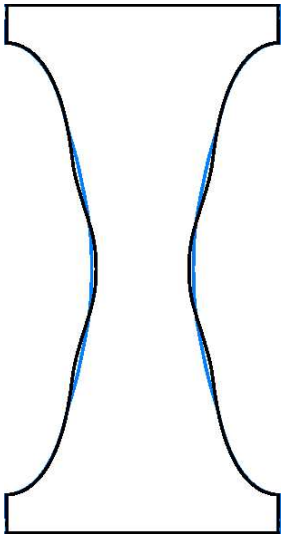

(b)

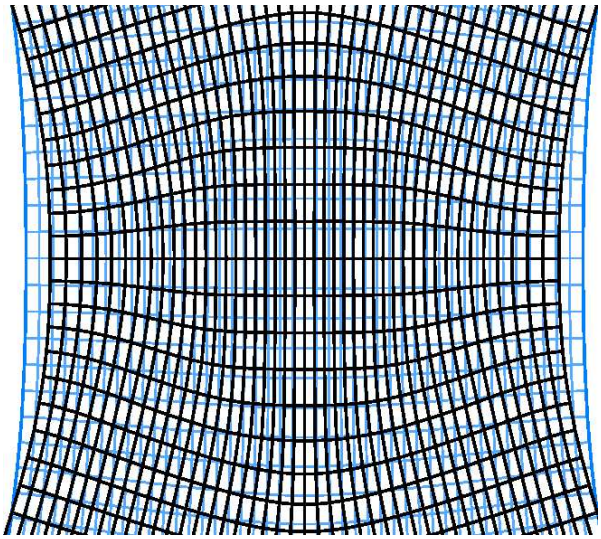

Fig. 61. (a) Deformed specimens at a macroscopic strain of 0.15 for EPON 862 (blue) and the fictitious material "E" (Black); (b) Close-up within the necking region showing the deformed mesh

Tangent modulus method including thermal softening

We recall the plastic part of the total rate of deformation tensor :

$$\boldsymbol{D^p} = \dot{\bar{\epsilon}}\boldsymbol{p} \tag{A.92}$$

A linear interpolation is used to estimated the effective plastic strain rate :

$$\dot{\bar{\epsilon}} \;=\; (1-\theta)\dot{\bar{\epsilon}}_t + \theta\dot{\bar{\epsilon}}_{t+\Delta t} \tag{A.93}$$

The taylor expansion of $\dot{\bar{\epsilon}}(\sigma_e, T) = \dot{\epsilon_0}\exp\Big(-\frac{A(s-\alpha\sigma_h)}{T}\big(1-(\frac{\sigma_e}{s-\alpha\sigma_h})^m\big)\Big)$ gives :

$$\dot{\bar{\epsilon}}_{t+\Delta t} \;=\; \dot{\bar{\epsilon}}_t + \frac{\partial\dot{\bar{\epsilon}}}{\partial\sigma_e}\dot{\sigma}_e + \frac{\partial\dot{\bar{\epsilon}}}{\partial T}\dot{T} \tag{A.94}$$

Assuming adiabatic conditions, the balance of energy gives :

$$\dot{T} \;=\; \frac{\chi\boldsymbol{\tau} : \boldsymbol{D^p}}{\rho C_p} = \frac{\chi\boldsymbol{\tau} : \boldsymbol{p}}{\rho C_p}\dot{\bar{\epsilon}} \tag{A.95}$$

Defining :

$$\boldsymbol{p} = \frac{1}{\sqrt{2}\sigma_e}\boldsymbol{\sigma_d}' \tag{A.96}$$

and writing (A.94) and (A.95) into (A.93), we obtain :

$$\dot{\bar{\epsilon}} \;=\; \frac{1}{1-\frac{\partial\dot{\bar{\epsilon}}}{\partial T}\frac{\chi\boldsymbol{\tau}:\boldsymbol{\sigma_d}'}{\sqrt{2}\sigma_e\rho C_p}\theta\Delta t}(\dot{\bar{\epsilon}}_t + \theta\Delta t\frac{\partial\dot{\bar{\epsilon}}}{\partial\sigma_e}\dot{\sigma}_e) \tag{A.97}$$

In (A.97) $\dot{\sigma}_e$ must be assessed. As

$$\sigma_e \;=\; \sqrt{\frac{1}{2}\boldsymbol{\sigma_d}' : \boldsymbol{\sigma_d}'} \tag{A.98}$$

we obtain :

$$\dot{\sigma}_e = \sqrt{\frac{1}{2}\overset{\triangledown}{\boldsymbol{\sigma_d}'} : \boldsymbol{\sigma_d}'} = \frac{1}{2\sigma_e}(\boldsymbol{\sigma_d}' : \overset{\triangledown}{\boldsymbol{\sigma_d}}') = \frac{1}{2\sigma_e}(\boldsymbol{\sigma_d}' : \overset{\triangledown}{\boldsymbol{\sigma_d}}) \tag{A.99}$$

$$= \frac{1}{2\sigma_e}\big((\boldsymbol{\sigma_d}' : \overset{\triangledown}{\boldsymbol{\sigma}}) - (\boldsymbol{\sigma_d}' : \overset{\triangledown}{\boldsymbol{b}})\big) = \frac{1}{2\sigma_e}\big((\boldsymbol{\sigma_d}' : (\underline{\boldsymbol{\mathcal{L}}} : \boldsymbol{D^e})) - (\boldsymbol{\sigma_d}' : (\underline{\boldsymbol{\mathcal{R}}} : \boldsymbol{D}))\big)$$

$$= \frac{1}{2\sigma_e}\big((\boldsymbol{\sigma_d}' : (\underline{\boldsymbol{\mathcal{L}}} : (\boldsymbol{D} - \boldsymbol{D^p} - \boldsymbol{D^{th}}))) - (\boldsymbol{\sigma_d}' : (\underline{\boldsymbol{\mathcal{R}}} : \boldsymbol{D^p}))\big) \tag{A.100}$$

$$= \frac{1}{2\sigma_e}\big(\boldsymbol{\sigma_d}' : (\underline{\boldsymbol{\mathcal{L}}} : \boldsymbol{D}) - \boldsymbol{\sigma_d}' : (\underline{\boldsymbol{\mathcal{L}}} : \boldsymbol{D^p}) - \boldsymbol{\sigma_d}' : (\underline{\boldsymbol{\mathcal{L}}} : \boldsymbol{D^{th}}) - \boldsymbol{\sigma_d}' : (\underline{\boldsymbol{\mathcal{R}}} : \boldsymbol{D^p})\big)$$

$$= \frac{1}{2\sigma_e}\big((\underline{\boldsymbol{\mathcal{L}}} : \boldsymbol{\sigma_d}') : \boldsymbol{D} - (\underline{\boldsymbol{\mathcal{L}}} : \boldsymbol{\sigma_d}') : \boldsymbol{D^p} - (\underline{\boldsymbol{\mathcal{L}}} : \boldsymbol{\sigma_d}') : \boldsymbol{D^{th}}$$
$$-\boldsymbol{\sigma_d}' : (\underline{\boldsymbol{\mathcal{R}}} : \boldsymbol{D^p})\big) \tag{A.101}$$

Considering (A.92) and the following properties :

$$\underline{\boldsymbol{\mathcal{L}}} : \boldsymbol{\sigma_d}' = 2G\boldsymbol{\sigma_d}' \tag{A.102}$$

$$\boldsymbol{D^{th}} = \gamma\dot{T}\boldsymbol{I} \tag{A.103}$$

(A.101) reads

$$\dot{\sigma}_e = \frac{1}{2\sigma_e}\big(2G\boldsymbol{\sigma_d}' : \boldsymbol{D} - 2G\boldsymbol{\sigma_d}' : (\frac{1}{\sqrt{2}\sigma_e}\dot{\bar{\epsilon}}\boldsymbol{\sigma_d}') - 2G\boldsymbol{\sigma_d}' : (\gamma\dot{T}\boldsymbol{I})$$
$$-\boldsymbol{\sigma_d}' : \underline{\boldsymbol{\mathcal{R}}} : (\frac{1}{\sqrt{2}\sigma_e}\dot{\bar{\epsilon}})\boldsymbol{\sigma_d}'\big) \tag{A.104}$$

Using (A.95) into (A.104), we get :

$$\begin{aligned}\dot{\sigma_e} &= \frac{1}{2\sigma_e}\big(2G\boldsymbol{\sigma_d}' : \boldsymbol{D} - \frac{2G}{\sqrt{2}\sigma_e}\boldsymbol{\sigma_d}' : \boldsymbol{\sigma_d}'\dot{\bar{\epsilon}} - \frac{2G\gamma\chi\boldsymbol{\tau} : \boldsymbol{\sigma_d}'}{\sqrt{2}\sigma_e\rho C_p}\boldsymbol{\sigma_d}' : \boldsymbol{I}\dot{\bar{\epsilon}} \\ &\quad -\frac{1}{\sqrt{2}\sigma_e}\boldsymbol{\sigma_d}' : \underline{\boldsymbol{\mathcal{R}}} : \boldsymbol{\sigma_d}'\dot{\bar{\epsilon}}\big) \\ &= \frac{G}{\sigma_e}\boldsymbol{\sigma_d}' : \boldsymbol{D} - \dot{\bar{\epsilon}}\big(\frac{G}{\sqrt{2}{\sigma_e}^2}\boldsymbol{\sigma_d}' : \boldsymbol{\sigma_d}' + \frac{G\gamma\chi\boldsymbol{\tau} : \boldsymbol{\sigma_d}'}{\sqrt{2}{\sigma_e}^2\rho C_p}\boldsymbol{\sigma_d}' : \boldsymbol{I} \\ &\quad +\frac{1}{2\sqrt{2}{\sigma_e}^2}\boldsymbol{\sigma_d}' : \underline{\boldsymbol{\mathcal{R}}} : \boldsymbol{\sigma_d}'\big) \end{aligned} \tag{A.105}$$

Using (A.97) and (A.98) into (A.105), we finally obtain :

$$\begin{aligned}\dot{\sigma_e} &= \frac{G}{\sigma_e}\boldsymbol{\sigma_d}' : \boldsymbol{D} - \frac{1}{1 - \frac{\partial\dot{\bar{\epsilon}}}{\partial T}\frac{\chi\boldsymbol{\tau}:\boldsymbol{\sigma_d}'}{\sqrt{2}\sigma_e\rho C_p}\theta\Delta t}(\dot{\bar{\epsilon}}_t + \theta\Delta t\frac{\partial\dot{\bar{\epsilon}}}{\partial\sigma_e}\dot{\sigma_e})\big(\sqrt{2}G + \frac{G\gamma\chi\boldsymbol{\tau} : \boldsymbol{\sigma_d}'}{\sqrt{2}{\sigma_e}^2\rho C_p}\boldsymbol{\sigma_d}' : \boldsymbol{I} \\ &\quad +\frac{1}{2\sqrt{2}{\sigma_e}^2}\boldsymbol{\sigma_d}' : \underline{\boldsymbol{\mathcal{R}}} : \boldsymbol{\sigma_d}'\big) \end{aligned} \tag{A.106}$$

We define the following quantities :

$$H = \sqrt{2}G + \frac{G\gamma\chi\boldsymbol{\tau} : \boldsymbol{\sigma_d}'}{\sqrt{2}{\sigma_e}^2\rho C_p}\boldsymbol{\sigma_d}' : \boldsymbol{I} + \frac{1}{2\sqrt{2}{\sigma_e}^2}\boldsymbol{\sigma_d}' : \underline{\boldsymbol{\mathcal{R}}} : \boldsymbol{\sigma_d}' \tag{A.107}$$

$$EP3 = \frac{1}{1 - \frac{\partial\dot{\bar{\epsilon}}}{\partial T}\frac{\chi\boldsymbol{\tau}:\boldsymbol{\sigma_d}'}{\sqrt{2}\sigma_e\rho C_p}\theta\Delta t} \tag{A.108}$$

$$\xi = H\theta\Delta t\frac{\partial\dot{\bar{\epsilon}}}{\partial\sigma_e}EP3 \tag{A.109}$$

Therefore, (A.106) reads :

$$\dot{\sigma_e} = \frac{1}{1+\xi}(\frac{G}{\sigma_e}\boldsymbol{\sigma_d}' : \boldsymbol{D} - EP3H\dot{\bar{\epsilon}}_t) \tag{A.110}$$

As $\boldsymbol{P} = \underline{\boldsymbol{\mathcal{L}}} : \boldsymbol{p}$, (A.110) reads :

$$\dot{\sigma_e} = \frac{1}{1+\xi}(\frac{1}{\sqrt{2}}\boldsymbol{P} : \boldsymbol{D} - EP3H\dot{\bar{\epsilon}}_t) \tag{A.111}$$

We substitute the value of $\dot{\sigma_e}$ in (A.111) into the plastic multiplier of (A.97) :

$$\begin{aligned}
\dot{\bar{\epsilon}} &= EP3(\dot{\bar{\epsilon}}_t + \theta\Delta t\frac{\partial\dot{\bar{\epsilon}}}{\partial\sigma_e}\dot{\sigma_e}) \\
&= EP3\dot{\bar{\epsilon}}_t + EP3\theta\Delta t\frac{\partial\dot{\bar{\epsilon}}}{\partial\sigma_e}\frac{1}{1+\xi}(\frac{1}{\sqrt{2}}\boldsymbol{P} : \boldsymbol{D} - EP3H\dot{\bar{\epsilon}}_t) \\
&= EP3(\frac{1}{1+\xi})\dot{\bar{\epsilon}}_t + \frac{\xi}{\sqrt{2}H(1+\xi)}\boldsymbol{P} : \boldsymbol{D}
\end{aligned} \tag{A.112}$$

Finally, the update of quantities is made by the tangent modulus method. It reads :

$$\begin{aligned}
\overset{\triangledown}{\boldsymbol{\sigma}} &= \underline{\boldsymbol{\mathcal{L}}} : \boldsymbol{D^e} = \underline{\boldsymbol{\mathcal{L}}} : \boldsymbol{D} - \underline{\boldsymbol{\mathcal{L}}} : \boldsymbol{D^p} - \underline{\boldsymbol{\mathcal{L}}} : \boldsymbol{D^{th}} = \underline{\boldsymbol{\mathcal{L}}} : \boldsymbol{D} - \dot{\bar{\epsilon}}(\boldsymbol{P} + \frac{\gamma\chi\boldsymbol{\tau} : \boldsymbol{p}}{\rho C_p}\underline{\boldsymbol{\mathcal{L}}} : \boldsymbol{I}) \\
&= \underline{\boldsymbol{\mathcal{L}}} : \boldsymbol{D} - (EP3(\frac{1}{1+\xi})\dot{\bar{\epsilon}}_t + \frac{\xi}{\sqrt{2}H(1+\xi)}\boldsymbol{P} : \boldsymbol{D})(\boldsymbol{P} + \frac{\gamma\chi\boldsymbol{\tau} : \boldsymbol{p}}{\rho C_p}\underline{\boldsymbol{\mathcal{L}}} : \boldsymbol{I}) \\
&= \underline{\boldsymbol{\mathcal{L}}} : \boldsymbol{D} - EP3(\frac{1}{1+\xi})\dot{\bar{\epsilon}}_t(\boldsymbol{P} + \frac{\gamma\chi\boldsymbol{\tau} : \boldsymbol{p}}{\rho C_p}\underline{\boldsymbol{\mathcal{L}}} : \boldsymbol{I}) - \frac{\xi}{\sqrt{2}H(1+\xi)}\big((\boldsymbol{P} : \boldsymbol{D})\boldsymbol{P} \\
&\quad + \frac{\gamma\chi\boldsymbol{\tau} : \boldsymbol{p}}{\rho C_p}(\boldsymbol{P} : \boldsymbol{D})\underline{\boldsymbol{\mathcal{L}}} : \boldsymbol{I}\big)
\end{aligned} \tag{A.113}$$

Using the property $(\boldsymbol{a} \otimes \boldsymbol{b}) : \boldsymbol{c} = (\boldsymbol{b} : \boldsymbol{c})\boldsymbol{a}$ (A.113) can be written as :

$$\begin{aligned}
\overset{\triangledown}{\boldsymbol{\sigma}} &= \underline{\boldsymbol{\mathcal{L}}} : \boldsymbol{D} - EP3(\frac{1}{1+\xi})\dot{\bar{\epsilon}}_t(\boldsymbol{P} + \frac{\gamma\chi\boldsymbol{\tau} : \boldsymbol{p}}{\rho C_p}\underline{\boldsymbol{\mathcal{L}}} : \boldsymbol{I}) \\
&\quad - \frac{\xi}{\sqrt{2}H(1+\xi)}\big((\boldsymbol{P} \otimes \boldsymbol{P}) : \boldsymbol{D} + \frac{\gamma\chi\boldsymbol{\tau} : \boldsymbol{p}}{\rho C_p}((\underline{\boldsymbol{\mathcal{L}}} : \boldsymbol{I}) \otimes \boldsymbol{P}) : \boldsymbol{D}\big)
\end{aligned}$$

Or,

$$\begin{aligned}
\overset{\triangledown}{\boldsymbol{\sigma}} &= \big(\underline{\boldsymbol{\mathcal{L}}} - \frac{\xi}{\sqrt{2}H(1+\xi)}\big(\boldsymbol{P} \otimes \boldsymbol{P} + \frac{\gamma\chi\boldsymbol{\tau} : \boldsymbol{p}}{\rho C_p}(\underline{\boldsymbol{\mathcal{L}}} : \boldsymbol{I}) \otimes \boldsymbol{P}\big)\big) : \boldsymbol{D} \\
&\quad - EP3(\frac{1}{1+\xi})\dot{\bar{\epsilon}}_t(\boldsymbol{P} + \frac{\gamma\chi\boldsymbol{\tau} : \boldsymbol{p}}{\rho C_p}\underline{\boldsymbol{\mathcal{L}}} : \boldsymbol{I})
\end{aligned} \tag{A.114}$$

With the definition of :

$$\boldsymbol{P_{th}} = \boldsymbol{P} + \frac{\gamma\chi\boldsymbol{\tau} : \boldsymbol{p}}{\rho C_p}\underline{\boldsymbol{\mathcal{L}}} : \boldsymbol{I} \tag{A.115}$$

we can write (A.114) under the form :

$$\overset{\triangledown}{\boldsymbol{\sigma}} = \left(\underline{\boldsymbol{\mathcal{L}}} - \frac{\xi}{\sqrt{2}H(1+\xi)}(\boldsymbol{P_{th}} \otimes \boldsymbol{P})\right) : \boldsymbol{D} - EP3(\frac{1}{1+\xi})\dot{\bar{\epsilon}}_t \boldsymbol{P_{th}} \tag{A.116}$$

Finally, the tangent modulus reads :

$$\overset{\triangledown}{\boldsymbol{\sigma}} = \underline{\boldsymbol{\mathcal{L}}}^{\boldsymbol{tan}} : \boldsymbol{D} - \boldsymbol{RFBJ} \tag{A.117}$$

where

$$\underline{\boldsymbol{\mathcal{L}}}^{\boldsymbol{tan}} = \underline{\boldsymbol{\mathcal{L}}} - \frac{\xi}{\sqrt{2}H(1+\xi)}(\boldsymbol{P_{th}} \otimes \boldsymbol{P}) \tag{A.118}$$

and

$$\boldsymbol{RFBJ} = EP3(\frac{1}{1+\xi})\dot{\bar{\epsilon}}_t \boldsymbol{P_{th}} \tag{A.119}$$

VITA

Xavier (Marc Nicolas) Poulain was born in Calais, France. He obtained his Bachelor of Science degree in mechanial engineering from CESTI Paris/Supmeca in 2002 and his Master of Science degree in mechanics from Université Paris VI in 2002. For two years he worked as a Stress Analysis engineer and Project engineer. He arrived at College Station, Texas in the fall of 2005 to pursue a doctoral degree in aerospace engineering at Texas A&M University and graduated with his Ph.D. in December 2010. During his stay in the graduate school, he has worked as a teaching assistant and as a research assistant in the Department of Aerospace Engineering. His primary research interest is in the broad area of computational materials science, with emphasis on polymer and polymer composite science, finite element analysis, multiscale modeling, viscoplasticity and fracture mechanics. He may be contacted via email at: xavier.m.poulain@gmail.com.

Mailing address:
Xavier Poulain
Texas A&M University
Department of Aerospace Engineering
H. R. Bright Building, # 701, Ross Street - TAMU 3141
College Station, TX 77843-3141

The typist for this dissertation was Xavier Poulain.